

Multiscale Modeling of Reaction and Diffusion in Zeolites

Vom Promotionsausschuss der
Technischen Universität Hamburg-Harburg
zur Erlangung des akademischen Grades
Doktor-Ingenieur (Dr.-Ing.)
genehmigte Dissertation

von
Niels Hansen

aus
Hamburg

2010

1. Gutachter: Prof. Dr. Dr. h. c. Frerich J. Keil
2. Gutachter: Prof. Dr. Andreas Liese
3. Gutachter: Prof. Dr. Alexis T. Bell

Tag der mündlichen Prüfung: 23.02.2010

Acknowledgments

This work has been carried out with the Department of Chemical Reaction Engineering (Prof. Frerich J. Keil) at the Hamburg University of Technology in Germany. The project entailed joint work with the Department of Chemical Engineering (Prof. Alexis T. Bell) at the University of California in Berkeley, USA.

First of all, I would like to express my gratitude to my supervisors. To Prof. Keil who gave me the possibility to work in this field of research. He has been an outstanding advisor and teacher. The faithful atmosphere in the group as well as the possibility to carry out part of the work abroad has been a rewarding and enjoyable experience. To Prof. Bell, I am thankful for giving me the opportunity to work in his group as a visiting scholar and for offering invaluable assistance, support and guidance.

Next I would like to thank Prof. Rajamani Krishna for his advice and the discussions about modeling multicomponent adsorption and diffusion in zeolites.

I am grateful to Prof. Joachim Sauer for giving me the possibility to visit his group and for the invaluable support he gave me regarding the quantum chemical modeling of reactions in zeolites.

I am indebted to many former and current group members in Hamburg and Berkeley for providing support and assistance. In Hamburg I would like to thank, in particular, Sven Jakobtorweihen for guiding my first steps in the field of molecular simulations, Andreas Heyden for introducing me into the field of quantum chemical calculations, Nils Zimmermann for support with Gnuplot and the great time in Berkeley 2008, Till Brüggemann for helping me with some calculations presented in chapter 8, and Klaus Mandel for all the computer support. I would also like to thank all other colleagues for providing a nice and relaxed working environment: Achim Bartsch, Christina Laarmann, Aykut Argönül, Denis Chaykin, Diana Khashimova, Kobiljon Kholmatov, Alexander Rudenko, Diana Tranca, and Hermine Oppelaar.

In Berkeley I would like to thank, in particular, Jason Bronkema, Vladimir Galvita, Andrew Behn, Fuat Celik, Will Vining, Xiaobo Zheng, Vladimir Shapovalov, Anthony Goodrow, Joe Swisher and Maerian Morris for support and discussions.

I have also benefited from many discussions with different people at various institutions: Prof. Berend Smit, Christian Tuma, Torsten Kerber, Jens Döbler, Alexander Hofmann, Stian Svelle, Thomas Dargel, Tomáš Bučko, and Uwe Huniar.

For providing computer time the “Norddeutscher Verbund für Hoch- und Höchstleistungsrechnen” (HLRN) is acknowledged. Special thanks go to Bernd Kallies for continuous technical support.

I would also like to convey thanks to the German Research Foundation (DFG) for providing the financial means for this project within the priority program SPP 1155.

Further, I thank my family for their unconditional support and encouragement during the course of the thesis.

Finally, I owe special gratitude to Ines Lühmann for her tremendous patience and consideration in the most crucial stage of this work.

Meinen Eltern

Contents

I	Introduction	1
1	Background and scope	3
2	Outline	7
II	Molecular modeling	9
3	Electronic structure methods	11
3.1	Introduction	11
3.2	Schrödinger equation	12
3.2.1	Born-Oppenheimer approximation	13
3.2.2	Variational principle	15
3.3	Hartree-Fock method	15
3.4	Møller-Plesset perturbation theory	18
3.5	Coupled-cluster theory	19
3.6	Density functional theory	21
3.6.1	Gaussian basis sets	24
3.6.2	Plane-wave basis sets	25
4	Molecular simulation methods	27
4.1	Introduction	27
4.2	Statistical thermodynamics	28
4.3	Molecular dynamics simulations	30
4.4	Monte Carlo simulations	31
4.4.1	The grand canonical Monte Carlo method	34

5	Rates of elementary reactions	37
III	Nitrous oxide decomposition on dinuclear oxygen bridged iron sites in Fe-ZSM-5	39
6	A reaction mechanism for the nitrous oxide decomposition on dinuclear oxygen bridged iron sites in Fe-ZSM-5	41
6.1	Introduction	42
6.2	Computational details	43
6.3	Results and discussion	47
6.3.1	Formation of dinuclear iron sites	49
6.3.2	N ₂ O decomposition on Z ⁻ [HOFeOFeOH] ²⁺ Z ⁻ sites . . .	51
6.3.3	N ₂ O decomposition on Z ⁻ [FeOFe] ²⁺ Z ⁻ sites	56
6.3.4	Effect of antiferromagnetic coupling	59
6.4	Conclusion	61
7	Microkinetic modeling of nitrous oxide decomposition on dinuclear oxygen bridged iron sites in Fe-ZSM-5	63
7.1	Introduction	64
7.2	Theoretical methods	65
7.3	Results and discussion	67
7.3.1	Effects of water vapor on the catalyst surface and the apparent rate constant	67
7.3.2	Simulation of temperature-programmed reaction experiments	70
7.4	Conclusion	74
IV	Alkylation of benzene over H-ZSM-5: A multi-scale investigation	75
8	Theoretical investigation of benzene alkylation with ethene over H-ZSM-5	77
8.1	Introduction	78
8.2	Theory	80
8.3	Results and discussion	84
8.3.1	Reaction mechanism for the T5 cluster	84

8.3.2	Reaction mechanism for the T17 cluster	87
8.3.3	Reaction mechanism for the T33 cluster	90
8.4	Conclusion	100
9	Analysis of diffusion limitation in the alkylation of benzene over H-ZSM-5 by combining quantum chemical calculations, molecular simulations, and a continuum approach	101
9.1	Introduction	102
9.2	Continuum approach for diffusion and reaction	104
9.3	Parameterization	111
9.4	Results and discussion	117
9.4.1	Intrinsic kinetics	117
9.4.2	Effects of diffusional mass transfer	120
9.4.3	Effectiveness factor	125
9.5	Conclusion	127
9.6	Nomenclature	128
10	Reactor simulation of benzene ethylation and ethane dehydrogenation catalyzed by ZSM-5: A multiscale approach	131
10.1	Introduction	132
10.2	Reactor model	133
10.3	Performance of PL and LH models	134
10.4	Dehydrogenation of ethane	139
10.5	Parameterization	141
10.6	Results and discussion	143
10.6.1	Intrinsic kinetics	143
10.6.2	Effects of diffusion limitation	144
10.6.3	Effects of hydrogen removal	145
10.7	Conclusion	146
10.8	Nomenclature	147
11	Quantum chemical modeling of benzene ethylation over H-ZSM-5 approaching chemical accuracy: A hybrid MP2:DFT study	149
11.1	Introduction	150
11.2	Computational details	153

11.2.1	DFT calculations applying periodic boundary conditions	154
11.2.2	MP2 and DFT cluster calculations	155
11.2.3	Complete basis set extrapolation	157
11.2.4	PBE+D//PBE calculations	159
11.2.5	CCSD(T) calculations	159
11.2.6	Calculation of intrinsic rate coefficients	160
11.3	Results and discussion	160
11.3.1	Adsorption of reactants and products	160
11.3.2	Reaction steps	170
11.4	Conclusion	181
V	Back matter	183
12	Summary	185
	Appendices	189
A	Supporting information for chapter 7	189
B	Supporting information for chapter 9	197
B.1	Simulation methodologies	198
B.2	Fitting of adsorption isotherms for C ₂ H ₄ , C ₆ H ₆ , and C ₈ H ₁₀ in MFI and validation of ideal adsorbed solution theory	201
B.3	Extraction of M-S diffusivities from MD simulation data	204
B.4	Derivation of the rate expression for the two-step alkylation	210
B.5	conversion between simulated rates on MFI and experimental rates on AB-97 TM	211
B.6	Program structure for the solution of the diffusion-reaction equation	212
B.7	Additional data illustrating the influence of temperature and partial pressures on observed macroscopic rate orders	213
C	Supporting information for chapter 10	215
C.1	Simulation methodologies	216
C.2	Fitting of adsorption isotherms for C ₂ H ₆ and H ₂ in MFI	218

C.3	Extraction of M-S diffusivities from MD simulation data	219
C.4	Determination of rate coefficients for ethane dehydrogenation	222
C.5	Langmuir-Hinshelwood and power law fit parameters	226
D	Supporting information for chapter 11	233
D.1	Location of the acidic site in the MFI framework	234
D.2	Partition functions for reactant and transition states	235
D.3	Cluster size dependence of adsorption energies and intrinsic energy barriers	238
D.4	Fit parameters	243
D.5	BSSE calculations on transition structures	244
	Bibliography	245
	Published work	281
	Conferences	283
	Lebenslauf	285

Part I

Introduction

Background and scope

1

The advent of computational power during the past decades has opened up a new branch of science – often referred to as the “third way” of doing science – which is based on so-called computer experiments. In computer experiments properties of matter are studied by computer simulations based on a model of the reality.¹ Both the model and the method of solution depend on the purpose of the simulation. For tailoring the next generation of materials with applications in catalysis, organic electronics, nanotechnology etc., a molecular level understanding of diffusive, sorptive, and reactive processes is often important as well as knowledge of the electronic structure.²⁻⁴

In the field of heterogeneous catalysis, a long-standing goal of theoretical studies has been the development of methods to predict the effects of catalyst composition and structure on the rates of catalyzed reactions, as well as the distribution of products formed from a specific set of reactants. The different time scales on which the elementary processes involved in a heterogeneously catalyzed reaction occur, require the use of a modeling hierarchy often referred to as multiscale approach. It should be noted though that the term “multiscale approach” is by no means restricted to a specific set of methods involved in describing the different time and length scales. In fact it is used in various disciplines for a variety of modeling approaches.⁵⁻¹¹ In the present context we use the term for a modeling approach starting with quantum chemical calculations at the active center of the catalyst over the determination of adsorption isotherms and diffusivities using atomistic molecular simulations, towards the continuum modeling of zeolite catalyst particles and fixed bed reactors. The information from the various levels are combined by a hierarchical procedure, that is, results from calculations at smaller scales are used as input information to parameterize models that cover larger scales.

Computational methods that describe the behavior of matter at the molecular level can be divided into two main sub-disciplines. The first is com-

putational quantum chemistry, which yields the (electronic) structure and reactivity of molecules. The second is the field of molecular simulation which are classical simulations that enable the behavior of materials to be studied at the atomic level and allow the determination of bulk properties. The computational methods used in quantum chemistry can be subdivided into *ab initio* (Hartree-Fock, MP2 etc.) and semi-empirical approaches. *Ab initio* methods do not require any input except the nuclear coordinates of the system under study. Semi-empirical methods contain certain parametrized terms which make them computationally less expensive but also less transferable. The two techniques usually associated with the term molecular simulation are Monte Carlo (MC) and Molecular Dynamics (MD). The choice of the appropriate method does not exclusively depend on the physical question to be answered but also on the computational resources which are available. However, for systems containing more than a few hundred atoms, quantum chemical calculations are at their current limit and a combination of modeling approaches has to be used. Within the field of heterogeneous catalysis it has been demonstrated in a number of instances that theoretically determined overall kinetics, selectivities, or conversions of reactions are described correctly by such approaches.¹²⁻¹⁴

Among the different catalyst supports used in heterogeneous catalysis, nanoporous materials such as zeolites form an important group. Zeolites are crystalline aluminosilicates built from corner sharing TO_4 units, where the T-atoms usually refer to Si, Al, or in some cases also P. They started their commercial success with the use of zeolites in oil refining and the petrochemical industry.^{15,16} Among the few million zeolite structures that are theoretically feasible,¹⁷ 191 known zeolite structures are registered by the International Zeolite Association (IZA).¹⁸ Out of these, around 10% are reported to be used in commercial operation.¹⁹ These materials exhibit interesting phenomena such as thermal stability, ion exchange capability, and different forms of shape selectivity.²⁰ The use of molecular simulations has improved our understanding of the physical processes occurring in zeolites considerably²¹⁻²³ and the role of molecular modeling in the development of zeolite catalytic processes will become increasingly important.²⁴

All simulation methods applied to extended systems, even those based on quantum mechanics, require assumptions about the physical laws governing the behavior of the material. It is therefore important to compare results obtained from simulation to those obtained experimentally. Modern spectroscopy and microscopy allow detailed insights into the structure of catalytic materials and to monitor concentration profiles of guest molecules.²⁵⁻³¹ Both simulation and experiment are complementary in that simulations allow to

study systems at conditions which are not accessible experimentally while experimental results often raise questions which can only be answered on the basis of detailed atomistic simulations. Some recent examples where the interplay between simulation and experiments has led to a better understanding of physical phenomena can be found in refs 32–35.

In the present work we use atomistic and continuum-level modeling to calculate intrinsic and apparent rates of two zeolite catalyzed reaction systems based on a detailed understanding of the underlying reaction mechanism and the diffusion and adsorption behavior of reactants and products. Rate expressions obtained in this way are more likely to offer a good description of the kinetics over a wide range of reaction conditions than those developed empirically. For the investigation of the first system – nitrous oxide decomposition over Fe-ZSM-5 – we combine density functional theory calculations with transition state theory and microkinetic modeling. For the second system – benzene alkylation with ethene or ethane, respectively – we combine quantum chemical calculations, transition state theory, molecular simulations and a continuum approach. A detailed outline of this thesis is given in the next chapter.

Outline

2

This thesis is divided into five parts. In the first part the structure of the thesis is outlined and the topic is introduced. The second part provides an overview over the theoretical approaches used. Because many different methods have been employed in the present work it is far beyond the scope of this thesis to present a detailed review of all of the computational approaches. Instead, readers are referred to the appropriate textbooks and former dissertations for more detailed information.

In the present thesis two different reaction systems have been studied with different methods and objectives. The first system is the nitrous oxide decomposition over dinuclear iron sites in the zeolite Fe-ZSM-5, presented in the third part of the thesis (chapters 6 and 7). This reaction system is characterized by a relatively large number of elementary steps all of which have been implemented into a microkinetic model to study the macroscopic behavior of this system.

The second reaction system which has been investigated is the alkylation of benzene with ethene and ethane over the zeolite H-ZSM-5. This system is described in the fourth part of the thesis (chapters 8 to 11). In contrast to the nitrous oxide decomposition the alkylation can be described by only a few elementary steps which allows the utilization of more sophisticated quantum chemical approaches (MP2, CCSD(T)). In particular, dispersion interactions have to be taken into account. Furthermore, diffusion limitation plays a role because of the tight fit of the involved molecules into the zeolite channels. As a consequence the macroscopic description requires an explicit consideration of the multicomponent diffusion in contrast to the mikrokinetic model used for the nitrous oxide decomposition.

The fifth part of this thesis contains the summary and the appendix in which further numerical data and other supporting information are provided that are not essential to follow the text.

The individual parts of the thesis are self-contained. All relevant simu-

lation details and – where necessary – lists of symbols are provided in the respective chapters and the related appendices. It should be noted that for some physical quantities more than one unit is used throughout this thesis. The reason is, that different scientific communities prefer to use different units for certain physical quantities. A prominent example is the energy. Studies reporting quantum chemical calculations on gas phase clusters often use kcal/mol while studies related to solid state physics or surface science often use electron volts (eV). By contrast, the engineering community prefers to use SI units such as J/mol. Depending on the focus of the individual chapters either kcal/mol or kJ/mol are used as units of energy.

Part II

Molecular modeling

Electronic structure methods

3

This chapter reviews briefly the basic concepts and underlying approximations of the electronic structure methods used in the present thesis. These are the Hartree-Fock method, Møller-Plesset perturbation theory, the coupled-cluster theory, and density functional theory.

3.1 Introduction

Electronic structure methods are methods to predict and understand the structure of materials at a molecular and atomic level. They can be subdivided into *ab initio* and semi-empirical methods. In a very strict sense, the term *ab initio* refers to methods which are systematically improvable in the sense that they are members of a hierarchy which converges to the exact solution of the electronic Schrödinger equation. Examples for *ab initio* methods are the Hartree-Fock method and the Møller-Plesset perturbation theory. They do not require any input except the nuclear coordinates of the system under study. Semi-empirical methods contain parametrized terms which make them computationally less expensive. However, they may produce wrong results if they are applied to systems for which they are not

designed. Density functional theory (DFT) lacks the systematic improvability and is therefore often not considered as true *ab initio* method. However, depending on the functional, no or only a few fit parameters are involved in a DFT calculation, compared to semi-empirical methods. Therefore density functional theory is sometimes referred to as *first principles* approach.

3.2 Schrödinger equation

The starting point for our discussion is the time-independent one-particle Schrödinger equation,

$$\left\{ -\frac{\hbar^2}{2m}\nabla^2 + \mathcal{V} \right\} \Psi(\mathbf{r}) = E\Psi(\mathbf{r}), \quad (3.1)$$

which refers to a single particle (e. g. an electron) of mass m which is moving through space (given by a position vector \mathbf{r}) under the influence of an external field \mathcal{V} (which might be the electrostatical potential due to the nuclei of a molecule). With \hbar we denote Planck's constant divided by 2π and Ψ is the wave function which gives a complete description of the system. The energy of the particle is denoted as E . By using the Hamiltonian operator,

$$\mathcal{H} = -\frac{\hbar^2}{2m}\nabla^2 + \mathcal{V}, \quad (3.2)$$

we can reduce equation 3.1 to $\mathcal{H}\Psi = E\Psi$. The Schrödinger equation falls into the class of partial differential eigenvalue equations. For the solution of the equation it is necessary to find values of E and wave functions Ψ such that, when the wave function is operated upon by the Hamiltonian, it returns the wave function multiplied by the energy.

An exact solution of the Schrödinger equation is only possible for a few simple problems such as the particle in the box, the harmonic oscillator, the particle on a ring, the particle on a sphere, and the hydrogen atom, all of which are dealt with in introductory textbooks.^{36–38} For any polyelectronic atomic or molecular systems, a closed-form solution is not possible. For the general case of a system containing K nuclei with coordinates \mathbf{R} and N electrons with coordinates \mathbf{r} , the Schrödinger equation reads

$$\mathcal{H}(\mathbf{R}, \mathbf{r})\Psi(\mathbf{R}, \mathbf{r}) = E\Psi(\mathbf{R}, \mathbf{r}). \quad (3.3)$$

In the absence of relativistic effects, external electrostatic or magnetic fields and if the interaction between particles is restricted to Coulomb interactions, the molecular Hamiltonian operator $\mathcal{H}(\mathbf{R}, \mathbf{r})$ is given by

$$\mathcal{H}(\mathbf{R}, \mathbf{r}) = T_n + T_{el} + V_{n,el} + V_{el,el} + V_{n,n}, \quad (3.4)$$

where (in atomic units)

$$T_n = -\frac{1}{2} \sum_{\nu}^K \frac{\nabla_{\nu}^2}{M_{\nu}} \quad (3.5)$$

is the operator of the kinetic energy of the nuclei (∇_{ν}^2 is the Laplace operator for the coordinates of the ν -th nucleus),

$$T_{el} = -\frac{1}{2} \sum_i^N \nabla_i^2 \quad (3.6)$$

is the operator of the kinetic energy of the electrons,

$$V_{n,el} = - \sum_i^N \sum_{\nu}^K \frac{Z_{\nu}}{r_{i,\nu}} \quad (3.7)$$

is the Coulomb attraction between the nuclei possessing the charges Z_{ν} and the electrons,

$$V_{el,el} = \sum_i^N \sum_j^N \frac{1}{r_{ij}} \quad (3.8)$$

is the Coulomb repulsion between the electrons, and

$$V_{n,n} = \sum_{\nu}^K \sum_{\mu}^L \frac{Z_{\nu} Z_{\mu}}{r_{\nu\mu}} \quad (3.9)$$

is the Coulomb repulsion between the nuclei.

3.2.1 Born-Oppenheimer approximation

Due to the complexity of the Schrödinger equation it is necessary to find approximate solutions, which are accurate enough to provide useful information. A central approximation has been proposed in 1927 by Born and Oppenheimer.^{39,40} It consists in a separation of the motion of the light and therefore “fast” electrons from that of the “slow” nuclei. Hence one can consider the electrons in a molecule to be moving in the field of fixed nuclei (“clamped nuclei approximation”). Within this approximation, the first term in equation 3.4, the kinetic energy of the nuclei, can be neglected and the last term, the repulsion between the nuclei, can be considered to be constant. Any constant added to an operator only adds to the operator eigenvalues and

has no effect on the operator eigenfunctions. The remaining terms in equation 3.4 are called the electronic Hamiltonian. The solution to a Schrödinger equation involving the electronic Hamiltonian,

$$\mathcal{H}_{\text{elec}} \Psi_{\text{elec}} = E_{\text{elec}} \Psi_{\text{elec}}, \quad (3.10)$$

is the electronic wave function

$$\Psi_{\text{elec}} = \Psi_{\text{elec}}(\mathbf{r}; \mathbf{R}), \quad (3.11)$$

which describes the motion of the electrons and *explicitly* depends on the electronic coordinates but depends *parametrically* on the nuclear coordinates as does the electronic energy,

$$E_{\text{elec}} = E_{\text{elec}}(\mathbf{r}; \mathbf{R}). \quad (3.12)$$

That means that the electronic Schrödinger equation has to be solved for a given nuclear geometry. The geometry dependent electronic energy plays the role of the potential energy in the Schrödinger equation for the nuclear motion. It is therefore generally termed “potential energy surface” (PES). It has to be emphasized that concepts such as “potential energy curve” or “potential energy surface” which are extensively used in the present work, as well as geometrical structures are only defined within the Born-Oppenheimer approximation. Because the procedure of obtaining the PES using the Born-Oppenheimer approximation is closely connected to the adiabatic theorem⁴¹ it is often referred to as adiabatic approximation⁴² and the PES itself is called an adiabatic surface. It should be noted though that sometimes it is distinguished between the adiabatic and the Born-Oppenheimer approximation depending whether or not the “adiabatic diagonal correction” is included into the Schrödinger equation for the nuclear motion.^{43,44} Here we use both terms synonymously.

From now on we concentrate solely on the electronic problem (equation 3.10) and drop the subscript “elec”. In most cases the Born-Oppenheimer approximation is a very good approximation. Generally, it is only necessary to go beyond it in cases of degeneracies or near degeneracies or at very high energies for the nuclear motion. In the present work all quantum chemical calculations are carried out assuming that the Born-Oppenheimer approximation is valid. For some reactions presented in chapters 6 and 7 however, where non-adiabatic effects play a role, it is attempted to estimate the possible influence of these effects on the reaction dynamics. This is done within the framework of the Landau-Zener formula⁴⁵ as described in detail in the thesis of Heyden.⁴⁶

3.2.2 Variational principle

The variational principle is one of the corner stones of quantum chemistry. As stated above, one consequence of there being no exact solution to the multielectron Schrödinger equation is that the wave function may adopt more than one functional form; no form is necessarily more 'correct' than another. The variational principle now states that for any function $\Psi' \neq \Psi_0$ where Ψ_0 is the exact ground state solution of the eigenvalue equation $\mathcal{H}\Psi = E\Psi$, the expectation value of \mathcal{H} does not exceed the exact ground state eigenvalue E_0 ,

$$\frac{\int \Psi'^* \mathcal{H} \Psi' d\mathbf{r}}{\int \Psi'^* \Psi' d\mathbf{r}} \geq E_0, \quad (3.13)$$

where Ψ'^* is the complex conjugate of Ψ' . The consequence of the variational principle is that for every trial function Ψ' which depends on a set of parameters, the energy E will be a function of these parameters and the optimal set of the parameters leads to a minimum of the energy. If only linear variations of the trial functions are allowed, i. e. if

$$\Psi' = \sum_{i=1}^n c_i \psi_i, \quad (3.14)$$

where $\{\psi_i\}$ is a *fixed* set of n basis functions, the problem of finding the optimum set of coefficients, $\{c_i\}$, can be reduced to a matrix diagonalization. This result is central for the development of algorithms for finding approximate solutions to the Schrödinger equation (see next section).

3.3 Hartree-Fock method

A wave function which should be used for describing the electronic structure of a given system has to satisfy three requirements, in addition to being an approximate or exact solution to the electronic Schrödinger equation. It has to be normalized, antisymmetric with respect to the permutation of two electrons, and it has to include the spin of an electron. The simplest antisymmetric wave function which can be used to describe the ground state of an N -electron system, is a single determinant of the form

$$\Psi = \frac{1}{\sqrt{N!}} \begin{vmatrix} \chi_1(1) & \chi_2(1) & \cdots & \chi_N(1) \\ \chi_1(2) & \chi_2(2) & \cdots & \chi_N(2) \\ \vdots & \vdots & \ddots & \vdots \\ \chi_1(N) & \chi_2(N) & \cdots & \chi_N(N) \end{vmatrix}. \quad (3.15)$$

The individual entries are called spin orbitals and are products of a spatial orbital, $\psi(\mathbf{r})$, and a spin function $\eta(s)$ which depends on the spin of the electron. There are only two possible spin functions which are commonly denoted by α and β and which can be chosen to be orthogonal. The rows of the determinant are numbered by the electrons and the columns by spin orbitals. Having two electrons occupying the same spin orbital corresponds to having two columns of the determinant equal, which makes it zero. Thus no more than one electron can occupy a spin orbital (Pauli exclusion principle). Such determinants in which the elements are not numbers but orbitals are called ‘‘Slater determinants’’.⁴⁷

Using a Slater determinant as trial wave function, Ψ' , we obtain the energy corresponding to this wavefunction from

$$\int \Psi'^* \mathcal{H} \Psi' d\tau = E' \geq E_0. \quad (3.16)$$

This result follows from the variational principle and the normalization of the Slater determinant. The integration over τ also includes the two spin orientations. The variational flexibility in the wave function is in the choice of the spin orbitals. By minimizing E' with respect to the choice of spin orbitals we can derive an equation, called the Hartree-Fock equation, which determines the optimal spin orbitals. The Hartree-Fock equation is an eigenvalue equation of the form

$$f(i)\chi(i) = \varepsilon_i\chi(i), \quad (3.17)$$

where $f(i)$ is an effective one-electron operator, called the Fock operator. It has the form

$$f(i) = -\frac{1}{2}\nabla_i^2 - \sum_{\nu=1}^K \frac{Z_\nu}{r_{i\nu}} + v^{\text{HF}}(i), \quad (3.18)$$

where $v^{\text{HF}}(i)$ is the *average* potential experienced by the i th electron due to the presence of the other electrons. The essence of the Hartree-Fock approximation is to replace the complicated many-electron problem by a one-electron problem in which electron-electron repulsion is treated in an average way. The Hartree-Fock potential $v^{\text{HF}}(i)$, or equivalently the ‘‘field’’ seen by the i th electron, depends on the spin orbitals of the other electrons (i. e. the Fock operator depends on its eigenfunctions). Thus, the Hartree-Fock equation is nonlinear and must be solved iteratively. The solution procedure is called the self-consistent-field (SCF) method. A detailed illustration of the computational aspects of the SCF procedure is presented in the book of Szabo and Ostlund (ref. 48). To efficiently calculate approximate solutions to the Schrödinger equation for polyatomic molecules, the molecular orbital theory

is used.⁴² Molecular wave functions are expressed by determinants involving single-electron wave functions called *molecular* orbitals, ψ_i . These molecular orbitals are constructed from linear combinations of *atomic* orbitals, ϕ_i (basis functions),

$$\psi_i = \sum_{\lambda=1}^L c_{\lambda i} \phi_{\lambda}, \quad i = 1, \dots, L \quad (3.19)$$

where the atomic orbitals are in turn linear combinations of atom-centered Gaussian-type functions,

$$\phi_{\lambda} = \sum_{\rho=1}^M d_{\rho\lambda} \phi_{\rho}^{\text{GF}}, \quad (3.20)$$

with usually *fixed* expansion coefficients $d_{\rho\lambda}$. The introduction of these kind of molecular wave functions into the Hartree-Fock equation leads to a set of algebraic equations for the unknown expansion coefficients $c_{\lambda i}$ which are called Roothaan-Hartree-Fock equations for closed shell molecules where all electron spins are paired.⁴⁹

$$\mathbf{FC} = \mathbf{SC}\boldsymbol{\varepsilon}. \quad (3.21)$$

In the latter equation, \mathbf{C} is a $L \times L$ matrix of the expansion coefficients $c_{\lambda i}$. The entire procedure is known as LCAO-MO-SCF (linear combination of atomic orbitals-molecular orbitals-self consistent field). The resulting working equations are derived in detail in the book of Helgaker et al.⁵⁰ A simple illustration of the method is reported in reference 51.

For unrestricted open shell molecules, separate spatial orbitals for α and β spin are used and the Pople-Nesbet equations have to be solved,⁵²

$$\mathbf{F}^{\alpha}\mathbf{C}^{\alpha} = \mathbf{S}\mathbf{C}^{\alpha}\boldsymbol{\varepsilon}^{\alpha} \quad \text{and} \quad \mathbf{F}^{\beta}\mathbf{C}^{\beta} = \mathbf{S}\mathbf{C}^{\beta}\boldsymbol{\varepsilon}^{\beta}. \quad (3.22)$$

These two equations are the unrestricted generalization of the restricted Roothaan equations. The matrices $\boldsymbol{\varepsilon}^{\alpha}$ and $\boldsymbol{\varepsilon}^{\beta}$ are diagonal matrices of orbital energies. The $L \times L$ square matrices \mathbf{C}^{α} and \mathbf{C}^{β} have as columns the expansion coefficients for ψ_i^{α} and ψ_i^{β} . These equations can be solved in a manner similar to the way Roothaan's equations are solved, except that, since \mathbf{F}^{α} and \mathbf{F}^{β} depend on both \mathbf{C}^{α} and \mathbf{C}^{β} , the two matrix eigenvalue problems must be solved simultaneously.

The larger and more complete the set of basis functions in the Hartree-Fock method is, the greater is the degree of flexibility in the expansion of the spin orbitals and the lower will be the expectation value for the ground state energy. This is illustrated in figure 3.1. The lowest energy value achievable in this way is called the Hartree-Fock limit, E_{HF} .

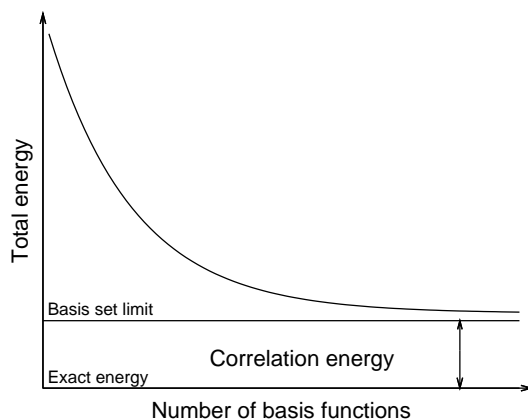


Figure 3.1: Illustration of the Hartree-Fock limit and correlation energy.

The use of a single Slater determinant as trial wave function introduces *exchange effects*, so-called because they arise from the requirement that $|\Psi|^2$ be invariant to the exchange of the space and spin coordinates of any two electrons. In particular, a Slater determinant incorporates *exchange correlation*, which means that the motion of two electrons with parallel spin is correlated (the probability of finding two electrons with the same spin at the same point in space is zero). Since the motion of electrons with opposite spin remains uncorrelated, it is customary to refer to a single determinantal wave function as an uncorrelated wave function and define a *correlation energy* (CE) by the equation

$$\text{CE} = E_{\text{exact}} - E_{\text{HF}}. \quad (3.23)$$

The missing correlation energy imposes severe restrictions to the practical use of the Hartree-Fock method. Consequently, much quantum-chemical research has been directed toward the calculation of correlation energies. One approach is based on a perturbation scheme that treats the Hartree-Fock orbitals as a zero-order wave function, so that the correlation energy can be calculated by perturbation theory (see next section).

3.4 Møller-Plesset perturbation theory

The idea behind perturbation theory is to express the true Hamiltonian operator as sum of a ‘zeroth-order’ Hamiltonian $\mathcal{H}^{(0)}$ (for which a set of molecular

orbitals can be obtained) and a perturbation $\mathcal{H}^{(1)}$:

$$\mathcal{H} = \mathcal{H}^{(0)} + \mathcal{H}^{(1)} \quad (3.24)$$

In Møller-Plesset perturbation theory the unperturbed Hamiltonian $\mathcal{H}^{(0)}$ is the sum of the one-electron Fock operators for the N electrons:

$$\mathcal{H}^{(0)} = \sum_{i=1}^N f(i) \quad (3.25)$$

To obtain an improvement on the Hartree-Fock energy it is necessary to use Møller-Plesset perturbation theory to at least second order. This level of theory is referred to as MP2. The determination of the second-order energy requires the calculation of a two-electron integral over spin orbitals obtained from a preceding Hartree-Fock calculation:

$$E_0^{(2)} = \frac{\sum_i^{\text{occupied}} \sum_{j>i}^{\text{virtual}} \iint \psi_i^*(1) \psi_j^*(2) \left(\frac{1}{r_{12}} \right) [\psi_a(1) \psi_b(2) - \psi_b(1) \psi_a(2)] d\tau_1 d\tau_2}{\varepsilon_a + \varepsilon_b - \varepsilon_i - \varepsilon_j}. \quad (3.26)$$

Møller-Plesset calculations are at present one of the most popular ways to incorporate electron correlation into molecular quantum mechanical calculations. However, they are computationally intensive due to their $\mathcal{O}(\mathcal{N}^5)$ scaling of the operational count (\mathcal{N} : system size) which imposes limits to the size of the molecular systems which can be handled. Two widely used methods to reduce the computational costs of MP2 calculations are the ‘‘frozen core’’ (FC) and the ‘‘resolution of the identity’’ (RI) approach. The assumption underlying the FC approach is that correlation energy contributions from electrons in core orbitals are nearly constant for reacting systems. These electrons can therefore be excluded from a given correlation scheme. The RI approach reduces computational costs by an approximate representation of four-centre integrals (see refs 53–58 for details). Although the formal $\mathcal{O}(\mathcal{N}^5)$ scaling behavior is retained, the prefactor has become much smaller. Moreover mass storage requirements are significantly reduced within the RI-scheme. In the present work both the FC and the RI approach are used in virtually all MP2 calculations. The validity of these approximations for the molecular systems studied in chapters 8 and 11 has been demonstrated in the thesis of Tuma.⁵⁹

3.5 Coupled-cluster theory

In coupled-cluster theory, the wave function is written as an exponential of a cluster operator \hat{T} acting on a single-determinant reference state, obtained

from a preceding Hartree-Fock calculation,

$$\Psi^{\text{CC}} = \exp(\hat{T})\Psi^{\text{HF}}. \quad (3.27)$$

The cluster operator \hat{T} is defined as

$$\hat{T} = \hat{T}_1 + \hat{T}_2 + \hat{T}_3 + \cdots + \hat{T}_n, \quad (3.28)$$

where n is the total number of electrons and the various \hat{T}_i operators generate all possible determinants having i excitations from the reference. For example

$$\hat{T}_2\Psi^{\text{HF}} = \sum_{i < j}^{\text{occ.}} \sum_{a < b}^{\text{vir.}} t_{ij}^{ab} \Psi_{ij}^{ab}, \quad (3.29)$$

where the amplitudes t are determined by the constraint that equation 3.27 be satisfied. The expansion of \hat{T} ends at n because no more than n excitations are possible. By expanding the exponential,

$$\exp(\hat{T}) = \hat{I} + \hat{T}_1 + \left(\hat{T}_2 + \frac{1}{2}\hat{T}_1^2 \right) + \left(\hat{T}_3 + \hat{T}_2\hat{T}_1 + \frac{1}{6}\hat{T}_1^3 \right) + \dots, \quad (3.30)$$

it can be seen that the effect of the $\exp(\hat{T})$ operator in equation 3.27 is to express Ψ^{CC} as a linear combination of Slater determinants that include Ψ^{HF} and all possible excitations of electrons from occupied to virtual spin orbitals. Truncating the cluster operator after the single (\hat{T}_1) and double (\hat{T}_2) excitations gives the coupled-cluster singles-and-doubles (CCSD) method, truncating it after \hat{T}_3 the CCSDT method etc. The computational problem is the determination of the cluster amplitudes t for all of the operators included in the particular approximation which results in a set of coupled, nonlinear equations in the amplitudes that must be solved iteratively. Coupled-cluster is closely connected with Møller-Plesset perturbation theory. Inclusion of only \hat{T}_2 gives an approximate approach, called the coupled-cluster doubles (CCD) method. The CCD energy is equivalent to $\text{MP}\infty(\text{D})$ where all disconnected contributions of products of doubles are included.⁶⁰ In practice the scaling behavior of coupled-cluster calculations imposes severe limits on the size of the systems that can be studied.⁶¹ The CCSD approximation has an $\mathcal{O}(\mathcal{N}^6)$ scaling of the operational count while the CCSDT approximation scales with $\mathcal{O}(\mathcal{N}^8)$. As a result, various approaches have been proposed to estimate the effects of the connected triples using perturbation theory. Of these, the most commonly used is the so-called CCSD(T) method⁶² which also includes a singles/triples coupling term and scales with $\mathcal{O}(\mathcal{N}^7)$. In chapter 11 we perform CCSD(T) calculations on small zeolite models to investigate the adequacy of MP2 and to provide corrections for higher order correlation effects if necessary.

3.6 Density functional theory

The central idea underpinning density functional theory (DFT) is that there is a relationship between the total electronic energy and the overall electronic density. This implies a significant reduction of computational complexity because the electronic density is a function of only three coordinates while the multielectron wave function calculated in Hartree-Fock theory is a function of $3N$ coordinates (N : number of electrons). The rigorous foundation of density functional theory is given in the theorems of Hohenberg and Kohn.⁶³ The first theorem states that once the ground-state electron density in position space is known, *any* ground state property is uniquely defined. That is, any ground-state property is a functional of the electron density in position space. This electron density can – in principle – be calculated from some N -electron wave function, i. e. from the ground state wave function for the system of interest, Ψ_0 , which corresponds to the ground state energy E_0 . One says, that the ground state electronic energy is a functional of the ground state electronic density, ρ_0 , and writes $E_0 = E_0[\rho_0]$. According to the variational principle, any wave function Ψ' different from Ψ_0 , will lead to a higher energy E' and also to a different electron density ρ' . This means that just as for the variational method for wave functions we also have a variational principle for density functionals,

$$E[\rho'] \geq E_0[\rho_0], \quad (3.31)$$

which is the second Hohenberg-Kohn theorem. It states that once the functional that relates the electron density in position space to the total electronic energy is known, one may calculate it approximately by inserting approximate densities. Furthermore, just as for the variational method for wave functions, one may improve any actual calculation by minimizing $E[\rho']$. This means that in density functional theory all ground state molecular properties can in principle be calculated without having to find the molecular wave function, from

$$E_0 = E_0[\rho_0] = \int \rho_0(\mathbf{r})v(\mathbf{r})d\mathbf{r} + F[\rho_0], \quad (3.32)$$

where $v(\mathbf{r})$ is the nuclear attraction potential energy function for an electron located at point \mathbf{r} . The central problem of DFT is that the functional $F[\rho_0]$ in the latter equation is unknown.

A practical scheme for calculating ground state properties from the electronic density was provided in 1965 by Kohn and Sham.⁶⁴ They suggested that $F[\rho(\mathbf{r})]$ should be approximated as the sum of three terms:

$$F[\rho(\mathbf{r})] = E_{\text{KE}}[\rho(\mathbf{r})] + E_{\text{H}}[\rho(\mathbf{r})] + E_{\text{XC}}[\rho(\mathbf{r})] \quad (3.33)$$

where $E_{\text{KE}}[\rho(\mathbf{r})]$ is the kinetic energy, $E_{\text{H}}[\rho(\mathbf{r})]$ is the electron-electron Coulombic energy, and $E_{\text{XC}}[\rho(\mathbf{r})]$ contains contributions from exchange and correlation. It is important to note that the first term in equation 3.33, $E_{\text{KE}}[\rho(\mathbf{r})]$, is defined as kinetic energy of a system of *non-interacting* electrons with the same density $\rho(\mathbf{r})$ as the real system:

$$E_{\text{KE}}[\rho(\mathbf{r})] = \sum_{i=1}^N \int \psi_i^*(\mathbf{r}) \left(-\frac{\nabla^2}{2} \right) \psi_i(\mathbf{r}) d\mathbf{r}. \quad (3.34)$$

The second term, also known as Hartree electrostatic energy, is given by:

$$E_{\text{H}}[\rho(\mathbf{r})] = \frac{1}{2} \iint \frac{\rho(\mathbf{r}_1)\rho(\mathbf{r}_2)}{|\mathbf{r}_1 - \mathbf{r}_2|} d\mathbf{r}_1 d\mathbf{r}_2. \quad (3.35)$$

Combining these two and adding the electron-nuclear interaction leads to the full expression for the energy of an N -electron system within the Kohn-Sham scheme:

$$\begin{aligned} E[\rho(\mathbf{r})] &= \sum_{i=1}^N \int \psi_i^*(\mathbf{r}) \left(-\frac{\nabla^2}{2} \right) \psi_i(\mathbf{r}) d\mathbf{r} + \frac{1}{2} \iint \frac{\rho(\mathbf{r}_1)\rho(\mathbf{r}_2)}{|\mathbf{r}_1 - \mathbf{r}_2|} d\mathbf{r}_1 d\mathbf{r}_2 \\ &+ E_{\text{XC}}[\rho(\mathbf{r})] - \sum_{A=1}^M \int \frac{Z_A}{|\mathbf{r} - R_A|} \rho(\mathbf{r}) d\mathbf{r}. \end{aligned} \quad (3.36)$$

The latter equation acts to *define* the exchange-correlation energy functional $E_{\text{XC}}[\rho(\mathbf{r})]$, which thus contains not only contributions due to exchange and correlation but also a contribution due to the difference between the true kinetic energy of the system and $E_{\text{KE}}[\rho(\mathbf{r})]$. Kohn and Sham wrote the density $\rho(\mathbf{r})$ of the system as the sum of the square moduli of a set of one-electron orthonormal orbitals:

$$\rho(\mathbf{r}) = \sum_{i=1}^N |\psi_i(\mathbf{r})|^2. \quad (3.37)$$

By using this expression for the electron density and applying the appropriate variational condition, the following one-electron Kohn-Sham equation results:

$$\left\{ -\frac{\nabla_1^2}{2} - \left(\sum_{A=1}^M \frac{Z_A}{r_{1A}} \right) + \int \frac{\rho(\mathbf{r}_2)}{r_{12}} d\mathbf{r}_2 + V_{\text{XC}}[\mathbf{r}_1] \right\} \psi_i(\mathbf{r}_1) = \varepsilon_i \psi_i(\mathbf{r}_1). \quad (3.38)$$

In this equation, ε_i are the orbital energies and V_{XC} is known as the exchange-correlation functional, related to the exchange-correlation energy by

$$V_{\text{XC}}[\mathbf{r}] = \left(\frac{\delta E_{\text{XC}}[\rho(\mathbf{r})]}{\delta \rho(\mathbf{r})} \right). \quad (3.39)$$

The total energy is then calculated from equation 3.36. To solve the Kohn-Sham equations a self-consistent approach is taken. An initial guess of the density is fed into equation 3.38 from which a set of orbitals can be derived leading to an improved value for the density, which is then used in a second iteration, and so on until convergence is achieved.

Because the set of equations which need to be solved to obtain ground state energies using density functional theory are formally very similar to those resulting from Hartree-Fock theory, it should be emphasized that density functional theory is a completely different, formally rigorous, way of approaching any interacting problem, by mapping it exactly to a much easier-to-solve non-interacting problem.

A central issue when applying density functional theory is the choice of the exchange-correlation functional. Up-to-date overviews of the applicability of density functionals are given in refs 65–69. Here we give only a brief overview over the basic ideas involved in functional development. The first attempts to find a form for the exchange-correlation functional (or potential) started from the exact result for a uniform electron gas, in which case the exchange potential is inversely proportional to the cubic root of the local density,

$$V_X^{\text{LDA}} = -\frac{3}{4} \left(\frac{3}{\pi} \right)^{1/3} \rho^{1/3}, \quad (3.40)$$

so that the exchange functional E_X equals

$$E_X^{\text{LDA}}[\rho] = -\frac{3}{4} \left(\frac{3}{\pi} \right)^{1/3} \int \rho^{4/3}(\mathbf{r}) d\mathbf{r}. \quad (3.41)$$

This approximation is called the *local density approximation* (LDA). The correlation part V_C^{LDA} has been determined numerically by quantum Monte Carlo calculations.⁷⁰ The results have been expressed as a complicated function V_C^{VWN} of ρ by Vosko, Wilk, and Nusair (VWN).⁷¹ Since the LDA is based on the uniform-electron-gas model it is appropriate for systems where ρ varies slowly with position. Functionals that go beyond the LDA aim to correct for the variation of electron density with position. They do this by including the gradient of ρ in the integrand,

$$E_{XC}^{\text{GGA}}[\rho] = \int f(\rho(\mathbf{r}), \nabla\rho(\mathbf{r})) d\mathbf{r}, \quad (3.42)$$

where f is some function of the electron density and its gradient. The letters GGA stand for *generalized gradient approximation*. The term *gradient corrected functional* is also used. One such functional applied in the present

work was proposed by Perdew, Burke, and Ernzerhof (PBE) that has no empirical parameters.^{72,73} Finally we want to mention the widely used class of hybrid exchange-correlation functionals. In the construction of hybrid functionals some of the DFT exchange is replaced by Hartree-Fock exchange. These type of functionals are in general advantageous for the calculation of activation energies but are also computationally more demanding than pure density functionals. One of the most popular hybrid functional is the B3LYP functional which can be written as:⁷⁴

$$E_{XC}^{B3LYP} = (1-a_0)E_X^{LSDA} + a_0E_X^{HF} + a_X\Delta E_X^{B88} + a_C E_C^{LYP} + (1-a_C)E_C^{VWN}. \quad (3.43)$$

Here ΔE_X^{B88} is Becke's gradient correction to the exchange functional,⁷⁵ E_C^{LYP} denotes the Lee-Yang-Parr correlation functional (which also includes density gradient terms),⁷⁶ and E_C^{VWN} denotes the VWN local correlation expression. The coefficients $a_0 = 0.2$, $a_X = 0.72$, and $a_C = 0.81$ are based on fitting to heats of formation of small molecules. Note that there are small differences in the implementation of the B3LYP functional between different quantum chemical program packages. The actual implementation should therefore be checked within the manuals.

3.6.1 Gaussian basis sets

For DFT-calculations on molecular systems, the Kohn-Sham orbitals can be determined by a numerical procedure, analogously to numerical Hartree-Fock methods. The Kohn-Sham orbitals can be expanded in atom-centered basis functions similar to equation 3.19. The basis functions are normally the same as used in wave function based methods. The variational procedure again leads to a matrix equation in the atomic orbital basis,

$$\mathbf{HC} = \mathbf{SC}\boldsymbol{\varepsilon}, \quad (3.44)$$

where the matrix \mathbf{H} is analogous to the Fock matrix. The exchange-correlation part, however, is given in terms of the electronic density, and possibly also involves derivatives of the density (depending on the functional). Therefore, the corresponding integrals cannot be evaluated analytically but must be generated by a numerical integration on a grid of a certain density which has to be specified in advance. This means that from a practical point of view the set-up of a density functional calculation involves more parameters to be specified than a Hartree-Fock or MP2 calculation does.

3.6.2 Plane-wave basis sets

In quantum chemical calculations of molecular systems, orbitals are usually expanded into a set of atom-centered Gaussian basis functions. For the study of crystalline systems which consist of a repeating pattern of objects, these type of basis functions are not a natural choice. In such systems the effective potential, V_{eff} , (as well as the electronic density) is a periodic function with the periodicity of the lattice,

$$V_{\text{eff}}(\mathbf{r} + \mathbf{T}) = V_{\text{eff}}(\mathbf{r}). \quad (3.45)$$

The eigenstates of the Schrödinger equation can be chosen in such a way that with each wave function ψ , a wave vector \mathbf{k} is associated, to hold

$$\psi(\mathbf{r} + \mathbf{T}) = e^{i\mathbf{k}\cdot\mathbf{T}}\psi(\mathbf{r}), \quad (3.46)$$

for every lattice vectors \mathbf{T} (Bloch's theorem⁷⁷). A natural choice of basis functions for periodic systems are therefore linear combinations of plane waves of the form

$$\phi_{\mathbf{G}}^{\text{PW}} = \frac{1}{\sqrt{\Omega}}e^{i\mathbf{G}\cdot\mathbf{r}}, \quad (3.47)$$

where \mathbf{G} is a wave vector of the correct periodicity and Ω is the volume of the simulation cell. There are two potential problems with the practical use of these basis functions in the Kohn-Sham equations. The first is related to the fact that electronic wave functions show rapid oscillations in regions close to the atomic nuclei. Consequently a large number of plane waves would be required to model this behavior making the calculations prohibitively expensive. A popular way to deal with this problem is to replace the 'true' potential in these core regions with a much weaker one called a *pseudopotential*. This represents the way in which the valence electrons interact with the combined nucleus plus core electrons.⁷⁸ A pseudopotential is a potential function that gives wave functions with the same shape as the true wave function outside the core region but with fewer nodes inside the core region as illustrated in figure 3.2. The second issue is the size of the basis set. In principle an infinite number of reciprocal lattice vectors \mathbf{G} is required to represent the wave functions with infinite accuracy. In practice, the expansion coefficients of the wave functions decrease with increasing $|\mathbf{k} + \mathbf{G}|$ so that the plane wave expansion can be effectively truncated at a finite number of terms, i. e. limited to all waves with kinetic energy lower than some energy cutoff,⁸⁰

$$|\mathbf{k} + \mathbf{G}| \leq E_{\text{cut}}. \quad (3.48)$$

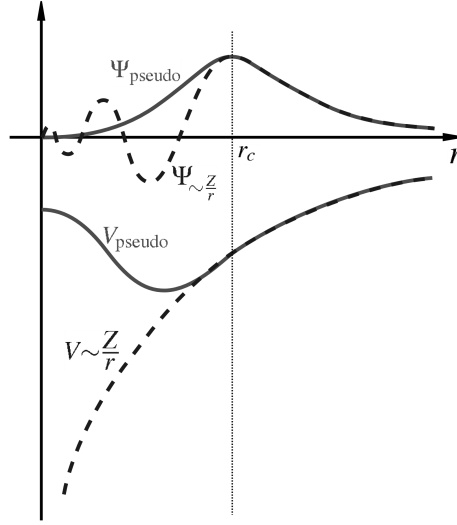


Figure 3.2: Schematic illustration of all-electron (dashed lines) and pseudo-electron (solid lines) potentials and their corresponding wave functions. The radius at which all-electron and pseudoelectron match is designated r_c .⁷⁹

The truncation of the basis set leads to an error in the computed physical quantities, but this error can be easily handled by increasing the cutoff. As a result, the quality of plane-wave basis sets is specified by a single parameter.

The number of plane waves for a given cutoff depends on the size of the unit cell and can be estimated from

$$N_{\text{PW}} \approx \frac{1}{2\pi^2} \Omega E_{\text{cut}}^{3/2}. \quad (3.49)$$

For a practical calculation the size of the basis set has to be chosen by gradually increasing the cutoff energy until convergence in the total energy is achieved.

Molecular simulation methods

4

A brief introduction to the molecular simulation techniques used for calculating adsorption isotherms and diffusion coefficients is given as well as to the basics of statistical thermodynamics.

4.1 Introduction

Molecular simulation can be defined as computational statistical mechanics. There is a clear distinction between this and computational quantum chemistry on the one side and continuum modeling on the other side. In contrast to quantum chemistry, molecular simulation is based on classical physics. Still, molecular simulation samples atomistic level phenomena, in contrast to continuum modeling but interactions between atoms are treated with empirical potential functions (force fields). As a result, larger length and time scales can be accessed than with quantum chemical methods but at the expense of some loss in chemical realism. The outcome of such a simulation hinges on the quality of the force field.⁸¹ The force field parameters are usually fitted against experimental data, although in recent years also force fields based on quantum mechanical calculations are reported.⁸²⁻⁸⁴

In the framework of the present work, molecular dynamics (MD) and Monte Carlo (MC) simulations have been employed to obtain diffusion coefficients and adsorption isotherms of hydrocarbons in the zeolite MFI. All the procedures used can be regarded as well established. We therefore limit this chapter to the introduction of the theoretical background and the basic ideas of MD and MC. All simulation details, references to the force fields used in the simulations, and details about the extraction of diffusion coefficients from MD simulation data are given in appendices B and C. For more details on the methodologies and applications the reader is referred to the thesis of Jakobtorweihen,⁸⁵ the standard textbooks^{86,87} and recent review papers.^{22,88–90}

4.2 Statistical thermodynamics

All macroscopic properties of matter are averages of molecular properties with respect to time or position, mostly with respect to both of them. While thermodynamics provides relationships between various macroscopic properties of bulk matter it does not provide numerical values for any given property. To obtain such information the properties of microscopic mechanical models based on quantum or classical mechanics must be averaged. The methods of this averaging, which will predict average values for macroscopic properties, constitute the science of statistical mechanics.⁹¹ Statistical mechanics supplies the elements to understand and predict macroscopic phenomena and the calculation of macroscopic properties from the properties of the individual molecules building up the system. The treatment of systems in equilibrium is usually referred to as statistical thermodynamics.⁹² For most of the systems one cannot obtain analytical solutions in the frame of statistical mechanics. Computer simulation methods enable it to study such systems and predict their properties by the use of techniques that consider small replications of the macroscopic system with manageable numbers of atoms or molecules. A simulation generates representative configurations of these small replications in such a way that accurate values of structural and thermodynamic properties can be obtained with a feasible amount of computation. Simulation techniques also enable the time-dependent behaviour of atomic and molecular systems to be determined, providing a detailed picture of the way in which a system changes from one conformation or configuration to another.

In general, properties such as pressure or heat capacity will depend on the positions and the momenta of the N particles that comprise the system. Each

position vector \mathbf{r}_i and momentum vector \mathbf{p}_i has 3 components in Cartesian coordinates that can be represented by

$$\mathbf{r}_i = (x_i, y_i, z_i)^T \quad (4.1)$$

$$\mathbf{p}_i = (p_{xi}, p_{yi}, p_{zi})^T = (m_i v_{xi}, m_i v_{yi}, m_i v_{zi})^T, \quad (4.2)$$

where each of the vectors corresponds to an orthogonal direction. The dimensionality of the entire $(\mathbf{r}^N, \mathbf{p}^N)$ system is $3 \times 2N$ or $6N$. This $6N$ -dimensional vector defines a state for the N particle system in what is known the phase space. In phase space the state of a system, according to classical theory, is a single point. In essence, phase space is equivalent to a set of reference coordinates for the position \mathbf{r}_i and momentum \mathbf{p}_i vectors of each particle or molecule i in the system. Subsets of phase space are configuration space – the $3N$ -dimensional vector of spatial coordinates – and momentum space – the $3N$ -dimensional vector of momenta. The progression of a system can be viewed as a trajectory in $6N$ phase space.

The instantaneous value of any physical property A can be written as $A(\mathbf{p}^N(t), \mathbf{r}^N(t))$. During time, the instantaneous value of the property A fluctuates as a result of interactions between particles. The value that can be measured experimentally is an average of A during the time of the measurement and is therefore known as time average. As the time during which the measurement is made increases to infinity, the value of the following integral approaches the true average value of the property:

$$A_{ave} = \lim_{\tau \rightarrow \infty} \frac{1}{\tau} \int_{\tau=0}^{\tau} A(\mathbf{p}^N(t), \mathbf{r}^N(t)) dt. \quad (4.3)$$

To calculate average values of the properties of the system, it would therefore appear to be necessary to simulate the dynamic behavior of the system (i. e. to determine values of $A(\mathbf{p}^N(t), \mathbf{r}^N(t))$, based upon a model of the intra- and intermolecular interactions). Although this is in principle relatively straightforward to do, for large numbers of atoms or molecules (of the order of 10^{23}) it is not even feasible to determine an initial configuration of the system. Using the techniques of statistical mechanics developed by Boltzmann and Gibbs this problem can be solved by replacing a single system evolving in time by a large number of replications of the system that are considered simultaneously. The time average is then replaced by an ensemble average

$$\langle A \rangle = \iint A(\mathbf{p}^N, \mathbf{r}^N) \rho(\mathbf{p}^N, \mathbf{r}^N) d\mathbf{p}^N d\mathbf{r}^N. \quad (4.4)$$

The angle brackets $\langle \rangle$ indicate an ensemble average, or expectation value i. e., the average value of the property A over all replications of the ensemble

generated by the simulation. The probability density $\rho(\mathbf{p}^N, \mathbf{r}^N)$ is the probability of finding a configuration with momenta \mathbf{p}^N and positions \mathbf{r}^N . The ensemble average of the property A is then determined by integrating over all possible configurations of the system. In accordance with the ergodic hypothesis, which is one of the fundamental axioms of statistical mechanics, the ensemble average is equal to the time average. Under conditions of constant number of particles N , volume V , and temperature T (NVT ensemble or canonical ensemble), the probability density is the Boltzmann distribution

$$\rho(\mathbf{p}^N, \mathbf{r}^N) = \frac{\exp(-E(\mathbf{p}^N, \mathbf{r}^N)/(k_B T))}{Q}, \quad (4.5)$$

where $E(\mathbf{p}^N, \mathbf{r}^N)$ is the energy, Q is the so-called partition function, k_B is the Boltzmann constant and T is the temperature. The partition function is more generally written in terms of the Hamiltonian \mathcal{H} ,

$$\mathcal{H}(\mathbf{p}^N, \mathbf{r}^N) = \sum_{i=1}^N \frac{|\mathbf{p}_i|^2}{2m_i} + U(\mathbf{r}_1, \dots, \mathbf{r}_N) \quad (4.6)$$

representing the total energy of the system which is the sum of the kinetic energy and the potential energy. For a system of N identical particles the partition function for the canonical ensemble is

$$Q_{NVT} = \frac{1}{N!} \frac{1}{h^{3N}} \iint \exp\left[-\frac{\mathcal{H}(\mathbf{p}^N, \mathbf{r}^N)}{k_B T}\right] d\mathbf{p}^N d\mathbf{r}^N. \quad (4.7)$$

The factor $1/N!$ arises from the indistinguishability of the particles, and the factor $1/h^{3N}$ (h : Planck constant) is required to ensure that the partition function is equal to the quantum mechanical result for a particle in a box.³⁸

4.3 Molecular dynamics simulations

Molecular Dynamics calculates the “real” dynamics of the system, from which time averages of properties can be determined. Sets of atomic positions are derived by applying Newton’s equation of motion. Molecular dynamics is a deterministic method which means, that the state of the system at any future time can be predicted from its current state. The equations of motion are integrated numerically by dividing the calculation into a series of very short time steps (typically between 1 femtosecond and 10 femtoseconds; 10^{-15} s to 10^{-14} s).³⁸ A widely used integrator is the Verlet algorithm⁹³ which was also

applied in the present work:

$$\mathbf{r}(t + \Delta t) = \mathbf{r}(t) + \mathbf{v}(t)\Delta t + \frac{\mathbf{f}(t)}{2m}\Delta^2 t \quad (4.8)$$

$$\mathbf{v}(t + \Delta t) = \mathbf{v}(t) + \frac{\mathbf{f}(t) + \mathbf{f}(t + \Delta t)}{2m}\Delta t. \quad (4.9)$$

At each step, the forces \mathbf{f} on the atoms are computed and combined with the current positions \mathbf{r} and velocities \mathbf{v} to generate new positions and velocities a short time ahead. During the time interval the velocities and forces associated with each atom are assumed to be constant. The atoms are then moved to the new positions, the resulting forces are computed, and so on. In this way a molecular dynamics simulation generates a trajectory that describes how the dynamic variables change with time. From the trajectories the diffusion coefficients were obtained as time averages as explained in detail in appendices B and C (equations B.1, B.7, and C.2). A typical MD simulation was run for 1 ns with time steps of 1 fs.

4.4 Monte Carlo simulations

In a Molecular Dynamics simulation the successive configurations of the system are connected in time. This is not the case in a Monte Carlo simulation, where each configuration depends only upon its predecessor configuration and not upon any other of the configurations previously visited. A Monte Carlo simulation generates configurations of a system by making random changes to the positions, orientations or conformations of the species present. The potential energy of each configuration of the system, together with the values of other properties, can be calculated from the positions of the atoms. The Monte Carlo method thus samples from the $3N$ -dimensional configuration space. There is no momentum contribution in a Monte Carlo simulation, in contrast to a Molecular Dynamics simulation. In fact the integration over momenta can be carried out analytically because the double integral in equation (4.7) can be separated into two separate integrals, one over positions and the other over the momenta, after introducing the expression for the Hamiltonian from equation (4.6):

$$Q_{NVT} = \frac{1}{N!} \frac{1}{h^{3N}} \int \exp\left[-\frac{|\mathbf{p}_i|^2}{2mk_B T}\right] d\mathbf{p}^N \int \exp\left[-\frac{U(\mathbf{r}^N)}{k_B T}\right] d\mathbf{r}^N. \quad (4.10)$$

This separation is possible only if the potential energy function, $U(\mathbf{r}^N)$, is not dependent upon the velocities (this is a safe assumption for almost all

potential functions in common use). The integral over the momenta can now be performed analytically, the result being:

$$\int \exp\left[-\frac{|\mathbf{p}_i|^2}{2mk_B T}\right] d\mathbf{p}^N = (2\pi mk_B T)^{3N/2}. \quad (4.11)$$

The partition function can thus be written:

$$Q_{NVT} = \frac{1}{N!} \left(\frac{2\pi mk_B T}{h^2}\right)^{3N/2} \int \exp\left(-\frac{U(\mathbf{r}^N)}{k_B T}\right) d\mathbf{r}^N. \quad (4.12)$$

The integral over the positions is often referred to as the configurational integral, Z_{NVT} :

$$Z_{NVT} = \int \exp\left(-\frac{U(\mathbf{r}^N)}{k_B T}\right) d\mathbf{r}^N. \quad (4.13)$$

In an ideal gas there are no interactions between the particles and so the potential energy function, $U(\mathbf{r}^N)$, equals zero and $\exp(-U(\mathbf{r}^N)/k_B T)$ is equal to one for every gas particle in the system. The integral of 1 over the coordinates of each atom is equal to the volume, and so for N ideal gas particles the configurational integral is given by V^N . This leads to the following result for the canonical partition function of a (monoatomic) ideal gas:

$$Q_{NVT}^{\text{ideal}} = \frac{V^N}{N!} \left(\frac{2\pi mk_B T}{h^2}\right)^{3N/2}. \quad (4.14)$$

This is often written in terms of the de Broglie thermal wavelength, Λ :

$$Q_{NVT} = \frac{V^N}{N! \Lambda^{3N}} \quad (4.15)$$

where $\Lambda = \sqrt{h^2/2\pi k_B T m}$.

By combining equations (4.11) and (4.13) it can be seen that the partition function for a “real” system has a contribution due to the ideal gas behaviour (the momenta) and a contribution due to the interactions between the particles. Any deviations from ideal gas behaviour are due to the interactions within the system as a consequence of these interactions. This enables to write the partition function as:

$$Q_{NVT} = Q_{NVT}^{\text{ideal}} Q_{NVT}^{\text{excess}}. \quad (4.16)$$

The excess part of the partition function is given by

$$Q_{NVT}^{\text{excess}} = \frac{1}{V^N} \int \exp\left[-\frac{U(\mathbf{r}^N)}{k_B T}\right] d\mathbf{r}^N. \quad (4.17)$$

The important conclusion is that all of the deviations from ideal gas behaviour are due to the presence of interactions between the atoms in the system, as calculated using the potential energy function. This energy function is dependent only on the positions of the atoms and not on their momenta, and so a Monte Carlo simulation is able to calculate the excess contributions that give rise to the deviations from ideal gas behaviour.

Taking into account equation (4.4) the numerical problem which has to be solved is not the configurational part of the partition function itself but averages of the type

$$\langle A \rangle = \frac{\int \exp[-\beta U(\mathbf{r}^N)] A(\mathbf{r}^N) d\mathbf{r}^N}{\int \exp[-\beta U(\mathbf{r}^N)] d\mathbf{r}^N}. \quad (4.18)$$

Metropolis et al.⁹⁴ solved this problem by the so-called importance sampling, meaning that the configuration space is sampled according to the probability density of the system. Almost all Monte Carlo schemes rely on Markov processes as the generating engine for the set of states used. A Markov process is a mechanism which, given a system in one state o , generates a new state n of that system. It does so in a random manner. It will not generate the same new state every time it is given the initial state o . The probability of generating the state n given o is called the transition probability $P(o \rightarrow n)$ for the transition from o to n . For a true Markov process all the transition probabilities should satisfy two conditions:⁹⁵

1. They should not vary with time.
2. They should depend only on the properties of the current states o and n , and not on any other states the system has passed through.

The transition probabilities must also satisfy the constraint

$$\sum_n P(o \rightarrow n) = 1. \quad (4.19)$$

To ensure that it is the desired probability distribution which is generated after the system has come to equilibrium, the condition must hold that in equilibrium the average number of accepted moves from o to any other state n is exactly cancelled by the number of reverse moves (condition of detailed balance):

$$\rho(o)P(o \rightarrow n) = \rho(n)P(n \rightarrow o). \quad (4.20)$$

Taking into account that a Monte Carlo move consists of two stages, namely a trial move from state o to state n and the decision to either accept or reject this trial move, the transition probability can be broken down into two parts:

$$P(o \rightarrow n) = \alpha(o \rightarrow n) \times \text{acc}(o \rightarrow n). \quad (4.21)$$

The selection probability $\alpha(o \rightarrow n)$ or underlying matrix of the Markov chain is the probability, given a state o , that the algorithm will generate a new target state n , and $\text{acc}(o \rightarrow n)$ is the acceptance ratio or acceptance probability.

The condition of detailed balance can be rewritten as

$$\frac{P(o \rightarrow n)}{P(n \rightarrow o)} = \frac{\alpha(o \rightarrow n)\text{acc}(o \rightarrow n)}{\alpha(n \rightarrow o)\text{acc}(n \rightarrow o)} = \frac{\rho(n)}{\rho(o)}. \quad (4.22)$$

In the original Metropolis scheme α is chosen to be a symmetric matrix ($\alpha(o \rightarrow n) = \alpha(n \rightarrow o)$), which simplifies equation (4.22) to

$$\frac{\text{acc}(o \rightarrow n)}{\text{acc}(n \rightarrow o)} = \frac{\rho(n)}{\rho(o)}. \quad (4.23)$$

Many choices for $\text{acc}(o \rightarrow n)$ satisfy this condition. The choice of Metropolis et al.⁹⁴ is

$$\text{acc}(o \rightarrow n) = \begin{cases} \frac{\rho(n)}{\rho(o)} & \text{if } \rho(n) < \rho(o) \\ 1 & \text{if } \rho(n) \geq \rho(o) \end{cases}. \quad (4.24)$$

The acceptance probabilities can be rewritten as

$$\text{acc}(o \rightarrow n) = \min\left(1, \frac{\rho(n)}{\rho(o)}\right) \quad (4.25)$$

$$\text{acc}(n \rightarrow o) = \min\left(1, \frac{\rho(o)}{\rho(n)}\right). \quad (4.26)$$

4.4.1 The grand canonical Monte Carlo method

In the conventional NVT , NVE , and NPT ensembles the number of molecules is fixed. For some systems however, one would like to obtain information on the average number of particles in a system as a function of the external conditions. For example in adsorption studies one would like to know the amount of material adsorbed as a function of the pressure and temperature of the reservoir with which the material is in contact. A natural ensemble to solve this problem is the grand canonical ensemble (or μVT ensemble). In this ensemble, the temperature, volume, and chemical potential are fixed values. In the experimental setup, the adsorbed gas is in equilibrium with the gas in the reservoir. The equilibrium conditions are that the temperature and chemical potential of the gas inside and outside the adsorbent must be equal. The gas that is in contact with the adsorbent can be considered as a reservoir that imposes a temperature and chemical potential

on the adsorbed gas. Thus, in the grand canonical ensemble the temperature and chemical potential are imposed and the number of particles is allowed to fluctuate during the simulation.

In terms of the fugacity f of the fluid in the reservoir the grand canonical partition function can be written as^{87,96}

$$\Xi = \sum_N \frac{(\beta f V)^N}{N!} \int \exp(-\beta U(\mathbf{s}^N)) d\mathbf{s}^N. \quad (4.27)$$

The reduced coordinates \mathbf{s} are defined by

$$\mathbf{r}_i = L\mathbf{s}_i \quad \text{with} \quad L = V^{1/3} \quad \text{for} \quad i = 1, 2, \dots, N. \quad (4.28)$$

For the probability density the following relation holds:

$$\rho_i(N) \propto \frac{(\beta f V)^N}{N!} \exp(-\beta U(\mathbf{s}_i^N)) \quad (4.29)$$

Acceptable trial moves for sampling this distribution are:

1. Displacement of particles: A particle is selected at random and given a new conformation. This move is accepted with a probability⁸⁷

$$\text{acc}(o \rightarrow n) = \min(1, \exp\{-\beta[U(n) - U(o)]\}) \quad (4.30)$$

2. Rotation of particles: A particle is selected at random and given a random rotation around the center of mass. The move is accepted with the probability given by equation (4.30).
3. Insertion and removal of particles: A particle is inserted at a random position or a randomly selected particle is removed. The creation of a particle of species A is accepted with a probability^{97,98}

$$\text{acc}(N_A \rightarrow N_A + 1) = \min\left(1, \frac{\mathcal{W}_A(n)}{\langle \mathcal{W}_A^{\text{IG}} \rangle} \frac{f_A V \beta}{(N_A + 1)}\right), \quad (4.31)$$

and the removal of a particle is accepted with a probability

$$\text{acc}(N_A \rightarrow N_A - 1) = \min\left(1, \frac{\langle \mathcal{W}_A^{\text{IG}} \rangle}{\mathcal{W}_A(o)} \frac{N_A}{f_A V \beta}\right). \quad (4.32)$$

Note that the latter two equations apply if the molecules are grown atom by atom using the configurational-bias Monte Carlo approach.^{99,100} A detailed derivation of the acceptance rules is given in the thesis of Jakobtorweihen.⁸⁵

Rates of elementary reactions

5

Rate coefficients for elementary reactions on the catalyst surface are obtained by conventional transition state theory,^{101–103}

$$k_{\text{TST}}(T) = \frac{k_{\text{B}}T}{h} \frac{Q_{\text{TS}}(T)}{Q_{\text{R}}(T)} \exp\left(\frac{-E^{\ddagger}}{RT}\right), \quad (5.1)$$

where k_{B} is Boltzmann's constant, h is Planck's constant, T is the absolute temperature and E^{\ddagger} is the difference in electronic energies between the transition state and the reactant state. With Q_{TS} and Q_{R} we denote the partition functions of the transition state and the reactant state, respectively. The partition functions were calculated using the assumption of immobile adsorption, that is, a complete conversion of frustrated rotational and translational degrees of freedom into vibrations. If the energy of the ground vibrational state is defined as $\sum h\nu/2$ (i. e. E^{\ddagger} does not contain zero-point energy corrections) the partition function of the reactant is given by

$$Q_{\text{R}}(T) = \prod_{i=1}^{3n-6} \frac{\exp(-\Theta_{\text{vib},i}/(2T))}{1 - \exp(-\Theta_{\text{vib},i}/T)} \quad \text{with} \quad \Theta_{\text{vib},i} = \frac{\tilde{\nu}_i c h}{k_{\text{B}}}. \quad (5.2)$$

In this equation $\tilde{\nu}_i$ is the i th wave number and c is the speed of light. All other quantities are defined above. The partition function of the transition state is also evaluated with equation 5.2 but with the product running from $i=1$ to $3n-7$ as the vibrational degree of freedom corresponding to the reaction coordinate is missing.

For the nitrous oxide decomposition we report rates for barrierless adsorption processes. These were obtained from the desorption rate and the equilibrium constant for adsorption,^{46,104}

$$k_{\text{des}}(T) = \frac{k_{\text{B}}T}{h} \exp\left(\frac{-\Delta E_{\text{des}}}{RT}\right); \quad k_{\text{ads}} = k_{\text{des}}K_{\text{equil}}, \quad (5.3)$$

where ΔE_{des} is the zero-point corrected energy difference between the separated species and the adsorbed complex. The equilibrium constant based upon 1 bar standard state for adsorption of the gas phase species A on the zeolite surface Z is given by

$$K_{\text{equil}}(T) = \frac{Q_{\text{ZA}}(T)}{Q_{\text{Z}}(T)Q_{\text{A}}(T)(k_{\text{B}}T/p^0)} \exp\left(\frac{-(E_{\text{ZA}} - E_{\text{Z}} - E_{\text{A}})}{RT}\right). \quad (5.4)$$

The partition functions Q_{ZA} and Q_{Z} are calculated according to equation 5.2. The partition function of the gas phase species, Q_{A} , consists of translational, rotational, vibrational, and electronic contributions. The energies E_{X} are electronic energies and are negative in sign.

For the nitrous oxide decomposition we also report rate coefficients for spin-surface crossings. Because the minimum-energy structure on the seam of two potential energy surfaces is not a stationary point, the partition function cannot be calculated according to equation 5.2. Instead we estimate the rate coefficients for these processes in a way similar to the rate coefficients for desorption,⁴⁶

$$k_{\text{low} \rightarrow \text{high}} = \frac{k_{\text{B}}T}{h} \exp\left(\frac{-\Delta E}{RT}\right); \quad k_{\text{high} \rightarrow \text{low}} = k_{\text{low} \rightarrow \text{high}} K_{\text{equil}}, \quad (5.5)$$

where ΔE is the difference in electronic energy between the minimum on the seam of the two potential energy surfaces and the reactant state. To estimate if very low spin surface probabilities could lower the rate coefficient given by equation 5.5 significantly, thermally averaged spin transition probabilities are calculated with the Landau-Zener formula,⁴⁵

$$\bar{P}_{12} = \int_0^{\infty} \left(1 - \exp\left\{-\frac{4\pi^2 H_{12}^2}{h\nu |\text{grad}(E_1) - \text{grad}(E_2)|}\right\}\right) \frac{\exp(-\nu^2/2k_{\text{B}}T)}{\int_0^{\infty} \exp(-\nu^2/2k_{\text{B}}T) d\nu} d\nu \quad (5.6)$$

where H_{12} is the spin-orbit coupling energy. As will be shown in chapter 7, rates of spin-surface crossing were never rate-limiting in this work and, hence, spin-surface crossing should not have an influence on the overall kinetics on the reaction network studied.

Part III

Nitrous oxide decomposition on
dinuclear oxygen bridged iron
sites in Fe-ZSM-5

6

A reaction mechanism for the nitrous oxide decomposition on dinuclear oxygen bridged iron sites in Fe-ZSM-5

*The reaction mechanism for the decomposition of nitrous oxide (N_2O) on hydroxylated and dehydroxylated dinuclear oxygen bridged extraframework iron sites in Fe-ZSM-5 has been studied using density functional theory. The results show that if two charge exchange sites in the zeolite are in close proximity, two isolated dihydroxylated iron sites readily form an oxygen bridged iron site while releasing water. Different mechanisms for N_2O decomposition were examined on these hydroxylated dinuclear iron sites. The activity for the N_2O decomposition on these sites is low. At elevated temperatures, water desorbs from hydroxylated sites and N_2O is readily decomposed on dehydroxylated iron sites. The rate-limiting step in the reaction path is N_2O dissociation. The overall activity of the N_2O decomposition on dinuclear iron sites is qualitatively the same as that on isolated, single iron sites reported previously by Heyden et al. [*J. Phys. Chem. B* 109, 1857 (2005)]. More important than the nuclearity of the iron site (mono- or dinuclear) for the activity of Fe-ZSM-5 in N_2O decomposition is the influence of small amounts of water in the reaction system on the nature of the iron site. As in the case of isolated, single iron sites, only the dehydroxylated dinuclear iron sites show a significant activity for N_2O dissociation, while the hydroxylated sites are virtually inactive.*

6.1 Introduction

The application of microporous materials as catalytic hosts for transition metals has become an important area from the viewpoint of environmental catalysis.^{20,105,106} Special attention is addressed to iron-exchanged ZSM-5 because these materials are very active for the catalytic decomposition and catalytic reduction of N_2O emitted from industrial waste streams.^{107,108} The state of iron in Fe-ZSM-5 is strongly dependent on the method of iron exchange, the level of Fe exchange (i.e. the Fe/Al ratio), and the pretreatment of the as-exchanged material. It is therefore not surprising that different research groups report experimental findings, which seem inconsistent with one another concerning the nature of the active site and the rate-limiting step of the N_2O decomposition. Both mononuclear and dinuclear iron sites have been proposed as the principal active site,^{109–112} and either N_2O dissociation or O_2 desorption have been suggested as the rate-limiting step in the overall process of N_2O decomposition.^{113–118} An extensive review on the preparation and characterization of Fe-ZSM-5 catalyst materials is given by Heijboer.¹¹⁹ In this study, an effort is made to relate the methods of catalyst preparation to the iron species produced and their role in $\text{NO}_x/\text{N}_2\text{O}$ removal and selective oxidation. A conclusion of this work is that it seems impossible at present to prepare a Fe-ZSM-5 sample that contains exclusively a single active iron species. Moreover, no single experimental technique is capable of defining the structure of active sites unambiguously.

Given the diversity of the Fe-containing sites present in Fe-ZSM-5, it seems reasonable to use theoretical methods as a complement to experimental methods in order to obtain a clearer view of what types of Fe sites might be involved in N_2O decomposition to N_2 and O_2 , and the mechanism by which this process occurs. Important progress has been made recently in two comprehensive theoretical studies of the mechanism and kinetics of N_2O decomposition on isolated, single extraframework iron sites in the absence^{115,116} and presence of NO .¹²⁰ It was found that N_2O decomposition is first order with respect to N_2O concentration and that water impurities in the gas stream have a strong inhibiting effect. The proposed reaction mechanisms together with the rate coefficients calculated for each elementary step were able to explain and reproduce various transient and steady state experiments.

The present study is an extension of the work conducted by Heyden et al.^{115,120} to dinuclear oxygen bridged iron sites. The formation of such complexes is proposed for over-exchanged Fe-ZSM-5 prepared by the sublimation technique^{121,122} as well as upon activation treatments of Fe-ZSM-5 prepared

by other routes.^{119,123,124} For dinuclear Fe-complexes a number of molecular active site structures have been proposed compensating one¹²⁵ or two lattice charges.¹²⁶ This study focuses on the investigation of $Z^-[-\text{OFeOFeO}]^{2+}Z^-$ sites (Z^- represents the charge exchange sites in the zeolite) which were proposed by Chen and Sachtler,¹²⁷ El-Malki et al.,¹²⁸ Marturano et al.,¹²⁹ Čík et al.,¹³⁰ and Starokon et al.¹³¹ There are very few quantum chemical studies on dinuclear Fe-complexes serving as active site models in zeolites,^{132–135} and only in the work of Yakovlev et al.¹³⁵ were parts of the zeolitic framework included in the cluster model. In the latter study several catalytic cycles of the N_2O decomposition on a dinuclear Fe-complex are discussed from a thermodynamic point of view. Neither activation energies nor rates of elementary reactions were reported and spin-surface crossing was not considered. It is the aim of the present study to analyze the energetics and kinetics of the N_2O decomposition on hydroxylated and dehydroxylated dinuclear oxygen bridged extraframework iron sites. It is demonstrated that the formation of such complexes occurs readily if two charge exchange sites in the zeolite are in close proximity. Of particular interest was to examine whether single or di-/oligonuclear iron sites are more active for decomposition of N_2O . In addition, we determined the rate-limiting step in the N_2O decomposition on dinuclear iron sites and the order of the reaction. We illustrate how the nature of the active site and the associated reaction mechanism change with temperature. Finally, we studied the influence of antiferromagnetic coupling of the two iron centers on the reaction mechanism of the N_2O decomposition.

In the present chapter we introduce a detailed reaction mechanism for the N_2O decomposition on dinuclear iron sites. In chapter 7 we will report the rate parameters for all elementary processes and use them to simulate the N_2O decomposition under various conditions.

6.2 Computational details

As noted in the Introduction, this study focuses on the investigation of $Z^-[-\text{OFeOFeO}]^{2+}Z^-$ complexes. Therefore, two Al substituted T-sites in close proximity are required to charge balance the active site. The Al distribution in Fe-ZSM-5 has been the subject of several theoretical studies using statistical methods^{136–140} and quantum chemical calculations.^{141–144} According to Rice et al.¹³⁹ 5T rings are the preferable exchange sites for Fe cations in Fe-ZSM-5. Goodman et al.¹⁴⁰ noted that the open ZSM-5 channel structure favors Al pairs that lie along one side of a channel wall rather than across a channel. Quantum chemical calculations have revealed that Al substitutes

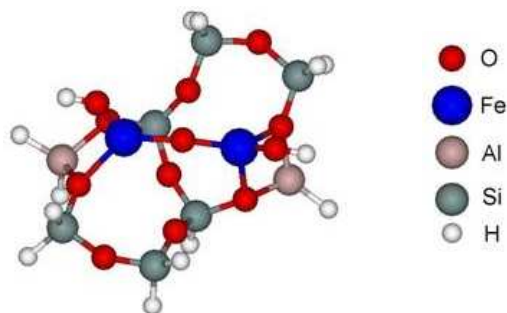


Figure 6.1: Active site model $Z^-[\text{HOFeOFeOH}]^{2+}Z^-$, for the N_2O decomposition in Fe-ZSM-5.

preferentially at T9 and T12 position. Combining these findings, an inter-ring bridging structure consisting of two adjoining 5T rings where in one ring the T9 and in the other ring the T12 site is substituted by Al, was used in the present work as model of the catalytically active site. We note, though, that since the distribution of framework Al during zeolite synthesis may be controlled kinetically rather than energetically, as concluded by Han et al.,¹⁴⁵ a number of other possible dinuclear structures may also be present in Fe-ZSM-5.

The catalytically active center and a portion of the zeolite framework are represented by a 34-41 atom cluster consisting of a pair of 5T rings sharing an edge (see figure 6.1). All Si atoms were placed in their crystallographic positions as reported by Olson et al.¹⁴⁶ The Si-O bonds not belonging to the 5T rings were replaced by terminal Si-H bonds oriented in the direction of the former Si-O bond. The Si-H bond length was set to 1.487 Å, which is the optimized bond length for SiH_4 at the B3LYP/TZVP level of theory. The resulting coordinates for the terminal H atoms were then held fixed throughout all subsequent calculations while all other coordinates were allowed to relax. The Si-atoms at the T9 and T12 positions were substituted by Al-atoms. The present cluster model is similar to the one of Yakovlev et al.¹³⁵ The two models differ only in the methods used to determine the fixed atom positions. Yakovlev et al.¹³⁵ first optimized the Si-H distances of the terminal hydrogen atoms for the ZH_2 model and then kept the positions of these atoms frozen in all subsequent calculations. As a result, the cluster model used in the present work resembles the crystallographic structure of ZSM-5 more closely than the cluster model used by Yakovlev et al.¹³⁵ Nevertheless, it is noted that this subtle difference in the two models is not expected to affect electronic energy differences significantly.

Calculation of the ground state energy of a dinuclear metal cluster by density functional methods is complicated by the spin coupling of the unpaired electrons in the metal centers.^{147–150} The spin coupling parameter J can be calculated using the original broken-symmetry approach proposed by Noodleman through the following equation:¹⁵¹

$$E_{\text{HS}} - E_{\text{BS}} = -2S_1S_2J. \quad (6.1)$$

Here S_1 and S_2 are the total spins of the two interacting paramagnetic centers. The first energy term, E_{HS} , corresponds to the high spin solution and the second one, E_{BS} , to the broken-symmetry solution, a single-determinant wave function with $S_z = 0$ and opposite spins at the two paramagnetic centers. Equation 6.1 was shown to give accurate results for self-interaction free methods.¹⁵² For DFT calculations not corrected for the self-interaction error the following non-projected approach was demonstrated to give accurate coupling constants.^{152,153}

$$E_{\text{HS}} - E_{\text{BS}} = -(2S_1S_2 + S_2)J. \quad (6.2)$$

Equation 6.2 was used in the present work to calculate coupling constants for the dinuclear oxygen bridged iron site.

The representation of the open-shell low spin coupling ($M_S = 1$) of the two iron centers by a single determinant method such as DFT usually gives a heavily spin contaminated wave function which makes the results questionable especially for energetics.¹⁵⁴ As a consequence, it is necessary to apply a multireference method; however, this is impractical for the system sizes studied in this work. Therefore, if the reaction mechanism is not influenced by antiferromagnetic coupling it is computationally more practical to ignore the antiferromagnetic nature of the system and to perform spin-unrestricted open-shell calculations for ferromagnetically coupled high-spin states.¹⁵⁵ In the present work the catalytic cycles for the decomposition of N_2O on dinuclear oxygen bridged iron sites were determined using spin-unrestricted open-shell calculations for ferromagnetically coupled high spin states. For the most relevant reaction steps additional broken-symmetry calculations have been carried out to study the influence of antiferromagnetic coupling on the reaction mechanism of the N_2O decomposition and to validate the ferromagnetically coupled high-spin calculations. As mentioned above, all reported results for antiferromagnetically coupled states are subject to large spin contamination. We obtained numbers for the expectation value $\langle \hat{S}^2 \rangle$ ranging between 3.9 for ground states and 4.9 for transition states, far away from the correct value, $S(S + 1) = 0$, for a singlet state.

For the ferromagnetically coupled high spin states quantum chemical calculations of the geometry and potential energy minima were performed for spin potential energy surfaces with spin multiplicity $M_S = 7$ to 11, using gradient-corrected spin density-functional theory (DFT). To represent the effects of exchange and correlation, Becke’s 3-parameter exchange functional⁷⁵ together with the correlation functional of Lee, Yang and Parr (B3LYP)⁷⁶ was used with a very fine numerical grid size (m5).¹⁵⁶ The B3LYP functional has proven to be effective for a number of reactions involving iron oxide molecules,^{157–160} leading us to conclude that a DFT-B3LYP approach can also be used successfully to investigate N₂O decomposition on dinuclear oxygen bridged iron sites in Fe-ZSM-5. Basis sets at the triple-zeta level with polarisation functions (TZVP) were used for all atoms including iron.¹⁶¹ Electronic energy differences were found to be converged with respect to the basis set size. All calculations were carried out using the TURBOMOLE V5.7 suite of programs¹⁶² in C1 symmetry. Our calculations on different spin potential energy surfaces (PESs) revealed that the energy difference between different PESs is usually significant so that only energies of PES minima for the ground state are reported. Spin contamination was not observed for ground-state minimum structures. Some spin contamination was observed for transition states and minimum structures on the seam of two PESs. Nevertheless, in all cases it was still possible to distinguish clearly between states of different spin multiplicities.

Two recent DFT studies have demonstrated that the B3LYP functional gives very accurate results for the coupling constant J of dinuclear Fe complexes in models of metalloenzymes, with four to five unpaired electrons on each cation, using directly the energies corresponding to the broken-symmetry wave function.^{152,163} These results suggest that the DFT/B3LYP approach can also be used successfully to study antiferromagnetic coupling in dinuclear oxygen bridged iron sites in Fe-ZSM-5. In the present study we computed broken-symmetry solutions for the most relevant reaction steps (determined from ferromagnetic DFT calculations) along the catalytic cycle to investigate the influence of antiferromagnetic coupling in dinuclear oxygen bridged iron sites on the reaction mechanism. For each broken-symmetry solution we computed the Mulliken spin densities to check whether the number of unpaired electrons was close to the formal integer value (3.5 – 3.7 for an Fe(II)- d^4 center and 3.8 – 4.1 for an Fe(III)- d^5 center).¹⁶³

During the geometry optimizations, energies were converged to 10^{-7} Ha and the maximum norm of the cartesian gradient to 10^{-4} Ha/bohr. Transition states were localized using a combination of interpolation and local methods. The growing-string method¹⁶⁴ was used in mass-weighted coordin-

ates with a maximum of 13 to 16 nodes. After the two ends of the growing string join, the growing-string method was terminated and an approximate saddle point was obtained. To refine the position of the saddle point, the modified-dimer method¹⁶⁵ was employed. A gradient norm convergence criterion of 5×10^{-4} Ha/bohr was used for the transition state searches. Minimum potential energy structures on the seam of two PESs were determined with a multiplier penalty function algorithm (see Heyden et al.¹¹⁵ and Heyden⁴⁶ for details). Converged minimum energy crossing point structures had a maximum energy difference between both PESs of less than 10^{-6} Ha.

6.3 Results and discussion

The nuclearity of the active site in Fe-ZSM-5 for the decomposition of N_2O is still a matter of active debate in the literature. While it has been proposed that different preparation and pretreatment methods produce different kinds of active sites, Pirngruber et al.¹²⁴ have observed that differently prepared zeolites show qualitatively similar catalytic behavior in N_2O decomposition. The present study supports this experimental finding by demonstrating that the overall behavior of the N_2O decomposition on dinuclear oxygen bridged iron sites does not differ considerably from that on isolated, single iron sites. In addition, we show that oxygen migration over a dinuclear iron structure is not expected to be the rate-limiting step of the catalytic cycle.

In what follows, we first present calculations showing how dinuclear oxygen bridged iron sites can be formed. Second, two different catalytic cycles for the N_2O decomposition on hydroxylated dinuclear iron sites are presented. Third, we show, how N_2O dissociates on dehydroxylated dinuclear iron sites. The latter mechanism takes place at elevated temperatures after water has desorbed from the catalytic surface. Fourth, we show that the reaction mechanism for N_2O decomposition on dinuclear oxygen bridged iron sites is essentially unchanged if antiferromagnetic coupling is taken into account.

In table 6.1 geometries of the transition states as well as the imaginary frequencies associated with the transition state mode for the N_2O dissociation steps on the ferromagnetically coupled PES are summarized. Table 6.2 lists the imaginary frequencies of all other transition states on the ferromagnetically coupled PES. In table 6.3 geometries and imaginary frequencies associated with the transition state mode for transition states determined with the BS approach are presented. Coupling constants for the N_2O decomposition on $\text{Z}^-[\text{FeOFe}]^{2+}\text{Z}^-$ are summarized in table 6.4. Enthalpies discussed in the text are averaged over a temperature range from 600 to 800 K.

Table 6.1: Geometries and imaginary frequencies of the transition states in N₂O decomposition on ferromagnetically coupled dinuclear oxygen bridged iron sites.

elementary step	$R_{\text{NN}'}$ (Å)	$R_{\text{N}'\text{O}}$ (Å)	$\angle\text{NN}'\text{O}^{\text{a}}$ (deg)	ω (cm ⁻¹)
$\text{Z}^-[\text{HOFeOFeOH}]^{2+}(\text{ON}_2)\text{Z}^- \leftrightarrow \text{Z}^-[\text{HOFeOFeOH}]^{2+}\text{Z}^- + \text{N}_2$	1.10	1.61	153.4	690 <i>i</i>
$\text{Z}^-[\text{HOFe}(\text{ON}_2)\text{-FeOH}]^{2+}\text{Z}^- \leftrightarrow \text{Z}^-[\text{HOFeO-FeOH}]^{2+}\text{Z}^- + \text{N}_2$	1.14	1.38	137.4	502 <i>i</i>
$\text{Z}^-[\text{HOFeO-(N}_2\text{O)FeOH}]^{2+}\text{Z}^- \leftrightarrow \text{Z}^-[\text{HOFeO-OFeOH}]^{2+}\text{Z}^- + \text{N}_2$	1.13	1.42	136.9	673 <i>i</i>
$\text{Z}^-[\text{FeOHFeOH}]^{2+}(\text{ON}_2)\text{Z}^- \leftrightarrow \text{Z}^-[\text{OFeOHFeOH}]^{2+}\text{Z}^- + \text{N}_2$	1.11	1.51	145.0	820 <i>i</i>
$\text{Z}^-[\text{OFeOHFeOH}]^{2+}(\text{ON}_2)\text{Z}^- \leftrightarrow \text{Z}^-[\text{OOFeOHFeOH}]^{2+}\text{Z}^- + \text{N}_2$	1.13	1.50	131.3	810 <i>i</i>
$\text{Z}^-[\text{FeOFe}]^{2+}(\text{ON}_2)\text{Z}^- \leftrightarrow \text{Z}^-[\text{FeOFeO}]^{2+}\text{Z}^- + \text{N}_2$	1.13	1.43	136.7	619 <i>i</i>
$\text{Z}^-[\text{FeOFeO}]^{2+}(\text{ON}_2)\text{Z}^- \leftrightarrow \text{Z}^-[\text{OFeOFeO}]^{2+}\text{Z}^- + \text{N}_2$	1.12	1.46	137.7	770 <i>i</i>
$\text{Z}^-[\text{FeOFe}]^{2+}(\text{ON}_2)\text{Z}^- \leftrightarrow \text{Z}^-[\text{OFeOFe}]^{2+}\text{Z}^- + \text{N}_2$	1.13	1.44	136.7	650 <i>i</i>
$\text{Z}^-[\text{OFeOFe}]^{2+}(\text{ON}_2)\text{Z}^- \leftrightarrow \text{Z}^-[\text{OFeOFeO}]^{2+}\text{Z}^- + \text{N}_2$	1.13	1.45	137.6	754 <i>i</i>

^aThe connectivity of the atoms is assumed to be NN'O.

Table 6.2: Imaginary frequencies of transition states on the ferromagnetically coupled PES not involved in N₂O dissociation.

elementary step	ω (cm ⁻¹)
Z ⁻ [HOFe ₂ O ₂ FeOH] ²⁺ Z ⁻ ↔ Z ⁻ [HOFe ₂ FeOH] ²⁺ Z ⁻ + O ₂	16 <i>i</i>
Z ⁻ [O ₂ FeOHFeOH] ²⁺ Z ⁻ ↔ Z ⁻ [FeOHFeOH] ²⁺ Z ⁻ + O ₂	90 <i>i</i>
Z ⁻ [FeOFeO ₂] ²⁺ Z ⁻ ↔ Z ⁻ [FeOFe] ²⁺ Z ⁻ + O ₂	78 <i>i</i>
Z ⁻ [HOFeOHFe(OH) ₂] ²⁺ Z ⁻ ↔ Z ⁻ [HOFeOFeOH] ²⁺ (OH ₂)Z ⁻	1141 <i>i</i>
Z ⁻ [HOFeOOFeOH] ²⁺ Z ⁻ ↔ Z ⁻ [HOFe ₂ O ₂ FeOH] ²⁺ Z ⁻	118 <i>i</i>
Z ⁻ [HOFe ₂ FeOH] ²⁺ Z ⁻ ↔ Z ⁻ [HeOHFeOH] ²⁺ Z ⁻	18 <i>i</i>
Z ⁻ [OFeOHFeOH] ²⁺ Z ⁻ {M _S = 9} ↔ Z ⁻ [OFeOFeOH ₂] ²⁺ Z ⁻	943 <i>i</i>
Z ⁻ [OFeOHFeOH] ²⁺ Z ⁻ {M _S = 11} ↔ Z ⁻ [HOFeOFeOH] ²⁺ Z ⁻	1291 <i>i</i>
Z ⁻ [FeOHFeOH] ²⁺ Z ⁻ ↔ Z ⁻ [FeOFeOH ₂] ²⁺ Z ⁻	1141 <i>i</i>
Z ⁻ [OOFeOHFeOH] ²⁺ Z ⁻ ↔ Z ⁻ [O ₂ FeOHFeOH] ²⁺ Z ⁻	754 <i>i</i>
Z ⁻ [HOFeO ₂ OFeOH] ²⁺ Z ⁻ ↔ Z ⁻ [HOFeOOFeOH] ²⁺ Z ⁻	382 <i>i</i>
Z ⁻ [HOFeO ₂ FeOH] ²⁺ Z ⁻ ↔ Z ⁻ [HOFeOFeOH] ²⁺ Z ⁻	180 <i>i</i>
Z ⁻ [OFeOFeO] ²⁺ Z ⁻ ↔ Z ⁻ [FeOOFeO] ²⁺ Z ⁻	629 <i>i</i>
Z ⁻ [FeOOFeO] ²⁺ Z ⁻ ↔ Z ⁻ [FeO ₂ FeO] ²⁺ Z ⁻	260 <i>i</i>
Z ⁻ [FeO ₂ FeO] ²⁺ Z ⁻ ↔ Z ⁻ [FeOFeO ₂] ²⁺ Z ⁻	145 <i>i</i>

Table 6.3: Geometries and imaginary frequencies of transition states for key reactions on the antiferromagnetically coupled PES^a.

elementary step	$R_{\text{NN}'}$ (Å)	$R_{\text{N}'\text{O}}$ (Å)	$\angle \text{NN}'\text{O}^{\text{a}}$ (deg)	ω (cm ⁻¹)
Z ⁻ [FeOFe] ²⁺ (ON ₂)Z ⁻ ↔ Z ⁻ [FeOFeO] ²⁺ Z ⁻ + N ₂	1.13	1.41	136.6	635 <i>i</i>
Z ⁻ [FeOFeO] ²⁺ (ON ₂)Z ⁻ ↔ Z ⁻ [OFeOFeO] ²⁺ Z ⁻ + N ₂	1.13	1.46	137.0	756 <i>i</i>
Z ⁻ [OFeOFeO] ²⁺ Z ⁻ ↔ Z ⁻ [FeOOFeO] ²⁺ Z ⁻				745 <i>i</i>
Z ⁻ [FeOOFeO] ²⁺ Z ⁻ ↔ Z ⁻ [FeO ₂ FeO] ²⁺ Z ⁻				335 <i>i</i>
Z ⁻ [FeO ₂ FeO] ²⁺ Z ⁻ ↔ Z ⁻ [FeOFeO ₂] ²⁺ Z ⁻				409 <i>i</i>
Z ⁻ [FeOFeO ₂] ²⁺ Z ⁻ ↔ Z ⁻ [FeOFe] ²⁺ Z ⁻ + O ₂				108 <i>i</i>

^aThe connectivity of the atoms is assumed to be NN'O.

6.3.1 Formation of dinuclear iron sites

The existence of Z⁻[Fe(OH)₂]⁺ sites in Fe-ZSM-5 prepared by solid state exchange of H-ZSM-5 with FeCl₃ and by high temperature pretreatment of Fe/Al-MFI has been demonstrated in XAFS investigations.^{166,167} A recent DRIFTS study of Krishna and Makkee¹⁶⁸ also shows that high temperature catalyst preparation or pretreatment leads to isolated dihydroxylated iron species Z⁻[Fe(OH)₂]⁺. Figure 6.2 illustrates a mechanism by which an oxygen bridged iron site of type Z⁻[HOFeOFeOH]²⁺Z⁻ is formed from two Z⁻[Fe(OH)₂]⁺ species while releasing water. This reaction is calculated to be

Table 6.4: Fe–Fe distances and Fe–O–Fe bond angles for antiferromagnetically coupled iron atoms, energy differences between the ferromagnetic and antiferromagnetic PES, and coupling constants for $Z^-[\text{HOFeOFeOH}]^{2+}Z^-$ and dehydroxylated sites.

	R_{FeFe} (Å)	$\angle\text{FeOFe}$ (deg)	$E_{\text{HS}} - E_{\text{BS}}$ (kcal/mol)	J^a (cm^{-1})
$Z^-[\text{HOFeOFeOH}]^{2+}Z^-$	3.55	158.2	6.8	−157.5
$Z^-[\text{FeOFe}]^{2+}Z^-$	3.07	117.7	4.1	−143.4
$Z^-[\text{FeOFe}]^{2+}(\text{ON}_2)Z^-$	3.11	119.2	3.9	−138.1
TS 1	3.26	129.5	5.5	−194.1
$Z^-[\text{FeOFeO}]^{2+}Z^-$	3.20	128.3	2.7	−95.5
$Z^-[\text{FeOFeO}]^{2+}(\text{ON}_2)Z^-$	3.23	128.9	2.4	−82.7
TS 2	3.40	123.2	2.5	−87.2
$Z^-[\text{OFeOFeO}]^{2+}Z^-$	3.26	133.6	1.8	−62.2
TS 3	3.55	136.4	−2.0	68.2
$Z^-[\text{FeOOFeO}]^{2+}Z^-$	3.76		0.1	−2.5
TS 4	4.40		−0.1	2.1
$Z^-[\text{FeO}_2\text{FeO}]^{2+}Z^-$	3.66		−0.1	3.4
TS 5	3.57	132.4	3.2	−110.9
$Z^-[\text{FeOFeO}_2]^{2+}Z^- \{M_S = 1\}$	3.30	133.0	5.5	−194.0
SC	3.33	135.1	5.2	−182.4
$Z^-[\text{FeOFeO}_2]^{2+}Z^- \{M_S = 3\}$	3.28	131.7	5.5	−128.7
TS 6	3.17	123.8	4.1	−95.7

^aThe coupling constants were calculated using the nonprojected approach (eqn 6.2). Transition states connecting the minima are denoted as TS, the minimum on the seam of two potential energy surfaces is denoted as SC.

endothermic with an enthalpy of reaction of $\Delta H_{\text{R}} = 18.8$ kcal/mol. The reaction mechanism consists of a sequence of three slightly endothermic elementary reactions, none of which has a reaction barrier larger than 10.6 kcal/mol. As a result, the overall barrier for the reaction $Z^-[\text{HOFeOH.HOFeOH}]^{2+}Z^- \rightarrow Z^-[\text{HOFeOFeOH}]^{2+}Z^- + \text{H}_2\text{O}$ is calculated as the energy difference between $Z^-[\text{HOFeOFeOH}]^{2+}Z^- + \text{H}_2\text{O}$ and $Z^-[\text{HOFeOH.HOFeOH}]^{2+}Z^-$, $E^\ddagger = 19.2$ kcal/mol. Considering the low H_2O partial pressure in industrial exhaust streams the entropy gain in desorbing a water molecule outweighs the higher energy of the products and significant more dinuclear iron species than isolated $Z^-[\text{Fe}(\text{OH})_2]^+$ sites are present in equilibrium at low temperatures. Steady-state simulations of the catalytic surface taking into account the whole reaction network presented in this work show that the formation of

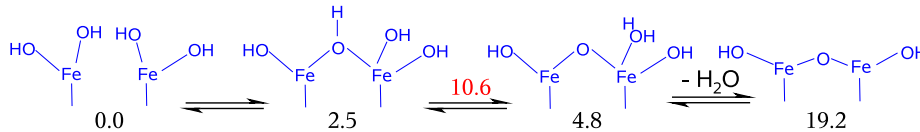


Figure 6.2: Formation of a dinuclear oxygen bridged iron site from two dihydroxylated single iron sites. All energies are zero-point corrected, in kcal/mol and with reference to $Z^-[\text{HOFeOH}_2\text{HOFeOH}]^{2+}Z^-$ with the appropriate amounts of H_2O . Energies of potential energy minima are in black. Energies of transition states are in red. Structures in blue are on the ferromagnetically coupled PES with $M_S = 11$. The left Fe atom in each structure represents the T9 site, the right Fe atom represents the T12 site.

$Z^-[\text{HOFeOFeOH}]^{2+}Z^-$ sites takes place already at room temperature if two iron sites are in close proximity.

6.3.2 N_2O decomposition on $Z^-[\text{HOFeOFeOH}]^{2+}Z^-$ sites

A catalytic cycle for the decomposition of N_2O on $Z^-[\text{HOFeOFeOH}]^{2+}Z^-$ sites is illustrated in figure 6.3. Nitrous oxide adsorbs on $Z^-[\text{HOFeOFeOH}]^{2+}Z^-$ through the O-end with an enthalpy of adsorption of $\Delta H_{\text{ads}} = -0.8$ kcal/mol. The activation barrier for the reaction of $Z^-[\text{HOFeOFeOH}]^{2+}(\text{ON}_2)Z^-$ to form $Z^-[\text{HOFeOOFeOH}]^{2+}Z^-$ and N_2 is $E^\ddagger = 40.2$ kcal/mol. The peroxo structure $Z^-[\text{HOFeOOFeOH}]^{2+}Z^-$ was calculated to have a lower energy than the structure that would appear if the oxygen was deposited on top of the iron. This result is in line with DFT calculations on isolated, single iron sites conducted by Heyden et al.¹¹⁵ In the latter study it was shown that the reaction of $Z^-[\text{Fe}(\text{OH})_2]^+(\text{ON}_2)$ to form $Z^-[\text{OFe}(\text{OH})_2]^+$ and N_2 is endothermic, with an enthalpy of reaction of $\Delta H_{\text{R}} = 16.7$ kcal/mol and an activation energy of $E^\ddagger = 42.8$ kcal/mol on the sextet PES. In the present study an enthalpy of reaction of $\Delta H_{\text{R}} = 18.9$ kcal/mol and an activation energy of more than 40.0 kcal/mol has been calculated for the corresponding reaction, i.e. for $Z^-[\text{HOFeOFeOH}]^{2+}(\text{ON}_2)Z^- \rightarrow Z^-[\text{HOFeOFeOOH}]^{2+}Z^- + \text{N}_2$ (not shown in figure 6.3). The formation of the peroxo structure $Z^-[\text{HOFeOOFeOH}]^{2+}Z^-$ is slightly exothermic with an enthalpy of reaction of $\Delta H_{\text{R}} = -1.4$ kcal/mol. From the latter structure $Z^-[\text{HOFe}_2\text{O}_2\text{FeOH}]^{2+}Z^-$ is formed by surmounting an activation barrier of $E^\ddagger = 6.5$ kcal/mol. This reaction is endothermic with an enthalpy of reaction of $\Delta H_{\text{R}} = 5.2$ kcal/mol. Molecular oxygen can desorb from $Z^-[\text{HOFe}_2\text{O}_2\text{FeOH}]^{2+}Z^-$. The O_2 desorp-

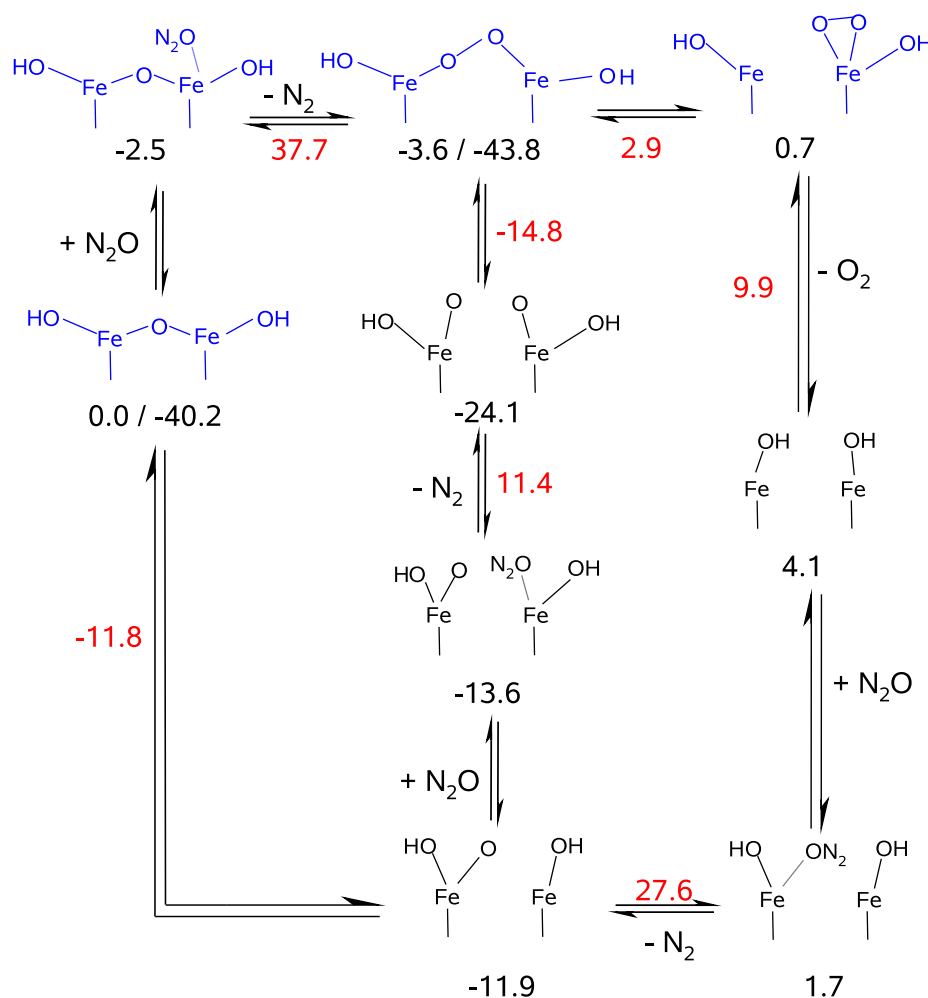


Figure 6.3: Catalytic cycle of the N₂O dissociation on Z-[HOFeOFeOH]²⁺Z⁻ sites. All energies are zero-point corrected, in kcal/mol and with reference to Z-[HOFeOFeOH]²⁺Z⁻ with the appropriate amounts of N₂O, N₂, and O₂. Energies of potential energy minima are in black. Energies of transition states are in red. Black structures are on the ferromagnetically coupled PES with $M_S = 9$. Structures in blue are on the PES with $M_S = 11$. Multiple numbers under a PES minimum structure correspond to different catalytic cycles. The left Fe atom in each structure represents the T9 site, the right Fe atom represents the T12 site.

tion barrier is $E^\ddagger = 9.2$ kcal/mol and the enthalpy of desorption is 1.7 kcal/mol. A N₂O molecule can dissociate on each hydroxylated iron site

of $Z^-[\text{HOFe}_2\text{FeOH}]^{2+}Z^-$. N_2O adsorbs from the O-end on the T9 site with an enthalpy of adsorption of $\Delta H_{\text{ads}} = -0.2$ kcal/mol. The activation energy for the reaction of $Z^-[\text{HOFe}(\text{ON}_2)\text{FeOH}]^{2+}Z^-$ to form $Z^-[\text{HOFeO}_2\text{FeOH}]^{2+}Z^-$ and N_2 is $E^\ddagger = 25.9$ kcal/mol. This reaction is exothermic by $\Delta H_{\text{R}} = -15.0$ kcal/mol. On the T12 site N_2O adsorbs from the O-end with an enthalpy of adsorption of $\Delta H_{\text{ads}} = 0.2$ kcal/mol. The activation energy for the reaction, $Z^-[\text{HOFeO}(\text{N}_2\text{O})\text{FeOH}]^{2+}Z^- \rightarrow Z^-[\text{HOFeO}_2\text{FeOH}]^{2+}Z^- + \text{N}_2$, is $E^\ddagger = 25.0$ kcal/mol. The enthalpy of reaction of this exothermic step is $\Delta H_{\text{R}} = -11.9$ kcal/mol. The peroxo structure $Z^-[\text{HOFeO}_2\text{FeOH}]^{2+}Z^-$ is formed from $Z^-[\text{HOFeO}_2\text{FeOH}]^{2+}Z^-$. This exothermic reaction, $\Delta H_{\text{R}} = -18.5$ kcal/mol, involves surmounting a small barrier of $E^\ddagger = 9.4$ kcal/mol and closes the catalytic cycle on $Z^-[\text{HOFeO}_2\text{FeOH}]^{2+}Z^-$ sites. An alternative path goes from $Z^-[\text{HOFeO}_2\text{FeOH}]^{2+}Z^-$ back to $Z^-[\text{HOFeO}_2\text{FeOH}]^{2+}Z^-$, which closes the catalytic cycle on $Z^-[\text{HOFeO}_2\text{FeOH}]^{2+}Z^-$ sites. The latter reaction is highly exothermic with an enthalpy of reaction of $\Delta H_{\text{R}} = -27.9$ kcal/mol and a very small activation energy of $E^\ddagger = 0.1$ kcal/mol. Due to the high activation barrier for N_2O dissociation on $Z^-[\text{HOFeO}_2\text{FeOH}]^{2+}Z^-$ compared to the formation of the oxygen bridge, $Z^-[\text{HOFeO}_2\text{FeOH}]^{2+}Z^- \rightarrow Z^-[\text{HOFeO}_2\text{FeOH}]^{2+}Z^-$, the latter reaction is much more likely, and hardly any $Z^-[\text{HOFeO}_2\text{FeOH}]^{2+}Z^-$ is expected to be present under reaction conditions.

An alternative cycle starting from $Z^-[\text{HOFeO}_2\text{FeOH}]^{2+}Z^-$ is illustrated in figure 6.4. As in the previous cycle $Z^-[\text{HOFe}_2\text{FeOH}]^{2+}Z^-$ is formed. Isolated $Z^-[\text{FeOH}]^+$ sites are active in N_2O decomposition.¹²⁰ However, if such species are in close proximity they tend to form an oxygen bridged structure. The reaction $Z^-[\text{HOFe}_2\text{FeOH}]^{2+}Z^- \rightarrow Z^-[\text{FeOHFeOH}]^{2+}Z^-$ is exothermic with an enthalpy of reaction of $\Delta H_{\text{R}} = -10.9$ kcal/mol and a very small barrier of $E^\ddagger = 2.0$ kcal/mol. N_2O dissociation occurs on $Z^-[\text{FeOHFeOH}]^{2+}Z^-$ only on the dehydroxylated iron atom since the reaction barrier on the hydroxylated iron atom is considerably higher. N_2O adsorbs from the O-end with an enthalpy of adsorption of $\Delta H_{\text{ads}} = -2.2$ kcal/mol. The activation energy for the reaction $Z^-[\text{FeOHFeOH}]^{2+}(\text{ON}_2)Z^- \rightarrow Z^-[\text{OFeOHFeOH}]^{2+}Z^- + \text{N}_2$ is $E^\ddagger = 32.3$ kcal/mol. This reaction is exothermic with an enthalpy of reaction of $\Delta H_{\text{R}} = -8.4$ kcal/mol. The species $Z^-[\text{OFeOHFeOH}]^{2+}Z^-$ is more stable on the 11-et PES than on the nonet PES. A negligible spin change barrier of about $E^\ddagger = 1.6$ kcal/mol was found for the spin inversion process. The enthalpy of reaction is $\Delta H_{\text{R}} = -3.6$ kcal/mol. Due to the low barrier both structures are in equilibrium. $Z^-[\text{OFeOHFeOH}]^{2+}Z^- \{M_S = 11\}$ is a possible active site for N_2O dissociation. N_2O adsorbs from the O-end with an enthalpy of adsorption of $\Delta H_{\text{ads}} = 0.1$ kcal/mol. The activation energy for the reaction $Z^-[\text{OFeOHFeOH}]^{2+}(\text{ON}_2)Z^- \rightarrow Z^-[\text{OOFeOHFeOH}]^{2+}Z^- + \text{N}_2$ is

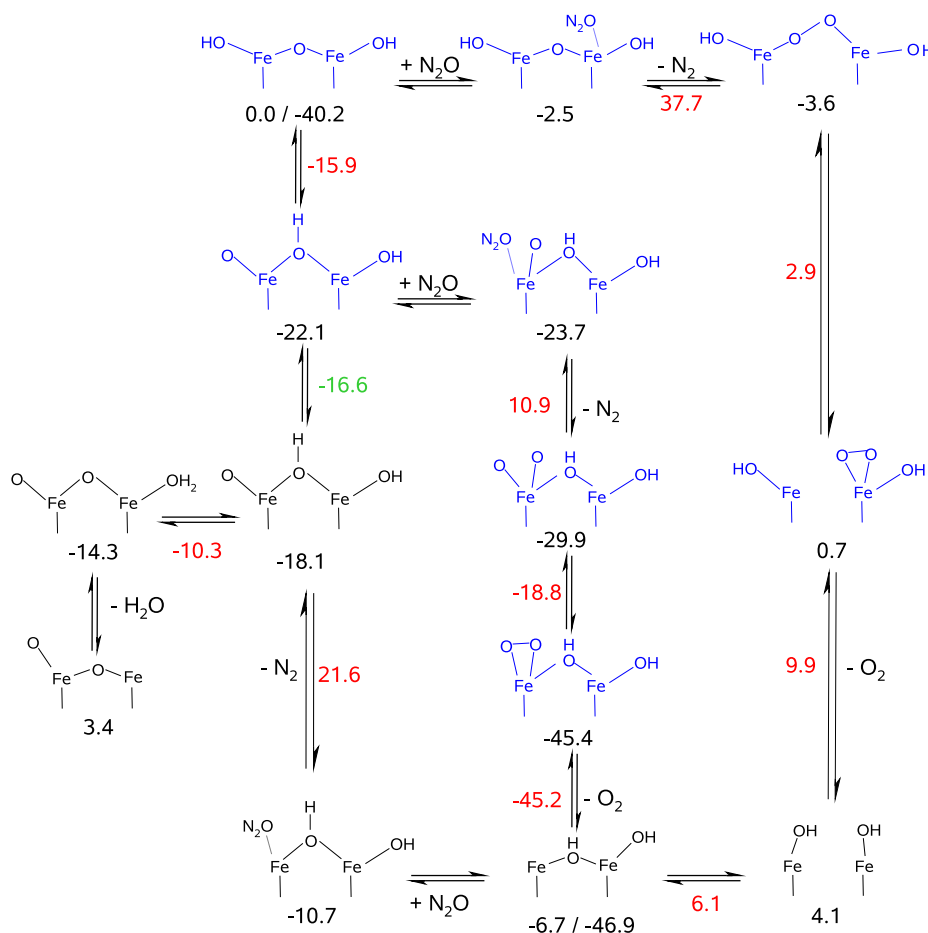


Figure 6.4: Alternative catalytic cycle of the N₂O dissociation on Z⁻[HOFeOFeOH]²⁺Z⁻ sites. All energies are zero-point corrected, in kcal/mol and with reference to Z⁻[HOFeOFeOH]²⁺Z⁻ with the appropriate amounts of N₂O, N₂, O₂, and H₂O. Energies of potential energy minima are in black. Energies of transition states are in red. Energies of minima on the seam of two PESs are in green. Black structures are on the ferromagnetically coupled PES with $M_S = 9$. Structures in blue are on the PES with $M_S = 11$. Multiple numbers under a PES minimum structure correspond to different catalytic cycles. The left Fe atom in each structure represents the T9 site, the right Fe atom represents the T12 site.

$E^\ddagger = 34.7$ kcal/mol. This step is exothermic with an enthalpy of reaction of $\Delta H_R = -6.8$ kcal/mol. Diatomic oxygen can be formed from dioxo species Z⁻[OOF₂OHFeOH]²⁺Z⁻. This reaction is exothermic with an enthalpy of

reaction of $\Delta H_R = -15.0$ kcal/mol and has an activation energy of $E^\ddagger = 11.2$ kcal/mol. Molecular oxygen desorbs readily from $Z^-[\text{O}_2\text{FeOHFeOH}]^{2+}Z^-$. The activation energy for this process is $E^\ddagger = 0.2$ kcal/mol, the enthalpy of reaction was calculated to be $\Delta H_R = -2.5$ kcal/mol. An alternative path goes from $Z^-[\text{OFeOHFeOH}]^{2+}Z^- \{M_S = 11\}$ to $Z^-[\text{HOFeOFeOH}]^{2+}Z^-$. This process is exothermic with an enthalpy of reaction of $\Delta H_R = -18.0$ kcal/mol and has a relatively small activation energy of $E^\ddagger = 6.2$ kcal/mol. As a result, this reaction is more likely to occur than the N_2O dissociation on $Z^-[\text{OFeOHFeOH}]^{2+}Z^- \{M_S = 11\}$.

To conclude, owing to the high activation energy for $Z^-[\text{HOFeOFeOH}]^{2+}Z^- + \text{N}_2\text{O} \rightarrow Z^-[\text{HOFeOFeOH}]^{2+}Z^- + \text{N}_2$, both catalytic cycles presented show only a minor activity in N_2O decomposition. This result is in agreement with a recent theoretical study of isolated, single iron sites reported by Heyden et al.¹¹⁵ In that study an activation energy of 41.5 kcal/mol was calculated for the first dissociation of N_2O on $Z^-[\text{Fe}(\text{OH})_2]^+$ sites. A value only slightly larger than the activation energy calculated for the dissociation of N_2O on $Z^-[\text{HOFeOFeOH}]^{2+}Z^-$ sites (37.7 kcal/mol). By contrast, Yakovlev et al.¹³⁵ concluded from quantum chemical calculations on a similar active site model that $Z^-[\text{HOFeOFeOH}]^{2+}Z^-$ species are active for the decomposition of N_2O . However, this conclusion is based entirely on thermodynamic aspects; no transition states were calculated in the work of Yakovlev et al.¹³⁵ In addition, the dissociation of N_2O on $Z^-[\text{HOFeOFeOH}]^{2+}Z^-$ sites to form $Z^-[\text{HOOFeOFeOH}]^{2+}Z^-$ species was calculated to be exothermic by -11.9 kcal/mol by Yakovlev et al.¹³⁵ compared to $+16.7$ kcal/mol in the present study. This difference can be attributed to differences in the density functionals and the basis sets used in these two studies and to the failure to account for spin surface crossing in the work of Yakovlev et al.¹³⁵ In the latter study all geometry optimizations were carried out in the local spin density approximation (LSDA) using Slater exchange¹⁶⁹ and Vosko-Wilk-Nusair correlation functionals.⁷¹ At the LSDA geometry the energy was computed at the GGA level using the exchange-correlation functional of Perdew and Wang.¹⁷⁰ As a consequence, the ground state of $Z^-[\text{HOFeOFeOH}]^{2+}Z^-$ lies on the nonet PES while in the present work it lies on the 11-et PES. Furthermore, in the study of Yakovlev et al.¹³⁵ spin transitions along the reaction path were not considered so that all calculations with an even number of electrons were carried out on the nonet PES.

6.3.3 N₂O decomposition on Z⁻[FeOFe]²⁺Z⁻ sites

Figure 6.5 illustrates the catalytic cycle on Z⁻[FeOFe]²⁺Z⁻ sites. Water can desorb from Z⁻[OFeOHFeOH]²⁺Z⁻ { $M_S = 9$ } and Z⁻[OFeOFe]²⁺Z⁻ is formed. This process is endothermic. The overall barrier is determined by the energy difference between Z⁻[OFeOFe]²⁺Z⁻ and Z⁻[OFeOHFeOH]²⁺Z⁻ { $M_S = 9$ } ($E^\ddagger = 21.5$ kcal/mol). Water can also desorb from Z⁻[FeOHFeOH]²⁺Z⁻. This process is endothermic with an enthalpy of reaction of $\Delta H_R = 21.6$ kcal/mol. The overall barrier is determined by the energy difference between Z⁻[FeOFe]²⁺Z⁻ and Z⁻[FeOHFeOH]²⁺Z⁻ ($E^\ddagger = 22.8$ kcal/mol). Both processes are expected to occur at elevated temperatures when the entropy gain in desorbing H₂O outweighs the enthalpy term.

The fully dehydroxylated site Z⁻[FeOFe]²⁺Z⁻ is active for N₂O decomposition, and hence in what follows we will only discuss the reaction path from Z⁻[FeOFe]²⁺Z⁻ to Z⁻[OFeOFeO]²⁺Z⁻ via Z⁻[FeOFeO]²⁺Z⁻. The path via Z⁻[OFeOFe]²⁺Z⁻ is very similar. N₂O adsorbs on Z⁻[FeOFe]²⁺Z⁻ through the O-end with an enthalpy of adsorption of $\Delta H_{\text{ads}} = -2.7$ kcal/mol. The activation barrier for the reaction of Z⁻[FeOFe]²⁺(ON₂)Z⁻ to form Z⁻[FeOFeO]²⁺Z⁻ and N₂ is $E^\ddagger = 25.6$ kcal/mol. With respect to the gas phase the latter reaction has an activation energy of 21.0 kcal/mol. This is slightly lower than the activation barrier calculated by Heyden et al.¹¹⁵ for the N₂O decomposition on Z⁻[FeO]⁺ sites to form Z⁻[OFeO]⁺ species ($E^\ddagger = 24.3$ kcal/mol on PES with $M_S = 6$). The enthalpy of reaction for Z⁻[FeOFe]²⁺(ON₂)Z⁻ → Z⁻[FeOFeO]²⁺Z⁻ is $\Delta H_R = -12.6$ kcal/mol. The structure Z⁻[FeOFeO]²⁺Z⁻ is an active site for N₂O decomposition. N₂O adsorbs through the O-end on the unoccupied Fe atom with an enthalpy of adsorption of $\Delta H_{\text{ads}} = -3.6$ kcal/mol. The activation energy for the reaction Z⁻[FeOFeO]²⁺(ON₂)Z⁻ → Z⁻[OFeOFeO]²⁺Z⁻ + N₂ is $E^\ddagger = 30.1$ kcal/mol. With respect to the gas phase the latter reaction has an activation energy of 24.8 kcal/mol. The activation energy for depositing two oxygen atoms on the same iron atom was calculated to be $E^\ddagger = 42.4$ kcal/mol with respect to the gas phase, i.e. with respect to Z⁻[FeOFeO]²⁺Z⁻. Therefore, the dissociation of two N₂O molecules on the same iron atom is very unlikely to occur. This result is in line with the two recent DFT studies on isolated, single iron sites.^{115,120} For N₂O dissociation on Z⁻[OFeOH]⁺ we calculated an activation energy of 43 kcal/mol with respect to the gas phase making this step unlikely to occur except at elevated temperatures.¹²⁰ In contrast, the N₂O dissociation barrier on Z⁻[OFeO]⁺ and Z⁻[FeO₂]⁺ sites was previously calculated to be only 12.0 kcal/mol and 17.3 kcal/mol, respectively.¹¹⁵ The reason that the N₂O dissociation barrier on Z⁻[OFeOH]⁺ is significantly higher than on Z⁻[OFeO]⁺ or Z⁻[FeO₂]⁺ is that a superoxide species (O₂⁻) cannot be formed on Z⁻[OFeOH]⁺ before the third

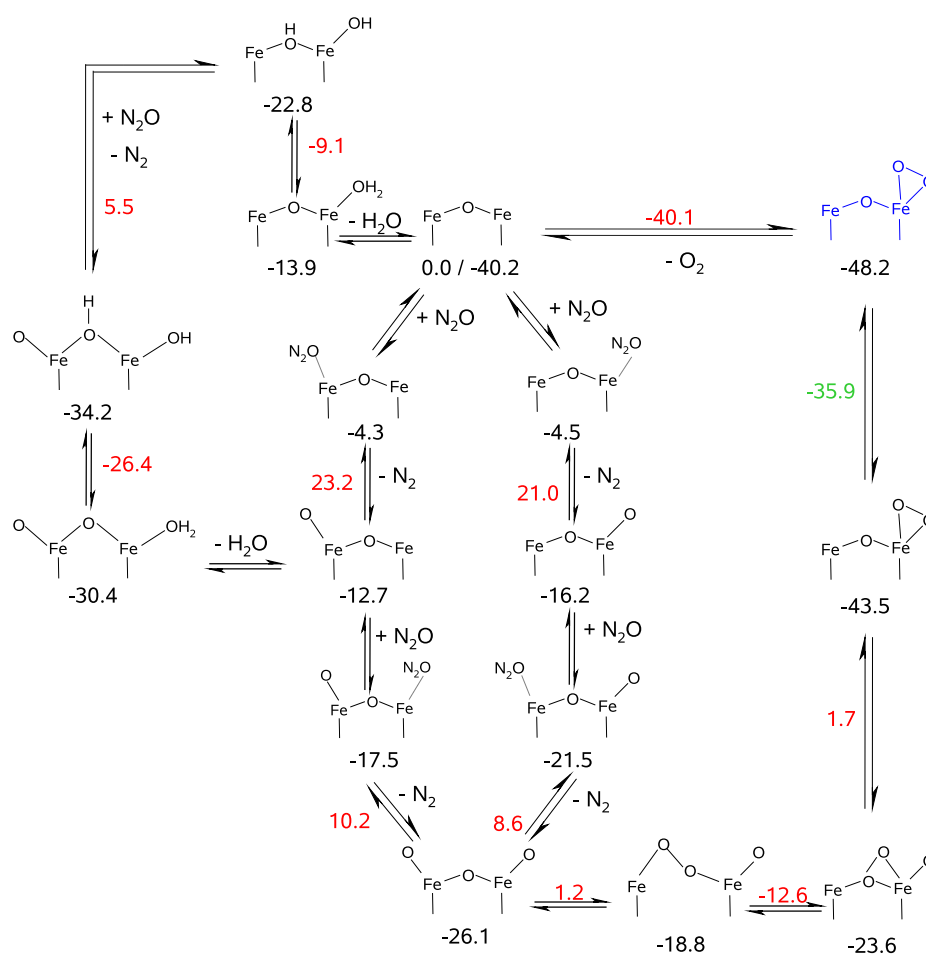


Figure 6.5: Catalytic cycle of the N_2O dissociation on $\text{Z}^-[\text{FeOFe}]^{2+}\text{Z}^-$ sites. All energies are zero-point corrected, in kcal/mol and with reference to $\text{Z}^-[\text{FeOFe}]^{2+}\text{Z}^-$ with the appropriate amounts of N_2O , N_2 , O_2 , and H_2O . Energies of potential energy minima are in black. Energies of transition states are in red. Energies of minima on the seam of two PESs are in green. Black structures are on the ferromagnetically coupled PES with $M_S = 9$. Structures in blue are on the PES with $M_S = 11$. The left Fe atom in each structure represents the T9 site, the right Fe atom represents the T12 site.

oxygen atom is deposited on the iron atom as is possible on $\text{Z}^-[\text{OFeO}]^+\text{Z}^-$ or $\text{Z}^-[\text{FeO}_2]^+\text{Z}^-$ sites. Likewise, on $\text{Z}^-[\text{FeOFeO}]^{2+}\text{Z}^-$ a superoxide species cannot be formed before the third oxygen atom is deposited on the iron. This also explains why larger iron-oxo clusters are observed to be significantly less active for the dissociation of N_2O .^{110,124} Here, an oxygen atom has to be deposited

on an iron atom similar to an iron atom in $Z^-[\text{OFeOFeO}]^{2+}Z^-$.

The enthalpy of the reaction, $Z^-[\text{FeOFeO}]^{2+}(\text{ON}_2)Z^- \rightarrow Z^-[\text{OFeOFeO}]^{2+}Z^- + \text{N}_2$, is $\Delta H_{\text{R}} = -5.4$ kcal/mol. For molecular oxygen to desorb from $Z^-[\text{OFeOFeO}]^{2+}Z^-$ an oxygen atom has to migrate from one iron atom to the other. This migration proceeds via a peroxo structure $Z^-[\text{FeOOFeO}]^{2+}Z^-$. The activation energy for this process was calculated to be $E^\ddagger = 27.3$ kcal/mol. The reaction is endothermic with an enthalpy of reaction of $\Delta H_{\text{R}} = 8.3$ kcal/mol. A superoxide $Z^-[\text{FeOFeO}_2]^{2+}Z^-$ is formed from the peroxo structure $Z^-[\text{FeOOFeO}]^{2+}Z^-$ via a stable intermediate $Z^-[\text{FeO}_2\text{FeO}]^{2+}Z^-$. For the reaction, $Z^-[\text{FeOOFeO}]^{2+}Z^- \rightarrow Z^-[\text{FeO}_2\text{FeO}]^{2+}Z^-$, we calculated an activation energy of $E^\ddagger = 6.2$ kcal/mol. This process is exothermic with $\Delta H_{\text{R}} = -5.3$ kcal/mol. An activation energy of $E^\ddagger = 25.3$ kcal/mol was calculated for the reaction $Z^-[\text{FeO}_2\text{FeO}]^{2+}Z^-$ to form the superoxide $Z^-[\text{FeOFeO}_2]^{2+}Z^-$. This reaction is exothermic with an enthalpy of reaction of $\Delta H_{\text{R}} = -19.4$ kcal/mol. The latter structure is more stable on the 11-et PES than on the nonet PES. A small spin change barrier of $E^\ddagger = 7.6$ kcal/mol was found for the spin inversion process. The enthalpy of reaction is $\Delta H_{\text{R}} = -4.8$ kcal/mol. Due to the low activation energy, $Z^-[\text{FeOFeO}_2]^{2+}Z^- \{M_S = 9\}$ and $Z^-[\text{FeOFeO}_2]^{2+}Z^- \{M_S = 11\}$ are in equilibrium. Molecular oxygen can desorb from $Z^-[\text{FeOFeO}_2]^{2+}Z^- \{M_S = 11\}$. The O_2 desorption barrier is $E^\ddagger = 8.1$ kcal/mol and the enthalpy of desorption $\Delta H_{\text{des}} = 7.1$ kcal/mol. As in all catalytic cycles reported in this study O_2 desorption is fast and, hence, oxygen inhibition is not projected to occur.

This conclusion differs from that of Kiwi-Minsker et al.,¹⁷¹ who have reported that the steady-state rate of N_2O decomposition on very low Fe-content Fe-ZSM-5 is zero-order at temperatures below 600 K, and have drawn from this observation that O_2 desorption is rate-limiting. We have shown previously that this experimental observation can be explained theoretically for isolated iron sites in Fe-ZSM-5. In this case, the second N_2O dissociation step is rate-limiting at low temperatures¹¹⁶ and the presence of small amounts of NO results in N_2O reaction orders of 0.1.^{46,120} However, for dinuclear oxygen bridged Fe sites, such as would be found in highly exchanged Fe-ZSM-5 ($\text{Fe}/\text{Al} \approx 1.0$), the rate of the second N_2O dissociation step is rapid relative to the first, so that zero-order kinetics in N_2O should not be observed.

To conclude, along the catalytic cycle on $Z^-[\text{FeOFe}]^{2+}Z^-$ the rate-limiting step is the first N_2O dissociation step, explaining the observed first order kinetic in N_2O partial pressure. The barrier heights with respect to the gas phase for the two successive N_2O dissociation steps are 21.0 kcal/mol and 24.8 kcal/mol, respectively. For isolated, single iron sites Heyden et al.¹¹⁵ calculated activation energies of 24.0 kcal/mol and 17.3 kcal/mol, respect-

ively. For oxygen migration to be rate-limiting on dinuclear iron sites the activation energy for this process would need to be about 50 kcal/mol. Only then would $Z^-[\text{OFeOFeO}]^{2+}Z^-$ become an abundant surface intermediate and oxygen migration would become a rate-limiting step in the overall reaction network presented in the present work. The difference between this hypothetical value and the one calculated in the present work (27.3 kcal/mol) is about 22 kcal/mol, which is much larger than the error inherent in the calculation of transition states using DFT-B3LYP. Therefore, the overall steady-state behavior of N_2O decomposition on dinuclear iron sites is qualitatively the same as on isolated, single iron sites. The N_2O decomposition activity of Fe-ZSM-5 is affected less by the nuclearity (mono- or dinuclear) of the active iron sites than by the presence of H_2O impurities in the reaction system. As in the case of isolated, single iron sites, only fully dehydroxylated dinuclear iron sites show a significant activity for N_2O dissociation.

6.3.4 Effect of antiferromagnetic coupling

Figure 6.6 illustrates the energy splitting between the ferromagnetic and antiferromagnetic PES for the N_2O decomposition on $Z^-[\text{FeOFe}]^{2+}Z^-$ sites. The energy difference between the two surfaces is calculated to be 4.1 kcal/mol for $Z^-[\text{FeOFe}]^{2+}Z^-$ and 3.9 kcal/mol for the N_2O adsorbed state. After passing the first transition state where the energy difference is 5.5 kcal/mol, the difference decreases to 2.7 kcal/mol for $Z^-[\text{FeOFeO}]^{2+}Z^-$ and 2.4 kcal/mol for the N_2O adsorbed state, consistent with a larger Fe-Fe distance. The influence of antiferromagnetic coupling on the activation energies is small. For the first transition state along the catalytic cycle the activation energy is 23.9 kcal/mol on the antiferromagnetic PES and 25.5 kcal/mol on the ferromagnetic PES. For the second transition state the activation energies are 30.0 and 30.1 kcal/mol, respectively. These differences are smaller than the error inherent in the determination of transition states using DFT/B3LYP (in particular for the broken symmetry calculations). For the reaction $Z^-[\text{OFeOFeO}]^{2+}Z^- \rightarrow Z^-[\text{FeOOFeO}]^{2+}Z^-$ the antiferromagnetic state was calculated to be higher in energy by 2 kcal/mol. As a consequence the activation energy on the antiferromagnetic PES ($E^\ddagger = 31.1$ kcal/mol) is 3.8 kcal/mol higher than on the ferromagnetic PES ($E^\ddagger = 27.3$ kcal/mol). For the peroxo structure $Z^-[\text{FeOOFeO}]^{2+}Z^-$ and the intermediate $Z^-[\text{FeO}_2\text{FeO}]^{2+}Z^-$ antiferromagnetic coupling was found to be very weak, because of the larger Fe-Fe distance. For the reaction $Z^-[\text{FeO}_2\text{FeO}]^{2+}Z^- \rightarrow Z^-[\text{FeOFeO}_2]^{2+}Z^-$ we calculated a energy difference between both PES of 3.2 kcal/mol for the transition state and 5.5 kcal/mol for the superoxide. For molecular oxygen

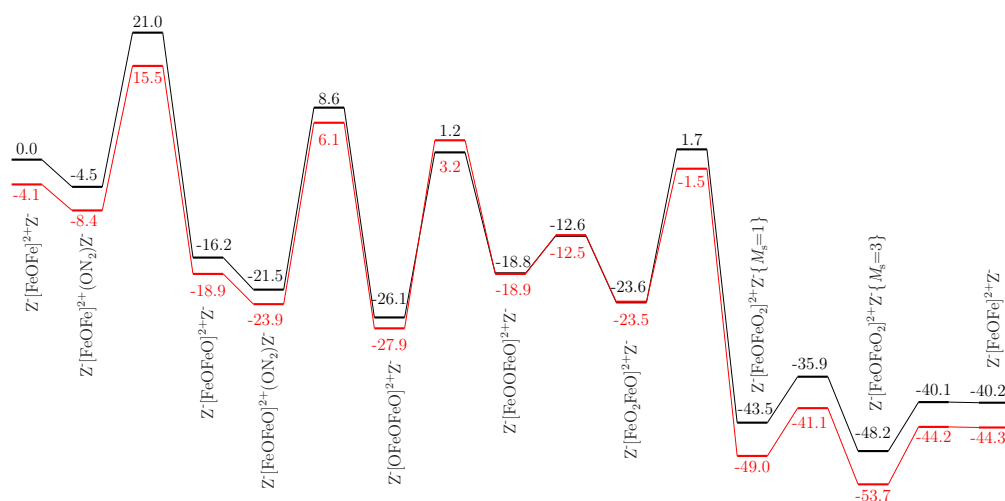


Figure 6.6: Reaction energy diagram of the nitrous oxide decomposition on dehydroxylated dinuclear iron sites for ferromagnetically coupled high spin states (black curve) and antiferromagnetically coupled broken-symmetry states (red curve). All energies are zero-point corrected, in kcal/mol and with reference to $Z^-[\text{FeOFe}]^{2+}Z^-$ with the appropriate amounts of N_2O , N_2 , and O_2 . Black numbers correspond to the ferromagnetically coupled states; the energies are the same as in figure 6.5. Red numbers correspond to the antiferromagnetically coupled states.

to desorb in its ground state (a triplet $^3\Sigma_g^-$) a surface crossing from the antiferromagnetic singlet to the antiferromagnetic triplet surface has to occur. The barrier for this process was calculated to be 7.9 kcal/mol. The energy difference between both PES at the crossing point is 5.2 kcal/mol. As on the ferromagnetic PES $Z^-[\text{FeOFeO}_2]^{2+}Z^-$ is more stable in the higher spin state. The energy difference between the ferromagnetic and the antiferromagnetic PES is 5.5 kcal/mol. The O_2 desorption barrier was calculated to be 9.5 kcal/mol. The coupling constants along the catalytic cycle calculated using equation 6.2 are in the range from 3 to -190 cm^{-1} (see table 6.4), which are common values for oxo-bridged diiron complexes in biochemistry.¹⁷²

It can be concluded that antiferromagnetic coupling does not affect the main mechanistic aspects of the catalytic cycle such as the rate-limiting step and the approximate height of the reaction barriers. However, the overall activity of the catalytic cycle is mainly controlled by the fractions of the active sites $Z^-[\text{FeOFe}]^{2+}Z^-$, $Z^-[\text{FeOFeO}]^{2+}Z^-$, and $Z^-[\text{OFeOFe}]^{2+}Z^-$. The

formation of these active sites requires the desorption of water from the inactive species $Z^-[\text{HOFeOFeOH}]^{2+}Z^-$, which predominate at low temperatures. The energy difference between the ferromagnetic and the antiferromagnetic PES for $Z^-[\text{HOFeOFeOH}]^{2+}Z^-$ was calculated to be 6.8 kcal/mol. This relatively large value shows that the strength of antiferromagnetic coupling does not depend exclusively on the Fe-Fe distance but also on the angle formed by the two iron ions and the bridging group.^{172,173} The magnetic coupling is strongest for Fe-O-Fe bond angles between 120° and 180°, and decreases considerably for lower bond angles (e.g. 90°).¹⁷³ For $Z^-[\text{HOFeOFeOH}]^{2+}Z^-$ the bond angle was calculated to be 158.2°, a value much larger than the bond angles for the dehydroxylated structures (see table 6.4). As a result the energy difference between the inactive $Z^-[\text{HOFeOFeOH}]^{2+}Z^-$ site and the active dehydroxylated sites is slightly larger on the antiferromagnetic than on the ferromagnetic PES. Even though this observation suggests that antiferromagnetic coupling slightly reduces the overall activity of diiron sites the effect of antiferromagnetic coupling on the reaction mechanism is small and will be quantified in chapter 7, reporting simulations of the kinetics of N₂O decomposition.

6.4 Conclusion

Three catalytic cycles for the N₂O decomposition on dinuclear oxygen bridged extraframework iron sites in Fe-ZSM-5 have been investigated using density functional theory. The hydroxylated iron site, $Z^-[\text{HOFeOFeOH}]^{2+}Z^-$, is projected to dominate the catalytic surface at low temperatures. This site shows a low activity for N₂O decomposition. At higher temperatures water can desorb, and N₂O decomposition on $Z^-[\text{FeOFe}]^{2+}Z^-$ becomes the slow process in the overall kinetic. On this site N₂O decomposition deposits an oxygen atom on each iron atom, followed by subsequent oxygen atom recombination and desorption of O₂. This sequence is favoured over decomposition of two N₂O molecules occurring on the same iron atom. In all of the catalytic cycles examined in this work, oxygen desorption was found to be fast and N₂O decomposition was found to be first order with respect to N₂O partial pressure. Therefore, there are many qualitative similarities between the mechanisms of N₂O decomposition on single iron sites reported by Heyden et al.¹¹⁵ and that on dinuclear oxygen bridged iron sites presented in the present work. Both type of sites are poisoned by small amounts of water. As a result, the nuclearity (mono- or dinuclear iron site) of the catalytically active site for N₂O decomposition appears to be less important than catalyst poisoning by traces of water in the gas streams. Antiferromagnetic coupling was shown to

have no effect on the reaction mechanism.

7

Microkinetic modeling of nitrous oxide decomposition on dinuclear oxygen bridged iron sites in Fe-ZSM-5

The decomposition of N_2O on dinuclear oxygen-bridged iron sites in Fe-ZSM-5 was simulated under steady-state conditions considering the reaction mechanism and the rate parameters proposed in chapter 6 on the basis of DFT calculations. The presence of low concentrations of water vapor in the feed stream (ppb to ppm levels) affects the calculated values for the apparent activation energy and the preexponential factor and, hence, can explain the wide spread in the experimental values for these quantities as well as the appearance of an apparent compensation effect. The activity of the dinuclear oxygen-bridged site was compared to the activity of the mononuclear iron sites proposed earlier by Heyden et al. [J. Phys. Chem. B 2005, 109, 1857]. The latter one was found to be slightly more active. The microkinetic models for both mononuclear and dinuclear iron sites were used to reproduce temperature programmed reaction experiments reported for Fe-ZSM-5 samples with low and high iron content. This analysis leads to the conclusion that at very low Fe/Al ratios mononuclear iron sites prevail, whereas at higher Fe/Al ratios both mono- and dinuclear iron sites are likely to be present simultaneously.

7.1 Introduction

Nitrous oxide, N_2O , is both a greenhouse gas and a contributor to ozone destruction in the stratosphere.^{174,175} A reduction of the emissions of N_2O from adipic acid and nitric acid plants can be achieved by decomposition and zeolites exchanged with $3d$ ions have been shown to be particularly active catalysts for this process.^{106,176} Notable among these materials is Fe-ZSM-5, which is able to maintain its activity under industrial tail gas conditions of nitric acid plants.^{108,177} Although Fe-ZSM-5 has been extensively studied by many groups,^{109,110,113,114,118,124,131,168,178–185} the structure of the active site remains a subject of discussion in the literature.¹⁸⁶ A question of particular interest is the nuclearity of the catalytically active site.^{119,127–131} According to a critical evaluation of this subject by Pirngruber et al.¹⁸⁷ many results concerning the nuclearity of the active site published in the past need to be reconsidered due to misinterpretation of experimental data. However, for most Fe-ZSM-5 samples, with the exception of those having very low iron content, it is reasonable to assume that a distribution of active iron species exists, that depends on the iron content and the catalyst preparation and activation procedures and that several types of sites differing in iron nuclearity contribute to the observed activity.^{111,124,188–190} Due to this variety of Fe-species the unequivocal assignment of catalytic properties to a single type of iron is difficult by experimental methods alone. Theoretical methods can in principle be used to separate the contribution of an individual species from the total activity of all active species and, therefore, to investigate the importance of a particular type of site. The capability of mononuclear extraframework iron sites to catalyze N_2O decomposition in the absence and the presence of NO has been demonstrated recently in two comprehensive DFT studies reported by Heyden et al.^{115,120} In chapter 6 we have shown that dinuclear oxygen-bridged extraframework iron sites are also active for N_2O decomposition and exhibit activation energies for elementary processes involved in N_2O decomposition that are very similar to those determined for mononuclear iron sites. Furthermore, the results presented in chapter 6 suggest that larger iron oxide clusters exhibit a very low activity in N_2O decomposition as was found experimentally.^{119,180}

The exploration of the reaction mechanism on a specific active site model requires the investigation of all possibly relevant elementary processes on this site. Most often, the resulting reaction mechanism is too complex to assess which rate processes are most relevant simply by inspection of the magnitude of the rate coefficients for these processes. This difficulty can be overcome by microkinetic modeling, on the basis of which it is possible

to determine processes that are most relevant in a complex reaction network and to investigate the influence of rate parameters in a systematic manner.¹⁹¹ Rate expressions for catalyzed reactions obtained in this way are more likely to offer a good description of the kinetics over a wide range of reaction conditions than those developed empirically because they are based on an understanding of the reaction mechanism.

The application of this approach to N₂O decomposition on mononuclear iron sites in Fe-ZSM-5¹¹⁶ has identified two hidden parameters not described in experimental studies, the fraction of iron sites that are catalytically active and the effect of small partial pressures of H₂O on catalyst deactivation. It was demonstrated that these parameters are responsible for the wide spread in the values of the apparent preexponential factors and activation energies reported in the literature.

In the present chapter we report a microkinetic model for the mechanism and kinetics of N₂O decomposition occurring on dinuclear, oxygen-bridged extraframework iron sites in Fe-ZSM-5.¹⁹² It is the aim of this chapter to show the influences of the water partial pressure on the catalytic activity of such sites and to demonstrate the similarities in the catalytic properties of these sites to mononuclear iron sites. We also show that microkinetic analysis carried out with mono- and dinuclear iron sites can be used to ascertain which type of site is likely to be predominant in a given catalyst. This analysis leads to the conclusion, that at very low Fe/Al ratios mononuclear iron sites prevail, whereas at higher Fe/Al ratios both mono- and dinuclear iron sites are likely to be present simultaneously.

7.2 Theoretical methods

In chapter 6 we presented a detailed reaction mechanism for N₂O decomposition on dinuclear iron sites in Fe-ZSM-5, consisting of 39 elementary reactions involving 33 surface species. Activation barriers for each elementary process were determined using density functional theory (DFT). In the present chapter, equilibrium constants and reaction rate constants were computed using standard methods of statistical mechanics and absolute rate theory.¹⁹³ We used the harmonic approximation, and included the contributions of the translational, rotational, vibrational, and electronic partition function of all gaseous species participating in the reaction and the vibrational and electronic contribution of the zeolite cluster. Since the zeolite cluster is part of a solid, translational and rotational partition functions for the zeolite were assumed to be equal in the reactant and transition state. For elementary pro-

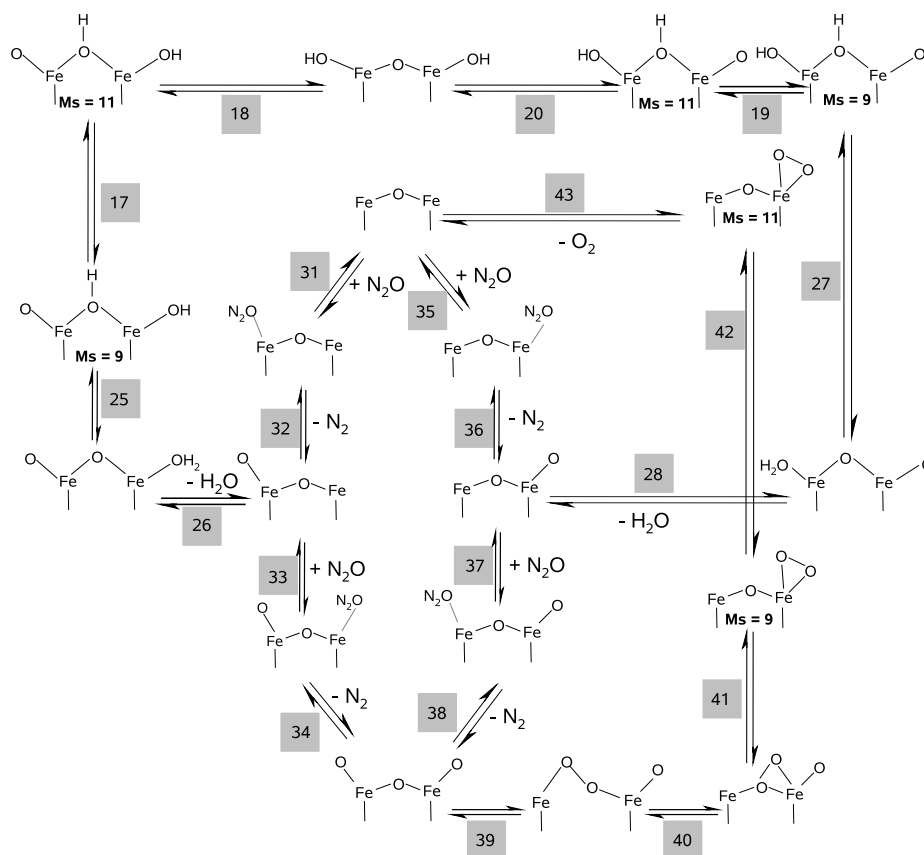


Figure 7.1: Reaction network of the N_2O dissociation on dinuclear oxygen-bridged extraframework iron sites in Fe-ZSM-5. For elementary steps which involve spin-surface crossing the spin multiplicities of the reactant and product state are specified. The reaction numbers refer to table A.1.

cesses in which the spin state changes during reaction, absolute rate theory was used under the assumption that the partition function of the hypothetical transition state (minimum on the seam of two potential energy surfaces (PESs)) and the partition function of the minimum state with lower spin multiplicity are identical except for the electronic energy. This procedure completely neglects a low spin-surface crossing probability. To estimate if very low spin-surface crossing probabilities could have a significant effect on the reaction rate constants, thermally averaged spin transition probabilities were calculated with the Landau-Zener formula⁴⁵ using a spin-orbit coupling energy, H_{12} , of 395 and 825 J/mol, as calculated by Danovich and Shaik¹⁹⁴ for the oxidative activation of H_2 by FeO^+ . Additional details concerning

the calculation of rate parameters and the estimation of errors can be found elsewhere.^{46,115} It is important to note, that the necessary correction for the reaction rates to account for a spin-inversion probability smaller than one is comparable to the error inherent in the DFT calculations of activation energies. In addition, the rates of spin-surface crossing were never rate-limiting in this work and, hence, spin-surface crossing should not influence the overall kinetics of the reaction network studied.

In the preceding chapter we demonstrated that antiferromagnetic coupling of the two iron atoms has no significant effect on the reaction mechanism. Moreover it has been experimentally shown that the strength of antiferromagnetic coupling decreases with increasing temperature.¹⁸⁷ Therefore, if not stated otherwise all simulated results have been obtained using the reaction rates determined for ferromagnetically coupled iron atoms. The results of all quantum chemical and statistical mechanics calculations are summarized in tables A.1 to A.3 of the supporting information accompanying this chapter. The order in which the reactions are listed in table A.1 is related to the description of the catalytic cycles presented in chapter 6.

For a fixed gas phase composition and temperature the steady-state material balance for surface species can be written as a set of linear equations that can be solved easily using standard methods.^{195–197} Simulations carried out with the entire reaction network reported in chapter 6, revealed that most of the processes do not contribute significantly to the overall kinetics and that the reaction mechanism shown in figure 7.1 is sufficient.

7.3 Results and discussion

7.3.1 Effects of water vapor on the catalyst surface and the apparent rate constant

In the previous chapter we showed, that desorption of water from dinuclear, oxygen-bridged iron sites is strongly endothermic. As a consequence, water vapor decreases the rate constant and has a strong influence on the distribution of dinuclear iron sites among the species $Z^-[\text{HOFeOFeOH}]^{2+}Z^-$, $Z^-[\text{OFeOFe}]^{2+}Z^-$, $Z^-[\text{FeOFeO}]^{2+}Z^-$, and $Z^-[\text{FeOFe}]^{2+}Z^-$. Figure 7.2 shows the effects of water on the distribution of the most abundant surface species at 600 and 700 K. At the higher temperature traces of water have very little effect on the distribution of the catalytically active sites $Z^-[\text{OFeOFe}]^{2+}Z^-$, $Z^-[\text{FeOFeO}]^{2+}Z^-$, and $Z^-[\text{FeOFe}]^{2+}Z^-$ unless the H_2O partial pressure becomes larger than 10^{-7} bar. Under these conditions the inactive site is dom-

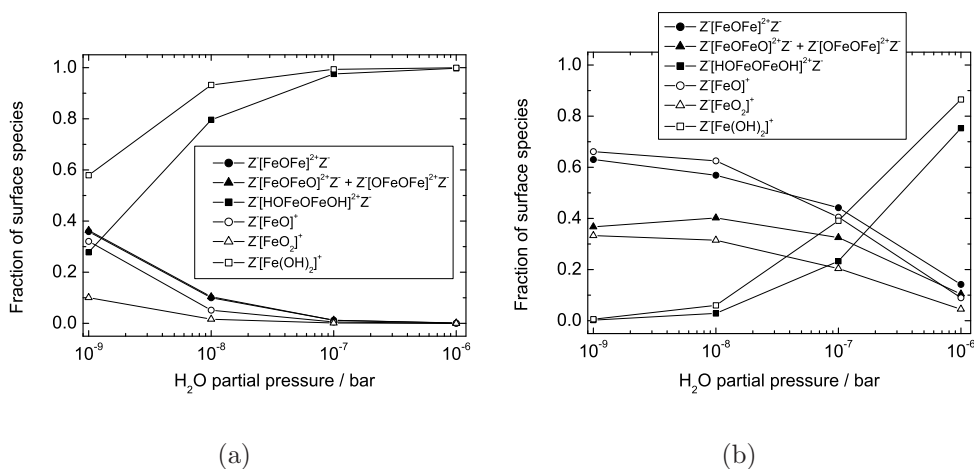


Figure 7.2: Surface composition of dinuclear and mononuclear iron sites as a function of H₂O partial pressure at temperatures of (a) 600 and (b) 700 K.

inant, that is, $Z^-[\text{HOFeOFeOH}]^{2+}Z^-$. At 600 K significant concentrations of active sites are present only at water partial pressures below 10⁻⁸ bar. A comparison of the distribution of species for mononuclear and dinuclear iron sites reveals similar patterns. The fraction of the inactive species is always lower for the dinuclear site because desorption of water was calculated to be slightly less endothermic than for mononuclear sites.

In analogy to mononuclear iron sites¹¹⁶ an Arrhenius plot of the apparent first-order rate coefficient for N₂O decomposition will not be linear and depends on the H₂O partial pressure in the feed up to a temperature of 725 K (figure 7.3(a)). In heterogeneous catalysis a decrease of the slope of the Arrhenius plot is usually assigned to the transition from the kinetically controlled to the diffusion controlled regime.¹⁹⁸ However, in the present case, it is the change in the surface composition and, hence, the increase in the N₂O decomposition activity which causes the nonlinearity of the Arrhenius plot. Figure 7.3(b) shows the change in the most abundant surface species associated with the upper curve of figure 7.3(a) (10⁻⁹ bar water pressure). In the temperature regime where the slope of the Arrhenius plot becomes smaller, the fraction of inactive sites $Z^-[\text{HOFeOFeOH}]^{2+}Z^-$ decreases rapidly in favour for the active sites. The activation energy for N₂O dissociation on these sites is considerably smaller.

Experimental measurements of the apparent activation energy and pre-exponential factor for N₂O decomposition are most often made over the tem-

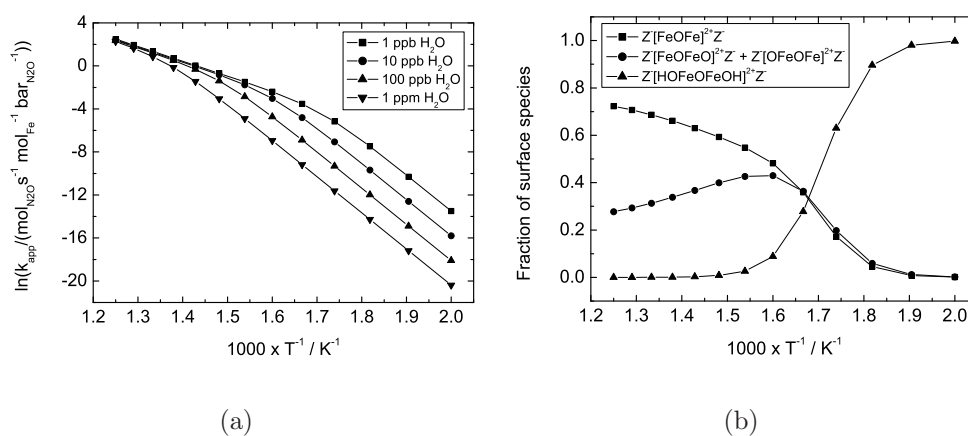


Figure 7.3: (a) Arrhenius plots of the first-order N_2O decomposition for different H_2O partial pressures. (b) Variation of catalyst surface with temperature at H_2O partial pressure of 10^{-9} bar.

perature range of 500-700 K, where small amounts of water have a strong effect on the apparent rate parameters. Heyden et al.¹¹⁶ have shown that the reported values of the apparent preexponential factor correlate with the apparent activation energy over a wide range of values. Virtually all of this variation is attributable to the effects of small concentrations of water vapor in the feed.

The solid lines shown in figure 7.4 represent values of the apparent preexponential factor and the apparent activation energies predicted on the basis of the reaction mechanism presented for mononuclear iron sites¹¹⁵ and the mechanism presented for dinuclear oxygen-bridged iron sites.¹⁹² The latter calculations were performed for both, antiferromagnetically and ferromagnetically coupled iron atoms. All calculations were conducted for the temperature interval of 600 to 700 K. The lowest preexponential factor and activation energy were calculated for a zero partial pressure of water, while the highest values were obtained for a water pressure of 10^{-7} bar. The figure shows that the reaction rate constants calculated for the dinuclear iron site follow the same compensation relation as the ones for the mononuclear iron site. It is noted that for the same temperature and water partial pressure the specific activity of iron is fourfold higher for the mononuclear sites relative to the dinuclear sites, assuming ferromagnetic coupling between the iron atoms in the latter structure. The apparent reaction rate constants calculated under the assumption of antiferromagnetic coupling of iron atoms in the dinuclear

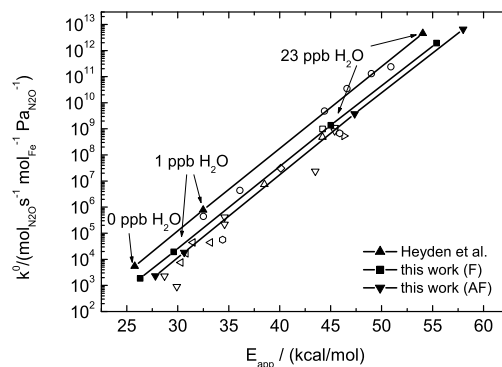


Figure 7.4: Plot of logarithm of experimental and computed apparent pre-exponential factor versus apparent activation energy. Open symbols represent experimental data, closed symbols represent simulations from Heyden et al.¹¹⁶ and the present work for ferromagnetically (F) and antiferromagnetically (AF) coupled iron atoms. \square ref. 109, \circ ref. 179, \triangle ref. 180, ∇ ref. 124, \triangleleft ref. 181, \triangleright ref. 114, \hexagon ref. 118.

structure are smaller than the ones for the ferromagnetically coupled case by a factor of approximately two.

It should be noted, that the preexponential factors for the experimental data presented in figure 7.4 were determined assuming that all iron atoms participate in N_2O decomposition. If only a fraction of the total iron is in the form of mono- or dinuclear Fe sites, e.g. part of the Fe is in the form of large inactive iron oxide particles, the experimental preexponential factor will be underestimated. This may be one reason for the observation of a large spread in preexponential factors at constant activation energies seen in figure 7.4.

7.3.2 Simulation of temperature-programmed reaction experiments

The activity of Fe-ZSM-5 for N_2O decomposition has often been studied by temperature-programmed reaction (TPR). It should be noted that such experiments will only represent steady-state kinetics if the catalyst reaches a steady state at each temperature during the temperature increase. If this condition is not satisfied discrepancies between steady-state experiments and TPR experiments may arise.¹⁷¹ However, at temperatures above 700 K it can

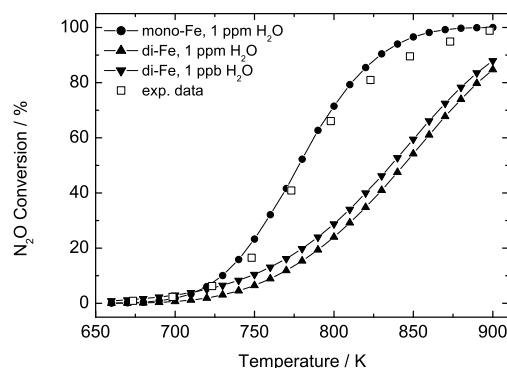


Figure 7.5: Experimental¹¹⁰ and simulated temperature programmed reaction profile for a Fe-ZSM-5 sample with low iron content (0.08 wt%, Fe/Al = 0.017). The experimental results were obtained using 3.3 vol% of N₂O in He (total flow 150 cm³/min). The simulated TPR profiles were determined for an H₂O partial pressure of 1 ppm for mononuclear iron sites and 1 ppm and 1 ppb for dinuclear iron sites. It is assumed that all iron sites are in the form of mononuclear or dinuclear iron sites, respectively.

be assumed that steady-state is reached very fast. For this reason the choice of the experimental data against which to compare microkinetic simulations must be done with care, since these simulations are based on the assumption of steady-state for all species at each reaction temperature. Berlier et al.¹¹⁰ have carried out a temperature-programmed reaction experiment for N₂O decomposition at temperatures above 700 K using a sample of Fe-ZSM-5 with very low iron content (0.08wt%, Fe/Al = 0.017) in order to minimize the presence of dimeric and larger oxide clusters so as to obtain a single-site model catalyst in which isolated Fe cations predominate. It is, therefore, reasonable to assume that for this catalyst all of the iron is present as mononuclear species, all of which are potentially active. Because the temperatures used in the experiments reported by Berlier et al. were in excess of 700 K, the influence of water on the observed reaction rates is expected to be small. Figure 7.5 compares the experimental results of Berlier et al.¹¹⁰ with simulations carried out assuming that all of the iron atoms in the catalyst are active and the partial pressure of water vapor in the feed stream is 1 ppm. The reactor is assumed to operate in plug flow, and is represented by a series of 20 stirred tank reactors. Because the simulated curve becomes independent of the water partial pressure in the upper half of the temperature range and

is only slightly dependent on the water partial pressure in the lower half, the simulation is virtually parameter-free. It is seen that for this case the assumption that all active sites are in the form of mononuclear cations gives a very good representation of the experimental data. By contrast, figure 7.5 shows that it was not possible to reproduce the experimental results of Berlier et al.¹¹⁰ using the reaction rates calculated for the dinuclear iron site. As mentioned above the reaction rates on dinuclear iron sites are calculated to be smaller by a factor of around four at fixed temperature and H₂O partial pressure than those for mononuclear iron sites. Although it seems that the presented rates for the different active site models can be used to interpret experimental results in terms of the most abundant active species one should keep in mind that a factor of four can be caused by an error in the activation energy of 2 kcal/mol at temperatures above 700 K, which is in the error range of the B3LYP functional for the determination of activation energies.¹⁹⁹

A further confirmation of the proposed reaction mechanism on mononuclear iron sites was reported recently by Kondratenko and Pérez-Ramírez.²⁰⁰ These authors evaluated several kinetic models proposed in the literature for their ability to describe the transient responses of the reactants and products in the temporal analysis of products (TAP) reactor. The best description was obtained considering the reaction scheme proposed by Heyden et al.¹¹⁵

For over-exchanged Fe-ZSM-5 samples it is generally accepted that di- or oligonuclear Fe-species are present in the catalyst as well as small iron oxide clusters.^{111,124,188,189} However, experiments have shown that small clusters of Fe₂O₃ are not active for N₂O decomposition.^{119,180} As shown in figure 7.6(a) the reaction mechanism for the dinuclear iron site can be fitted to the experimental results reported by Pirngruber et al.¹²⁴ for an over-exchanged Fe-ZSM-5 sample prepared by chemical vapor deposition (4 wt% iron content, Fe/Al = 1.1). Good agreement is obtained for a water partial pressure of 10⁻⁷ bar assuming that 65% of the total iron is present as dinuclear iron sites (i.e. 35% of the total iron is assumed to be in the form of larger inactive iron oxide particles). It should be emphasized that due to water poisoning only a fraction of these dinuclear iron sites participates in steady-state N₂O decomposition. Figure 7.6(b) shows the fraction of hydroxylated (poisoned) dinuclear iron sites as a function of reaction temperature. At 670 K approximately 65% of the dinuclear iron sites are hydroxylated, i.e., only 35% participate in N₂O decomposition. As a result only 23% of the total iron takes part in steady state N₂O decomposition at this temperature. This fraction of the potentially active iron increases with increasing temperature. Under the same conditions the mechanism for mononuclear iron sites overpredicts the experimental results considerably. However, good agreement with the

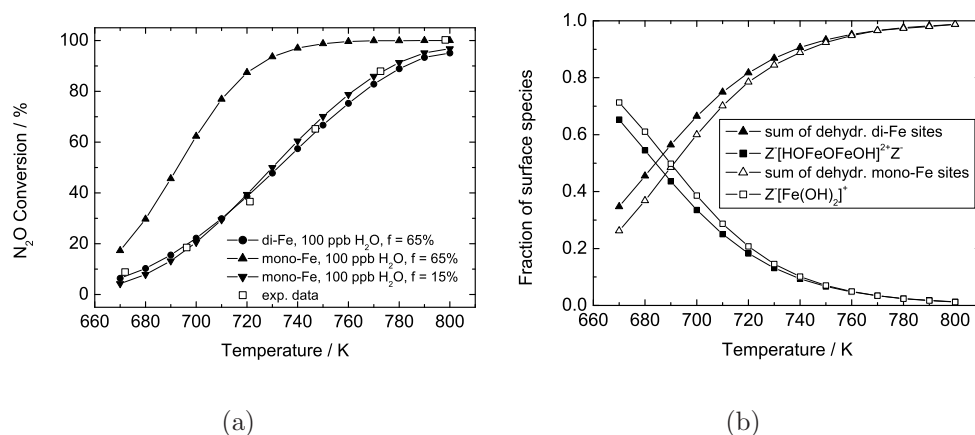


Figure 7.6: (a) Experimental¹²⁴ and simulated temperature programmed reaction profile for a Fe-ZSM-5 sample with high iron content (4.0 wt%, Fe/Al = 1.1) prepared by chemical vapor deposition. The experimental results were obtained using 0.25 vol% of N_2O in He (total flow $50\text{ cm}^3/\text{min}$). The simulated TPR profiles were determined for an H_2O partial pressure of 0.1 ppm. Reactor simulations of dinuclear Fe sites have been performed assuming that 65% of the total iron in the system is in the form of dinuclear Fe species (35% of the total iron is in the form of larger inactive iron oxide particles). Reactor simulations of mononuclear Fe sites have been performed assuming that 65% or 15%, respectively of the total iron in the system is in the form of mononuclear Fe species (35% or 85%, respectively of the total iron is in the form of larger inactive iron oxide particles). (b) Surface composition of dinuclear and mononuclear iron sites in TPR simulation. The curves for mononuclear iron sites belong to the simulation with $f = 15\%$.

experimental data can be achieved for a simulation based on mononuclear iron sites but such agreement requires the assumption that only 15% of the total iron is in the form of mononuclear iron sites (hydroxylated plus dehydroxylated sites). These results, suggest that the iron present in the sample of Fe-ZSM-5 used in those studies most likely contains both mononuclear and dinuclear iron sites.

7.4 Conclusion

Rate parameters for the decomposition of N_2O on dinuclear oxygen-bridged iron sites in Fe-ZSM-5 determined from first principles calculations were used to study the influence of water vapor on the distribution of dinuclear iron sites between catalytically active and inactive forms and on the apparent first-order rate constant. The presence of low concentrations of water vapor in the feed stream (ppb to ppm levels) affects the calculated values for the apparent activation energy and preexponential factor and, hence, can explain the wide spread in the experimental values for these quantities, as well as the appearance of an apparent compensation effect. This pattern is very similar to that reported previously for mononuclear iron species in Fe-ZSM-5.^{115,116} Simulations of temperature-programmed reaction experiments reported in the literature were carried out based on the mechanism and kinetics developed for mononuclear and dinuclear iron sites. The results obtained for mononuclear sites are in very good agreement with the experimental findings for Fe-ZSM-5 with an iron loading of 0.08 wt% ($\text{Fe}/\text{Al} = 0.017$). The simulations suggest that all of the iron in the catalyst is active. Simulations based on mono- and dinuclear sites were carried out and compared with experiments conducted with Fe-ZSM-5 containing 4 wt% iron ($\text{Fe}/\text{Al} = 1.1$). In this case, good agreement was obtained with the simulations carried out assuming that 65% of the total iron in the catalyst is in the form of dinuclear sites or that 15% of the total iron in the catalyst is in the form of mononuclear sites, and that the content of water vapor in the feed is 100 ppb. The sensitivity of the simulations with respect to the water content was small for both, the low iron loaded and high iron loaded catalyst, since the experiments all involved temperatures >700 K.

Part IV

Alkylation of benzene over H-ZSM-5: A multi-scale investigation

Theoretical investigation of benzene alkylation with ethene over H-ZSM-5

8

Benzene alkylation with ethene over zeolite H-ZSM-5 has been investigated using density functional theory. Three different reaction mechanisms – two one-step schemes and one two-step scheme – have been studied on three cluster models of increasing size representing parts of the H-ZSM-5 framework. In the one-step schemes ethene protonation and C–C bond formation occur simultaneously. The two-step scheme starts with the formation of a stable ethoxide intermediate which subsequently reacts with benzene to form the reaction product. Activation energies obtained from the DFT results have been improved by single-point MP2 calculations. The calculated intrinsic activation energies of the one-step schemes are similar to the activation energy of the alkylation step in the two-step scheme. Numerical values of the MP2 corrected activation energies are in good agreement with experimental data. The largest cluster (33 T-atoms) was found to stabilize protonated ethylbenzene as a stable intermediate. The results of this study show the importance of using relatively large clusters for investigations of hydrocarbon transformation occurring in zeolites.

8.1 Introduction

Ethylbenzene is used primarily as an intermediate in the production of styrene,²⁰¹ as well as a paint solvent and an intermediate in the pharmaceutical industry,²⁰² and is produced at the world-wide level of $\sim 22 \times 10^6$ t per year.²⁰³ Most of this production is by the alkylation of benzene by ethene catalyzed by metal halogenide-based liquid catalysts such as AlCl_3 and BF_3 that are corrosive and difficult to dispose.^{20,204} The use of zeolite catalysts offers an environmentally friendly route to ethylbenzene and the possibility of achieving superior product selectivity through pore size control.^{205–209} ZSM-5, a medium pore zeolite, is particularly well suited for the gas-phase alkylation of aromatics and has been used in the Mobil/Badger process since 1980.^{210–212} Moreover, ZSM-5 shows a higher resistance to coking compared to cage-type zeolites such as faujasite.^{205,206,213}

The mechanism by which zeolites catalyze the alkylation of arenes has been investigated experimentally and found to depend on the structure of the zeolite. Smirniotis and Ruckenstein have reported that the alkylation of bulky aromatics with relatively large alkylating agents over small or medium pore zeolites occurs via a Langmuir-Hinshelwood (LH) mechanism, while the alkylation of relatively small aromatics over large pore zeolites follows the Rideal-Eley (RE) mechanism.²¹⁴ It must be recognized, however, that in the case of zeolite catalysts it is not possible to assume that any of the reactants are truly in the gas phase because they are all subjected to electric field gradients and confinement effects once inside the zeolite pores.²⁰⁶ In fact, different experimental studies have concluded that the mechanism of benzene ethylation catalyzed by H-ZSM-5 is best described by a Langmuir-Hinshelwood mechanism, in which the initial step is the co-adsorption of the reactants at the acid site.^{214,215}

Neutron, Raman and X-ray diffraction measurements as well as Monte Carlo simulations show that the channel intersections are the preferred sites for benzene adsorption for loadings up to 4 molecules per unit cell.^{216–220} Since the pore size of H-ZSM-5 closely matches the dimensions of the reaction product, ethylbenzene, it can be assumed that the formation of this product occurs preferentially on acid sites located in the channel intersections. Mechanistic studies of benzene alkylation on different zeolites suggest that the olefin and benzene do not compete for adsorption on the acid site. The olefin is assumed to interact with the Brønsted acid site, while benzene adsorbs edge-on next to the adsorbed olefin.²²¹ The protonated olefin then reacts with the more weakly adsorbed benzene to form alkylbenzene. However, mechanistic details involved in going from the reactants to the final

products are not well understood.

There have been relatively few theoretical studies of benzene ethylation over zeolites. Vos et al. have estimated the activation energy for this process using a fully relaxed T4 cluster.²²² The same cluster model has also been used by Arstad et al.²²³ In both studies it was assumed that ethene adsorbs on the Brønsted acid site while benzene adsorbs edge-on next to the previously adsorbed ethene. While these studies find slightly different structures for the adsorbed and transition state complexes, and as a consequence slightly different activation energies, both studies conclude that ethylbenzene is formed in one, concerted step. Since the clusters used to represent the active site are small, they do not account for electrostatic interactions of the walls with the ionic transition-state structure. A more realistic representation of the zeolite has been used by Namuangruk et al.²²⁴ These authors employed the ONIOM3 method²²⁵ on a 84T cluster representation of two supercages of faujasite in order to calculate the structures of the adsorbed state and the transition state. Two reaction mechanisms were considered, a two-step reaction involving the formation of a covalently bonded ethoxide intermediate via a carbenium ion-like transition state in the first step and a one-step mechanism in which protonated ethene reacts directly with benzene. The activation energy for the one-step mechanism was 5 kcal/mol lower than that for the reaction step in the two-step mechanism. Nevertheless, it was suggested that the two-step mechanism could contribute significantly to the overall rate of benzene alkylation because ethoxide formation is favored kinetically. The calculated adsorption energies were found to agree well with experimental data. It should be noted, though, that this agreement is to some extent a consequence of the choice of the ONIOM approach. An ONIOM2(B3LYP/6-31G(d,p):HF/3-21G) representation, for example, over-predicts the adsorption energy of ethene²²⁶ and considerably under-predicts the adsorption energy of benzene.²²⁷ On the other hand, an ONIOM2(B3LYP/6-311++G(d,p):UFF) representation²²⁸ as well as an ONIOM3(MP2/6-311++G(d,p):HF/6-31G(d):UFF) representation²²⁴ provide very good agreement with the experimental adsorption energies for both ethene and benzene.

The aim of the present chapter is to elucidate the mechanism of benzene ethylation occurring in H-ZSM-5 using density functional theory (DFT). DFT calculations were carried out on three cluster models of progressively larger size. The size of the cluster used was found to have a significant effect on the reaction energetics and kinetics. It was also concluded that a large cluster size is required in order to capture all of the mechanistic details.

8.2 Theory

The catalytically active center and a portion of the zeolite framework were represented by clusters containing 5, 17, and 33 T-sites, respectively. Initially all Si atoms were placed at their crystallographic positions, as reported by Olson et al.¹⁴⁶ The location of Al in the zeolite framework is difficult to define. Both experimental^{145,229–232} and theoretical^{231–234} studies aimed at determining the preferential locations for Al substitution into ZSM-5 do not lead to a definitive conclusion because the differences in the energies associated with replacement of a Si by Al at different T sites are small. Thus, the location of Al atoms in the zeolite framework is controlled more by the kinetics of zeolite synthesis than by thermodynamics. Nevertheless, there is some evidence that Al siting is not random and that the T12 site is preferred.^{229,233} Based on these findings and other theoretical studies on H-ZSM-5,^{235–237} Al was located at the T12 position (see figure 8.1). Terminal Si-O bonds were replaced by Si-H bonds oriented in the direction of the former Si-O bond. The Si-H bond length was set to 1.487 Å, which is the optimized bond length for SiH₄ at the B3LYP/TZVP level of theory. For the T5 cluster, the resulting coordinates for the terminal H atoms along with the coordinates for the Si atoms were held fixed throughout all subsequent calculations. For the T17 and T33 clusters (figures 8.2 and 8.3) only the terminal H atoms were held fixed while all other coordinates were allowed to relax. Based on the crystallographic position numbers used by Olson et al.¹⁴⁶ for an orthorhombic unit cell, the bridging hydroxyl group is either Al12-O24(H)-Si12, Si3-O20(H)-Al12, or Si11-O11(H)-Al12. In accordance with the literature,²³⁵ the first site is called the “channel intersection” position (CIS) and the second site is called the “alternative channel intersection” position (ACIS). Since the O11 atom can be regarded as part of the straight channel wall, we refer to the third site as the “straight channel wall” position (SCW).

Quantum chemical calculations were performed with the TURBOMOLE suite of programs¹⁶² in C1 symmetry, using gradient-corrected DFT. Becke’s 3-parameter exchange functional⁷⁵ and the correlation functional of Lee, Yang and Parr were used to represent the effects of exchange and correlation (B3LYP).⁷⁶ The default numerical grid size (m3) was used.¹⁵⁶ Although it is well known that DFT does not properly account for dispersive interactions,²³⁸ hybrid DFT methods have proven to be very useful for elucidating the mechanism of reactions involving hydrocarbon transformation in zeolites.^{157,237,239–243} In order to make calculations feasible for the large T33 cluster and to allow for comparisons with earlier cluster calculations,^{222,223} basis sets at the double- ζ level with polarisation functions (SV(P))²⁴⁴ were

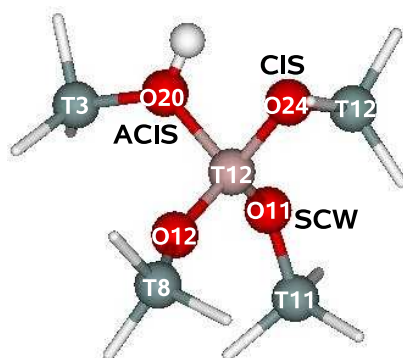


Figure 8.1: T5 cluster model of the acid site in H-ZSM-5. The atoms are labelled according to the crystallographic position numbers given by Olson et al.¹⁴⁶ Depending on its position, the bridging hydroxyl group is referred to as ACIS-, CIS-, or SCW-site, respectively.

used for all atoms. During the structure optimizations, energies were converged to 10^{-6} Ha and the maximum norm of the Cartesian gradient was converged to 10^{-3} Ha/bohr. Transition states were localized using a combination of interpolation and local methods. For the T5-cluster the growing-string method¹⁶⁴ was used in mass-weighted coordinates with a maximum of 13 to 16 nodes. After the two ends of the growing string joined, the growing-string method was terminated and an approximate saddle point was identified. The PRFO method was employed to refine the position of the saddle point.²⁴⁵ Converged transition state structures from the T5 cluster were transferred to larger clusters and used as the initial guesses. Subsequent refinement was carried out with the modified-dimer method.¹⁶⁵ A gradient-norm convergence criterion of 5×10^{-4} Ha/bohr was used for the transition state searches. To confirm that the transition states were connected to the correct energy minima, each transition state was perturbed slightly along the reaction coordinate in the reactant and product directions. The perturbed geometries were then used as starting points for energy minimization. In each case the desired energy minimum was obtained.

The error in energy barriers obtained from DFT is often too large to calculate rate constants within an accuracy of one order of magnitude, even if hybrid functionals are used.²⁴⁶ To improve the theoretical estimate of the intrinsic activation energies we conducted MP2 single-point energy calculations employing the quadruple- ζ basis set from Dunning's correlation-consistent polarised valence series, cc-pVXZ²⁴⁷ for all atoms. We used the parallelized version of the TURBOMOLE 'ricc2'-module^{248,249} and employed the resolu-

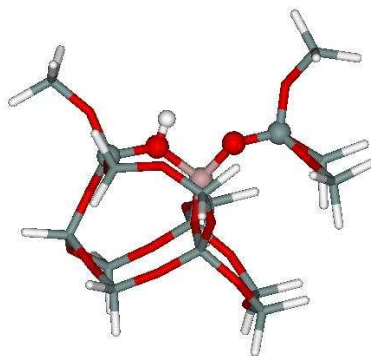


Figure 8.2: T17 cluster model of the active site for benzene alkylation viewed along the sinusoidal channel. The bridging hydroxyl group is in the ACIS position.

tion of the identity (RI) approximation^{250–254} with optimized auxiliary basis sets^{255,256} in combination with a frozen-core (FC) ansatz. Electrons in molecular orbitals corresponding to carbon 1s, oxygen 1s, aluminium 1s, and silicon 1s atomic orbitals were excluded from the MP2 correlation scheme. The use of both RI and FC approximation leads to a considerable reduction in computer time and introduces only a small error. Recent applications of this approach to zeolite catalysed hydrocarbon reactions and proton jumps in zeolites are reported in refs. 59,238,257 and 258. To estimate the error introduced by the FC approximation in the present study, we calculated the intrinsic activation energy for the one-step alkylation on the T5 cluster (using the DFT-converged geometries; see figure 8.4) employing an all electron (AE) correlation treatment. The energy difference between the RI-MP2(AE) and RI-MP2(FC) calculation is <0.1 kcal/mol. To justify the use of DFT-converged transition state structures for single point RI-MP2(FC) calculations, we also calculated the intrinsic activation energy of the one-step alkylation for the T5 cluster by optimizing both reactant and transition state at the RI-MP2(FC)/cc-pVTZ level (the terminating SiH_3 groups were held fixed). The difference in electronic energy between the activation energy obtained from single point RI-MP2(FC) calculations on the DFT-converged structures and the optimized calculation is <0.3 kcal/mol leading us to conclude that the use of DFT-converged structures for single point RI-MP2(FC)/cc-pVQZ calculation is a reasonable approximation for both energy minima and transition state structures. In the following all RI-MP2(FC) calculations are referred to simply as MP2 calculations.

The reason for using the T33 cluster was to account for the electrostatic

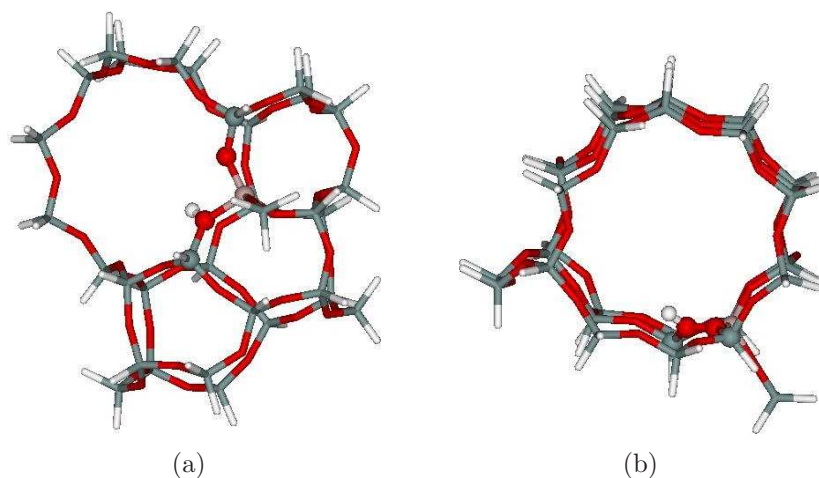


Figure 8.3: T33 cluster model of the active site for benzene alkylation viewed along the sinusoidal channel (a) and the straight channel (b), respectively. The bridging hydroxyl group is in the ACIS position.

stabilisation of the ionic transition state structure through the framework atoms. However, single point MP2 calculations with large basis sets cannot be carried out for reasons of computational costs for the T33 cluster even if the RI and FC approximations are used. In order to improve the activation energy obtained from DFT calculations on this cluster we carved out T5 clusters similar to the one shown in figure 8.1 from the DFT-converged T33 geometries of both transition state and adsorption complex and used these for single point MP2 calculations. A corrected intrinsic activation energy, $E_{a,\text{corr}}$, was then obtained from

$$E_{a,\text{corr}} = E_{a,\text{T33}}^{\text{DFT}} + (E_{a,\text{T5}\leftarrow\text{T33}}^{\text{MP2}} - E_{a,\text{T5}\leftarrow\text{T33}}^{\text{DFT}}), \quad (8.1)$$

where $E_{a,\text{T33}}^{\text{DFT}}$ is the activation energy obtained on the T33-cluster at the DFT level. $E_{a,\text{T5}\leftarrow\text{T33}}^{\text{MP2}}$ denotes the activation energy obtained from single point MP2 calculations on the T5 cluster cut out from the DFT optimized T33 structures. Likewise, $E_{a,\text{T5}\leftarrow\text{T33}}^{\text{DFT}}$ is the activation energy obtained from single point DFT calculations on this cluster. The term in brackets can thus be interpreted as the high level correction to the DFT activation energy calculated for the T33 cluster.

Intrinsic reaction rate constants were computed using standard statistical mechanics and absolute rate theory.¹⁹³ We used the harmonic approximation, and assumed that adsorbate and transition state are rigid in space and have only vibrational degrees of freedom.

8.3 Results and discussion

Three reaction mechanisms were considered. Two of them are concerted schemes, which differ only in whether or not the position of the acidic hydrogen changes during the course of reaction. The third mechanism involves the formation of a stable ethoxide intermediate in the first step. In what follows we review first the energetics for each of the mechanisms obtained using the T5 cluster. Second, we illustrate the energetic and structural differences that arise using the T17 cluster. Third, we present the results for the T33 cluster and show that not only energetic and structural but also mechanistic differences are obtained. Fourth, we discuss the results of the present study in the light of previous theoretical studies and, where available, experimental data. All computed adsorption and reaction energies reported in this section are zero-point energy corrected DFT results obtained with the B3LYP functional in combination with the SV(P) basis set (see section 8.2 for details). Activation energies presented for the T5 and T17 cluster were also calculated at this level of theory. Both DFT and MP2-corrected activation energies are presented for the T33 cluster.

8.3.1 Reaction mechanism for the T5 cluster

Figure 8.4 illustrates the alkylation mechanism in which the position of the Brønsted acidic proton moves from the ACIS to the CIS site during the reaction. Initially, ethene adsorbs on the acid site while benzene adsorbs edge-on next to the active site. The O20-H1 bond is slightly elongated compared to the bare cluster (0.999 Å in the adsorbed state and 0.975 Å for the bare cluster), indicative of only weak interaction between ethene and the proton. The C1-C2 double bond length is virtually unchanged (1.335 Å in the gas phase and 1.341 Å in the adsorbed state). An adsorption energy of $\Delta E_{\text{ads}} = -8.0$ kcal/mol was calculated for the co-adsorption of ethene and benzene from the gas phase. It should be noted that the opposite scenario, i.e. benzene adsorbed on the acid site and ethene co-adsorbed, was also evaluated. While this configuration cannot be ruled out based on adsorption energies, a physically meaningful transition state for the formation of ethylbenzene could not be obtained in this case. Therefore, it appears that ethylbenzene is formed only when ethene interacts with the acid site. In the one-step mechanism, ethene is protonated and attacked by the adsorbed benzene to produce ethylbenzene. The activation energy for this process is $E^\ddagger = 28.4$ kcal/mol. In going from the reactant state to the transition state the O20-H1 distance lengthens from 0.999 Å to 1.634 Å. The length of the C1-

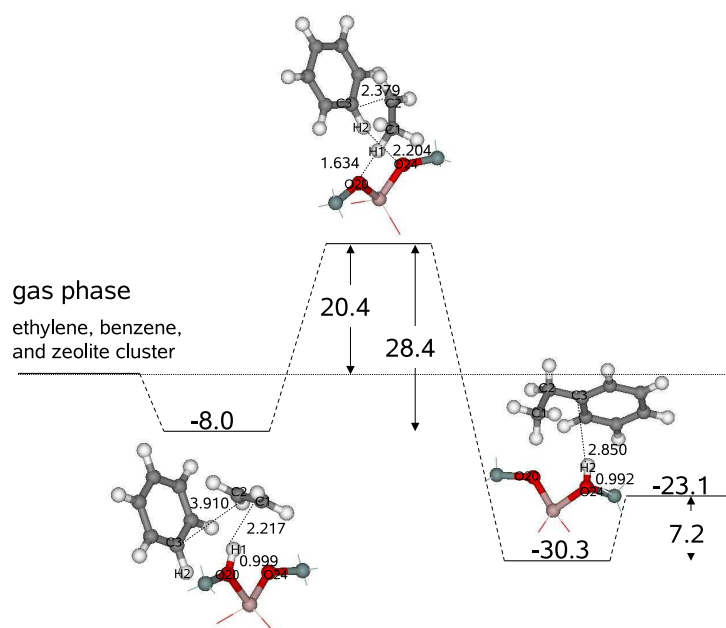


Figure 8.4: Energy profile (T5 cluster) for the one-step reaction involving a position change of the acidic hydrogen from the ACIS to the CIS site during the reaction. Energies are zero-point corrected. Interatomic distances are given in Å.

C2 bond increases from 1.341 Å to 1.429 Å, while the distance between the bond forming C-atoms of ethene and benzene (C2-C3) decreases from 3.910 Å to 2.379 Å. The imaginary frequency associated with vibration along the reaction coordinate is $192i \text{ cm}^{-1}$. The desorption energy for the product ethylbenzene is $\Delta E_{\text{des}} = 7.2 \text{ kcal/mol}$.

The second one-step mechanism, illustrated in figure 8.5, differs from the one presented in figure 8.4 in that the acidic proton remains in the same position after the reaction as it was before the reaction. Both mechanisms lead to similar adsorption energies; however, the activation energy for the mechanism shown in figure 8.5 is lower by 2.3 kcal/mol. Compared to the first mechanism, the distances between bond forming and bond breaking atoms of the transition state are longer (i.e. C2-C3 and H2-O20 / H2-O24). The imaginary frequency associated with vibration along the reaction coordinate is $196i \text{ cm}^{-1}$. The energy to desorb ethylbenzene is $\Delta E_{\text{des}} = 6.9 \text{ kcal/mol}$.

In the two-step mechanism shown in figure 8.6, ethene is first adsorbed on the acid site. As already mentioned above, the interaction of ethene with the acid site is weak. The length of the O20-H1 bond increases from 0.975

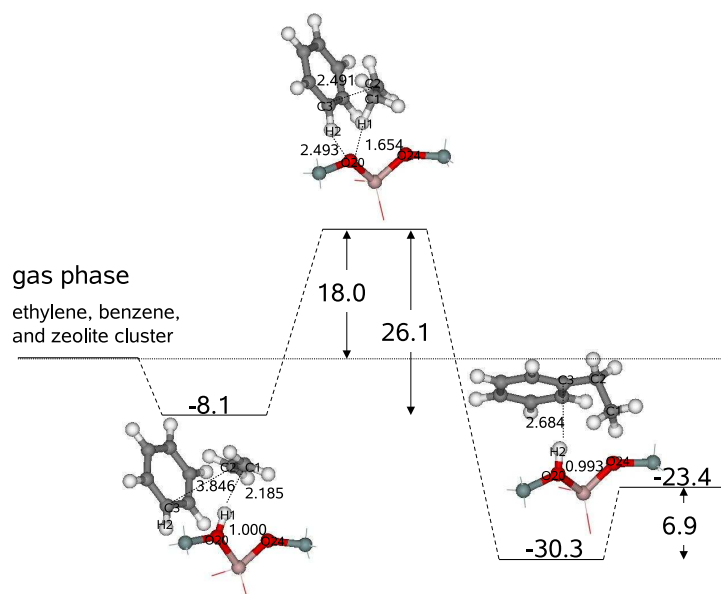


Figure 8.5: Energy profile (T5 cluster) for the one-step reaction in which the acidic hydrogen remains on the ACIS site during the reaction. Energies are zero-point corrected. Interatomic distances are given in Å.

Å to 1.000 Å, while the length of the C1-C2 double bond remains almost unchanged compared to the gas phase (1.341 Å in the adsorbed state and 1.335 Å in the gas phase). Protonation of ethene leads to a covalently bonded ethoxide. The activation energy calculated for this process is $E^\ddagger = 17.1$ kcal/mol. In the transition state the O20-H1 bond is lengthened to 1.407 Å, while the C1-C2 bond length increases to 1.400 Å. The imaginary frequency associated with the transition mode is $469i$ cm⁻¹. The ethoxide species is more stable by 11.3 kcal/mol relative to the π -complex. Benzene interacts only weakly with the ethoxide species (figure 8.6(b)). The activation energy calculated for the formation of ethylbenzene is $E^\ddagger = 33.9$ kcal/mol and, thus, is 6-8 kcal/mol higher than that for the one-step mechanisms. In the transition state the distances between the bond forming atoms (C2 and C3) are significantly shorter (2.176 Å) than those seen in the transition states of the one-step mechanisms. The imaginary frequency associated with vibration along the reaction coordinate of the transition state mode is $141i$ cm⁻¹. Note that the proton is donated to the SCW site in this case. A reaction channel resulting in proton donation to the ACIS or CIS site could not be identified.

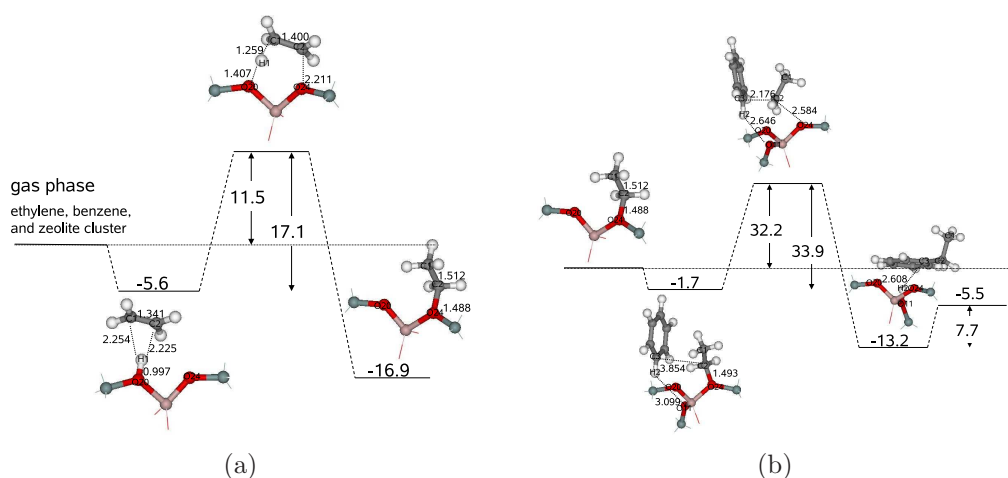


Figure 8.6: Energy profile (T5 cluster) for (a) the protonation of ethene to give an ethoxide species, (b) alkylation step. Energies are zero-point corrected. Interatomic distances are given in Å.

8.3.2 Reaction mechanism for the T17 cluster

Figure 8.7 illustrates the first of the one-step mechanisms occurring on the T17 cluster. The adsorption energy of the co-adsorbed complex is higher than that for the T5 cluster by 1 kcal/mol, reflecting the greater interaction of the adsorbates with the increased number of framework atoms. The characteristic distances between the adsorbed complex and the framework are slightly larger than those for the T5 cluster. The distance between ethene and the acid site (H1-C1) is larger by 0.1 Å, while the distance between the bond forming C atoms of benzene and ethene is larger by 0.2 Å. The activation energy for the formation of ethylbenzene is $E^\ddagger = 30.8$ kcal/mol which is 2.5 kcal/mol higher than that calculated for the T5 cluster. The imaginary frequency associated with vibration along the reaction coordinate is $161i$ cm^{-1} . The atomic distances O20-H1 and C2-C3 are only slightly larger than for the T5 cluster. However, the O24-H2 distance (2.715 Å) is significantly larger, showing the influence of the additional framework atoms surrounding the active site. While the T5 cluster does not represent a particular pore architecture, the additional wall atoms included in the T17 cluster cause the transition state to rotate into the free space of the channel intersection rather than remaining close to the cluster. The distance between the reaction product and the acid site is larger by 0.4 Å compared to the T5 cluster resulting in a desorption energy of only 4.8 kcal/mol.

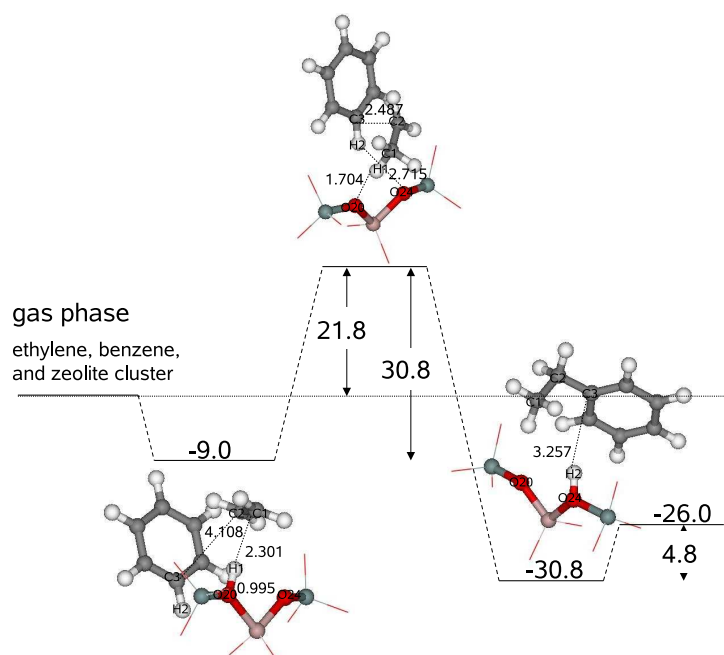


Figure 8.7: Energy profile (T17 cluster) for the one-step reaction involving a position change of the acidic hydrogen from the ACIS to the CIS site during the reaction. Energies are zero-point corrected. Interatomic distances are given in Å.

Figure 8.8 illustrates the second one-step mechanism occurring for the T17 cluster. The adsorption energy of the co-adsorbed complex is higher than that for the corresponding mechanism for the T5 cluster by 0.9 kcal/mol. The distance between the bond-forming C2 and C3 atoms is larger than for the case of the T5 cluster (2.535 Å vs. 2.491 Å) as is the distance between the bond-forming H2 and O20 atoms (2.644 Å vs. 2.493 Å). The activation energy for the formation of ethylbenzene is $E^\ddagger = 30.8$ kcal/mol, which is 1.2 kcal/mol higher than that calculated for the T5 cluster. The imaginary frequency associated with vibration along the reaction coordinate is $142i$ cm^{-1} . The characteristic atomic distances of the transition state (i.e O20-H1, O20-H2, and C2-C3) are all slightly longer than those for the T5 cluster. The distance between the reaction product and the acid site is larger by 0.3 Å compared to that for the T5 cluster, resulting in an adsorption energy that is lower by 5.7 kcal/mol.

The differences between the two one-step schemes for the T17 cluster are qualitatively the same as those calculated for the T5 cluster. For the second

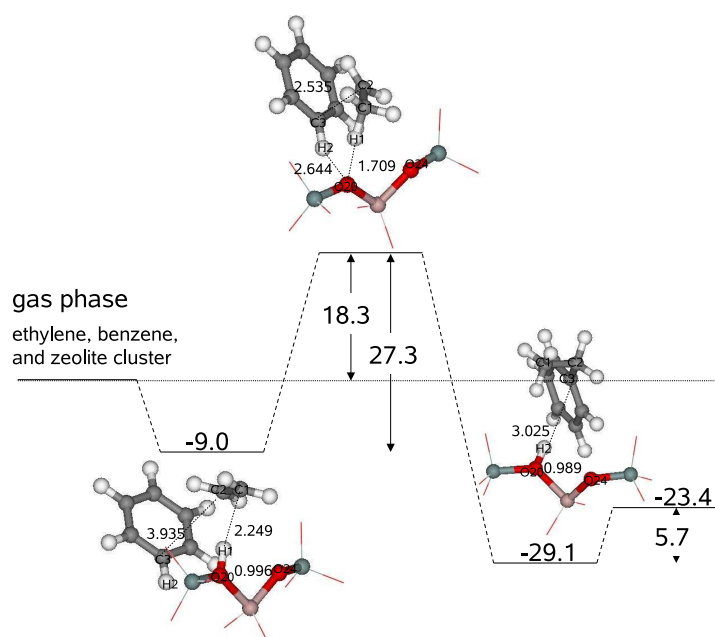


Figure 8.8: Energy profile (T17 cluster) for the one-step reaction in which the acidic hydrogen remains on the ACIS site during the reaction. Energies are zero-point corrected. Interatomic distances are given in Å.

mechanism, the reactants are slightly closer to the active site in the adsorbed state, while the distance between the bond forming C-atoms (C2-C3) is larger in the transition state. The activation energy for the second mechanism is lower than that for the first one by 3.5 kcal/mol.

Figure 8.9(a) shows the formation of the ethoxide on the T17 cluster. The adsorption energy for the π -complex formation ($\Delta E_{\text{ads}} = 5.5$ kcal/mol) is very similar to that for the T5 cluster, indicating that ethene adsorption is not strongly affected by the presence of the wall atoms. However, the C1-H1 and C2-H1 distances are larger than those found for the T5 cluster. The same holds for the transition state (O20-H1 and C2-O24 distances). The activation energy is 4.1 kcal/mol higher than that for the T5 cluster. The imaginary frequency for vibration along the reaction coordinate is $352i$ cm^{-1} . The ethoxide species is stabilized by 10.1 kcal/mol relative to the π -complex. The C-O bond length of the ethoxide is virtually the same as that determined for the T5 cluster (1.488 Å on T5 and 1.493 Å on T17). Benzene interacts weakly with the ethoxide ($\Delta E_{\text{ads}} = -2.9$ kcal/mol). The activation barrier for ethylbenzene formation is $E^\ddagger = 39.8$ kcal/mol, about 6 kcal/mol larger than that for the T5 model. The imaginary frequency for vibration along

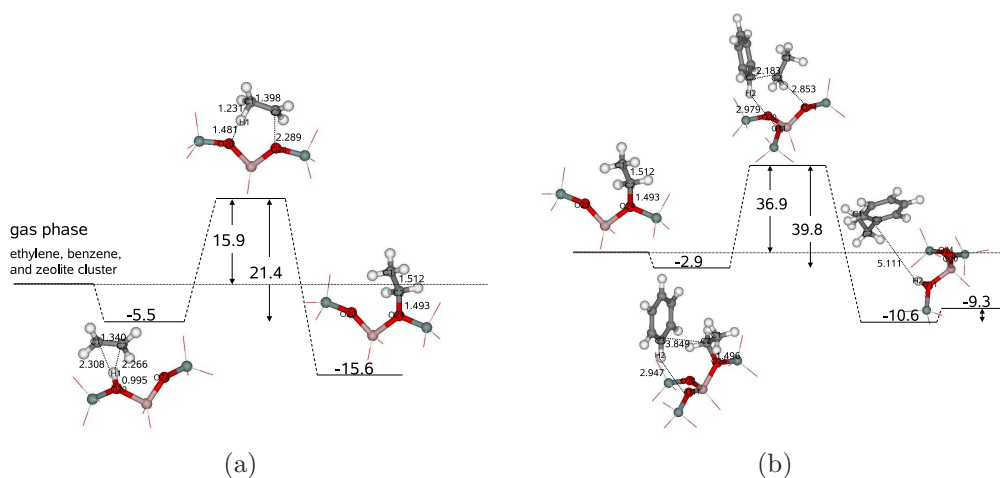


Figure 8.9: Energy profile (T17 cluster) for (a) the protonation of ethene to give an ethoxide species, (b) alkylation step. Energies are zero-point corrected. Interatomic distances are given in Å.

the reaction coordinate is $128i \text{ cm}^{-1}$. As before, the proton is donated to the SCW site. The stable product state is far away from the acid site due to steric constraints imposed by the walls of the straight channel. Consequently the computed desorption energy is low ($\Delta E_{\text{des}} = 1.3 \text{ kcal/mol}$).

8.3.3 Reaction mechanism for the T33 cluster

Figure 8.10 illustrates the alkylation mechanism in which the position of the acidic proton changes from the ACIS to CIS site. The interatomic distances between ethene and the Brønsted site (H1-C1) and between the adsorbates (C2-C3) are larger than those for the T5 cluster but not to the same extent as was the case for the T17 cluster. This reflects the effects of confinement imposed by the additional framework atoms on the opposite side of the active center. The adsorption energy was calculated to be $\Delta E_{\text{ads}} = -13.6 \text{ kcal/mol}$, which is significantly larger than that determined for the smaller clusters. The activation energy for the formation of ethylbenzene is $E^\ddagger = 24.3 \text{ kcal/mol}$. This value is 4-6 kcal/mol lower than that calculated for the smaller clusters. The observed stabilizing effect of the zeolite micropore on the ionic transition state is well known^{236,259-261} and can be on the order of 10 to 30% of activation energies obtained for small clusters. In the transition state, the distance between the bond forming C-atoms (C2-C3) is larger than that obtained for the smaller clusters (T33: 2.716 Å; T17: 2.487 Å; T5: 2.379

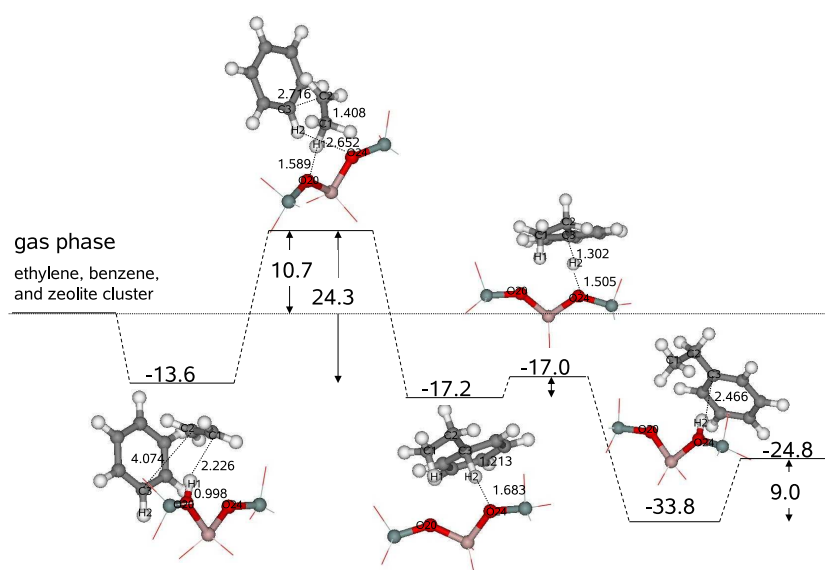


Figure 8.10: Energy profile (T33 cluster) for the one-step reaction involving a position change of the acidic hydrogen from the ACIS to the CIS site during the reaction. Energies are zero-point corrected. Interatomic distances are given in Å.

Å). The distance between the bond breaking H1 and O20 atoms is smallest for the T33 cluster (T33: 1.589 Å; T17: 1.704 Å; T5: 1.634 Å). The distance between the bond forming O2 and H24 atoms lies between those for the smaller clusters (T33: 2.652 Å; T17: 2.715 Å; T5: 2.204 Å), indicating the effect of confinement imposed by the framework atoms on the opposite side of the active center. The imaginary frequency for vibration along the reaction coordinate is $155i$ cm^{-1} .

However, the most significant difference between the large cluster and the smaller clusters is that the large cluster is able to stabilize an ionic intermediate. While ethylbenzene was formed directly from the first transition state on the T5 and T17 clusters, a stable carbenium ion (protonated ethylbenzene) was found on the T33 cluster. The intermediate has an elongated C3-H2 bond of 1.213 Å. The C1-C2 and the C2-C3 bond lengths are 1.529 Å and 1.547 Å, respectively. The corresponding bond lengths of protonated ethylbenzene in the gas phase are 1.124 Å (C3-H2), 1.526 Å (C1-C2), and 1.588 Å (C2-C3). In addition to a significantly longer C3-H2 bond, the adsorbed structure also possesses a larger angle between the plane spanned by the aromatic ring atoms and the C2-atom (157.6°) compared to the gas phase (139.3°). In the transition state the C3-H2 bond length increases to 1.302

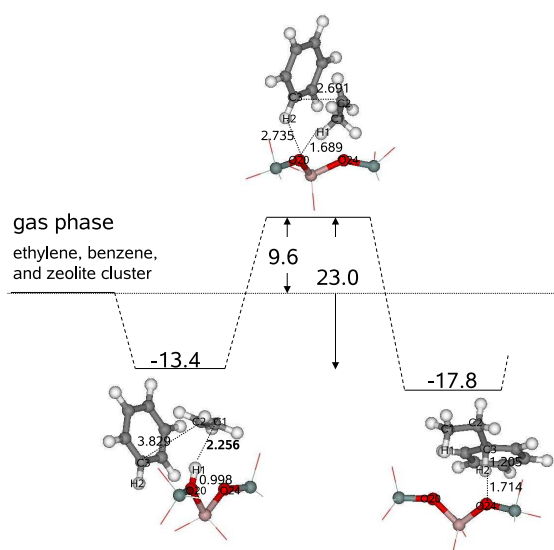


Figure 8.11: Energy profile (T33 cluster) for the alternative one-step reaction involving a position change of the acidic hydrogen from the ACIS to the CIS site during the reaction. Energies are zero-point corrected. Interatomic distances are given in Å.

Å. The imaginary frequency for vibration along the reaction coordinate is $483i \text{ cm}^{-1}$, and the product ethylbenzene interacts only weakly with the acid site. Compared to the bare cluster, the O24-H2 distance is slightly elongated from 0.979 Å to 0.991 Å . The C1-C2 distance is virtually unchanged (1.539 Å in the gas phase and 1.538 Å in the adsorbed state). The same holds for the C2-C3 distance (1.516 Å in the gas phase and 1.518 Å in the adsorbed state).

A mechanism in which the proton does not change its position could not be identified, in contrast to what was found for the smaller clusters, even though two different initial reactant states both corresponding to a different transition state structure could be found. However, structure optimization from the slightly perturbed transition states towards the products lead to very similar intermediate states, i.e. protonated ethylbenzene, in which the proton (H2) points towards the CIS site in both cases.

The reaction scheme with the alternative reactant and transition states is shown in figure 8.11. It exhibits the same characteristics as those for the second one-step mechanisms on the smaller clusters, i.e. smaller interatomic distances in the reactant state and a smaller activation energy. The protonated ethylbenzene has a slightly shorter C3-H2 bond length. Because of

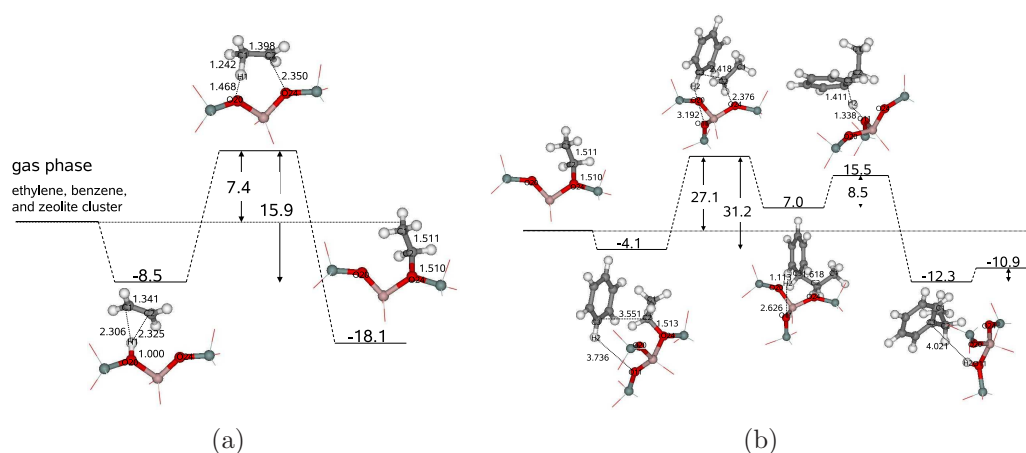


Figure 8.12: Energy profile (T33 cluster) for (a) the protonation of ethene to give an ethoxide species, (b) alkylation step. Energies are zero-point corrected. Interatomic distances are given in Å.

the similarities in the two protonated intermediates the calculation of the transition state for the back donation of the proton to the zeolite framework was not pursued.

Figure 8.12(a) shows the formation of an ethoxide species on the T33 cluster. In the adsorbed π -complex, the O20-H1 bond length is 1.000 Å, while the length of the C1-C2 double bond remains almost unchanged compared to that for ethene in the gas phase (1.341 Å in the adsorbed state and 1.335 Å in the gas phase). The protonation of ethene to give a covalently bonded ethoxide has an activation energy of 15.9 kcal/mol, which is only 1.2 kcal/mol lower than that for the T5 cluster. In the transition state the O20-H1 bond is lengthened to 1.468 Å, while the C1-C2 bond length increases to 1.398 Å. The imaginary frequency for vibration along the reaction coordinate is $309i$ cm^{-1} . The ethoxide intermediate is stabilized by 9.6 kcal/mol with respect to the π -complex. The CO bond length is only slightly longer than the computed distances for the smaller clusters. Benzene interacts weakly with the ethoxide ($\Delta E_{\text{ads}} = -4.1$ kcal/mol). The C2-O24 bond length is 1.513 Å and thus virtually unchanged (figure 8.12(b)). The activation energy for the ethylbenzene formation is $E^\ddagger = 31.2$ kcal/mol, which is 2.7 kcal/mol smaller than the corresponding value for the T5 cluster. In the transition state the C2-O24 distance is lengthened to 2.376 Å. The distance between the reacting carbon atom of the ethene (C2) and benzene (C3) is 2.418 Å. The distance between the hydrogen atom to be back-donated to the framework and the accepting oxygen (O11) now decreases to 3.192 Å. The imaginary frequency

Table 8.1: Adsorption energies (zero-point corrected) and enthalpies (at 300 K) of ethene (E), benzene (B), ethylbenzene (Eb), and ethene plus benzene (E+B) on the ACIS site and of benzene adsorbed in the vicinity of the ethoxide intermediate for different cluster sizes (in kcal/mol); experimental heats of adsorption are given for comparison, where available.

		E on ACIS	B on ACIS	Eb on ACIS	E+B on ACIS	B on ethoxide
T5 (this work)	E_{ads} (ΔH_{ads})	-5.6 (-5.8)	-6.2 (-5.5)	-6.8 (-6.1)	-8.0 (-6.6)	-1.7 (-0.7)
T17 (this work)	E_{ads} (ΔH_{ads})	-5.5 (-5.2)	-5.2 (-4.5)	-5.6 (-4.9)	-9.0 (-7.9)	-2.9 (-1.3)
T33 (this work)	E_{ads} (ΔH_{ads})	-8.5 (-8.4)	-10.0 (-9.5)	-9.5 (-9.2)	-13.6 (-12.6)	-4.1 (-3.3)
T4 ^a (ref 222)	E_{ads}	-	-	-6.4	-7.3	-
T4 ^a (ref 223)	E_{ads}	-	-	-6.2	-7.9	-
exptl		-9.0 ^b	-14.3 ^c	-18.0 ^d	-	-
			-15.3 \pm 1.2 ^e	-20.7 \pm 1.2 ^e	-	-
			-15.2 ^f			

^aRelaxed cluster, B3LYP/6-31G*.

^bHY.²⁶²

^c2 molecules per unit cell, Si/Al = 82.²⁶³

^dSilicalite.²⁶⁴

^e2 molecules per unit cell, Si/Al = 34, but large amounts of extraframework Al.²⁶⁵

^f1 molecule per unit cell, Si/Al = 86.²⁶⁶

for vibration along the reaction coordinate is $189i\text{ cm}^{-1}$. Perturbation of the transition state structure in the direction of the product and subsequent optimization, leads again to a stable carbenium-like ion. Compared to the final adsorbed ethylbenzene, the C2-C3 bond length is considerable longer in the intermediate state (1.618 Å and 1.515 Å). The activation energy for back donation of the proton from the carbenium ion to the SCW-site of the zeolite framework is relatively large, 8.5 kcal/mol, when compared to the corresponding activation energy for the one-step mechanism. The reason is that the formation of the stable product requires extensive rearrangements in the zeolite cavity. The imaginary frequency for vibration along the reaction coordinate is $189i\text{ cm}^{-1}$. The calculated desorption energy for ethylbenzene from this site is 1.4 kcal/mol.

The stability of the ethoxide species is a critical issue for the two-step mechanism, and previous investigations have shown that the stability of alkoxide species depends strongly on the local structure of the Brønsted acid site.^{267,268} For this reason, the energy of ethoxide species bonded to the ACIS site was computed, in order to estimate the influence of the non-equivalency of the framework oxygen atoms surrounding the Al-atom. In contrast to the bridging hydroxyl group, the ethoxide species is somewhat more stable on the ACIS site than on the CIS site (energy difference: 1.5 kcal/mol for T33 cluster). The cluster size also has a small influence on the stability of the ethoxide species. The zero point energy corrected reaction energies for the ethoxide formation on the CIS site with respect to the π -complex are $\Delta E_{T5} = -11.3$ kcal/mol, $\Delta E_{T17} = -10.1$ kcal/mol, and $\Delta E_{T33} = -9.6$ kcal/mol for the T5, T17, and T33 cluster, respectively. The finding that the alkoxide species are much more stable than the corresponding adsorbed alkene is consistent with the findings of Nieminen et al.²⁶⁸, who investigated alkoxide formation in H-FER using a hybrid quantum mechanics/molecular mechanics (QM/MM) method. Contrary to these findings are the results reported by Namuangruk et al. in their study of benzene alkylation over H-FAU.²²⁴ Here, the π -complex and the ethoxide were found to be equally stable. A possible reason for this discrepancy might be that in the latter study only a very small reactive region consisting of 3 T-atoms was allowed to relax while the surrounding framework atoms were kept fixed in their crystallographic positions.

The computed adsorption energies and enthalpies of adsorption at 300 K for ethene, benzene, ethylbenzene, and ethene co-adsorbed with benzene are listed in table 8.1 for all of the clusters considered in this study. Also shown for comparison are theoretically obtained values of the adsorption energies reported by Vos et al.²²² and Arstad et al.²²³ and experimental values of the

Table 8.2: Intrinsic activation energies in kcal/mol; values obtained in the present work are zero-point energy corrected and reported as DFT results and MP2-corrected results (in brackets); values from the literature are DFT results and MP2/ONIOM results (in italics).

	concerted mechanism ^a		concerted mechanism ^b	stepwise mechanism ^c		
	TS1	TS2	TS1	TS1	TS2	TS3
T5 (this work)	28.3	N/A	26.1	17.1	33.9	N/A
T17 (this work)	30.8	N/A	27.3	21.4	39.8	N/A
T33 (this work)	24.3 (28.8)	0.2	N/A	15.9 (23.7)	31.2 (26.4)	8.5
	23.0 (25.5)	0.2				
T4 ^d (ref 222)	31.5	N/A	–	–	–	–
T4 ^e (ref 223)	31.3 <i>38.2</i>	N/A	–	–	–	–
T84 ^f (ref 224)	<i>33.4</i>	–	–	<i>30.1</i>	<i>38.2</i>	–

^aBrønsted H changes to CIS site during the reaction.

^bBrønsted H remains on ACIS site.

^cBrønsted H changes to SCW site during the reaction.

^dRelaxed T4-cluster, B3LYP/6-31G*.

^eFirst value, relaxed T4 cluster, B3LYP/6-31G*; second value, single-point MP2/6-311G** on DFT-converged geometry.

^fONIOM(MP2/6-311++G(d,p):HF/6-31G(d):UFF)//ONIOM(MP2/6-31G(d,p):HF/3-21G:UFF) applied to T84 cluster of H-FAU.

adsorption enthalpy,^{262–266} where these are available. Our theoretical results for ethylbenzene adsorption and ethene co-adsorption with benzene obtained using the T5 cluster are very similar to the values reported by Vos et al.²²² and Arstad et al.²²³ Due to their high reactivity, the adsorption of olefins, with the exception of ethene, is difficult to study experimentally.²⁶⁹ The interactions of ethene with Brønsted acid sites are so weak that the resulting complexes are unstable at room temperature²⁷⁰ and, hence, reliable values for heats of adsorption on other than pure silica MFI zeolites are hard to obtain. The only available experimental value is that reported by Cant and Hall for ethene adsorbed on faujasite ($\Delta H_{\text{ads}} = -9$ kcal/mol).²⁶² However, this value can only be regarded as a lower bound because the acidity of H-ZSM-5 is known to be larger than that of faujasite.^{271–275} Not surprisingly, the heats of adsorption obtained with T5 and T17 cluster are significantly lower than those observed experimentally due to the inability of such small clusters to properly account for all of the dispersive interactions of the adsorbate with the zeolite pore channels. However, when a T33 cluster is used to represent the zeolite, the difference between experimental and computed values becomes smaller.

The activation energies for benzene ethylation via all of the mechanisms considered in this study are summarized in table 8.2. In each case, the calculated activation energy is higher for the T17 than for the T5 cluster, but is lowest for the T33 cluster. Since the T33 cluster includes the atoms of an entire intersection, we expect the reported activation energies not to change very much for clusters larger than T33. This is supported by a recent study on alkene methylation over H-ZSM-5, which included a systematic investigation of the dependence of the activation energy on the cluster size.²⁵⁸ The calculated values of the activation energy obtained in the present study for the concerted mechanism, in which the proton moves to the CIS site during reaction, agree reasonably well with activation energies reported by Vos et al.²²² and Arstad et al.²²³ for T4 and T5 clusters, respectively. MP2-corrected values of the activation energies are shown in parentheses in table 8.2. With the exception of the second barrier in the two-step scheme the corrections are all positive. Table 8.2 shows that the MP2-corrected barriers are significantly smaller than the barriers reported by Namuangruk et al. for both the concerted and step wise mechanisms of benzene ethylation occurring in H-FAU.²²⁴ The reason might be that the stabilizing effect of the zeolite micropore is not so strong in the employed ONIOM approach because only a small part (12 T-atoms) of the cluster was treated quantum mechanically. This view is supported by comparing the single-point MP2 activation energies, $E_{\text{a},\text{T5}-\text{T33}}^{\text{MP2}}$, with the values reported by Namuangruk et al. The numbers computed in the present study are 37.5 and 35.8 kcal/mol for the two 1-step

Table 8.3: Rate coefficients for elementary processes on the T33 cluster calculated with MP2-corrected activation energies.

reaction scheme	constant ^a	T,K		
		600	650	700
Figure 8.10	k_1, s^{-1}	8.17×10^{-1}	4.97×10^0	2.33×10^1
	k_{-1}, s^{-1}	3.80×10^{-5}	9.75×10^{-4}	1.58×10^{-2}
Figure 8.11	k_1, s^{-1}	2.13×10^{-1}	1.01×10^0	3.82×10^0
	k_{-1}, s^{-1}	7.23×10^{-6}	1.48×10^{-4}	1.98×10^{-3}
Figure 8.12	k_1, s^{-1}	2.58×10^2	1.14×10^3	4.11×10^3
	k_{-1}, s^{-1}	1.20×10^1	1.12×10^2	7.65×10^2
	k_2, s^{-1}	3.19×10^2	1.84×10^3	8.26×10^3
	k_{-2}, s^{-1}	7.24×10^{-1}	6.98×10^0	4.87×10^1

^aRate coefficients for the reverse reaction are determined with respect to the final product

mechanisms and 28.5 and 35.9 kcal/mol for the first and second step of the 2-step mechanism and thus similar to the barriers reported by Namuangruk et al.²²⁴

Rate coefficients for all reaction steps investigated in this study are listed in table 8.3. The values were computed using the MP2-corrected barriers calculated for the T33 cluster, and all partition functions were evaluated with the frequencies from the DFT calculations. For the mechanisms presented in figures 8.10 and 8.11, it assumed that the co-adsorption and desorption of ethene and benzene are quasi-equilibrated and that the rate-limiting step is the reaction of the co-adsorbed reactants to form ethylbenzene. The results in table 8.3 show that the rate coefficient for the scheme shown in figure 8.10 is higher than that for the one shown in figure 8.11. This is surprising, since the barrier for the scheme shown in figure 8.11 is lower than that for the scheme shown in figure 8.10. The higher value of k_1 for the scheme shown in figure 8.10 is attributable to the higher value of the preexponential factor for this mechanism.

There are two critical steps in the scheme shown in figure 8.12. The first is the formation of an ethoxide species via the reaction of adsorbed ethene with the Brønsted acid proton of the zeolite. This process is referred to as Reaction 1. The MP2-corrected activation barrier for this reaction is 23.7 kcal/mol (see table 8.2), and the rate coefficient for this reaction, k_1 , is listed in table 8.3. The second critical step is the reaction of benzene adsorbed next to the ethoxide species to form ethylbenzene, Reaction 2. The MP2-corrected activation barrier for this process is 26.4 kcal/mol (see table 8.2),

and the rate coefficient for this reaction, k_2 , is also listed in table 8.3. It is evident that the rate coefficient for the reaction of ethoxide species with adsorbed benzene is significantly higher than that for the reaction of adsorbed benzene with adsorbed ethene via pathways shown in figures 8.10 or 8.11. This relationship is surprising, since the activation barriers are similar. The reason for the higher rate coefficient for the formation of ethylbenzene via the pathway involving ethoxide species is again the higher preexponential factor for this reaction.

Table 8.3 shows that the two-step scheme is favored kinetically over the one-step schemes. While this could lead to the conclusion that the one-step scheme is irrelevant it should be kept in mind that the rate constant for ethoxide formation (the first step in the two-step scheme) was calculated for the case of ethene entering an empty intersection. An excess of benzene is used in industrial practise. This lowers the probability that ethene finds an unoccupied intersection, since benzene adsorbs much more strongly than ethene in the channel intersections. It is therefore likely that both mechanisms take place simultaneously. Thus, the extend to which each mechanism contributes to the overall activity is hard to establish.

Experimental activation energies for the ethylation of benzene over zeolites are rare. Christensen et al. have reported experimental values for the apparent activation energy of benzene ethylation on H-ZSM-5 of 14.1 to 18.4 kcal/mol,²⁷⁶ whereas Becker et al. have reported an apparent activation energy over H-MOR of 10 kcal/mol.²⁷⁷ To compare our calculated values to the results of Christensen et al., we assumed that the reaction proceeds via the reversible adsorption of ethene and benzene followed by the rate-limiting step in which the two co-adsorbed species react to form ethylbenzene. For the case of low occupancies, the apparent activation energy, E_{app}^\ddagger , is given by

$$E_{\text{app}}^\ddagger = E^\ddagger + \Delta H_{\text{ads,B+E}}. \quad (8.2)$$

Taking values of $E^\ddagger = 28.8$ kcal/mol and $\Delta H_{\text{ads,B+E}} = -12.6$ kcal/mol, one obtains a value of $E_{\text{app}}^\ddagger = 16.2$ kcal/mol, in reasonable agreement with the experimentally observed values of 14.1 – 18.4 kcal/mol.

An important finding of the present study is the discovery that the formation of ethylbenzene involves a carbenium ion intermediate. Whether cationic species exist as true reaction intermediates or transition states within the zeolite pores, depends on charge delocalization over the cation and accessibility of the positive charge to framework oxygen atoms.²⁷⁴ Both experimental²⁷⁸ and theoretical studies conducted with small and large clusters^{260,267} show that small carbenium ions, e.g., protonated ethene, do not occur as stable species within zeolite channels, but are present in transition states

leading to the formation of alkoxide species. The conclusion about the stability of larger species, e.g., tert-butyl carbenium cations, depends on the choice of the computational model. Early quantum chemistry calculations employing small cluster models came to the conclusion that tert-butyl carbenium cations only occurred in the transition state,^{279,280} however, recent periodic DFT calculations using the full zeolite unit cell have shown that tert-butyl carbenium cations are stable intermediates.²³⁸ It has also been shown theoretically that cyclic carbenium ions, such as those formed during xylene disproportionation, are stable intermediates.^{281,282} Experimental evidence for persistent cyclic carbenium ions in zeolites has been reported, as well.^{272,283} Finally, it is noted that in the study of Namuangruk et al. on ethylbenzene formation over H-FAU, protonated ethylbenzene was not reported as stable intermediate.²²⁴ This might be a consequence of the computational method used (only 12 out of 84 T-atoms were treated quantum mechanically) or, alternatively, of the larger pore size of FAU compared to ZSM-5 which would lead to a lower degree of cation stabilization by the zeolite walls.

8.4 Conclusion

Three reaction mechanisms for the ethylation of benzene on H-ZSM-5 have been investigated using density functional theory. Two of the mechanisms are one-step schemes, which differ only by the position of the acidic proton before and after the reaction. The third mechanism is a two-step scheme. All mechanisms have been studied on clusters of 5, 17, and 33 T atoms. Both adsorption energies as well as activation energies depend on the cluster size. The reaction barriers on the T33 cluster are significantly smaller than those calculated for smaller clusters. The MP2-corrected apparent activation energies for this cluster are in good agreement with experimental data. The activation energies for the one-step schemes are slightly higher or similar to the activation energy for the alkylation step in the two step scheme. The activation energy of the ethoxide formation is smaller than the activation energy of the one-step alkylation independent of the computational method. Since the formation of surface ethoxide species is exothermic it lowers the apparent activation energy of the two-step mechanism. In practice both the one-step and the two-step schemes are likely to contribute to the overall activity because of the significantly higher loading of benzene in the zeolite pores. In contrast to the reaction mechanisms found using small clusters, the mechanism determined for the T33 cluster involves a carbenium cation intermediate.

9

Analysis of diffusion limitation in the alkylation of benzene over H-ZSM-5 by combining quantum chemical calculations, molecular simulations, and a continuum approach

A continuum model based on the Maxwell-Stefan (M-S) equations in combination with the ideal adsorbed solution theory (IAST) has been used to analyze the influence of adsorption thermodynamics and intra-particle diffusional transport on the overall kinetics of benzene alkylation with ethene over H-ZSM-5. The parameters appearing in the M-S equations were obtained from molecular dynamics simulations, and pure component adsorption isotherms were obtained from configurational-bias Monte Carlo simulations in the grand canonical ensemble. Rate coefficients for the elementary steps of the alkylation were taken from quantum chemical calculations. The intrinsic kinetics of two different reaction schemes were analysed. The simulations show that all apparent rate parameters of the alkylation are strongly dependent of the reaction conditions. By taking diffusional limitation into account, experimentally determined reaction rates and the orders in the partial pressures of reactants can be reproduced. The results of this study show that empirical power law rate expressions become inappropriate when used to correlate kinetic data over a broad range of conditions. In addition, it is demonstrated that the usual approaches to determine effectiveness factors for reactions in porous media, which assume a constant effective diffusivity, may lead to substantial deviations from rigorous simulations, whereas the simulation model developed here can be used to predict the effectiveness factor for zeolite particles for any set of reaction conditions.

9.1 Introduction

Gas phase alkylation of benzene using MFI zeolites has been practised industrially for over two decades.^{210,211,284} Renewed interest in this process has arisen recently due to two developments. The first is the discovery of new synthesis routes for producing zeolites with controlled mesoporosity, which exhibit higher catalytic activity, and sometimes improved selectivity, for reactions such as the alkylation of benzene with ethene.^{276,285} The second motivating factor is the possibility of replacing ethene with ethane as the alkylating agent by employing a bifunctional catalyst containing both dehydrogenation and acid sites, for example, PtH-MFI.^{286,287} Since intracrystalline diffusion can affect both modes of alkylation, there is considerable interest in developing theoretical methods that could account for the effects of zeolite architecture and particle size, as well as the effects of reactant and product partial pressures and reaction temperature.

Two approaches can be envisioned for describing the diffusion and reaction in zeolites. The first is kinetic Monte Carlo (kMC), a simulation methodology that includes the zeolite pore topology by coarse graining the zeolite lattice in terms of discrete adsorption/reaction sites. In this approach reactant and product molecules are assumed to move between lattice sites by hopping. Transformation of reactants to products can occur at those lattice sites that contain catalytically active centers.^{288–293} To make kMC simulations predictive, a large amount of microscopic information has to be determined beforehand in order to generate the list of all single-event probabilities.

The second approach is to use a continuum model with parameter inputs from molecular dynamics for the combined multicomponent diffusion-reaction problem. This approach eliminates the need to provide a list of all single-event probabilities but this occurs at the risk of over-simplifying the underlying physical processes. Special care has to be taken in order to properly describe multicomponent diffusion combined with reaction kinetics, both of which are strongly dependent on the zeolite pore topology and on the molecular loadings within the catalyst. The Maxwell-Stefan (M-S) equations^{294,295} have been demonstrated to describe correctly multicomponent diffusion in all-silica zeolites using as data input (a) the single-component diffusivities at zero loading and (b) information on the pure component adsorption isotherms.^{294,296–298} Specific guest molecule-zeolite host interactions as well as the lattice topology are included implicitly in the M-S diffusivities, and these parameters can be determined directly from pure component MD simulations for the zeolite of interest. It should be noted that for the M-S equations to be applicable to zeolites with Al/Si >0, the effect of lattice het-

erogeneities must be small.^{299,300} Low Al/Si ratios (<0.015) are used for the alkylation of benzene in H-ZSM-5,²⁷⁶ and consequently, the M-S equations are expected to give a reasonable description of the multicomponent diffusion behaviour for the constituent species.

The influence of intra-particle diffusional mass transfer on the overall rate of reaction occurring in a catalyst particle is usually characterized by the Thiele modulus, introduced in the late 1930s,³⁰¹ and the effectiveness factor derived from it. It is noted, however, that the first solution to the basic mathematical problem underlying the continuum description of the reaction-diffusion problem was presented by Jüttner in 1909.³⁰² In most analyses of such diffusion-reaction problems the species fluxes are described by Fick's law and the rate of reaction by Langmuir-Hinshelwood or power-law kinetics. Krishna and coworkers³⁰³ have recently demonstrated that for reactions occurring in zeolites Fick's law is only valid for low loadings of weakly confined guest molecules and vanishing correlation effects. When these limiting conditions are not met the correct description of diffusional flux can only be achieved using the M-S equations. Krishna and coworkers^{304,305} have also shown that the widely employed multicomponent Langmuir (MCL) approach used to calculate the fractional occupancies of the individual species fails for mixtures containing molecules with different saturation capacities. However, an accurate description of multicomponent adsorption can be obtained using a more sophisticated theory such as the ideal adsorbed solution theory (IAST).³⁰⁶ Applications of the above concepts to diffusion-reaction problems in zeolites have been reported in refs 303,304 and 307. For the above-mentioned reasons it is unlikely that the effectiveness factors determined on the basis of the usual approaches used to describe diffusion and reaction in porous media will lead to an accurate description of what actually occurs.

In the present chapter we show that the M-S equations in combination with IAST can be used to describe the alkylation of benzene with ethene catalyzed by H-ZSM-5. To make these simulations predictive, as many of the parameters as possible were determined from molecular simulations and quantum chemical calculations. A continuum model was used to describe the intrinsic rate of reaction as function of the local concentration of reactants at the active sites. The results of this work demonstrate that the apparent rate coefficient and the orders in the partial pressures of reactants are not constant but, in fact, are complex functions of the zeolite architecture and particle size and the manner by which the adsorption and diffusion of reacting species influence each other. It is also shown that the simulation model adopted can be used to predict the effectiveness factor for zeolite particles as a function

of their size for any set of reaction conditions.

This chapter is organized as follows. Section 9.2 presents the continuum approach used to describe alkylation of benzene with ethene in H-ZSM-5. The methods used to determine the parameters involved in describing adsorption, diffusion, and reactions of all species are presented in section 9.3. Predictions determined from the continuum model are compared in section 9.4 to predictions from an empirical rate law based on experimental data. The conclusions of this work are presented in section 9.5. Details of the simulation methods used to obtain information on the adsorption and diffusion of all species are given in the supporting information accompanying this chapter.

9.2 Continuum approach for diffusion and reaction

The change of loading with time of component i in a spherical zeolite crystal due to reaction and diffusion is described by the partial differential equation:³⁰⁸

$$\frac{\partial q_i}{\partial t} = -\frac{1}{\rho} \frac{1}{\xi^2} \frac{\partial}{\partial \xi} (\xi^2 N_i) + \frac{1}{\rho} \nu_i r; \quad i = 1, 2, \dots, n. \quad (9.1)$$

In this equation, q_i is the loading of species i , ρ is the zeolite density, ξ is the diffusion path, N_i is the molar flux of species i , ν_i is the stoichiometric coefficient, and r is the rate of reaction. We can rewrite equation 9.1 in terms of fractional occupancies, $\theta_i = q_i/q_{i,\text{sat}}$, which leads to

$$\frac{\partial \theta_i}{\partial t} = -\frac{1}{\rho q_{i,\text{sat}}} \frac{1}{\xi^2} \frac{\partial}{\partial \xi} (\xi^2 N_i) + \frac{1}{\rho q_{i,\text{sat}}} \nu_i r; \quad i = 1, 2, \dots, n. \quad (9.2)$$

The flux of species i , N_i , is calculated using the M-S theory of diffusion. For n -component diffusion, the M-S equations can be written as³⁰⁹

$$-\rho \frac{\theta_i}{RT} \nabla \mu_i = \sum_{\substack{j=1 \\ j \neq i}}^n \frac{q_j N_i - q_i N_j}{q_{i,\text{sat}} q_{j,\text{sat}} \mathcal{D}_{ij}} + \frac{N_i}{q_{i,\text{sat}} \mathcal{D}_i}; \quad i = 1, 2, \dots, n. \quad (9.3)$$

In the latter equation, μ_i is the molar chemical potential of species i , R is the gas constant, T is the absolute temperature, \mathcal{D}_i is the M-S diffusivity of component i , and \mathcal{D}_{ij} is the exchange coefficient between species i and j . The exchange coefficient quantifies correlation effects. The M-S diffusivity \mathcal{D}_i is sometimes referred to as the corrected diffusivity. The term on the left hand

side of equation 9.3 can be expressed in terms of a matrix of thermodynamic correction factors, Γ_{ij} , and the gradient in q_i ,

$$\frac{q_i}{RT} \nabla \mu_i = \sum_{j=1}^n \Gamma_{ij} \nabla q_j; \quad \Gamma_{ij} \equiv \frac{q_i}{q_j} \frac{\partial \ln f_i}{\partial \ln q_j} = \frac{q_i}{f_i} \frac{\partial f_i}{\partial q_j}; \quad i, j = 1, 2, \dots, n, \quad (9.4)$$

where f_i denotes the partial fugacity of species i . Application of equation 9.4 allows equation 9.3 to be rewritten in matrix form as

$$(\mathbf{N}) = -\rho[\Delta][\Gamma]\nabla(\mathbf{q}). \quad (9.5)$$

The elements of the matrix $[\Delta]$ can be related to the M-S diffusivities \mathcal{D}_i and \mathcal{D}_{ij} by

$$[\Delta] = [\mathbf{B}]^{-1}, \quad (9.6)$$

where the elements of $[\mathbf{B}]$ are

$$B_{ii} = \frac{1}{\mathcal{D}_i} + \sum_{\substack{j=1 \\ j \neq i}}^n \frac{\theta_j}{\mathcal{D}_{ij}}; \quad B_{ij} = -\frac{q_{i,\text{sat}}}{q_{j,\text{sat}}} \frac{\theta_i}{\mathcal{D}_{ij}}; \quad i, j = 1, 2, \dots, n. \quad (9.7)$$

From equation 9.3, it is possible to predict the flux of species i , N_i , in a binary (or multicomponent) mixture from pure component diffusion data by making the following two assumptions. First, we assume that \mathcal{D}_i in the mixture is the same as that for the pure component i estimated at the same occupancy as that of the *total* mixture defined by

$$\theta = \sum_{i=1}^n \frac{q_i}{q_{i,\text{sat}}} = \sum_{i=1}^n \theta_i. \quad (9.8)$$

This procedure has been explained in refs 294 and 310. Second, the elements \mathcal{D}_{ij} are estimated using the interpolation formula presented in refs 298 and 311:

$$q_{j,\text{sat}} \mathcal{D}_{ij} = [q_{j,\text{sat}} \mathcal{D}_{ii}]^{q_i/(q_i+q_j)} [q_{i,\text{sat}} \mathcal{D}_{jj}]^{q_j/(q_i+q_j)} = q_{i,\text{sat}} \mathcal{D}_{ji}. \quad (9.9)$$

The self-exchange coefficients \mathcal{D}_{ii} and \mathcal{D}_{jj} quantify the correlation effects of pure components i and j ; these terms can be determined from the self-diffusivity ($D_{i,\text{self}}$) and the M-S diffusivity for each pure component (\mathcal{D}_i)³⁰⁹

$$\mathcal{D}_{ii} = \frac{\theta_i}{\frac{1}{D_{i,\text{self}}} - \frac{1}{\mathcal{D}_i}} \text{ (pure component)}. \quad (9.10)$$

The self-exchange coefficients can be related to the M-S diffusivity by an empirical correlation³⁰⁹

$$\frac{\mathcal{D}_{ii}}{\mathcal{D}_i} = a_1 \exp(-a_2 \theta_i) + a_3 \exp(-a_4 \theta_i). \quad (9.11)$$

The constants a_i are obtained from MD simulations of the self- and M-S diffusivities for each of the components in the mixture. It should be emphasized that equation 9.11 is defined for the pure component i . In the case of mixtures, the fractional occupancy θ_i has to be replaced by the total occupancy of the mixture, θ (equation 9.8). M-S diffusivities are almost invariably loading dependent. For molecules whose adsorption isotherms exhibit inflection behavior, that is, can be described by a multisite Langmuir model

$$q = \frac{q_{\text{sat,A}} b_A f}{1 + b_A f} + \frac{q_{\text{sat,B}} b_B f}{1 + b_B f} + \dots, \quad (9.12)$$

where $q_{\text{sat,X}}$ denotes the saturation capacity on site X, b_X is the affinity constant, and f is the gas phase fugacity, the following expression for the loading dependence of \mathcal{D} has been suggested³¹²

$$\mathcal{D} = \mathcal{D}_A(0)x_A(1 - q_A/q_{\text{sat,A}}) + \mathcal{D}_B(0)x_B(1 - q_B/q_{\text{sat,B}}) + \dots, \quad (9.13)$$

where

$$x_A = \frac{q_A}{\sum_i q_i}, \quad x_B = \frac{q_B}{\sum_i q_i}, \quad (9.14)$$

are the fractions of the total loading present in sites A and B. For benzene and ethylbenzene, there is both theoretical and experimental evidence that these molecules are exclusively located inside the channel intersections below loadings of four molecules per unit cell.^{216–220,313} It is therefore reasonable to assume a linear decrease of \mathcal{D} with occupancy in this loading regime, that is, $x_B = 0$ in equation 9.13. This behavior has been proven to occur for 2-methylhexane in MFI by kMC simulations³¹⁴ and for *iso*-butane by both kMC and experimental studies.³¹⁵

The loading dependency of the ethene diffusivity can also be approximated by the simple relation

$$\mathcal{D} = \mathcal{D}(0)(1 - \theta). \quad (9.15)$$

In the present study we used the model of Reed and Ehrlich,³¹⁶ giving an improved description:

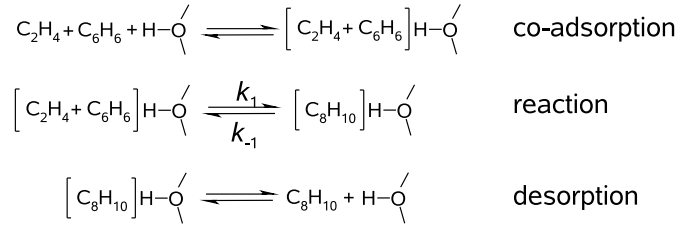
$$\mathcal{D} = \mathcal{D}(0) \frac{(1 + \varepsilon)^{z-1}}{(1 + \varepsilon/f)^z}, \quad (9.16)$$

with

$$\varepsilon = \frac{(\beta - 1 + 2\theta)f}{2(1 - \theta)}; \quad \beta = \sqrt{1 - 4\theta(1 - \theta)(1 - 1/f)}; \quad f = a \exp(b\theta). \quad (9.17)$$

The parameter z is the coordination number representing the maximum number of nearest neighbors. The factor f accounts for interaction between neighboring molecules. The parameters a and b are obtained by fitting them to MD data (see Krishna et al.³⁰⁹ for more detailed discussions and derivations).

We have shown in chapter 8 that the mechanism of benzene alkylation can be represented by a one-step mechanism involving the following elementary processes:



The rate equation corresponding to this mechanism is

$$\frac{r}{\rho} = \tilde{r} = k_1 q_{\text{E+B,H}^+} - k_{-1} q_{\text{EB,H}^+}, \quad (9.18)$$

where k_1 and k_{-1} are the rate coefficients for the forward and reverse reaction of ethene and benzene to form ethylbenzene, respectively; $q_{\text{E+B,H}^+}$ is the amount of coadsorbed “ethene + benzene” at the active sites and $q_{\text{EB,H}^+}$ is the amount of adsorbed ethylbenzene at the active sites. The application of equation 9.18 within the continuum approach requires analytical expressions to calculate $q_{\text{E+B,H}^+}$ and $q_{\text{EB,H}^+}$ from the species loadings q_{E} , q_{B} , and q_{EB} . For the derivation of such expressions it is assumed that benzene and ethylbenzene are located exclusively inside the channel intersections below loadings of four molecules per unit cell (see above). Furthermore, it is assumed that the acid sites are also located exclusively inside the intersections between the straight and the sinusoidal channel, or, more precisely, on the O atom next to the T12 site at the aperture of the sinusoidal channel (see chapter 8 for details). In fact, the location of the ethene molecule in the coadsorbed state can be characterized as in between the intersection and the sinusoidal channel. The third assumption is the equal accessibility of all adsorption sites for ethene. The maximum adsorption capacity of $q_{\text{E,sat}} = 22$

molecules per unit cell was obtained from MC simulations. This number is set equal to the number of adsorption sites available for ethene. These 22 sites are distributed over four intersections, four sinusoidal channels, and four straight channels out of which the the intersections have the largest free volume. Monte Carlo simulations carried out with all intersections artificially blocked with benzene molecules give a maximum ethene adsorption capacity of about nine molecules per unit cell, that is, each adsorbed benzene reduces the number of sites available for ethene adsorption by 3.25 molecules per unit cell. Likewise, MC simulations with all intersections artificially blocked by ethylbenzene have shown that each adsorbed ethylbenzene reduces the number of sites available for ethene by around 3.5 molecules per unit cell. Finally, we assume that if benzene occupies an intersection, the probability of ethene adsorption next to this benzene (defined as coadsorption) is the same as that of ethene adsorption at any other free site within the unit cell. For the number of adsorption sites per unit cell accessible for ethene in a ternary mixture of ethene, benzene, and ethylbenzene, $q_{E,tot}$, we can then write

$$q_{E,tot} = 22 - 3.25q_B - 3.5q_{EB}, \quad (9.19)$$

where q_B is the number of benzene molecules per unit cell and q_{EB} is the number of ethylbenzene molecules per unit cell. Next, we need to know, how many of the $q_{E,tot}$ sites are potentially available for coadsorption of benzene and ethene. This number is dictated by the number of benzene molecules present, such that the fraction of ethene coadsorbed with benzene is $q_B/q_{E,tot}$ and the concentration of coadsorbed “ethene + benzene”, q_{E+B} , can be obtained from

$$q_{E+B} = \frac{q_B}{22 - 3.25q_B - 3.5q_{EB}} q_E. \quad (9.20)$$

To complete the model for the forward rate we need to take into account that not every intersection contains a proton. Therefore we introduce γ as the number of protons per unit cell which are located in an intersection and define

$$\lambda = \frac{\gamma}{4} \quad (9.21)$$

as the active site density (average number of acid sites per intersection). In addition, we need to note that each ethylbenzene molecule present in the unit cell occupies an intersection that, if it were active, cannot be used for the forward reaction. Therefore, the active site density has to be lowered by the factor

$$\frac{q_B}{q_B + q_{EB}}. \quad (9.22)$$

In summary, the concentration of coadsorbed “ethene + benzene” at an acid site containing intersection becomes

$$q_{E+B,H^+} = \frac{q_B}{22 - 3.25q_B - 3.5q_{EB}} \cdot q_E \cdot \frac{q_B}{q_B + q_{EB}} \cdot \lambda. \quad (9.23)$$

A similar derivation can be used for the amount of adsorbed ethylbenzene at an acid site containing intersection. For q_{EB,H^+} we can write

$$q_{EB,H^+} = q_{EB} \cdot \frac{q_{EB}}{q_B + q_{EB}} \cdot \lambda. \quad (9.24)$$

The validity of equation 9.20 was tested against MC simulations for different ethene-benzene-ethylbenzene mixtures (see figure 9.1). After every few cycles the configuration inside the pore was stored. These configurations were then analyzed to determine the numbers of coadsorbed “ethene + benzene” molecules. A configuration was interpreted as coadsorbed if an ethene molecule was located next to an intersection occupied by benzene such that the distances between the carbon atoms of ethene and the center of the intersection was smaller than the specified sample radius. This method of counting is based on the active site model used in our DFT study³¹⁷ where the acid site is assumed to be located on the O atom next to the T12 site

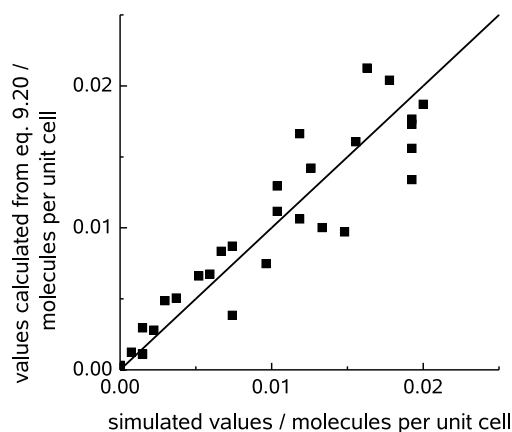
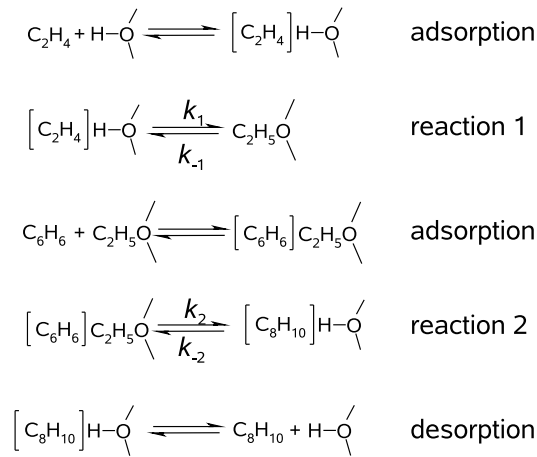


Figure 9.1: Amount of coadsorbed ethene plus benzene in the channel intersections of MFI at 653 K and various compositions of the corresponding ternary gas phase mixture as predicted by equation 9.20 and Monte Carlo simulations using a sampling radius of 4.8 Å. The total pressure was varied between 1×10^5 and 11×10^5 Pa.

at the aperture of the sinusoidal channel (see above). The sample radius was determined by the condition that for a unit cell in which all intersections are occupied by benzene while the remaining pore space is completely filled with ethene, the number of coadsorbed configurations should be four molecules per unit cell. This condition was fulfilled for a sampling radius of 4.8 Å. As can be seen in figure 9.1, the concentration of coadsorbed “ethene + benzene” obtained from MC simulations agrees reasonably well with the concentration estimated by means of equation 9.20. It can therefore be concluded that equation 9.20 is sufficiently accurate to be used for an estimation of the coadsorbed amount of “ethene + benzene” in the continuum model.

We have also shown in chapter 8 that the alkylation of benzene by ethene can be described by a two-step mechanism involving the following elementary processes:



Expressions analogous to equations 9.23 and 9.24 can be derived for the two-step mechanism of benzene alkylation with ethene (see section B.4 of the supporting information). These are given by

$$q_{\text{E,H}^+} = \frac{13 - 3.25(q_{\text{B}} + q_{\text{EB}} + q_{\text{eth}})}{22 - 3.25q_{\text{B}} - 3.5q_{\text{EB}} - q_{\text{eth}}} \cdot q_{\text{E}} \cdot \lambda, \quad (9.25)$$

and

$$q_{\text{eth+B}} = \frac{q_{\text{B}}}{4 - q_{\text{EB}}} \cdot q_{\text{eth}}, \quad (9.26)$$

for the amount of ethene adsorbed at the Brønsted acid sites, $q_{\text{E,H}^+}$, and the amount of benzene adsorbed next to an ethoxide, $q_{\text{eth+B}}$.

The system of partial differential equations (equation 9.2) was discretized with respect to the spatial coordinate using central differences (method

of lines), and the resulting system of ordinary differential equations was integrated using a fourth order Runge–Kutta scheme until the solution was stationary (see section B.6 of the supporting information for details). The profile of species concentration, $q(\xi)$, was taken to be symmetric at the center of the crystal, whereas the concentration of each species at the crystal surface was fixed to the value determined by adsorption equilibrium. Determination of the thermodynamic factors (equation 9.4) requires the calculation of the derivative of the partial fugacities with respect to the species concentrations. Details of these computations are given in ref. 318. Species fugacities inside the zeolite were calculated as partial fugacities of a hypothetical gas phase corresponding to the actual loading within the zeolite and were obtained by means of the IAST in its inverse formulation.^{306,319}

9.3 Parameterization

Pure component adsorption isotherms were obtained by MC simulation using the method described in section B.1 of the supporting information. These isotherms were fitted to a three-site Langmuir model (see section B.2 of the supporting information). Mixture adsorption isotherms were then calculated from the pure component adsorption isotherms by means of the IAST.³⁰⁶ As shown in section B.2 of the supporting information, IAST provides an accurate description of the adsorption isotherms for mixtures in the pressure regime relevant for the alkylation of benzene with ethene. The rate coefficients for the alkylation of benzene with ethene and the reverse reaction were determined in two steps.³¹⁷ The intrinsic activation energies of these processes were calculated by applying single-point MP2-corrections to DFT-converged stationary states on a large cluster model. This approach was justified using smaller clusters by comparing intrinsic activation energies obtained from MP2-optimized structures to those obtained from single point MP2-calculations on DFT-converged structures. The energy difference was <0.2 kcal/mol. Preexponential factors were determined using transition state theory (TST). For a detailed discussion of the level of theory used for obtaining the rate parameters as well as of the size of the model system used the reader is referred to the theory section of chapter 8. The rate coefficients obtained by this means are presented in table 9.1. The rate coefficients for the one-step scheme are 2.5 orders of magnitude smaller than those for the two-step scheme. While this could lead to the conclusion that the one-step scheme is irrelevant, it should be kept in mind that the rate coefficient for ethoxide formation (the first step in the two-step scheme) was calculated assuming that ethene enters an empty intersection. An excess of benzene

Table 9.1: Intrinsic rate coefficients for the one-step and two-step mechanisms.

reaction scheme	constant	T (K)					
		calcd values (chapter 8)			readjusted (effective) values		
		603	653	703	603	653	703
one-step	k_1, s^{-1}	8.17×10^{-1}	4.97×10^0	2.33×10^1	1.14×10^2	6.96×10^2	3.27×10^3
	k_{-1}, s^{-1}	3.80×10^{-5}	9.75×10^{-4}	1.58×10^{-2}	5.32×10^{-3}	1.37×10^{-1}	2.21×10^0
two-step	k_1, s^{-1}	2.58×10^2	1.14×10^3	4.11×10^3			
	k_{-1}, s^{-1}	1.20×10^1	1.12×10^2	7.65×10^2			
	k_2, s^{-1}	3.19×10^2	1.84×10^3	8.26×10^3			
	k_{-2}, s^{-1}	7.24×10^{-1}	6.98×10^0	4.87×10^1			

is used in industrial practice. This lowers the probability that ethene finds an unoccupied intersection, since benzene adsorbs much more strongly than ethene in the channel intersections. It is therefore likely that both mechanisms take place simultaneously. Thus, the extent to which each mechanism contributes to the overall activity is hard to establish. As a consequence, the overall kinetics of benzene alkylation were examined for both mechanisms and compared with experimental data of Christensen et al.²⁷⁶

The intrinsic activation barrier for the one-step alkylation of benzene with ethene determined from the QM calculations presented in chapter 8 is $E^\ddagger = 120.5 \text{ kJ mol}^{-1}$ and the intrinsic preexponential factor at 653 K is $A = 2.5 \times 10^{10} \text{ s}^{-1}$. For the two-step scheme the intrinsic activation barriers determined from QM calculations are $E^\ddagger = 99.2 \text{ kJ mol}^{-1}$ and $E^\ddagger = 110.5 \text{ kJ mol}^{-1}$, and the intrinsic preexponential factors at 653 K are $A_1 = 1.1 \times 10^{11} \text{ s}^{-1}$ and $A_2 = 1.4 \times 10^{12} \text{ s}^{-1}$, respectively. The values from theory cannot be compared with the apparent activation energy and apparent preexponential factor determined from experimental data, since the values of the apparent activation energy and preexponential factor depend on reaction conditions. To proceed, the rate of reaction per unit mass of catalyst as function of temperature and total pressure was simulated, maintaining the same benzene to ethene ratio in the gas phase ($B/E = 5$) as was used in the experiments performed by Christensen et al.²⁷⁶ These authors investigated the alkylation of benzene with ethene over mesoporous H-ZSM-5 synthesised by the carbon templating method.³²⁰ They reported an average distance between the mesopores of $0.04 \mu\text{m}$ leading to the conclusion that the measured reaction rates were not influenced by intraparticle diffusion.^{276,285} The turnover frequency and the apparent activation energy were calculated for a pressure of $2.5 \times 10^5 \text{ Pa}$ using the theoretically determined rate coefficients for the one-step scheme. These simulations underestimated the experimentally observed turnover frequency by a factor of around 400 and the apparent activation energy by 15 kJ mol^{-1} . By contrast, the simulated values using the theoretically determined rate coefficients for the two-step scheme overestimated the experimentally observed turnover frequency at $2.5 \times 10^5 \text{ Pa}$ by a factor of 4 and the apparent activation energy by 5 kJ mol^{-1} . As already noted above, the extent to which each mechanism contributes to the overall activity is hard to establish. To proceed we determined effective intrinsic rate coefficients by adjusting the theoretically determined ones so that the experimental data were reproduced reasonably well. Due to the smaller number of parameters required, these effective rate coefficients were based on the one-step mechanism. Furthermore, the decision was made to match not only the experimental data of Christensen et al.²⁷⁶ but also those of Lu et al.³²¹ (see

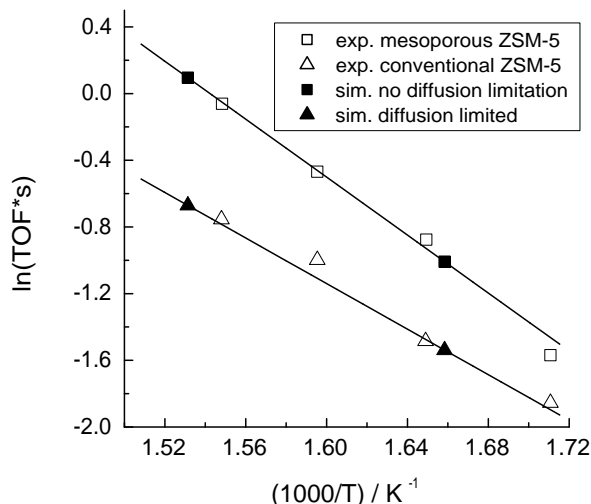


Figure 9.2: Experimental²⁷⁶ and simulated Arrhenius plots for the ethylation of benzene. The experimental data are reported for both mesoporous H-ZSM-5 and a sample of H-ZSM-5 free of mesopores at a total pressure of 2.5×10^5 Pa and a benzene to ethene ratio of 5.1. The conditions for the simulation were $p = 5 \times 10^5$ Pa, $y_B = 0.8338$, $y_E = 0.1660$, $y_{EB} = 0.0002$. For simulations of the turnover frequency in the mesoporous sample of H-ZSM-5 the exterior surface loadings were used. For the simulation of the turnover frequency in the nonmesoporous sample of H-ZSM-5, the zero-loading MD diffusivities were scaled down by 3.4 orders of magnitude (see table 9.2). The intrinsic rate coefficients used are listed on the right-hand side of table 9.1.

section 9.4.2). Therefore, the rate coefficients presented in the right-hand side of table 9.1 represent a compromise between the desire to reproduce the Arrhenius plot of Christensen et al.²⁷⁶ exactly and the desire to match kinetic data reported by Lu et al.³²¹ This objective could be achieved by multiplying the theoretically determined preexponential factor by a factor of 140, while leaving the theoretically determined intrinsic activation energy unchanged. As seen in figure 9.2, good agreement was obtained between the simulated Arrhenius plot and the experimental Arrhenius plot of Christensen et al.²⁷⁶, assuming a simulation pressure of 5.0×10^5 Pa (see upper curve of figure 9.2). It should be noted that agreement with the experimental data could also be achieved by carrying out the simulation at 2.5×10^5 Pa, but this required adjustment of the activation energy in addition to the preexponential factor.

Such adjustment, however, would lead to simulated rates which deviate from the data of Lu et al.³²¹ In particular, the apparent activation energy determined from simulation would now overestimate that determined experimentally by a significant amount (see section 9.4.2). Clearly, then a more accurate evaluation of the theoretically determined rate coefficients, requires a larger source of experimental data taken in the absence of intraparticle diffusional limitations over a wide range of temperatures and reactant partial pressure. Nevertheless, the effective rate coefficients obtained by the methods discussed can be used to analyze the effects of intraparticle diffusional mass transport on the alkylation of benzene with ethene occurring in H-ZSM-5.

Maxwell-Stefan diffusivities were extracted from extensive MD simulation campaigns as outlined in section B.3 of the supporting information. The extracted zero-loading M-S diffusivities, $\mathcal{D}_i(0)$, for ethene in the temperature range 603 K – 703 K are of the order $10^{-8} \text{ m}^2 \text{ s}^{-1}$. Experimental diffusivities of ethene at these temperatures are not available in the literature. However, at 300 K the simulated zero-loading M-S diffusivity is $0.9 \times 10^{-8} \text{ m}^2 \text{ s}^{-1}$ and thus in reasonable agreement with reported experimental values for ethane and ethene in MFI.^{322–325} It should be noted, that some authors report considerably smaller values^{326,327} which are of the order of $10^{-11} \text{ m}^2 \text{ s}^{-1}$ at room temperature. However, these values were most likely influenced by external transport resistances.³²⁶

For benzene and ethylbenzene, the extracted M-S diffusivities in the temperature range 603 K – 703 K are of the order of $10^{-10} \text{ m}^2 \text{ s}^{-1}$, which is significantly higher than most of the values reported experimentally. Thus, it becomes necessary to review what is known from both experiments and theory about the diffusivity of benzene and ethylbenzene.

The diffusion of benzene in MFI has been the subject of numerous experimental studies over the last 25 years.^{265,328–353} At room temperature most of the data lie in the range of $1 \times 10^{-15} \text{ m}^2 \text{ s}^{-1}$ (ref 328) to $7 \times 10^{-14} \text{ m}^2 \text{ s}^{-1}$ (ref 330). Diffusion coefficients at higher temperatures have been estimated by extrapolation, and are most often above of $10^{-11} \text{ m}^2 \text{ s}^{-1}$ at 600 K.³³⁷ However, direct measurements have been reported to yield smaller diffusivities.^{341,351} For example Masuda et al.³⁴¹ report an intracrystalline diffusivity for benzene of $5 \times 10^{-14} \text{ m}^2 \text{ s}^{-1}$ at 650 K. At this high temperature no difference was found between diffusion coefficients in silicalite and H-ZSM-5. At lower temperature, diffusivities in H-ZSM-5 have measured to be lower by 50% than those for silicalite. Measurements of the diffusion coefficient for ethylbenzene in MFI show a variation in the order of magnitude similar to that reported for benzene.^{265,328,334,339,345,354}

A number of theoretical efforts have been made to estimate the diffusion

coefficient for benzene. Conventional MD simulations are hampered by the long simulation times required for a reliable estimate of the diffusion coefficient. Rungsirisakun et al.³⁵⁵ have reported a value of $D_{\text{self}}(300\text{ K}) \approx 10^{-10}\text{ m}^2\text{ s}^{-1}$; however, the simulation time used by these authors (100 ps) was probably be too small to give a reliable estimate for the self-diffusion coefficient. Other authors have estimated the self-diffusion coefficient to be on the order of $10^{-15}\text{ m}^2\text{ s}^{-1}$ to $10^{-12}\text{ m}^2\text{ s}^{-1}$ based on MD simulations.^{356,357} Constrained reaction coordinate dynamics and dynamic MC simulations have also been used to estimate the diffusivity. Values of $D_{\text{self}}(300\text{ K}) \approx 10^{-14}\text{ m}^2\text{ s}^{-1}$ have been reported using these methods.^{358,359} Takaba et al.³⁶⁰ obtained a value of $D_{\text{self}}(300\text{ K}) \approx 10^{-15}\text{ m}^2\text{ s}^{-1}$ by means of dynamic MC simulations with rate constants estimated from semi-empirical quantum chemical calculations, and Snurr et al.³⁶¹ obtained values of $D_{\text{self}}(300\text{ K}) \approx 10^{-16}\text{ m}^2\text{ s}^{-1}$ from transition state theory calculations.

It is evident from the preceding discussion that reliable values of the zero-loading M-S diffusivities for benzene and ethylbenzene are not known and that the values estimated from MD mixture simulations in the present study are most likely too high. To deal with this problem, we have proceeded in the following way. Christensen et al.²⁷⁶ have reported an Arrhenius plot for benzene alkylation with ethene by H-ZSM-5 in which the zeolite crystallites had an average size about $2\ \mu\text{m}$. In this case, a significantly lower activity was observed relative to that seen for mesoporous H-ZSM-5, which the authors ascribed to diffusion limitation. We were able to match these data by simulation if the zero-loading M-S diffusivities for all species were reduced by 3.4 orders of magnitude (see lower curve in figure 9.2). For these simulations we used the same rate coefficients as in the absence of diffusion limitation (see above). The resulting diffusivities for ethene are then of the order $10^{-11}\text{ m}^2\text{ s}^{-1}$, while those for benzene and ethylbenzene are of the order $10^{-13}\text{ m}^2\text{ s}^{-1}$ (see table 9.2). Whereas the values obtained for benzene and ethylbenzene lie within the range of the experimental data discussed above, the scaled diffusivity for ethene is underestimated by one to two orders of magnitude. However, by scaling all diffusivities by the same factor the ratios between the zero-loading diffusivities as well as the coefficients describing loading dependency and self-exchange could be taken directly from the MD results summarized in tables B.2 and B.3 of the supporting information. Moreover, the overall activity of the crystallite is dominated by the diffusivities of benzene and ethylbenzene. The sensitivity of the simulated reaction rates with respect to the zero-loading diffusivity of ethene and the binary exchange parameters is discussed in section 9.4.2.

Table 9.2: Adjusted zero-loading M-S diffusivities for ethene, benzene, and ethylbenzene.

molecule	temperature [K]	$\bar{D}_i(0)$ [$10^{-13} \text{ m}^2 \text{ s}^{-1}$]
C ₂ H ₄	603	87.6
C ₂ H ₄	653	99.5
C ₂ H ₄	703	99.5
C ₆ H ₆	603	1.6
C ₆ H ₆	653	2.0
C ₆ H ₆	703	2.8
C ₈ H ₁₀	603	1.3
C ₈ H ₁₀	653	1.6
C ₈ H ₁₀	703	2.2

9.4 Results and discussion

9.4.1 Intrinsic kinetics

The intrinsic kinetics predicted by the model in the absence of diffusional mass transfer limitations can be established by examining plots of $q_{\text{E+B,H+}}$ (see equation 9.23) versus p_{E} and p_{B} . Figures 9.3 and 9.4 show such plots for 653 K and 703 K calculated on the assumption that $q_{\text{EB}} \approx 0$ and $\gamma = 4$. It is evident that at both temperatures the predicted dependence of the rate on the ethene partial pressure is essentially 1.0, whereas the dependence on the partial pressure of benzene is 0.4 at 653 K (figure 9.3(b)) and rises to 0.6 at 703 K (figure 9.4(b)). Additional calculations with $p_{\text{B}} = 10 \times 10^5 \text{ Pa}$ and $p_{\text{E}} = 3 \times 10^5 \text{ Pa}$ show that these numbers are essentially unaffected by the partial pressure of the co-adsorbed species (see figure B.6 in the supporting information). The change in the dependence on benzene partial pressure with temperature is a reflection of the effects of temperature on the adsorption of benzene from an ethene-benzene mixture. Figure 9.5 shows Arrhenius plots of the turnover frequency of benzene alkylation with ethene versus inverse temperature for a fixed ratio of benzene to ethene and different total pressures, ranging from $1 \times 10^5 \text{ Pa}$ to $5 \times 10^5 \text{ Pa}$. It is evident that both the apparent activation energy and the apparent preexponential factor are functions of the total pressure. The corresponding values are listed in table 9.3. The changes in these parameters are a direct consequence of the pressure and temperature dependency of the mixture adsorption equilibrium.

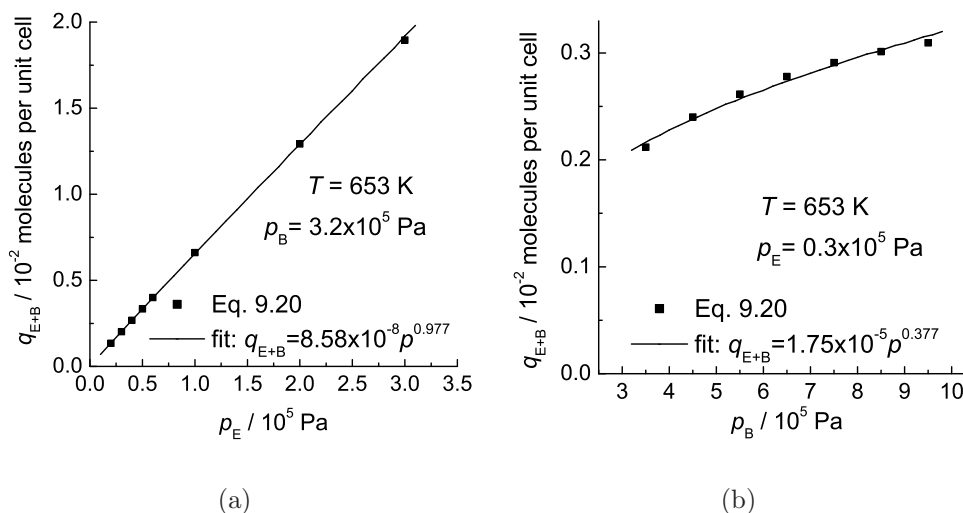


Figure 9.3: (a) Dependence of the amount of coadsorbed $C_2H_4 + C_6H_6$ on the ethene partial pressure at a fixed benzene partial pressure of 3.2×10^5 Pa and a fixed ethylbenzene partial pressure of 35 Pa at 653 K. (b) Dependence of the amount of coadsorbed $C_2H_4 + C_6H_6$ on the benzene partial pressure at a fixed ethene partial pressure of 0.3×10^5 Pa and a fixed ethylbenzene partial pressure of 35 Pa at 653 K.

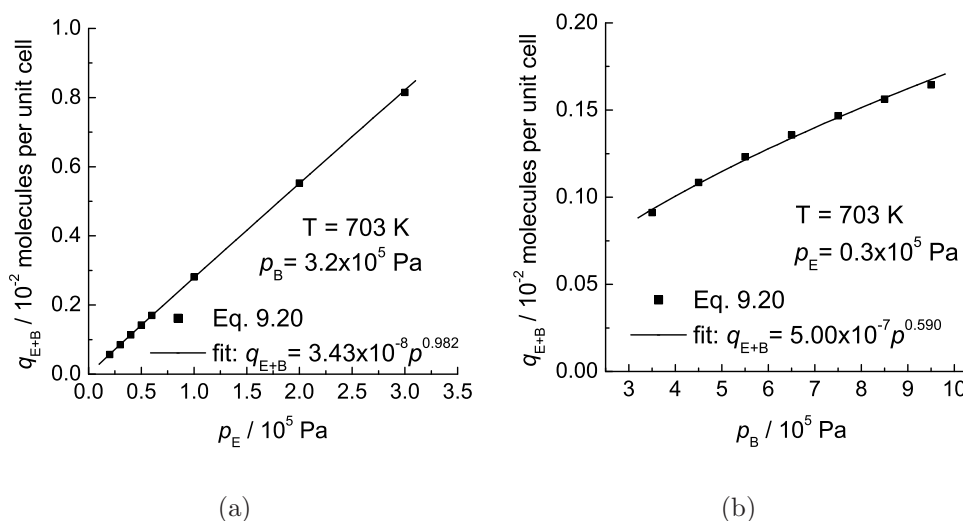


Figure 9.4: (a) Dependence of the amount of coadsorbed $C_2H_4 + C_6H_6$ on the ethene partial pressure at a fixed benzene partial pressure of 3.2×10^5 Pa and a fixed ethylbenzene partial pressure of 35 Pa at 703 K. (b) Dependence of the amount of coadsorbed $C_2H_4 + C_6H_6$ on the benzene partial pressure at a fixed ethene partial pressure of 0.3×10^5 Pa and a fixed ethylbenzene partial pressure of 35 Pa at 703 K.

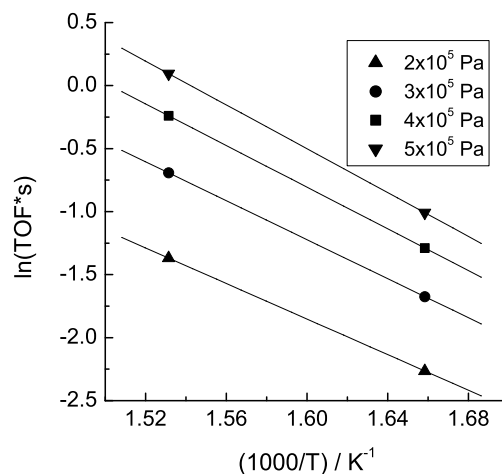


Figure 9.5: Arrhenius plots illustrating the pressure dependence of the apparent activation energy and the apparent preexponential factor.

The results presented in figures 9.3 to 9.5 clearly demonstrate that empirical power law kinetics cannot be used to describe the rate of benzene alkylation with ethene over H-ZSM-5 even in the absence of diffusional mass transfer. While such expressions may be useful for correlating results over a narrow range of reaction conditions, they become increasingly inappropriate as the range of reaction conditions broadens and all of the apparent rate parameters (e. g. preexponential factor, activation energy and reaction order) become functions of the reaction conditions.

Table 9.3: Apparent rate parameters obtained from simulations for different total pressures at constant $p_B/p_E = 5$.

pressure [10 ⁵ Pa]	E_{app} [kJ mol ⁻¹]	A_{app} [s ⁻¹]
2.0	58.7	1.25×10^4
3.0	64.3	6.95×10^4
4.0	68.7	2.46×10^5
5.0	72.3	6.63×10^5

9.4.2 Effects of diffusional mass transfer

Figure 9.6 illustrates the intraparticle concentration profiles of all species corresponding to the diffusion limited simulation at 653 K along with the turnover frequency as function of the radial coordinate. The figure shows that the benzene to ethene ratio on the exterior surface is higher by a factor of 6 than the ratio of partial pressures in the gas phase due to the differences in adsorption strength. It should be emphasized that the loading of ethylbenzene on the exterior surface is not zero but has a small value of 6.6×10^{-4} molecules per unit cell corresponding to a gas phase pressure of 35 Pa. In practise these conditions would be found at the reactor entrance. Due to diffusion limitations a strong increase of the product concentration towards the particle center takes place, accompanied by a strong decrease of the reactant concentrations.

The concentration profiles shown in figure 9.6(a) were calculated for two exchange scenarios. The full symbols represent the *finite* exchange scenario, that is, the binary exchange coefficients D_{ij} were obtained using the logarithmic interpolation formula (equation 9.9) along with equation 9.11 for the calculation of the self-exchange coefficients. The open symbols represent the *facile* exchange scenario, that is, the binary exchange coefficients approach infinity, resulting in a diagonal matrix $[\Delta]$. MD mixture simulations clearly show the existence of correlation effects for the present system (see section B.3 in the supporting information). It is of interest, however, to assess the significance of the exchange coefficients on the simulated concentration profiles. As seen in figure 9.6(a), correlation leads to higher reactant and lower product concentrations compared to uncorrelated diffusion. The largest effect of correlation has been calculated for the ethene concentration profile, due to the presence of the slow diffusing species benzene and ethylbenzene. While in the finite exchange scenario the ethene concentration in the particle center has decreased to 39% of its exterior surface value, this concentration drop is less distinct in the facile exchange scenario. In the latter case, the ethene concentration in the particle center has decreased to 61% of its exterior surface value. The effect on the benzene concentration is relatively small. In the finite exchange scenario the concentration at the particle center is 61% of its exterior surface concentration, while in the facile exchange scenario this value is 57%. Since ethene is the limiting species, the overall activity of the catalyst particle is higher by a factor of 1.1 in the facile exchange scenario. The effectiveness factors are 0.47 for the finite exchange scenario and 0.52 for the facile exchange scenario. Thus, we can conclude that while the inclusion of correlation effects in the M-S equations gives a physically correct description of multicomponent diffusion, the degree

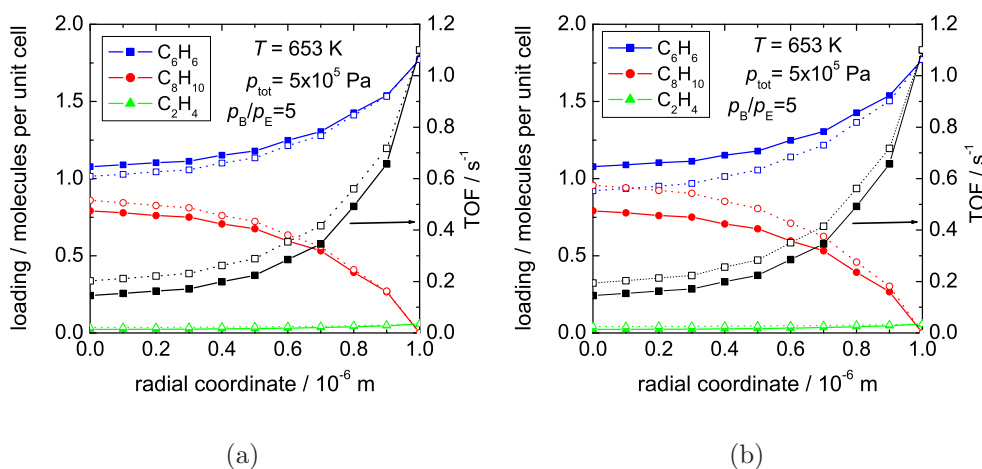


Figure 9.6: (a) Radial concentration and turnover frequency profiles for different diffusion limited scenarios. Solid lines represent: finite exchange and scaled diffusivities, that is, zero-loading M-S diffusivities were taken from table 9.2, and the parameters describing self-exchange were taken from tables B.2 and B.3 of the supporting information. Dotted lines represent: (a) facile exchange scenario, that is, $D_{ij} \rightarrow \infty$ and (b) unscaled ethene zero loading diffusivity, that is, $D_E(0) = 2.5 \times 10^{-8} \text{ m}^2 \text{ s}^{-1}$.

of correlations has a relatively little influence on the calculated effects of diffusive mass transfer for the present system. These effects are dominated by the diffusivities of benzene and ethylbenzene due to their significantly higher loadings within the zeolite compared to ethene.

A further point to be addressed is the effect of reducing the magnitude of ethene diffusivity. Concentration profiles of all species were calculated using the M-S diffusivity for ethene obtained from MD simulations at 653 K, that is, $2.5 \times 10^{-8} \text{ m}^2 \text{ s}^{-1}$, while keeping the diffusivities for benzene and ethylbenzene at their reduced values (see above). As a result the diffusivity of ethene was 5 orders of magnitudes larger than those of benzene and ethylbenzene. The calculated concentration profiles are shown in figure 9.6(b) (note that the finite exchange scenario was used for these calculations). The ethene concentration in the particle center increased to 72% of its exterior surface value. The benzene concentration in the particle center has dropped to 52% of its exterior surface value. By contrast, the ethene concentration dropped to 39% for the case of the reduced diffusivity of $9.95 \times 10^{-12} \text{ m}^2 \text{ s}^{-1}$ (see figure 9.6(a)). The profile of the turnover frequency is similar to that for

the case of facile exchange as is the value of the effectiveness factor (0.52). Therefore, the influence of the higher ethene diffusivity on the profile of catalytic activity is limited.

Figures 9.7 and 9.8 show the dependence of the overall rate of benzene alkylation with ethene predicted for a particle of H-ZSM-5 as functions of p_E and p_B and temperatures of 653 K and 703 K. In both cases, the particle is assumed to have a diameter of 2 μm . Also shown on these plots are the rates predicted by the power law expression developed by Lu et al.³²¹ to describe the alkylation of benzene by ethene on AB-97 for ethene pressures of 0.3×10^5 Pa to 3×10^5 Pa, benzene pressures of 3×10^5 Pa to 13×10^5 Pa, and temperatures of 653 K to 723 K. For this range of conditions, these authors reported values for n_E and n_B of 0.795 and 0.110, respectively, and a value for n_{EB} of 0.28. These orders and the values of the apparent preexponential factor and activation energy are given in table 9.4. The term AB-97 refers to a catalyst consisting mainly of H-ZSM-5 and alumina. The simulated rates per unit mass of MFI have been converted to rates per unit mass of AB-97 as outlined in section B.5 of the supporting information.

It is evident from table 9.4 that the activation energy appearing in the empirical rate law (21.7 kJ mol^{-1}) is significantly lower than the values obtained by Christensen et al.²⁷⁶ and those predicted by our model. Although the physical significance of this number is limited (see above) the deviation from the data of Christensen et al.²⁷⁶ may suggest the occurrence of external particle mass transfer limitation in addition to intra-particle diffusional limitation. The pellet size used by Christensen et al.²⁷⁶ was smaller by a factor of 10 than that used by Lu et al.³²¹ The latter authors also performed measurements using smaller pellet sizes and fitted these results to a Langmuir-Hinshelwood expression. The activation energy obtained in this case was 42.5 kJ mol^{-1} . However, the significance of this value is limited because of the inherently incorrect partial pressure dependences of the reaction rate

Table 9.4: Experimentally determined rate parameters for the power law rate expression of Lu et al.^{321,a}

n_E	n_B	n_{EB}	k_{10}^b	k_{20}^c	E_1^d	E_2^d
0.795	0.110	0.276	1.035×10^{-4}	1.281×10^{-1}	21.735	37.304

^aThe rate expression has the form $r = k_1 p_E^{n_E} p_B^{n_B} - k_2 p_{EB}^{n_{EB}}$.

The rate coefficients are calculated according to $k_i = k_{i0} \exp(-E_i/RT)$.

^bIn $\text{mol kg}_{\text{cat}}^{-1} \text{s}^{-1} \text{Pa}^{-0.905}$

^cIn $\text{mol kg}_{\text{cat}}^{-1} \text{s}^{-1} \text{Pa}^{-0.276}$

^dIn kJ mol^{-1}

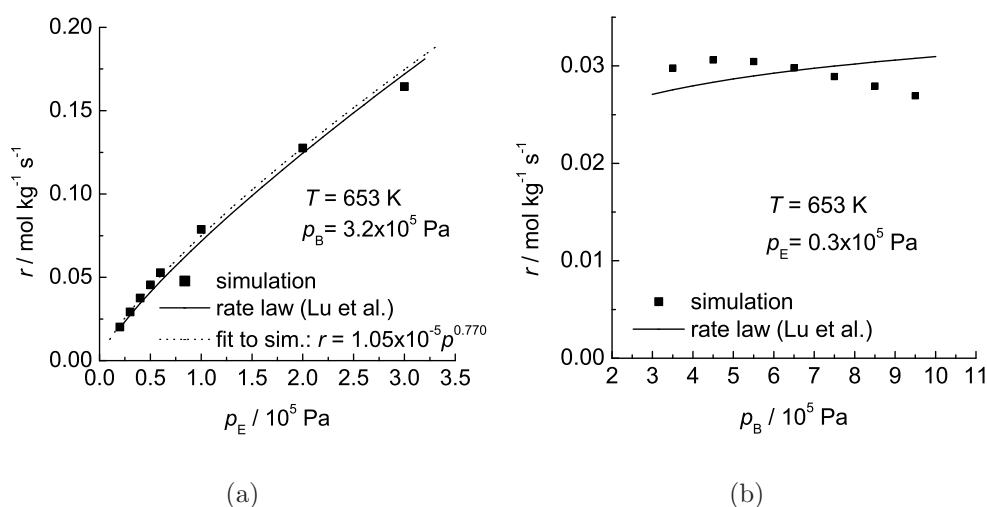


Figure 9.7: Simulated and experimental rates per unit mass of catalyst for the alkylation of benzene with ethene. (a) Constant benzene partial pressure of (3.2×10^5 Pa) at 653 K; (b) constant ethene partial pressure of 0.3×10^5 Pa at 653 K. The partial pressure of ethylbenzene was fixed to 35 Pa. The experimental data were calculated using the rate expression of Lu et al.³²¹

from the use of a Langmuir-Hinshelwood rate expression to fit the data.

Diffusion limitation affects the reaction rates significantly. Figure 9.7(a) shows the results of simulations at constant benzene partial pressure (3.2×10^5 Pa) and increasing ethene partial pressure at 653 K. Also shown are experimental data generated using the rate law of Lu et al.³²¹ The diffusion coefficients reported in table 9.2 were employed for the simulations. A particle diameter of $2 \mu\text{m}$ was used. In order to match the experimental data some assumptions about the porosity of the catalyst used for the experimental studies had to be made (see section B.5 of the supporting information for details). It was also necessary to assume the number of acid sites per unit cell since this number was not reported by Lu et al.³²¹ As can be seen from figure 9.7(a) good agreement with the experimental data is achieved assuming 1.1 acid sites per unit cell. The simulations were carried out for various ethene partial pressures at a constant benzene partial pressure of 3.2×10^5 Pa and a constant ethylbenzene partial pressure of 35 Pa. Fitting the simulated points to a power law of the form $r = Ap_E^n$ gave an exponent of 0.77, in good agreement with the experimental value ($n = 0.795$). Figure 9.7(b) shows

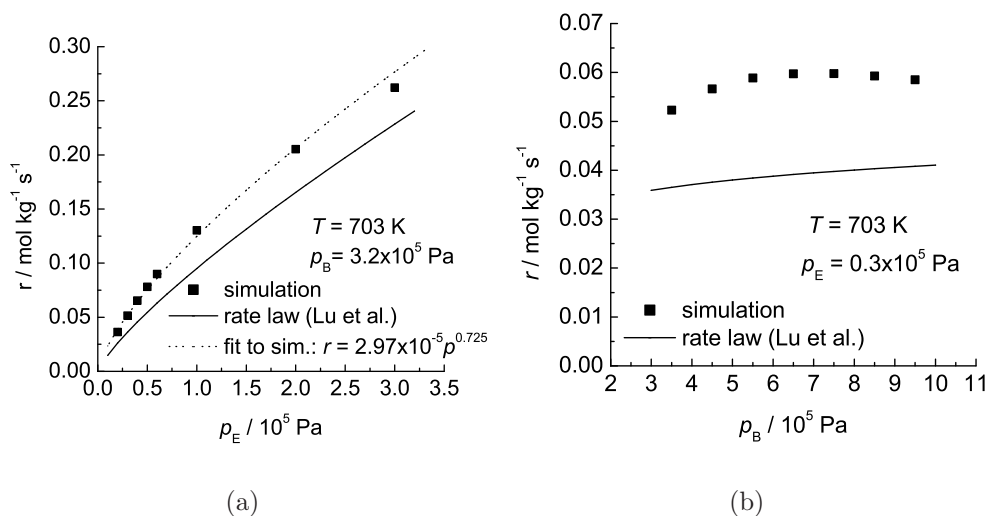


Figure 9.8: Simulated and experimental rates per unit mass of catalyst for the alkylation of benzene with ethene. (a) Constant benzene partial pressure of $(3.2 \times 10^5 \text{ Pa})$ at 703 K; (b) constant ethene partial pressure of $0.3 \times 10^5 \text{ Pa}$ at 703 K. The partial pressure of ethylbenzene was fixed to 35 Pa. The experimental data were calculated using the rate expression of Lu et al.³²¹

the rate of reaction as function of the benzene partial pressure at 653 K for constant ethene and ethylbenzene partial pressures of $0.3 \times 10^5 \text{ Pa}$ and 35 Pa, respectively. While the absolute numbers are in reasonable agreement, the simulations predict a decrease in the reaction rate with increasing benzene partial pressure, whereas the rate law predicts a slight increase. A comparison of our model with experimental measurement of the rate of reaction for a higher benzene partial pressure (see figure B.7(a)) and higher ethene partial pressure (see figure B.7(b)), are presented in section B.7 of the supporting information. The agreement for the dependence of the rate on ethene partial pressure is again good. For the benzene partial pressure dependence the agreement is better than in figure 9.7(b). The simulations again predict a maximum in the reaction rate with increasing benzene partial pressure.

At 703 K only a qualitative comparison between the simulation and the experimental data is possible because of the very small apparent activation energy appearing in the rate law of Lu et al.³²¹ (see above). Since our simulations match the experimental data at 653 K they will necessarily predict higher reaction rates at 703 K. Figure 9.8(a) shows the rate of reaction at

703 K as function of the ethene partial pressure for constant benzene partial pressure of 3.2×10^5 Pa and a constant ethylbenzene partial pressure of 35 Pa. The rate law of Lu et al.³²¹ predicts lower values as expected. However, the reaction order with respect to the ethene partial pressure ($n_E = 0.72$) agrees well with the experimental data. Figure 9.8(b) shows the simulated rate of reaction as function of the benzene partial pressure at 703 K for constant ethene partial pressure of 0.3×10^5 Pa and a constant ethylbenzene partial pressure of 35 Pa. The simulations again predict a higher activity. Similar results were obtained for higher benzene or ethene pressures, respectively (see figure B.8 in the supporting information). It should be emphasised that the benzene partial pressure has an influence on the reaction orders with respect to ethene. At 653 K and a fixed benzene partial pressure of 10×10^5 Pa the order is 0.87, compared to the order of 0.77 for a benzene partial pressure of 3.2×10^5 Pa. At 703 K and a fixed benzene partial pressure of 10×10^5 Pa the order is 0.83, compared to the order of 0.72 for a benzene partial pressure of 3.2×10^5 Pa.

9.4.3 Effectiveness factor

The conventional analysis of the influence of diffusional limitations on the rate for heterogeneously catalyzed reactions is often based on the assumptions of a pseudo first-order irreversible reaction and an effective diffusivity for the limiting reactant that is concentration independent. In the case of benzene alkylation with ethene the limiting reactant is usually ethene; therefore, the pseudo first-order kinetics can be written as

$$r = k_{\text{app}} C_E = k_{\text{app}} \frac{p_E}{RT}, \quad (9.27)$$

where k_{app} is the pseudo first-order rate coefficient and C_E denotes the gas phase concentration of ethene. The Thiele modulus can be expressed as

$$\phi = \frac{R}{3} \sqrt{\frac{k_{\text{app}} \rho_{\text{ZSM5}}}{D_{\text{E,eff}}}}, \quad (9.28)$$

where ρ_{ZSM5} is the zeolite density, $D_{\text{E,eff}}$ is the effective diffusivity of ethene, and R is the crystal radius (spherical geometry). The apparent first-order rate coefficient can be obtained directly from the simulated rate of reaction evaluated at the exterior surface of the crystal from equation 9.27. Evaluation of the effective diffusivity of ethene is less obvious. If the assumptions underlying the conventional analysis were valid, the zero-loading M-S diffusivity, $D_E(0)$, would be a reasonable choice. For a spherical particle, the

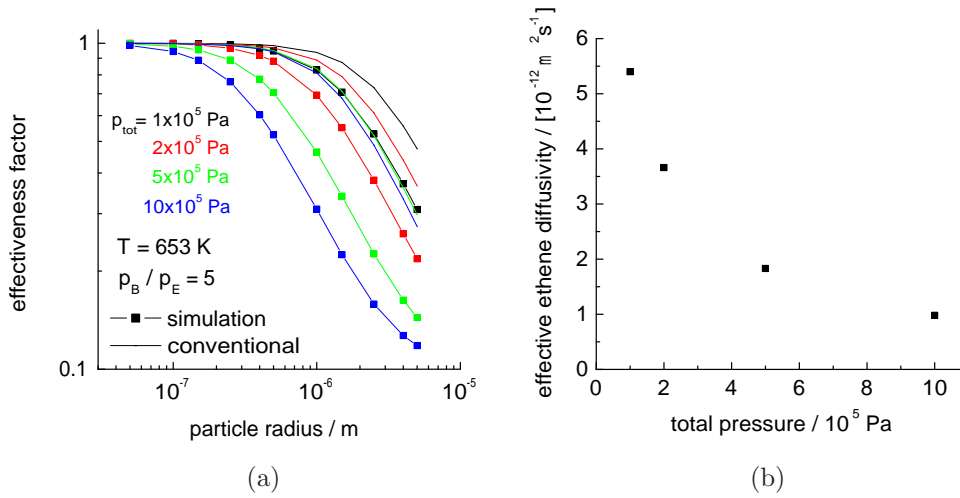


Figure 9.9: (a) Effectiveness factor as function of the particle radius for different gas phase pressures at 653 K and a benzene to ethene ratio of 5. (b) Effective ethene diffusivity as function of the total gas phase pressure.

effectiveness factor can then be obtained from

$$\eta = \frac{1}{\phi} \left(\frac{1}{\tanh(3\phi)} - \frac{1}{3\phi} \right). \quad (9.29)$$

The conventional analysis of mass transfer effects has been shown to lead to substantial errors for cases of strongly confined molecules.^{303,304,362}

Figure 9.9(a) shows plots of η versus particle radius for a temperature of 653 K, a p_B/p_E ratio of 5, and total pressures ranging from 1×10^5 Pa to 10×10^5 Pa obtained from rigorous simulations and of the effectiveness factors obtained from a conventional analysis using the zero-loading diffusivity of ethene to calculate the classical Thiele modulus. It is seen that the simulated values of η decreases significantly as the total pressure increases for a fixed particle size. The curve for the conventional analysis is resembled only at very low pressure. From these results it can be concluded that a conventional analysis is meaningful only if the diffusivities are measured at reaction conditions. Only then can the classical formulas be used to estimate the critical particle size to avoid extensive diffusion limitation. To extract the values of effective diffusivities from the simulations we can force-fit equation 9.5 into the form of Fick's law for each species, that is,

$$N_i = -\rho q_{i,\text{sat}} D_{i,\text{eff}} \nabla \theta_i, \quad (9.30)$$

where the effective Fick diffusivities of component i is a function of both, the elements of the matrix $[\Delta]$ and the gradients $\nabla\theta_i$ of all species (see ref. 363). The effective ethene diffusivities obtained from equation 9.30 are shown in figure 9.9(b) as function of the total gas phase pressure. They decrease by a factor of 5.5 as the pressure increases from 1×10^5 Pa to 10×10^5 Pa. Only if these effective diffusivities are used in the conventional analysis can reasonable agreement be achieved with the rigorous simulations. It is noted, that the effective diffusivities depend only weakly on the position inside the zeolite crystal. The strongest decrease is observed for 10×10^5 Pa gas phase pressure. However, in this case the effective diffusivity at the particle center is still 89% of its value at the particle exterior surface. While the simulation results shown in figure 9.9(a) were obtained at conditions found at the reactor inlet, we also calculated the effectiveness factor for higher ethylbenzene pressure in the gas phase, corresponding to 10% conversion. The values of the effectiveness factor lie slightly above those obtained at the inlet conditions.

9.5 Conclusion

The influence of adsorption thermodynamics and diffusion limitation on the alkylation of benzene with ethene over H-ZSM-5 has been analyzed by means of a continuum model based on the Maxwell-Stefan (M-S) equations in combination with the ideal adsorbed solution theory (IAST). All parameters needed to solve the resulting system of differential equations have been determined from molecular simulations and quantum chemical calculations. The macroscopic behavior of two different reaction schemes – a one-step scheme and a two-step scheme – has been studied. For both schemes a model has been proposed to describe the intrinsic rate of reaction as function of the local concentration of reactants at the active site. It has been demonstrated that the apparent rate coefficients and the orders in the partial pressures of the reactants are not constant but, in fact, a complex function of the zeolite architecture, particle size and reaction conditions. As a result, the widely used empirical power laws and Langmuir-Hinshelwood expressions become inappropriate when used to correlate rate data over a broad range of conditions. Moreover the usual approaches to calculate effectiveness factors for reactions in porous media can only be used at low loadings of the reactants inside the zeolite. In fact the effectiveness factor depends strongly on the reaction conditions. The adopted simulation model can be used to predict the effectiveness factor for any set of reaction conditions.

9.6 Nomenclature

Latin letters

A	pre-exponential factor in Arrhenius ansatz	s^{-1}
a_i	constants describing self-exchange in equation 9.11	–
a	Reed-Ehrlich parameter	–
$[\mathbf{B}]$	inverse of matrix $[\mathbf{\Delta}]$, equation 9.6	$\text{m}^{-2} \text{s}$
b_i	Langmuir affinity constants	Pa^{-1}
b	Reed-Ehrlich parameter	–
C_i	gas phase concentration of species i	mol m^{-3}
$D_{i,\text{self}}$	self-diffusivity	$\text{m}^2 \text{s}^{-1}$
\bar{D}_i	Maxwell-Stefan diffusivity of species i	$\text{m}^2 \text{s}^{-1}$
$\bar{D}_i(0)$	zero-loading M-S diffusivity of species i	$\text{m}^2 \text{s}^{-1}$
\bar{D}_{ii}	self-exchange diffusivity	$\text{m}^2 \text{s}^{-1}$
\bar{D}_{ij}	binary exchange diffusivity	$\text{m}^2 \text{s}^{-1}$
E	activation energy	J mol^{-1}
f_i	fugacity of species i	Pa
f	Reed-Ehrlich parameter	–
k	reaction rate coefficient	s^{-1}
k_{app}	apparent first order reaction rate coefficient	$\text{m}^3 \text{kg}^{-1} \text{s}^{-1}$
N_i	molar flux of species i	$\text{mol m}^{-2} \text{s}^{-1}$
n	number of species	–
n_i	exponent of species i in power law rate expression	–
p	pressure	Pa
q_i	molar loading of species i	mol kg^{-1}
$q_{i,\text{sat}}$	saturation loading of species i	mol kg^{-1}
R	gas constant, 8.314	$\text{J mol}^{-1} \text{K}^{-1}$
	radius	m
r	rate of reaction	$\text{mol m}^{-3} \text{s}^{-1}$
T	absolute temperature	K
t	time	s
x_i	fraction of total loading present on site i	–
y_i	gas phase mole fraction of species i	–
z	coordination number	–

Greek Letters

β_i	Reed-Ehrlich parameter	–
Γ_{ij}	thermodynamic factor	–
γ	number of protons per unit cell	–
$[\mathbf{\Delta}]$	matrix of Maxwell-Stefan diffusivities	$\text{m}^2 \text{s}^{-1}$

ε	Reed-Ehrlich parameter	—
η	effectiveness factor	—
θ	total occupancy of mixture	—
θ_i	fractional occupancy of component i	—
λ	average number of acid sites per intersection	—
μ_i	molar chemical potential	J mol ⁻¹
ν_i	stoichiometric coefficient of species i	—
ξ	diffusion path	m
ρ	density of zeolite	kg m ⁻³
ϕ	Thiele modulus	—

Subscripts

app	referring to apparent quantity
B	benzene
eff	referring to effective quantity
E	ethene
EB	ethylbenzene
eth	ethoxide
E,H+	ethene adsorbed on acid site
E+B,H+	ethene plus benzene adsorbed on acid site
EB,H+	ethylbenzene adsorbed on acid site
eth+B	benzene adsorbed next to ethoxide
i, j	components in mixture
sat	referring to saturation conditions

Vector and matrix notation

()	vector
[]	square matrix

10

Reactor simulation of benzene ethylation and ethane dehydrogenation catalyzed by ZSM-5: A multiscale approach

Rate expressions are vital for analysis, design and operation of chemical reactors. However, due to a simplified picture of the underlying physical processes, empirical power-law (PL) fits, and Langmuir-Hinshelwood (LH) expressions may not be reliable when extrapolated to conditions which were not included in the parameterization process. In the present chapter the extrapolation ability of LH and PL models are evaluated for the zeolite catalyzed alkylation of benzene with ethene. For this purpose, extrapolated data are compared to results obtained from a detailed continuum model based on the multiscale approach presented in chapter 9. It is demonstrated that extrapolation is in particular questionable if the gas phase composition is outside the fitting range. A second purpose of the present chapter is the extension of our continuum model to include the dehydrogenation of ethane. The parameters describing adsorption and diffusion are obtained from Monte Carlo and Molecular Dynamics simulations, respectively. Reaction rate constants are derived from quantum chemical calculations and transition state theory. We have used the extended continuum model in the design equation of a fixed-bed reactor and simulated the dehydroalkylation activity for different input conditions. Furthermore, the benefit from removing hydrogen from the reaction mixture using a membrane reactor is discussed.

10.1 Introduction

Gas phase alkylation of benzene using zeolite catalysts is an environmentally friendly alternative to liquid phase processes which deal with problems of corrosion and waste disposal.^{20,204} The zeolite ZSM-5 has been used for catalyzing the gas phase ethylation in the Mobil/Badger process since 1980.^{210,211,284} We have shown in chapter 9 that the apparent kinetics of this process can be successfully predicted by combining atomistic and continuum modelling. A major advantage of this multiscale approach is that it strictly separates intrinsic kinetics from adsorption and transport phenomena and thus discriminates between scale-dependent and scale-independent processes. By contrast, we note that the kinetic models used in industrial practice are frequently power law (PL) or Langmuir-Hinshelwood (LH) type expressions.³⁶⁴⁻³⁶⁶ Depending on the data used in identifying the parameters in these models, such models may include internal transport effects or even external and internal transport effects, in addition to intrinsic reaction kinetics. Moreover for mixtures containing molecules with different saturation loadings the LH approach has been shown to be thermodynamically inconsistent.^{304,305} It is therefore of interest to determine how these models perform compared to more rigorous approaches and how these models can be used for extrapolation purposes.^{367,368} A comparison with our model proposed in chapter 9 also offers the opportunity to assess the physical significance of the model parameters in the PL and LH expressions because all the relevant kinetic data is known exactly.

A drawback of the gas phase alkylation of benzene with ethene is the high energy requirement for the production of ethene. One alternative is to use benzene alkylation for reactive separation of ethene derived from another process, e.g. oxidative coupling of methane.³⁶⁹ Another alternative is to use ethane instead of ethene in the feed, i.e. dehydroalkylation. This reaction route requires a dehydrogenation function in the catalyst in addition to the acidic site for alkylation. Benzene alkylation with ethane and propane has been investigated experimentally over Pt- and Ga-containing zeolites.³⁷⁰⁻³⁷⁶ However, selectivities towards ethylbenzene and propylbenzene, respectively were all relatively low due to side reactions such as cracking, oligomerization and isomerization. In a recent study reported by Lukyanov and Vazhnova,^{286,287} benzene alkylation with ethane over Pt-MFI was investigated with the aim to identify reaction conditions and catalysts which provide higher selectivities. It was demonstrated that up to benzene conversion of 10% highly selective and stable benzene alkylation with ethane can be achieved.

In order to simulate this reaction we have extended our reaction-diffusion

model presented in chapter 9 to include the dehydrogenation of ethane in addition to the alkylation of benzene. For a theoretical analysis of the dehydrogenation it is essential to know the structure of the active site in order to calculate rate constants for the elementary steps. While in the study of Lukyanov and Vazhnova^{286,287} Pt was present as nanoparticles on the exterior surface of the zeolite, it has been demonstrated experimentally that Pt can also be dispersed inside the zeolite pore system, either in pure form or as bimetallic species with Ga.³⁷⁷⁻³⁸² The latter option seems to be more stable.³⁸¹ In the present study the dehydrogenation activity of small Ga_xPt_y extra-framework particles was studied using density functional theory and rate coefficients of all elementary steps were obtained from absolute rate theory. Using these kinetic data we then extended our diffusion-reaction model for MFI crystals (chapter 9) by incorporating the dehydrogenation of ethane in addition to the alkylation of benzene. Diffusivities and adsorption isotherms are obtained from molecular dynamics and Monte Carlo simulations, respectively. This model is then used to simulate the behavior of an isothermal fixed-bed reactor. Furthermore, the benefits of using a membrane reactor for this reaction are analysed.

This chapter is organized as follows. Section 10.2 presents the reactor model and the approach to solve the resulting equations. In section 10.3 the performance of LH and PL rate expressions is evaluated against the diffusion-reaction model for the alkylation of benzene with ethene presented in chapter 9. Section 10.4 presents the extension of our reaction-diffusion model by the dehydrogenation of ethane. The methods used to determine the parameters involved in describing adsorption, diffusion, and reactions are presented in section 10.5. Section 10.6 presents simulation results for the alkylation of benzene by ethane and comparison to literature data. The conclusions of this work are presented in section 10.7. Details of the simulation methods used to obtain information on the adsorption and diffusion of all species are provided in the supporting information accompanying this chapter.

10.2 Reactor model

An isothermal fixed-bed, plug-flow reactor is considered for the present study. It is assumed that the intra-crystalline diffusion resistance is the controlling transport phenomenon. Mass transport resistances from the bulk fluid to the catalyst surface as well as diffusion inside the meso- and macropores of the catalyst are neglected. The mole balance for component i in the reactor can

be expressed as

$$\frac{dF_i}{dz} + \frac{\tau}{L} \dot{m} \frac{1}{\rho R} n_i(z) = 0, \quad (10.1)$$

where F_i is the molar flow rate of species i and z is the length coordinate. The contact time is denoted as τ , L is the length of the reactor, and \dot{m} the mass flow rate through the reactor. The framework density of the MFI crystals is denoted as ρ and the crystal radius as R . The flux of species i at the crystallite outer surface is defined as $n_i(z)$. This flux is calculated from

$$n_i(z) = r_{\text{eff},i}(z) \rho \frac{R}{3}, \quad (10.2)$$

where $r_{\text{eff},i}(z)$ is the effective rate producing or consuming component i inside the catalyst particle, using the reaction-diffusion model we reported in chapter 9. This model requires the solution of the partial differential equation describing reaction and diffusion in a spherical geometry. The ordinary differential equation 10.1 was solved with Euler's method.

10.3 Performance of PL and LH models

For the alkylation of benzene both power law (PL) and Langmuir-Hinshelwood (LH) type rate expressions have been used to describe the rate of reaction as function of the process conditions.^{214,215,321,383} The PL rate expression is given by

$$r_B = \hat{k}_1 p_E^{n_E} p_B^{n_B} - \hat{k}_{-1} p_{EB}^{n_{EB}}, \quad (10.3)$$

where \hat{k}_1 and \hat{k}_{-1} are the apparent rate constants for the forward and reverse reaction, respectively. The partial pressure of component X is denoted as p_X while n_X is the reaction order with respect to component X. The mathematical form of the LH expression depends on the underlying reaction mechanism. If all species are adsorbed and the surface reaction is assumed to be the rate controlling step, the LH model reads

$$r_B = \frac{\hat{k}_1 p_E p_B - \hat{k}_{-1} p_{EB}}{(1 + K_B p_B + K_E p_E + K_{EB} p_{EB})^2}. \quad (10.4)$$

We can now take the view that our reaction-diffusion approach with a combination of molecular simulation techniques introduced in chapter 9 produces “experimental data” which can be used to obtain the parameters in equations 10.3 and 10.4. To find the parameters appearing in the PL and LH

models, we have minimized the sum of squares³⁸⁴

$$\min S = \sum_{i=1}^n [r_{B,i}(\text{EM}) - r_{B,i}(\text{FM})]^2, \quad (10.5)$$

where $r_{B,i}(\text{EM})$ and $r_{B,i}(\text{FM})$ are the rates obtained using the empirical rate law and the full continuum model, respectively. These rates are determined from fixed-bed differential reactor simulations by evaluating

$$r_B = \frac{F_{\text{in}}y_{B,\text{in}} - F_{\text{out}}y_{B,\text{out}}}{m_{\text{cat}}}, \quad (10.6)$$

where F_{in} and F_{out} are the molar fluxes at the reactor inlet and outlet, respectively and $y_{B,\text{in}}$ and $y_{B,\text{out}}$ are the inlet and outlet mole fractions of benzene. The catalyst mass is denoted as m_{cat} . The conversion was always below 2.2% in the differential reactor simulations. For the partial pressures appearing in the PL and LH expressions the arithmetic mean values from the reactor simulations were used.

Sets of 45 rates of reaction were generated at 603 K and 653 K by varying the total pressure from 1×10^5 Pa to 5×10^5 Pa and by using 9 subsets of compositions at each pressure point. The compositions were chosen such that the benzene to ethene ratio was between 1 and 90 (see tables C.5 and C.6 in appendix C for details). Note that no diffusion limitation was present. The intrinsic rate constants were identical to those used in chapter 9. The number of acid sites per unit cell was set to 1.1, a value which was also used before. At both temperatures the data sets could be fitted successfully to the LH expression. The fit to the PL expression was less successful (see figure 10.1). The fit parameters are listed in tables C.7 and C.8 of the supporting information accompanying this chapter. Also compiled are the activation energies and preexponential factors which were obtained assuming Arrhenius type temperature dependence of all rate and equilibrium constants.

The parity plots shown in figure 10.2 illustrate the extrapolation behaviour of both the PL and LH model. For figure 10.2(a), a pressure range of 6×10^5 Pa to 10×10^5 Pa was used at otherwise unchanged compositions of the feed while for figure 10.2(b) the temperature was changed to 703 K at otherwise unchanged pressures and compositions of the feed. As can be seen from figure 10.2(a) the rates obtained by extrapolation using the LH expression agree reasonable well with those obtained from the full continuum model. At some points the simulated rates are slightly underestimated. By contrast the rates predicted by the PL model overestimate those of the full continuum

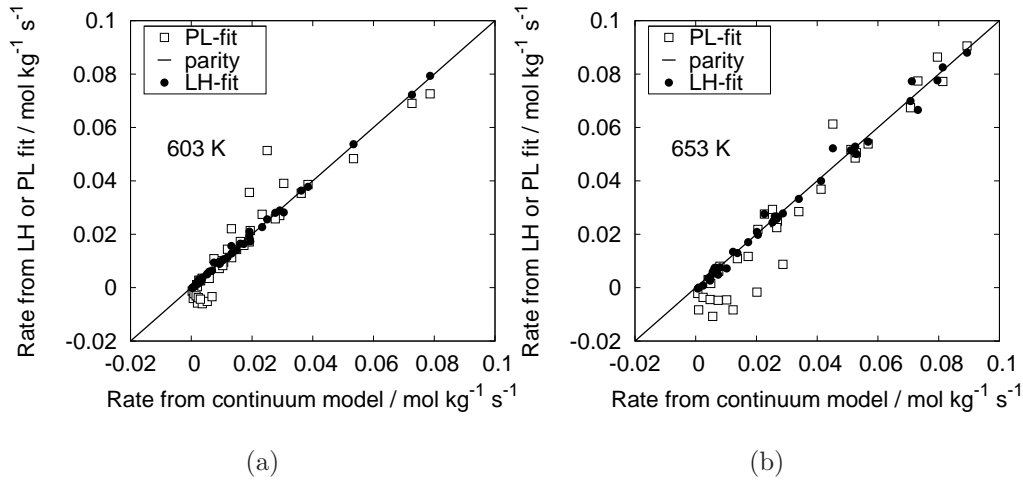


Figure 10.1: Comparison of fitted PL and LH rates to those calculated using the full continuum model with intrinsic rate constants of $k_{1,603\text{K}} = 1.14 \times 10^2 \text{ s}^{-1}$, $k_{-1,603\text{K}} = 5.32 \times 10^{-3} \text{ s}^{-1}$, $k_{1,653\text{K}} = 6.96 \times 10^2 \text{ s}^{-1}$, and $k_{-1,653\text{K}} = 1.37 \times 10^{-1} \text{ s}^{-1}$.

model. When extrapolating to higher temperatures, both the PL and LH model over-predict the rates of the full continuum model. It should be noted though that in order to extrapolate with the PL model, the parameters had to be fitted to 603 K and 653 K simultaneously with fixed values for the exponents, which reduces the numbers of adjustable parameters compared to the LH model. As can be seen from the individual fits (table C.8), the exponent for benzene in the PL expression depends strongly on the temperature and consequently large uncertainties are introduced into this model when using it to fit rate data over a broad temperature range. The activation energy parameter was extracted from the values of k at 603 K and 653 K. For the LH model a value of $E_1 = 44.3 \text{ kJ/mol}$ is obtained while the PL model gives $E_1 = 68.0 \text{ kJ/mol}$. The apparent activation energies calculated with the full continuum model are strongly dependent on both the total pressure and the gas-phase composition. At $1 \times 10^5 \text{ Pa}$, apparent activation energies are in the range from 49 kJ/mol to 60 kJ/mol while at $5 \times 10^5 \text{ Pa}$, E_a ranges from 66 kJ/mol to 90 kJ/mol (gas phase mole fractions of C_6H_6 , C_2H_4 , C_8H_{10} : 0.50, 0.49, 0.01 and 0.50, 0.25, 0.25). From these results it is obvious that the LH and PL models do not offer the required flexibility to calculate the rates for the alkylation of benzene with ethene over a wide range of process conditions. Due to the strong dependence of the apparent activation energies on total pressure and gas phase composition an unambiguous interpretation of

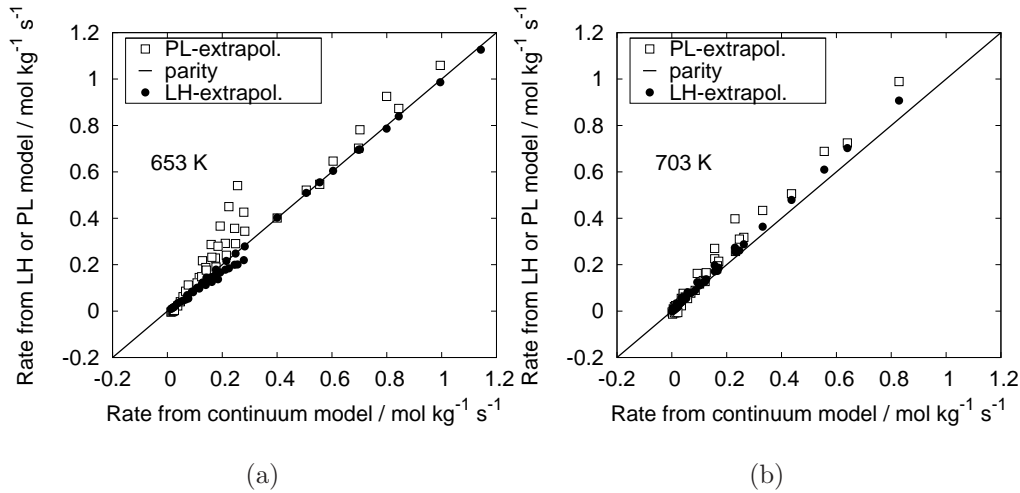


Figure 10.2: Comparison of extrapolated PL and LH rates and those of the full model. (a) Extrapolation to higher pressures. (b) Extrapolation to 703 K at otherwise unchanged pressures and gas-phase compositions. The intrinsic rate constants used in the full model are $k_{1,703\text{K}} = 3.27 \times 10^3 \text{ s}^{-1}$ and $k_{-1,703\text{K}} = 2.21 \times 10^0 \text{ s}^{-1}$.

the energy parameters appearing in the LH and PL expression as activation energies is not possible.

It is now of interest to determine how the LH and PL models perform when using them in a reactor design equation. This is illustrated in figures 10.3 and 10.4. The conversions in figure 10.3 have been determined for a benzene to ethene ratio in the feed of 5:1. As a consequence the molar fractions of all species were within or close to the fitting range. The conversion calculated with the LH expression are in reasonably good agreement with the full continuum model while the PL model overestimates the conversion for low contact times and underestimates the maximum conversion. At 703 K, both the LH and the PL model are in good agreement with the continuum simulations up to a contact time of 0.003 h. For larger contact times the PL model underestimates the simulation while the LH model is in good agreement with the continuum simulations up to the maximum conversion.

In calculating the simulation results shown in figure 10.4 the composition of the feed gas was changed to a benzene/ethene ratio of 2/3. As can be seen, both LH and PL models deviate significantly from the continuum simulations. Interestingly the maximum conversion predicted by our model is below the gas phase equilibrium conversion which is close to unity. This is

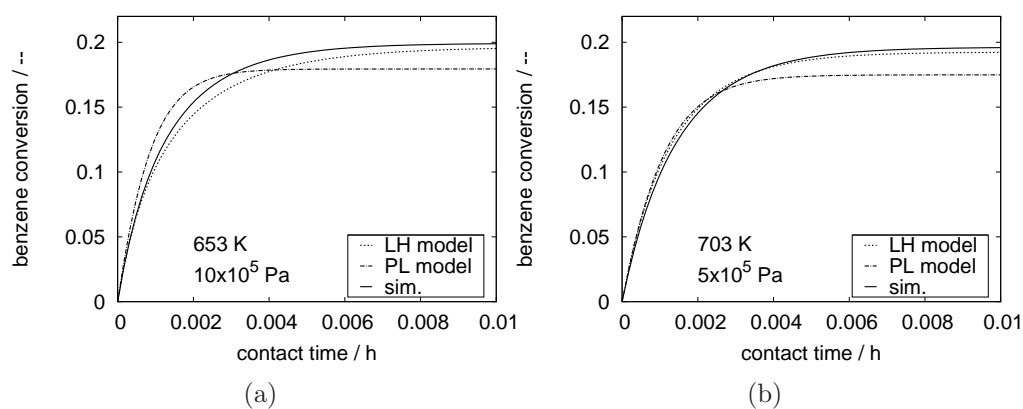


Figure 10.3: Effect of contact time on the conversion of benzene at 653 K and 703 K for a benzene to ethene molar ratio in the feed of 5:1.

a consequence of the strong adsorption of the product (ethylbenzene) which leads to a shift in the equilibrium composition towards the reactant side. This behavior is also captured qualitatively by the LH and the PL model. However both models predict significantly higher equilibrium conversions than the full continuum simulations. The degree to which the maximum conversion predicted by the continuum model stays below the gas phase equilibrium conversion depends on the ratio of intrinsic rate coefficients as predicted by the quantum chemical method as well as on the adsorption properties of ethylbenzene calculated using the ideal adsorbed solution theory which draws upon adsorption isotherms obtained from Monte Carlo simulations in the grand canonical ensemble.³⁸⁵ Experimental evidence for this behavior is rare. However, a maximum in transient kinetic data for the alkylation of benzene over zeolite Y could be explained by a build-up of ethylbenzene in the zeolite due to a strong adsorption constant.³⁸⁶

The present results support earlier studies that have shown the importance of a correct description of multicomponent adsorption by the ideal adsorbed solution theory instead of the multicomponent Langmuir description underlying the conventional LH rate expression.^{304,305} In what follows we concentrate on our continuum model and extend it to the ethane dehydrogenation reaction. The replacement of ethene by ethane as the alkylating agent using a bifunctional catalyst is an economically attractive option because alkanes are major constituents of natural gas and therefore widely available.³⁸⁷

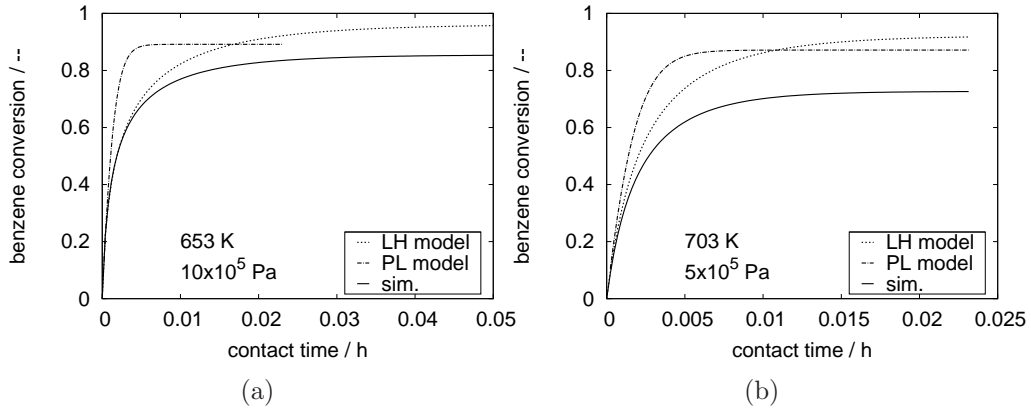


Figure 10.4: Effect of contact time on the conversion of benzene at 653 K and 703 K for a benzene to ethene molar ratio in the feed of 2:3.

10.4 Dehydrogenation of ethane

The dehydrogenation of ethane to ethene and hydrogen is a strongly equilibrium limited endothermic reaction. The mechanism of this reaction carried out over Ga_xPt_y -species comprises a series of steps all of which show small activation energies (see section C.4 of the supporting information). The theoretically determined rate coefficients for the dehydrogenation are larger than those for the alkylation over acid sites. This has two consequences. First, it is not necessary to consider all elementary steps leading to ethene and hydrogen in the model because the formation of ethene is a rapid process compared to the formation of ethylbenzene. This allows us to describe the intrinsic rate of reaction as following a one-step scheme with effective values for the forward and reverse rate coefficient,

$$r_{\text{deh}} = k_1 q_{\text{C2}} - k_{-1} q_{\text{E}} q_{\text{H}}, \quad (10.7)$$

where k_1 and k_{-1} are the intrinsic rate coefficients for the forward and reverse reaction, respectively and q_i denotes the loading of species i inside the zeolite channels. Second, it is necessary to ensure that the correct chemical equilibrium composition is approached inside the zeolite pores. Therefore we express the net forward reaction rate as

$$r_{\text{deh}} = k_1 \alpha \left(q_{\text{C2}} - \frac{1}{K_q} q_{\text{E}} q_{\text{H}} \right), \quad (10.8)$$

which avoids the problem of finding a rate coefficient for the reverse reaction. The value of k_1 is derived from quantum chemical calculations as described

in section C.4 of the supporting information. The factor α should account for the fact that only a fraction of the ethane is available for the dehydrogenation. It can be interpreted as the conditional probability that an ethane molecule which is adsorbed inside the zeolite pores is located close enough to a dehydrogenation site to be converted. As will be shown below, the simulation results are essentially independent of α which makes a detailed model unnecessary. The equilibrium constant K_q is defined as

$$K_q = \frac{q_{\text{H}}^{\text{eq}} q_{\text{E}}^{\text{eq}}}{q_{\text{C}_2}^{\text{eq}}}, \quad (10.9)$$

where q_{X}^{eq} is the loading of component X at chemical equilibrium. It should be emphasized that the mole fractions of the adsorbates in chemical equilibrium are not equal to the equilibrium mole fractions in the gas phase due to differences in the adsorption strength of the different species.^{89,388,389} This leads to a shift in the chemical equilibrium in the adsorbed phase towards the reactant side. In the case of thermodynamic equilibrium we can couple the equilibrium constant appearing in equation 10.9 to the gas phase equilibrium constant K_a calculated from the Gibbs free energy of reaction. When using the ideal adsorbed solution theory³⁰⁶ for the calculation of the adsorbed amounts, thermodynamic equilibrium is expressed as

$$p_i^0 x_i = p y_i, \quad (10.10)$$

where x and y represent the mole fractions in the adsorbed and gas phase, respectively. The total pressure in the gas phase is denoted as p while p_i^0 is the pressure of component i in the gas phase in equilibrium with an amount adsorbed that exerts the same spreading pressure of the mixture. With these quantities we are then able to express the equilibrium constant in terms of activities, K_a , by

$$\begin{aligned} K_a &= \prod_i a_i^{\nu_i} = (10^5 \text{ Pa})^{-\sum \nu_i} K_p = (10^5 \text{ Pa})^{-\sum \nu_i} \frac{p_{\text{H}}^{\text{eq}} p_{\text{E}}^{\text{eq}}}{p_{\text{C}_2}^{\text{eq}}} \\ &= (10^5 \text{ Pa})^{-\sum \nu_i} \frac{x_{\text{H}}^{\text{eq}} p_{\text{H}}^0 x_{\text{E}}^{\text{eq}} p_{\text{E}}^0}{x_{\text{C}_2}^{\text{eq}} p_{\text{C}_2}^0} = (10^5 \text{ Pa})^{-\sum \nu_i} \frac{q_{\text{H}}^{\text{eq}} p_{\text{H}}^0 q_{\text{E}}^{\text{eq}} p_{\text{E}}^0}{q_{\text{tot}}^{\text{eq}} q_{\text{C}_2}^{\text{eq}} p_{\text{C}_2}^0}. \end{aligned} \quad (10.11)$$

The latter expression can be rearranged to give a relation between the gas phase equilibrium constant, K_a , and the one calculated from the equilibrium adsorbed amounts,

$$K_q = \frac{q_{\text{H}}^{\text{eq}} q_{\text{E}}^{\text{eq}}}{q_{\text{C}_2}^{\text{eq}}} = K_a (10^5 \text{ Pa}) q_{\text{tot}}^{\text{eq}} \frac{p_{\text{C}_2}^0}{p_{\text{H}}^0 p_{\text{E}}^0}. \quad (10.12)$$

For reactor simulations of the dehydroalkylation, equation 10.1 has to be integrated subject to the constraint imposed by the chemical equilibrium of the dehydrogenation reaction. Therefore we have used an adaptive step size control which guarantess that

$$\frac{y_{\text{H}}(z)y_{\text{E}}(z)}{y_{\text{C}_2}(z)} \leq \frac{K_a}{p/(10^5 \text{ Pa})} \quad (10.13)$$

along the length coordinate z .

10.5 Parameterization

Pure component adsorption isotherms for ethane and hydrogen were obtained by MC simulations using the method described in section C.1 of the supporting information. These isotherms were fitted to analytical isotherm models (see section C.2 of the supporting information). Adsorption isotherms for ethene, benzene, and ethylbenzene were taken from chapter 9. Mixture adsorption isotherms were then calculated from the pure component adsorption isotherms by means of the IAST. Multicomponent diffusion was characterized by means of the Maxwell-Stefan equations.²³ The diffusivity data for ethene, benzene, and ethylbenzene were taken from chapter 9. The Maxwell-Stefan (M-S) diffusivities of ethane and hydrogen were obtained from MD calculations (see section C.3 of the supporting information). In chapter 9 we have adapted the magnitude of the diffusivities by fitting them to experimental results from diffusion-limited rate data. This became necessary because of the limited reliability of results from conventional MD simulations for diffusion of aromatic hydrocarbons in zeolites (see chapter 9 for details). The final M-S diffusivities for benzene and ethylbenzene were then of the order of $10^{-13} \text{ m}^2 \text{ s}^{-1}$ at reaction temperature which is still in agreement with experimental data.^{341,351} To be consistent with the calculations presented in chapter 9 we have scaled down the zero-loading M-S diffusivities of ethane and hydrogen by 3.4 orders of magnitude. The unscaled diffusivities of ethane and hydrogen are listed in table C.3 of the supporting information. The rate coefficients for the dehydrogenation of ethane were determined from quantum chemical calculation as outlined in section C.4 of the supporting information. The rate coefficients for the alkylation reaction were determined in two steps. Initially the rate coefficients determined in chapter 9 were taken to simulate the effect of contact time on the conversion of benzene and the results were compared to the experimental data reported by Lukyanov and Vazhnova.²⁸⁷ These data were measured for a zeolite sample with a Si/Al ratio of 15 which corresponds to six acid sites per unit cell provided that every negative charge

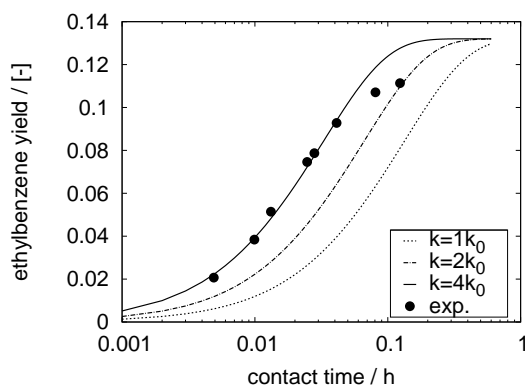


Figure 10.5: Adjustment of rate coefficients to experimental data. The experimental data are reported for a total pressure of 1×10^5 Pa and ethane to benzene molar ratio in the feed of 9:1. The conditions for the simulation were $p = 2 \times 10^5$ Pa, $y_B = 0.1$, $y_{C_2} = 0.9$, and $k_0 = 6.96 \times 10^2 \text{ s}^{-1}$.

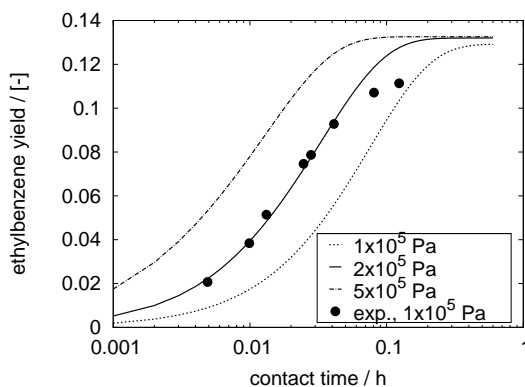


Figure 10.6: Effect of contact time and pressure on benzene conversion at 653 K for an ethane to benzene molar ratio in the feed of 9:1.

introduced by an Al is compensated by a proton. The size of the crystallites was reported to be in the range from 0.4 to 0.7 μm . As a result diffusion limitation is unlikely to occur. In our simulations we have used a value of 6 acid sites per unit cell. The number of dehydrogenation sites is proportional to the factor α in equation 10.8. However, for α being in the range from 0.01 to 1 essentially no change in the dehydroalkylation activity is observed because the dehydrogenation reaction is significantly faster than the alkylation. It turned out, however that the experimental alkylation activity was

Table 10.1: Equilibrium constant for ethane dehydrogenation and intrinsic rate coefficients at 653 K.

reaction	constant	
$\text{C}_2\text{H}_6 \leftrightarrow \text{C}_2\text{H}_4 + \text{H}_2$	k_1, s^{-1}	5.00×10^3
	$K_a, -$	4.21×10^{-5}
$\text{C}_6\text{H}_6 + \text{C}_2\text{H}_4 \leftrightarrow \text{C}_8\text{H}_{10}$	k_1, s^{-1}	2.78×10^3
	k_{-1}, s^{-1}	5.48×10^{-1}

underestimated. Therefore we increased the rate coefficient for the alkylation by a factor of four, a value which is acceptable when attempting quantitative predictions from first principles. We have also decided to increase the simulation pressure from 1×10^5 Pa to 2×10^5 Pa in order to match the experimental curve. The influence of the intrinsic rate coefficient and the total pressure on the simulated conversion-over-contact time-plots is illustrated in figures 10.5 and 10.6. The fitting strategy is similar to the one used in chapter 9 and tries to take into account both, errors in the adsorption isotherms as well as errors in the quantum chemical approaches used to determine the rate coefficients. The resulting rate coefficients are listed in table 10.1. In figures 10.5 and 10.6 we have plotted the ethylbenzene yield instead of the benzene conversion because of the occurrence of side reactions for higher contact times. These side reactions are responsible for a benzene conversion higher than the equilibrium conversion in the experiments reported by Lukyanov and Vazhnova.²⁸⁷ For the simulations ethylbenzene yield and benzene conversion are identical as no side reactions are considered.

10.6 Results and discussion

10.6.1 Intrinsic kinetics

The intrinsic kinetics can be established by using the rates of reaction on the outer crystal surface. The solution of the diffusion-reaction equation is not necessary because the rates depend solely on the adsorbed amounts. Figure 10.6 shows the effects of the input pressure on the contact time needed to get the maximum conversion for a ethane-benzene mixture of 9:1. As expected the increase of the inlet pressure leads to a decrease of the contact time and thus the amount of catalyst needed to reach full conversion. The maximum conversion predicted by the model stays slightly below the gas

phase equilibrium conversion (14.5 %). The reason is that with increasing conversion the concentration of adsorbed ethylbenzene increases and, consequently, the rate of the reverse reaction. As stated above, the degree to which the gas phase equilibrium is underestimated depends on the accuracy to which the ratio of rate coefficients was calculated by the quantum mechanical method and the accuracy of the adsorption isotherms obtained from Monte Carlo simulations. The finding that the maximum conversion predicted by the continuum model does not exceed the gas phase equilibrium conversion shows that the parameters describing adsorption and intrinsic reactions are consistent while it does not provide a quantitative prediction for the equilibrium conversion.

10.6.2 Effects of diffusion limitation

The effect of diffusion limitation on the dehydroalkylation activity was studied for two different scenarios. In the first scenario it is assumed that the dehydrogenation of ethane takes place in the gas phase while in the second scenario the dehydrogenation occurs inside the zeolite. The first scenario corresponds to the experimental situation in which the dehydrogenation function is located on the outer particle surface (e. g. as nanoparticles) while the second scenario corresponds to the picture of dispersed dehydrogenation sites inside the zeolite channels. Simulations have been conducted for a catalyst particle size of $2 \mu\text{m}$ at $5 \times 10^5 \text{ Pa}$ gas phase pressure. Figure 10.7 shows that the contact time required to achieve a certain conversion increases in the case of diffusion limitation, as expected. More interestingly it can be observed that the catalyst activity is higher when the dehydrogenation occurs inside the pores compared to the dehydrogenation in the gas phase. When ethene is produced exclusively in the gas phase it has to diffuse into the zeolite pores in order to be converted. The ethene production inside the pores has the advantage that the concentration profile of ethene inside the catalyst particle is less depleted and, consequently, the ethene concentration in the particle center is higher which leads to a higher rate of reaction. Both situations are illustrated in figure 10.8 which presents the ethene occupancy profiles, $\theta_E(\xi) = q_E(\xi)/q_{E,\text{sat}}$, over the radial coordinate ξ for both scenarios at a position close to the reactor inlet. This example nicely illustrates the potential of the simulation approach to gain insight into complex reaction systems.

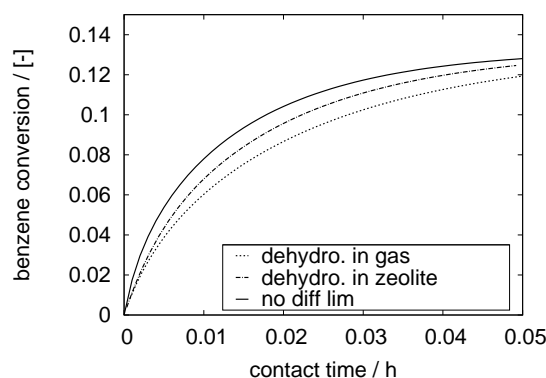


Figure 10.7: Effect of diffusion limitation on the benzene conversion at 653 K and 5×10^5 Pa for an ethane to benzene molar ratio in the feed of 9:1 and a particle size of $2 \mu\text{m}$. The full line represents the conversion without diffusion limitation. The dotted and the dot and dash line represent dehydrogenation in the gas phase and the zeolite, respectively.

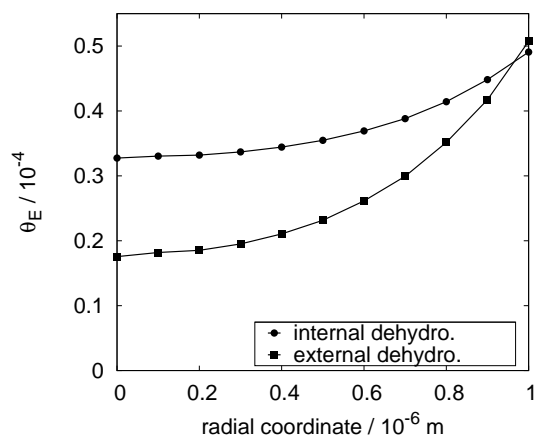


Figure 10.8: Radial occupancy profiles of ethene close to the reactor inlet for external and internal dehydrogenation at 653 K and 5×10^5 Pa for an ethane to benzene molar ratio in the feed of 9:1 and a particle size of $2 \mu\text{m}$.

10.6.3 Effects of hydrogen removal

Dehydroalkylation is strongly limited by thermodynamic equilibrium. An attractive approach is the use of a membrane reactor with a hydrogen se-

lective membrane. Beside the increase in benzene conversion this process would offer the benefit of separating the high valuable hydrogen from the reaction mixture.³⁹⁰ Here we have simulated a membrane reactor assuming hydrogen pressure equilibrium across the membrane, that is, after each integration step the hydrogen partial pressures on retentate and permeate sides were equilibrated by allowing hydrogen to flow from the reaction zone into the permeate stream. Figure 10.9 shows the effects of the ratio λ between sweep gas flow and reactant feed on the equilibrium conversion of benzene. It can be seen that the benzene conversion can be increased significantly by removing hydrogen from the reaction zone. For the highest simulated ratio ($\lambda = 10$) the benzene conversion is 30% which is an almost threefold increase compared to the normal fixed-bed operation mode.

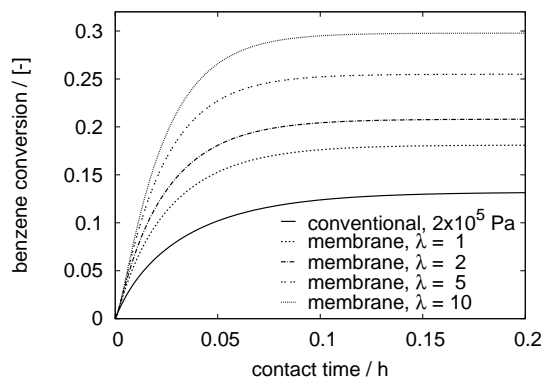


Figure 10.9: Effect of hydrogen removal on benzene conversion at 653 K and 2×10^5 Pa for an ethane to benzene molar ratio in the feed of 9:1. The pressure of the permeate stream was fixed to 1×10^5 Pa.

10.7 Conclusion

One of the key challenges in reaction engineering is the development of improved science-based scale-up methodologies leading to more efficient processes.³⁹¹ This can be accomplished by a multiscale approach combining atomistic and continuum modelling. In the present work we have performed reactor simulations for the alkylation of benzene with ethene in zeolite H-ZSM-5 based on a detailed continuum description of the reaction system. Kinetic data generated in the differential operation mode of the reactor were used to parameterize Langmuir-Hinshelwood and power-law rate expressions.

These rate expressions were then used to extrapolate to higher pressure and temperature and in a design equation for a fixed-bed reactor. It was demonstrated that the LH rate expression shows extrapolation capabilities comparable to the predictions of the continuum model as long as the gas phase composition remains within the fitting range. By contrast, the predictions of the power law rate expression deviate from those of the LH rate expression and the continuum model. In particular, a lower maximum conversion achievable in a fixed-bed reactor was predicted. When the gas-phase composition deviates significantly from that used for fitting, both the LH and the PL rate expressions deviate considerably from the predictions of the full continuum model and predict a higher maximum conversion in fixed-bed reactor simulations. These results suggest that for zeolite-catalyzed reactions producing strongly adsorbed products such as ethylbenzene LH and PL rate expressions may lack the required flexibility to describe the limit of full conversion.

The second objective of the present work was to include the dehydrogenation of ethane into our continuum model. The rate coefficients for this reaction were estimated by means of density functional calculations and absolute rate theory. The full model was shown to predict correctly the behavior of a fixed-bed reactor for the dehydroalkylation. Moreover we have demonstrated the potential of a membrane reactor for this reaction. The removal of hydrogen from the reactant mixture can increase the benzene conversion significantly.

All of these applications illustrate how detailed atomistic simulations can be linked to macroscopic reactor models in order to achieve a superior predictability compared to empirical kinetic rate expressions.

10.8 Nomenclature

Latin letters

a_i	activity of species i	–
F_i	molar flow rate of species i	mol s^{-1}
K	adsorption equilibrium constant	Pa^{-1}
K_a	chemical equilibrium constant	–
K_q	reaction equilibrium constant in adsorbed phase	mol kg^{-1}
k	intrinsic reaction rate coefficient	s^{-1}
\hat{k}	apparent reaction rate coefficient	$\text{mol kg}^{-1} \text{s}^{-1} \text{Pa}^{-n}$
L	length of reactor	m
m_{cat}	catalyst mass	kg
\dot{m}	mass flow rate	kg s^{-1}

n	molar flux through outer surface	$\text{mol s}^{-1} \text{m}^{-2}$
n	exponent in power law	–
p	pressure	Pa
q_i	molar loading of species i	mol kg^{-1}
R	radius of crystalline catalyst	m
r	rate of reaction	$\text{mol kg}^{-1} \text{s}^{-1}$
x_i	adsorbed phase mole fraction of species i	–
y_i	gas phase mole fraction of species i	–
z	length coordinate	m

Greek Letters

α	reaction probability	–
θ_i	fractional occupancy of component i	–
λ	ratio between sweep gas flow and reactant feed	–
ν_i	stoichiometric coefficient of species i	–
ξ	diffusion path	m
ρ	framework density of zeolite	kg m^{-3}
τ	contact time (m_{cat}/\dot{m})	s

Subscripts

B	benzene
C2	ethane
E	ethene
EB	ethylbenzene
eff	effective
H	hydrogen
sat	referring to saturation conditions

Superscripts

eq	referring to chemical equilibrium
----	-----------------------------------

11

Quantum chemical modeling of benzene ethylation over H-ZSM-5 approaching chemical accuracy: A hybrid MP2:DFT study

The alkylation of benzene by ethene over H-ZSM-5 is analyzed by means of a hybrid MP2:DFT scheme. Density functional calculations applying periodic boundary conditions (PBE functional) are combined with MP2 energy calculations on a series of cluster models of increasing size which allows extrapolation to the periodic MP2 limit. Basis set truncation errors are estimated by extrapolation of the MP2 energy to the complete basis set limit. Contributions from higher order correlation effects are accounted for by CCSD(T) coupled cluster calculations. The sum of all contributions provides the “final estimates” for adsorption energies and energy barriers. Dispersion contributes significantly to the potential energy surface. As a result, the MP2:DFT potential energy profile is shifted downwards compared to the PBE-profile. More importantly this shift is not the same for reactants and transition structures due to different self-interaction correction errors. The final enthalpies for ethene, benzene, and ethylbenzene adsorption on the Brønsted acid site at 298 K are -46 , -78 , and -110 kJ/mol. The intrinsic enthalpy barriers at 653 K are 117 and 119/94 kJ/mol for the one- and two-step alkylation, respectively. Intrinsic rate coefficients calculated by means of transition state theory are converted to apparent Arrhenius parameters by means of the multicomponent adsorption equilibrium. The simulated apparent activation energy (66 kJ/mol) agrees with experimental data (58-76 kJ/mol) within the uncertainty limit of the calculations.

Adsorption energies obtained by adding a damped dispersion term to the PBE energies (PBE+D), agree within ± 7 kJ/mol, with the “final estimates”, except for physisorption (π -complex formation) and chemisorption of ethene (ethoxide formation) for which the PBE+D energies are 12.4 and 26.0 kJ/mol, respectively larger than the “final estimates”. For intrinsic energy barriers, the PBE+D approach does not improve pure PBE results.

11.1 Introduction

Zeolites are used as catalysts in the petroleum and chemical industries to promote a large number of reactions.^{19,392} For this reason, considerable interest has been devoted in recent years towards the development of theoretical models for describing adsorption, diffusion, and reaction in zeolites and towards the clarification of how these processes are affected by zeolite structure and composition.^{22,23} The ultimate aim of such work is to simulate the activity and selectivity of zeolite catalysts from first principles. An essential part of this ongoing effort is the development of accurate methods for the prediction of the energies of adsorption/desorption and reaction, as well as the rate coefficients for these processes.

Density functional theory (DFT) is now routinely applied to calculate the energy profiles of chemical reactions for systems as large as zeolites. However, the use of DFT is hampered by the fact that functionals which can be used efficiently in solid-state simulations do not properly account for long-range dispersion interactions^{393,394} and are subject to the self-interaction error.^{395,396} This results in underestimated adsorption energies^{238,397} and energy barriers that are systematically too low,^{199,398} respectively. For non-covalently bonded complexes and large molecules^{399–401} as well as for solid-state and adsorption problems^{397,402,403} it has been shown that the dispersion interactions can be included by adding a damped dispersion term as a parameterized sum over atom pair C_6 contributions (DFT-D).^{397,399,400,402,403} Whether this also works for processes involving bond rearrangements is a subject of active research. A further issue with the computational modeling of reactions in zeolites is associated with the description of the long-range crystal potential and steric effects caused by confinement within the pores of these materials. While these effects can be taken into account, in principle, by using large clusters, such calculations often do not converge with increasing cluster size, suggesting that it would be best to use periodic calculations.²³⁸ The method of choice for correctly including both long-range electron correlation as well as the pore topology would be periodic MP2 calculations. However, for periodic systems, MP2 calculations are at present only feasible with small basis sets and for systems containing only a few atoms in the unit cell.^{404–406} For accurate calculation of reaction energies and energy barriers in extended systems, hybrid schemes such as the MP2:DFT scheme introduced by Tuma and Sauer^{59,238} can be applied. This approach combines MP2 calculations with Gaussian basis sets for the reaction site and plane-wave DFT for the full system under periodic boundary conditions. For a series of cluster models (**C**) a size-dependent “high-level” correction, defined as the difference between

MP2 and DFT energies is calculated,

$$\Delta E(\mathbf{C})_{\text{high}} = \Delta E(\mathbf{C})_{\text{MP2}} - \Delta E(\mathbf{C})_{\text{DFT}}, \quad (11.1)$$

and extrapolated to the periodic structure (\mathbf{S}). This periodic model limit, $\Delta \tilde{E}(\mathbf{S})_{\text{high}}$, is added to the plane-wave DFT energy for the periodic structure, $\Delta E(\mathbf{S})_{\text{DFT}}$, to get an estimate of the MP2 energy of the full periodic system,

$$\Delta \tilde{E}(\mathbf{S})_{\text{MP2}} = \Delta E(\mathbf{S})_{\text{DFT}} + \Delta \tilde{E}(\mathbf{S})_{\text{high}}. \quad (11.2)$$

In equation 11.2 and throughout the rest of this chapter we use a tilde to distinguish energies that were obtained through fitting and/or extrapolation from those obtained directly from quantum chemical calculations (MP2, PBE). This “periodic” MP2 energy, $\Delta \tilde{E}(\mathbf{S})_{\text{MP2}}$, is subsequently corrected for errors due to basis set incompleteness, calculated for cluster models (\mathbf{C}_{CBS}), $\Delta E(\mathbf{C}_{\text{CBS}})_{\text{MP2}}^{\text{CBS}}$, as well as for higher order correlation effects estimated by coupled cluster, CCSD(T), calculations for cluster model (\mathbf{C}_{CC}), denoted as $\Delta E(\mathbf{C}_{\text{CC}})_{\text{CCSD(T)}}$. The *final estimate* including all of these corrections, $\Delta \tilde{E}(\mathbf{S})_{\text{final estimate}}$, is obtained as

$$\Delta \tilde{E}(\mathbf{S})_{\text{final estimate}} = \Delta \tilde{E}(\mathbf{S})_{\text{MP2}} + \Delta E(\mathbf{C}_{\text{CBS}})_{\text{MP2}}^{\text{CBS}} + \Delta E(\mathbf{C}_{\text{CC}})_{\text{CCSD(T)}}. \quad (11.3)$$

The hybrid MP2:DFT approach has been applied previously to proton jumps in zeolites,²⁵⁷ adsorption of iso-butene²³⁸ and stability of *tert*-butyl carbenium ion⁴⁰⁷ in zeolite H-FER, and methylation of alkenes in H-ZSM-5.²⁵⁸ In all cases substantial improvement regarding the agreement with experimental data was achieved over pure DFT results.

The hybrid MP2:DFT calculations start with structure optimizations and frequency calculations at the DFT level with periodic boundary conditions. This can be followed by a reoptimization on the hybrid MP2:DFT potential energy surface using the high-level correction for an appropriate cluster size (\mathbf{C}_{OPT}) according to

$$\Delta E(\mathbf{S} : \mathbf{C})_{\text{MP2:DFT}} = \Delta E(\mathbf{S})_{\text{DFT}} + \Delta E(\mathbf{C}_{\text{OPT}})_{\text{high}}. \quad (11.4)$$

This reoptimization has been carried out in refs 238,257,407, but is not done in the present study. Here we follow ref. 258 and evaluate the “periodic” MP2 estimate and the final energy estimate according to eqs. (11.2,11.3) as single-point energies at the DFT optimized structures.

In the present study we employ the MP2:DFT hybrid scheme to revise our previous calculations for the alkylation of benzene with ethene over zeolite H-ZSM-5 which used cluster models of the active site to determine energy barriers and rate coefficients (see chapter 8). For the Al12-O20(H)-Si3 site^{258,408}

(numbering according to ref. 146) we considered both a one-step scheme, in which the precursor is represented by coadsorbed ethene and benzene at the acid site and a two-step mechanism in which ethene is first protonated to form an ethoxide species that subsequently reacts with benzene to form the product, ethylbenzene. The rate coefficients for these elementary steps, together with diffusivities obtained from molecular dynamics simulations, were then used in a continuum model of a zeolite crystal to calculate the overall activity as a function of the gas phase conditions. It turned out, however, that the theoretically determined rate coefficients for the one-step mechanism had to be increased by two orders of magnitude to achieve agreement with experimental data, while the rate coefficients for the two-step mechanism had to be lowered by a factor of four (see chapter 9). Moreover the apparent activation energy determined for the one-step mechanism was too low by 15 kJ/mol while that for the two-step mechanism was slightly higher than the experimental values. It is therefore reasonable to reconsider the alkylation of benzene using more sophisticated quantum chemical approaches in order to obtain a clearer view of the energetics and kinetics of this reaction.

The present study has two objectives. The first is to use the MP2:DFT methodology to calculate accurate intrinsic energy barriers for the benzene alkylation with ethene and to derive rate coefficients for all elementary steps which are based on quantum chemical calculations that are converged with respect to both system size and methodology. The second objective is to generate adsorption energies and energy barriers that can be used as benchmarks in the development of computationally less expensive approaches such as hybrid QM:force field methods^{282,408,409} or DFT+Dispersion methods.^{397,399}

The elementary processes to which the hybrid MP2:DFT approach was applied are summarized in scheme 1. Included are physical adsorption of ethene, benzene, and ethylbenzene via π -complex formation with a Brønsted acid site, Reactions **1-3**; coadsorption of ethene and benzene on a Brønsted acid site, Reaction **4**; reaction of ethene with a Brønsted acid site to form an ethoxide species, Reaction **5**; benzene adsorption next to the ethoxide species, Reaction **6**; and ethene adsorption in purely siliceous MFI, Reaction **7**. Energy barriers and rate coefficients were calculated for the one-step scheme (1s) and for both steps of the two-step mechanism, 2s(1) and 2s(2) (see chapter 8 for details).

This chapter is organized as follows. Section 11.2 describes the computational methods used. Section 11.3 discusses the results which are presented separately for adsorption and reaction steps. The conclusions are drawn in section 11.4.

relaxation effects.²³⁸ Second, single-point MP2 and DFT calculations were conducted on clusters of increasing size cut out from the plane-wave DFT optimized structures to determine the periodic MP2-limit by extrapolation. Third, single-point MP2 calculations with increasing basis set size were performed to determine the complete basis set limit. Additionally, CCSD(T) calculations on small cluster models were carried out to account for higher order correlation effects.

11.2.1 DFT calculations applying periodic boundary conditions

DFT calculations applying periodic boundary conditions were performed using the ab-initio total-energy and molecular-dynamics program VASP (Vienna ab-initio simulation program).⁴¹⁰⁻⁴¹³ The gradient-corrected exchange-correlation functional proposed by Perdew, Burke, and Ernzerhof (PBE)^{72,73} was employed. Plane-wave calculations were conducted using the projector-augmented wave (PAW) method,⁴¹⁴ adapted by Kresse and Joubert.⁴¹⁵ The plane-wave basis set kinetic energy cut-off was set to 400 eV. Brillouin-zone sampling was restricted to the gamma point. The unit cell parameters α , β , and γ were fixed to 90° in all calculations as no significant deviation from the orthorhombic system is expected.⁴¹⁶⁻⁴¹⁸ To estimate whether the unit cell vector lengths significantly affect adsorption and activation energies, we calculated these properties for some steps using two different sets of cell dimensions. The first set ($a = 20.022$ Å, $b = 19.899$ Å, $c = 13.383$ Å; UC1) comes from crystallographic data,⁴¹⁹ while the second set ($a = 20.157$ Å, $b = 20.033$ Å, $c = 13.473$ Å; UC2) results from optimization of an all-silica unit cell as detailed in ref. 258. To create an acidic site, one of the 96 Si atoms in the unit cell was replaced by an Al atom in the T12 site⁴⁰⁸ and the resulting negative charge was compensated by a proton bonded to one of the neighbouring framework oxygen atoms. Specifically the Al12-O20(H)-Si3 site (numbering according to ref. 146) was chosen^{258,317,408} because of its location at the intersection between straight and sinusoidal channels; for details see section D.1 of the supporting information.

Minima on the PBE potential energy surface were located using the conjugate gradient algorithm with fully relaxed atomic positions. Convergence was considered to be achieved when forces were below 10^{-4} eV/Å. Energies were converged to 10^{-5} eV in all cases. Transition states were located by transferring optimized transition state structures from our cluster study presented in chapter 8 into the periodic environment and reoptimizing them using the improved-dimer method.¹⁶⁵ Transition state structures were con-

sidered converged when forces on all atoms were smaller than $0.05 \text{ eV}/\text{\AA}$. Stationary points were characterised by harmonic frequencies obtained by diagonalization of the full dynamical matrices. The force constants were obtained by numerical differentiation of forces with a step size of 0.02 \AA . No scaling factor was applied for the frequencies. DFT energy calculations for gas-phase molecules were carried out using cubic boxes with edge lengths of 25 \AA to minimize interactions with the periodic images.²⁵⁸

11.2.2 MP2 and DFT cluster calculations

For the evaluation of the high-level correction (equation 11.1) single-point energy calculations were performed on clusters cut out from the plane-wave DFT-optimized periodic structures. A series of 16 cluster models of increasing size was constructed for all stationary points with the largest cluster containing 30 T-atoms. The cluster models were saturated with hydrogen atoms such that the terminating groups were SiO-H ($r(\text{O-H}) = 0.967 \text{ \AA}$) or AlO-H ($r(\text{O-H}) = 0.963 \text{ \AA}$).⁴²⁰ Figure 11.1 shows adsorbed ethylbenzene as an example for the largest system considered.

For each cluster model and gas-phase molecule, MP2 energies were computed with the TURBOMOLE program package¹⁶² using basis sets of triple- ζ quality.¹⁶¹ For carbon atoms and those oxygen atoms which connect two T-

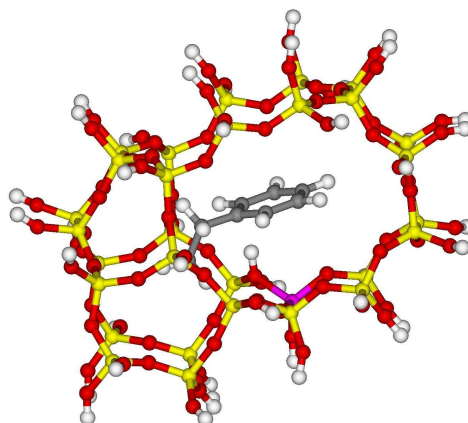


Figure 11.1: The largest system calculated with MP2/TZVP(P) in the present work is the 30T cluster with the overall composition $\text{C}_8\text{H}_{53}\text{O}_{81}\text{Si}_{29}\text{Al}$ (here: adsorbed ethylbenzene, viewed along the straight channel). Color codes: oxygen (red), silicon (yellow), aluminium (pink), hydrogen (white), carbon (gray).

atoms (T-O-T) the TZVPP basis set was chosen while for all other atoms the TZVP basis set was used. Following Tuma and Sauer,²³⁸ we denote this combination as TZVP(P) in the remainder of this chapter. We used the ‘ricc2’ module^{248,249} and employed the resolution of the identity (RI) approximation^{250–254} with optimized auxiliary basis sets^{255,256} in combination with a frozen-core approximation. Electrons in molecular orbitals corresponding to C 1s, O 1s, Al 1s, and Si 1s atomic orbitals were excluded from the MP2 correlation scheme.

DFT energies for each cluster model and gas phase molecule were computed within the RI approximation^{421–423} using the PBE functional^{72,73} and a basis set of quadruple- ζ quality (def2-QZVP).⁴²⁴ Energies were not corrected for BSSE which is expected to be negligible for this basis set. The employment of Gaussian-type orbitals (GTO) as basis sets for this part of the hybrid method differs from previous studies in which PBE energies for all cluster models were obtained with the same plane-wave methodology as was used for the periodic structure.^{238,258} However, it takes advantage of the fact that in GTO calculations the true dimensionality of the system is obeyed while in a plane-wave treatment of cluster models artificial effects such as interactions with replicated images have to be accounted for.⁴²⁵ Moreover, strict basis set consistency in calculating adsorption energies with plane-waves requires the use of the same box dimensions for each of the gas phase molecules, the adsorbed state and the unloaded state, necessitating a change in box size with increasing cluster size. To ensure the equivalency of both approaches, we have compared adsorption energies for ethene adsorption on the acid site for several cluster models. The energy difference between both approaches was below 0.5 kJ/mol leading us to conclude that the RI-DFT calculations employing GTO basis sets produce reliable results.

The differences between MP2 and PBE adsorption energies converge monotonically with the cluster size C_n (see below) and can be extrapolated to the periodic limit using the following analytical expression.²³⁸

$$E_{\text{HL-corr}}^{\text{fit}}(n) = E_{\text{disp}}(n) + E_{\text{add}} \quad (11.5)$$

It consists of an additive constant, E_{add} , which accounts for all effects contributing to MP2-PBE adsorption energy differences that do not strongly depend on the cluster size, for example the self-interaction correction (SIC) error, and a term

$$E_{\text{disp}}(n) = -s_6 \sum_i^{N_n-1} \sum_{j=i+1}^{N_n} \frac{\sqrt{C_6^i \cdot C_6^j}}{R_{ij}^6} f_d(R_{ij}), \quad (11.6)$$

which has the analytical form of a sum over damped atomic C_6 dispersion contributions for all atom pairs i and j at distance R_{ij} . N_n denotes the number of atoms in cluster \mathbf{C}_n . For the damping function $f_d(R_{ij})$ we use the functional form and the parameter values proposed by Grimme.³⁹⁹ The global scaling parameter, s_6 , depends on the particular exchange-correlation functional. For the PBE functional its value is 0.75.³⁹⁹ The five atomic C_6 coefficients, C_6^i , and the additional constant, E_{add} , are fitted for each reaction individually by minimizing

$$\Delta(\{C_6^i\}, E_{\text{add}}) = \sum_{n=1}^{n_{\text{max}}} [(\Delta E(n)_{\text{MP2}} - \Delta E(n)_{\text{PBE}}) - E_{\text{HL-corr}}^{\text{fit}}(n)]^2, \quad (11.7)$$

using a series of n_{max} cluster models \mathbf{C}_n of increasing size. The parameters obtained are given in section D.4 of the supporting information. Using the fitted C_6 parameters, $E_{\text{disp}}(\mathbf{S})$ is obtained by applying equation 11.6 to the periodic structure by means of lattice sums.³⁹⁷ The high-level correction for the periodic system \mathbf{S} ,

$$\Delta\tilde{E}(\mathbf{S})_{\text{high}} = \Delta\tilde{E}(\mathbf{S})_{\text{MP2}} - \Delta E(\mathbf{S})_{\text{PBE}} \approx E_{\text{disp}}(\mathbf{S}) + E_{\text{add}}, \quad (11.8)$$

has then to be added to the periodic DFT result, $\Delta E(\mathbf{S})_{\text{PBE}}$, to get estimates for the full ‘‘periodic’’ MP2 adsorption energy, $\Delta\tilde{E}(\mathbf{S})_{\text{MP2}}$, that has been introduced in equation 11.2.

The same procedure is applied to the apparent energy barriers which also show a monotonic decay. They are fitted according to eq. 11.7 and extrapolated to the periodic limit. The fit parameters obtained are given in section D.4 of the supporting information. In contrast, the high-level corrections for the intrinsic barriers have been obtained as difference of the high-level corrections of the apparent barriers and the respective adsorbate complexes. As shown in section D.3 of the supporting information, the differences between MP2 and PBE results for the intrinsic energy barriers depend only weakly on the cluster size and do not show a monotonic decay with increasing cluster size which makes fitting and direct extrapolation less reliable.

11.2.3 Complete basis set extrapolation

The incompleteness of Gaussian basis sets introduces an error in the MP2 calculations which can be accounted for approximately by extrapolation to the complete basis set (CBS) limit. BSSE-corrected^{426–428} RI-MP2 single-point energies obtained using Dunning’s correlation consistent polarized valence

triple- ζ and quadruple- ζ basis sets cc-pVXZ ($X = 3$ and 4)^{247,429} were used for this purpose. For the counterpoise-corrected Hartree-Fock (HF) energy contribution to the MP2 adsorption energy, $\Delta E_{\text{HF}}^{\text{cp}}(X)$, an exponential extrapolation scheme^{430,431} is employed,

$$\Delta E_{\text{HF}}^{\text{cp}}(X) = \Delta E_{\text{HF}}^{\text{CBS}} + b \exp(-cX), \quad (11.9)$$

while an inverse power law⁴³² is applied for the extrapolation of the counterpoise-corrected correlation energy contribution to the MP2 adsorption energy, $\Delta E_{\text{corr}}^{\text{cp}}(X)$,

$$\Delta E_{\text{corr}}^{\text{cp}}(X) = \Delta E_{\text{corr}}^{\text{CBS}} + bX^{-3}. \quad (11.10)$$

Following the recommendations in ref. 431 the parameter c in equation 11.9 is set to 1.5. The corresponding CBS limits, $\Delta E_{\text{HF}}^{\text{CBS}}$ and $\Delta E_{\text{corr}}^{\text{CBS}}$, along with the parameter b were calculated directly from two data points. The CBS limit correction, $\Delta E(\mathbf{C}_{\text{CBS}})_{\text{MP2}}^{\text{CBS}}$, was then obtained from

$$\begin{aligned} \Delta E(\mathbf{C}_{\text{CBS}})_{\text{MP2}}^{\text{CBS}} = & (\Delta E(\mathbf{C}_{\text{CBS}})_{\text{HF}}^{\text{CBS}} + \Delta E(\mathbf{C}_{\text{CBS}})_{\text{corr}}^{\text{CBS}}) - \\ & (\Delta E(\mathbf{C}_{\text{CBS}})_{\text{HF}}^{\text{TZVP(P)}} + \Delta E(\mathbf{C}_{\text{CBS}})_{\text{corr}}^{\text{TZVP(P)}}), \end{aligned} \quad (11.11)$$

which is the difference between BSSE-corrected adsorption energies extrapolated to the complete basis set limit and BSSE-uncorrected adsorption energies obtained with the TZVP(P) basis set calculated for cluster model \mathbf{C}_{CBS} . $\Delta E(\mathbf{C}_{\text{CBS}})_{\text{MP2}}^{\text{CBS}}$ is added to $\Delta \tilde{E}(\mathbf{S})_{\text{MP2}}$ obtained from equation 11.8 to get a BSSE-free MP2 adsorption energy for the periodic structure. This summation requires that the CBS limit correction is either independent of the cluster size or can at least be assumed constant from a certain cluster size on. To see whether one of these conditions is fulfilled we calculated $\Delta E(\mathbf{C}_{\text{CBS}})_{\text{MP2}}^{\text{CBS}}$ for clusters of increasing size. Due to the computational expense of these calculations we performed them only for clusters containing a maximum of 18 T-atoms.

A similar procedure can also be used for the intrinsic activation energies. However, as both the energy of the reactant structure and that of the transition state are calculated with the same number of basis functions the counterpoise procedure⁴²⁶ does not apply and may even lead to artificial results.⁴³³ Therefore the CBS limit corrections for intrinsic activation energies were obtained indirectly from the CBS limit corrections of the apparent activation energies and those of the associated adsorbate complex.

11.2.4 PBE+D//PBE calculations

With PBE+D//PBE we denote the evaluation of the energy of plane-wave DFT-optimized structures according to

$$E(\mathbf{S})_{\text{PBE+D//PBE}} = E(\mathbf{S})_{\text{PBE}} + E_{\text{disp}}(\mathbf{S}), \quad (11.12)$$

with the dispersion term given in equation 11.6 using the *transferable* C_6 -coefficients of Grimme.³⁹⁹ Adsorption energies calculated in this way still contain the self-interaction error but are significantly less expensive to obtain than those determined from the full MP2:DFT calculation because equation 11.6 can be applied directly to the periodic unit cell optimized by plane-wave DFT. By doing so, the computationally expensive determination of MP2 and DFT adsorption energies for a series of clusters as well as the basis set limit extrapolation procedure are avoided. It is therefore of great interest to evaluate further the transferability of the C_6 -coefficients published by Grimme³⁹⁹ to solid state and surface problems.³⁹⁷

11.2.5 CCSD(T) calculations

The reliability of MP2 to predict adsorption energies and energy barriers for the alkylation was assessed by performing single-point CCSD(T) calculations for all stationary points on a modified 3T cluster model. This modified model was obtained from the 3T model used in the cluster series calculations by replacement of SiO-H by Si-H terminations with a Si-H bond length of 1.455 Å²⁵⁸ (see figure 11.2). The CCSD(T) calculations were carried out with the

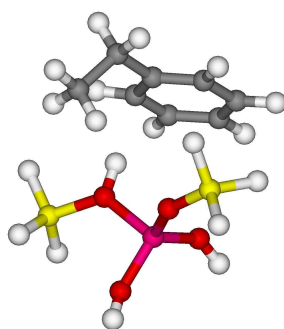


Figure 11.2: The largest system calculated with CCSD(T)/def2-TZVP in the present work is a 3T cluster with the overall composition $\text{C}_8\text{H}_{19}\text{O}_4\text{Si}_2\text{Al}$ (here: adsorbed ethylbenzene). Color codes: oxygen (red), silicon (yellow), aluminium (pink), hydrogen (white), carbon (gray).

MOLPRO code⁴³⁴ employing Ahlrichs' improved triple- ζ basis set⁴³⁵ (def2-TZVP), obtained from the EMSL Basis Set Exchange website,^{436,437} for all atoms. For our *final estimates* of adsorption energies and energy barriers we add the difference between CCSD(T) and RI-MP2 adsorption energies and energy barriers calculated on the same 3T cluster, $\Delta E(\mathbf{C}_3)_{\text{CCSD(T)}}$, to the "periodic" MP2 adsorption energies and energy barriers.

11.2.6 Calculation of intrinsic rate coefficients

Intrinsic rate coefficients are calculated from conventional transition state theory,^{101,102}

$$k(T) = \sigma \frac{k_{\text{B}}T}{h} \frac{Q_{\text{TS}}(T)}{Q_{\text{R}}(T)} \exp\left(\frac{-E^{\ddagger}}{RT}\right), \quad (11.13)$$

where k_{B} is Boltzmann's constant, h is Planck's constant, T is the absolute temperature and E^{\ddagger} is the difference in electronic energies between the transition state and the reactant state. With σ we denote a reaction path symmetry number⁴³⁸ while Q_{TS} and Q_{R} are the partition functions of the transition state and the reactant state, respectively. The most straight forward method to calculate the partition functions is to assume immobile adsorption, that is, a complete conversion of frustrated rotational and translational degrees of freedom into vibrations. However, contributions from low vibrational modes corresponding to rotational and translational movements of adsorbate molecules are often not adequately taken into account by this treatment⁴³⁹ and may lead to an underestimation of the partition function. As is shown in section D.2 of the supporting information, the assumption of immobile adsorption is a reasonable approximation for both the one-step mechanism and the elementary steps of the two-step mechanism.

11.3 Results and discussion

11.3.1 Adsorption of reactants and products

Periodic DFT structure optimization

Table 11.1 lists adsorption energies obtained for the two different sets of unit cell parameters. It can be seen that the interaction energy with the acid site increases in the order $\text{C}_8\text{H}_{10} < \text{C}_6\text{H}_6 < \text{C}_2\text{H}_4$ for the first set of unit cell parameters while for the second set C_6H_6 and C_8H_{10} show almost the same adsorption energy. The adsorption energy of ethene is hardly influenced by

Table 11.1: DFT (PBE) results for adsorption energies, ΔE , ZPVE-corrected adsorption energies, ΔE_0 , and adsorption enthalpies at 298 K, ΔH_{298} . Energies are reported in kJ/mol.

reaction	UC1			UC2		
	ΔE	ΔE_0	ΔH_{298}	ΔE	ΔE_0	ΔH_{298}
1	-31.5	-30.1	-29.0	-31.4	-28.8	-27.5
2	-24.0	-24.2	-21.6	-19.6	-19.5	-16.4
3	-16.6	-13.9	-11.5	-20.0	-18.0	-15.5
4	-40.7	-34.3	-30.4	-42.4	--	--
5	-53.5	-43.1	-45.7	-43.8	--	--
6^a	-2.0	2.1	5.1	-7.0	--	--
7^b	-4.2	-6.1	-1.4	--	--	--

^aThe ethyl group is bonded to O24.

^bAdsorption in channel intersection.

the size of the unit cell, while for benzene and ethylbenzene the changes are 4.3 kJ/mol and -3.4 kJ/mol when going from UC1 to UC2. For ethylbenzene adsorption it was confirmed that the electronic energy obtained with UC1 is reproduced when starting the structure optimization from the stationary point obtained with UC2 after adjusting the cell parameters according to UC1. It can therefore be concluded that the energy differences result exclusively from the change in cell parameters. To estimate the effect of the cell parameters on ZPVE- and finite temperature corrections we have computed these numbers for single molecule adsorption on the acid site using the UC2 cell parameters. The largest effect is obtained for ethene for which the thermal correction is higher by 1.5 kJ/mol for the UC2 cell parameters. For ethene located in pure silica MFI we have also calculated the energy of adsorption in the straight and sinusoidal channels, respectively, in addition to adsorption in the channel intersections. The electronic adsorption energies are +0.4 kJ/mol and -4.2 kJ/mol, respectively. The orientation of all adsorbate molecules within the unit cell is shown in figure 11.3

The absence of imaginary frequencies confirmed that all stationary points were true minima. The zero-point vibrational energies calculated from these PBE frequencies are shown in table 11.2 (7th row). The calculated wave numbers for the O-H stretching modes are 3705 cm⁻¹ (UC1, H on O20) and 3709 cm⁻¹ (UC2, H on O20), respectively, in good agreement with other theoretical studies on H-FER (3680 cm⁻¹)⁵⁹ and H-MOR (3709 cm⁻¹)⁴⁴⁰ employing similar plane-wave calculations. The calculated frequencies are lar-

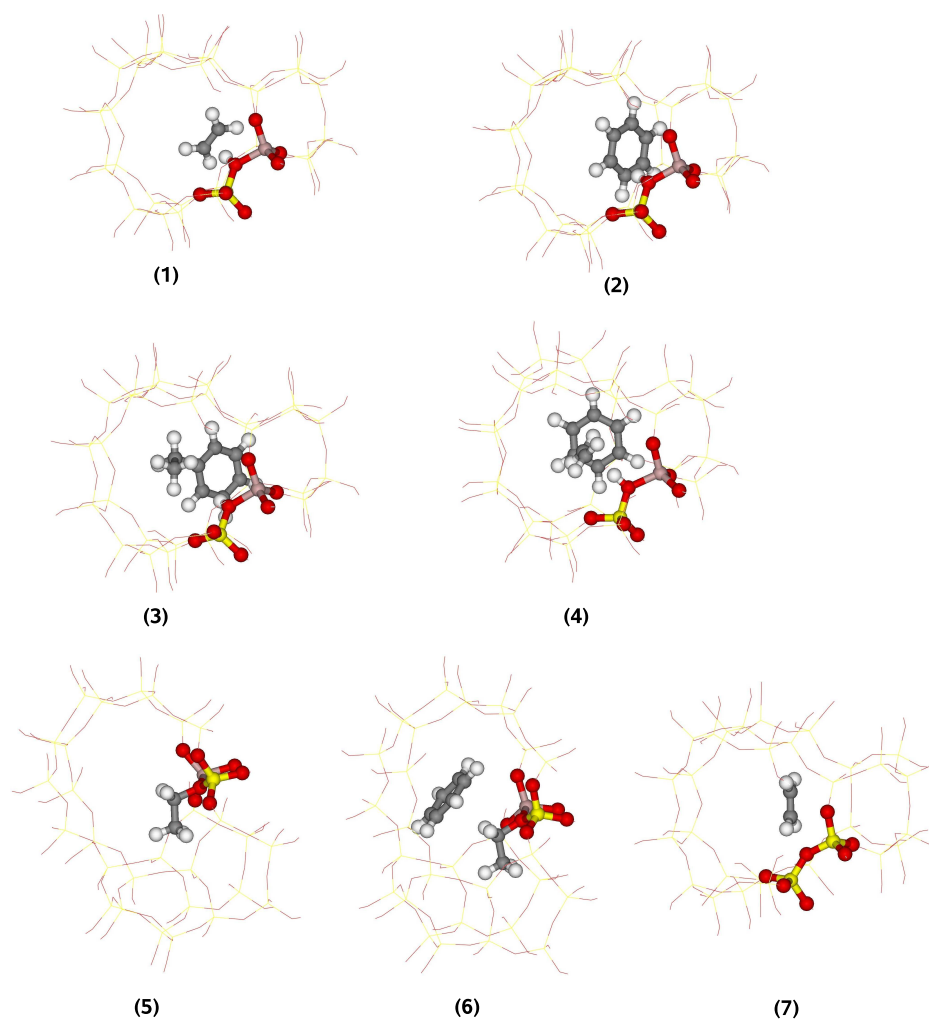


Figure 11.3: Adsorbed ethene, benzene, and ethylbenzene (1–3), coadsorbed ethene and benzene (4), ethoxide (5), benzene adsorbed next to ethoxide (6), and ethene adsorbed in the channel intersection of all-silica MFI (7).

ger than the experimental wave numbers of 3623 cm^{-1} (at 170 K)⁴⁴¹ and 3612 cm^{-1} (at 300 K)^{441,442}, as expected, due to the limited accuracy of harmonic DFT force constants and neglect of anharmonicities. The calculated redshifts of the O-H stretching modes induced by adsorption of ethene and benzene, -535 cm^{-1} and -498 cm^{-1} , respectively, are larger than the experimental values of -398 cm^{-1} (ref. 443) and -360 cm^{-1} (ref. 444), which is also a known characteristic of gradient corrected functionals in general and PBE

in particular.⁴⁴⁵ However, the difference of -38 cm^{-1} between the experimentally observed redshifts for ethene and benzene adsorption is predicted well by the calculated value (-38 cm^{-1}) leading us to conclude that the calculated adsorption complexes are reasonable representations of the precursors at the acid site.

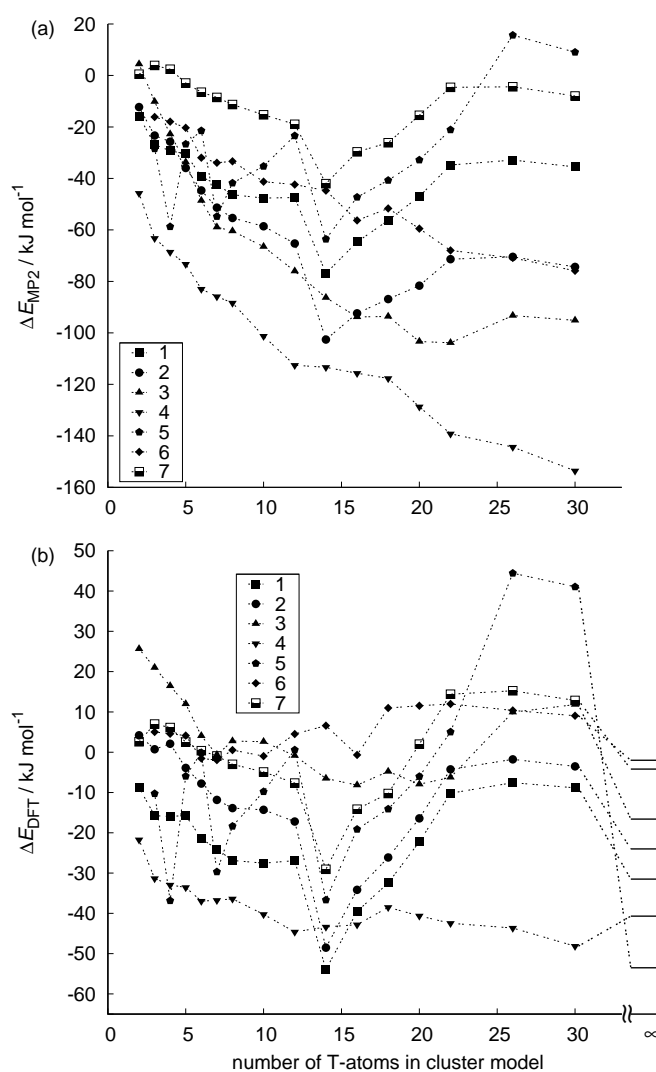


Figure 11.4: Adsorption energies obtained from single-point energy calculations on cluster models of increasing size. (a) MP2/TZVP(P) results. (b) DFT (PBE/QZVP) results. The periodic model limit is included for comparison.

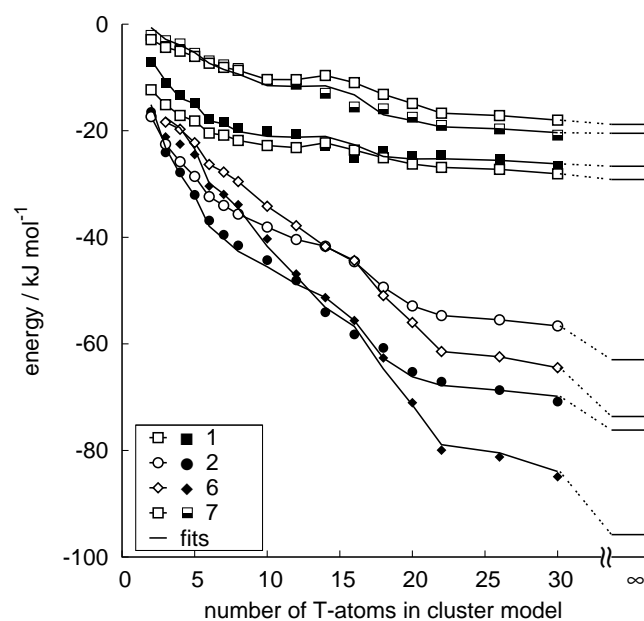


Figure 11.5: Differences in adsorption energies between MP2 and PBE (filled and partly filled symbols) and dispersion contributions to the adsorption energies as predicted by the parameter set published by Grimme³⁹⁹ (open symbols). Extrapolations to the full periodic limit are also included.

Cluster model convergence

Figure 11.4 shows the results of the single-point MP2 and PBE cluster calculations. The adsorption energies do not show a systematic behavior as a function of the cluster size. Up to a certain cluster size the adsorption energies become more negative and then less negative or even positive. Neither the size of the cluster at which the energies have their lowest value nor the magnitude by which the energies increase again seem to be predictable. If however the high-level correction is plotted, that is, the difference between MP2 and PBE adsorption energies, $\Delta E(\mathbf{C})_{\text{MP2}} - \Delta E(\mathbf{C})_{\text{PBE}}$, decreasing curves are obtained that converge asymptotically (see figures 11.5 and 11.6). With the exceptions of ethene physisorption and chemisorption (ethoxide formation) the decay is monotonic. These adsorption energy differences are used for fitting the analytical expression given in equation 11.6. The fit parameters and mean errors are presented in section D.4 of the supporting information. The high-level corrections, $\Delta \tilde{E}(\mathbf{S})_{\text{high}}$, are summarized in row 2 of table 11.2. Additional calculations addressing the influence of the cluster termination and

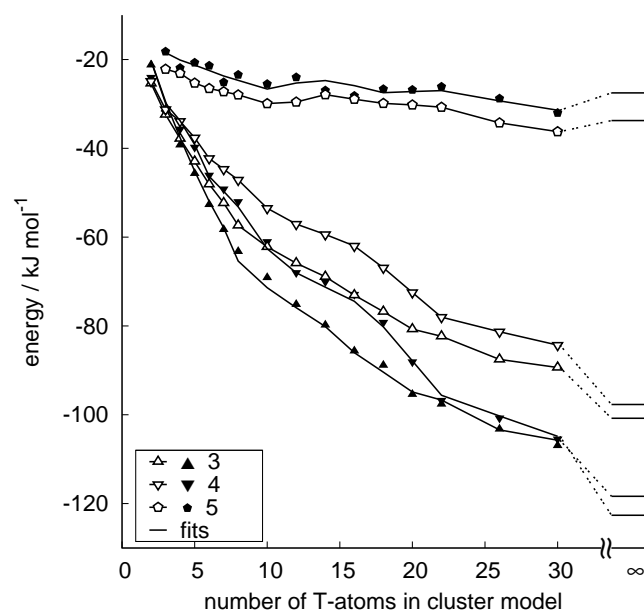


Figure 11.6: Differences in adsorption energies between MP2 and PBE (filled symbols) and dispersion contributions to the adsorption energies as predicted by the parameter set published by Grimme³⁹⁹ (open symbols). Extrapolations to the full periodic limit are also included.

the size of the unit cell from which the clusters were cut out, revealed that the high-level corrections are insensitive towards these issues (see section D.3 of the supporting information for a detailed discussion).

PBE+D//PBE results

Also shown in figures 11.5 and 11.6 are the dispersion contributions to the adsorption energies which are predicted using the set of *transferable* C_6 -parameters proposed by Grimme³⁹⁹ (open symbols). With the exception of ethene physisorption on the acid site and the formation of the ethoxide, the dispersion energy predicted by the Grimme parameters is less negative than the one obtained from the cluster series. It has to be kept in mind, however, that for the *final estimate* of the energy the positive basis set limit correction needs to be added which reduces the difference to PBE+D//PBE adsorption energies (see below). The dispersion energies for the periodic system, $\Delta E(\mathbf{S})_{\text{D//PBE}}$, are summarized in row 10 of table 11.2.

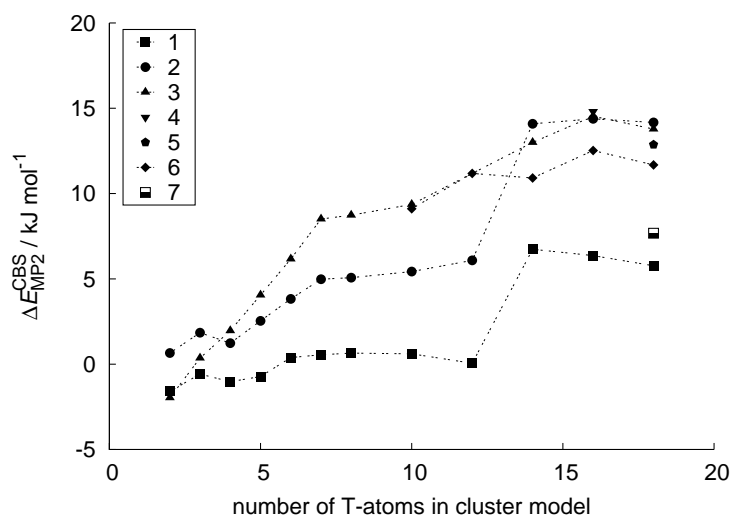


Figure 11.7: CBS-limit corrections for the formation of structures **1** to **7**. For structures **4**, **5**, and **7** the CBS-limit correction was calculated for one cluster size only (16T and 18T, respectively).

Extrapolation to complete basis set limit

Figure 11.7 shows the complete basis set limit correction for ethene, benzene, and ethylbenzene adsorption as well as for benzene adsorption next to the surface ethoxide as function of the cluster size for up to 18 T-atoms. The CBS-limit correction increases with the cluster size, although not always monotonically. Beyond the 14T cluster there are only weak changes of the CBS-limit correction for ethene and benzene which makes it reasonable to take the values from the 18T clusters as estimates for the periodic limit. For ethylbenzene and benzene adsorbed next to ethoxide, the CBS-limit corrections increase up to 16 T-atoms and level off for 18 T-atoms. Here we also took the numbers from the 18T clusters as estimates for the periodic limit. For the co-adsorption of ethene and benzene the CBS-limit correction was computed only for the T16 cluster because of the high computational costs associated with a 3-body counter poise correction. For the formation of ethoxide and for ethene adsorption in all-silica MFI, we computed the CBS-limit correction only for the T18 cluster. Note that the BSSE calculation for the ethoxide structure assumes fragments that resemble the corresponding carbenium ion and the negatively charged zeolite framework. The CBS-limit corrections used as estimates for the periodic limit are listed in the third row of table 11.2.

CCSD(T) corrections

The CCSD(T) corrections are listed in the fourth row of table 11.2. Compared to the previous application of the hybrid scheme to the protonation of isobutene in zeolite ferrierite,²³⁸ the CCSD(T) corrections computed in the present work are always positive. It should be noted that the CCSD(T) correction as defined above contains two contributions, the difference between CCSD(T) and canonical MP2 adsorption energies which are obtained along the CCSD(T) calculations and the difference between canonical MP2 results and RI-MP2 results. The latter difference is less or equal to 2 kJ/mol. Consequently, the “real” CCSD(T) corrections to the MP2:DFT adsorption energies are less than 8%. This is somewhat larger than in former applications of the hybrid scheme^{238,258} and might be attributed to the known tendency of MP2 to overrate electron correlation effects in unsaturated systems and complexes.⁴⁴⁶ We therefore note that the calculation of CCSD(T) corrections is an essential part of the hybrid approach in the present case.

Final estimates of adsorption energies and comparison with experimental data

The *final estimates* of the hybrid MP2:DFT adsorption energies are obtained from the sum of the PBE energy, the high-level correction extrapolated to the periodic limit, the complete basis set limit (CBS) correction, and the CCSD(T) corrections, eq. 11.3. Table 11.2 summarizes all of these contributions. The differences between the *final estimates* and the PBE results are substantial. For the physisorption structures **1–4** and **6–7** they are between 6.2 and 13.4 kJ/mol per CH_X unit. For ethylbenzene (**3**) and the co-adsorption of ethene and benzene (**4**) the total difference is as large as 100 kJ/mol. There are not only substantial quantitative changes, but also qualitative ones. PBE predicts the counter-intuitive sequence ethene > benzene > ethylbenzene for the adsorption strength, whereas our *final estimates* reverse this sequence.

In addition, table 11.2 contains the PBE+D//PBE adsorption energies calculated with the transferable parameters of Grimme,³⁹⁹ which show a substantial improvement compared to PBE results. The deviation from the *final estimates* is small, -6.4, -2.3, +2.7, and +6.6 kJ/mol (-8, -2, +2, and +8%) for **2**, **3**, **4**, and **6**, respectively, i. e. for all physisorption steps except ethene. For ethene physisorption on the silica wall (**7**), on the Brønsted site (**1**), and for ethoxide formation (**5**), PBE+D overestimates the binding energies by 6.5, 12.4, and 26 kJ/mol, in agreement with previous work for isobutene on H-FER.^{397,407}

Table 11.2: Adsorption energies obtained using the hybrid MP2:DFT scheme and PBE+D adsorption energies at the PBE optimized structures as predicted by the parameters of Grimme.³⁹⁹ Zero-point vibrational energies and thermal contributions to adsorption enthalpies are also included. Energies are reported in kJ/mol.

	1	2	3	4	5	6	7 ^a
$\Delta E(\mathbf{S})_{\text{PBE}}$	-31.5	-24.0	-16.6	-40.7	-53.5	-2.0	-4.2
$\Delta \tilde{E}(\mathbf{S})_{\text{high}}$	-26.7 ^b	-76.2 ^c	-118.3	-122.6	-27.5	-95.8	-20.5
$\Delta E(\mathbf{C}_{18})_{\text{MP2}}^{\text{CBS}}$	5.8	14.2	13.8	14.8 ^d	12.9	11.7	7.7
$\Delta E(\mathbf{C}_3)_{\text{CCSD(T)}}^{\text{e}}$	4.1	5.5	6.1	7.5	6.9	3.9	0.5
$\Delta \tilde{E}(\mathbf{S})_{\text{final estimate}}$	-48.3	-80.5	-115.1	-141.0	-61.3	-82.2	-16.5
difference to PBE	-16.8	-56.5	-98.5	-100.3	-7.7	-80.2	-12.3
$\Delta E(\mathbf{S})_{\text{ZPV}}$	1.4	-0.2	2.8	6.4	10.5	4.1	-1.9
$\Delta H(\mathbf{S})_{298} - \Delta E_0(\mathbf{S})_{\text{PBE}}^{\text{f}}$	1.1	2.6	2.3	3.9	-2.6	3.0	4.7
$\Delta H(\mathbf{S})_{653} - \Delta E_0(\mathbf{S})_{\text{PBE}}^{\text{g}}$	6.5	8.5	7.2	14.2	0.3	8.5	11.6
$\Delta E(\mathbf{S})_{\text{D//PBE}}$	-29.2	-63.0 ^h	-100.8	-97.7	-33.7	-73.6	-18.8
$\Delta E(\mathbf{S})_{\text{PBE+D//PBE}}$	-60.6	-86.9	-117.4	-138.3	-87.3	-75.6	-23.0

^aadsorption in channel intersection.

^bthis value remains the same for Al-O-Si(OH)₃ instead of Al-O-H termination.

^c-76.5 kJ/mol for the second set of unit cell parameters.

^dfor 16T cluster.

^edifference between CCSD(T) and RI-MP2 adsorption energies on a 3T cluster.

^fcontribution to enthalpy at 298 K ($\Delta E_0(\mathbf{S})_{\text{PBE}}$ is the ZPVE corrected adsorption energy).

^gcontribution to enthalpy at 653 K ($\Delta E_0(\mathbf{S})_{\text{PBE}}$ is the ZPVE corrected adsorption energy).

^h-60.9 kJ/mol for the second set of unit cell parameters.

Before we compare with experiment, we will make an attempt to determine the uncertainty of our *final estimates*. Different choices of the unit cell size in the DFT/plane-wave structure optimization lead to differences of up to around 5 kJ/mol in the adsorption energy. The use of DFT/plane-wave structures instead of reoptimizing the structures at the hybrid MP2:DFT level may lead to changes of up to 10 kJ/mol, as we learn from comparing DFT and DFT+D optimization results.³⁹⁷ Additional uncertainties are introduced by the fitting procedure and the extrapolation to the CBS limit. The maximum deviation between the reference data points and the fitted values are 3.7 kJ/mol (see table D.3 of the supporting information). Following ref. 258 we estimate the uncertainty in the CBS limit to ± 2.5 kJ/mol. As a conservative assumption, a range of ± 10 kJ/mol accounts for all uncertainties of our methodology, in agreement with previous applications of the hybrid MP2:DFT approach.^{238,258}

Table 11.3: Comparison of calculated adsorption energies and enthalpies with experiments (in kJ/mol).

		PBE+D	<i>final estimate</i>		Obsd
		$-\Delta E$	$-\Delta E$	$-\Delta H$	
Ethene	MFI, sinusoidal channel	32.9		(23.6) ^g	24–31 ^a
	MFI, intersection	23.0	16.5	13.7	
	H-MFI, Al12-O20(H)-Si3	60.6	48.3	45.8	38 ^b
Benzene	H-MFI, Al12-O20(H)-Si3	86.9	80.5	78.1	63.6 ^c 64±5 ^d
Ethylbenzene	H-MFI, Al12-O20(H)-Si3	117.4	115.1	110.0	87±5 ^d
Isobutene	FER	65.7 ⁱ		(48.1) ^h	49 ^e
Isobutene	H-FER	90.5 ^k	77.2 ^k	72.9 ^k	59–63 ^f

^asee ref. 447 for original references.

^bH,Na-Y zeolite, ref. 262.

^ccalorimetry, 1 molec/uc, Si/Al=86, ref. 266.

^d2 molec/uc, Si/Al=34, but large amounts of extraframework Al, ref. 265.

^ebut-1-ene in MFI (silicalite-1), ref. 448.

^festimated, see ref. 238.

^gestimated from PBE+D difference to intersection and the *final estimate* for the latter.

^hestimated from PBE+D difference to H-FER and the *final estimate* for the latter.

ⁱref. 397.

^krefs 238,407.

Table 11.3 compares adsorption enthalpies calculated from our *final estimates* by adding the zero-point vibrational energies and thermal corrections evaluated from PBE frequencies with available experimental data. Experimental heats of adsorption for ethene in acidic H-ZSM-5 are not available directly. The calculated enthalpy of adsorption at the acid site, -45.8 kJ/mol, is compared with the experimental value for an H,Na-Y zeolite.²⁶² Adsorption enthalpies in the aluminium free analogue, silicalite-1, are ranging from -24 to -31 kJ/mol (see ref. 447 and references therein). For ethene, adsorption in the channel intersections is not most favourable. Additional PBE+D//PBE calculations for two representative adsorption sites in the sinusoidal and straight channel yield -32.9 and -30.0 kJ/mol, respectively. If the difference of 9.9 kJ/mol between the sinusoidal channel and the intersection is added to the *final estimate* for the channel intersection, an ΔH value of -23.6 kJ/mol is obtained.

For benzene adsorption in H-ZSM-5, the most reliable experimental res-

ult (calorimetry, ref. 266) is -63.6 kJ/mol. Other results are ranging from -59.0 to -69.0 kJ/mol (see ref. 317 and references therein) indicating an uncertainty range of ± 5 kJ/mol. The experimental enthalpy of adsorption for ethylbenzene, (-87 kJ/mol, ref. 265), is 23 kJ/mol more negative than that for benzene.

The calculated adsorption enthalpies for ethene, isobutene (refs 238,407), benzene and ethylbenzene are more negative by 8, 10–14, 14, and 23 kJ/mol, respectively, than the experimental values. This small (2–4 kJ/mol per CH_x unit) and systematic overestimation of the strength of the binding to the Brønsted acid site we ascribe to the fact that the experimental sample contains a distribution of sites over different crystallographic positions and that these sites are not ordered into unit cells. In contrast, our calculated values refer to one particular site chosen such that the adsorbate can maximize its interaction with the acid site on the zeolite surface (channel intersection). Compared to previous B3LYP T33 cluster results for ethene, benzene, and ethylbenzene (see chapter 8), which were 3, 24, and 48 kJ/mol, respectively, too small (in absolute terms) our *final estimate* adsorption enthalpies are substantially improved.

11.3.2 Reaction steps

Periodic DFT structure optimization

Table 11.4 summarizes intrinsic energy and enthalpy barriers for the one-step and the two-step alkylation. The PBE energy barrier of the one-step alkylation is lower than the energy barriers of the two-step mechanism in contrast to what was found in our cluster study reported in chapter 8. There, the DFT-energy barrier of the ethoxide formation was the lowest of all elementary steps. Note that the energy barriers for the one-step mechanism and for the first step of the two-step scheme are hardly influenced by the set of unit cell parameters used in the calculation. Therefore, there is virtually no uncertainty connected with the choice of the unit cell for these elementary reactions. Only for the second barrier of the two-step scheme a difference of 6.1 kJ/mol is observed. To confirm that this difference is entirely attributable to the change in cell parameters we have changed the cell parameters of the UC2 transition state to UC1 and reoptimized the structure. The total energy of the UC1 transition state was reproduced within 0.1 kJ/mol. For the first step of the two-step mechanism we have calculated the zero-point vibrational energy and thermal correction for both, the UC1 and UC2 cell parameters. However, the influence of the cell size is rather small. The largest difference

Table 11.4: DFT (PBE) results for intrinsic energy barriers, E^\ddagger , ZPVE-corrected intrinsic energy barriers, E_0^\ddagger , and intrinsic enthalpy barriers at 650 K, H_{650}^\ddagger , for the one-step alkylation (1s) and the two-step alkylation (2s(1) and 2s(2)).

reaction channel	UC1			UC2		
	E^\ddagger	E_0^\ddagger	H_{650}^\ddagger	E^\ddagger	E_0^\ddagger	H_{650}^\ddagger
1s	84.3	79.5	71.9	84.3	--	--
2s(1)	91.6	89.3	80.7	91.2	87.0	79.3
2s(2)	95.9	90.9	87.1	89.8	--	--
1s, rev	173.1	158.5	158.1	174.8	--	--
2s(1), rev	113.7	102.3	99.8	103.5	--	--
2s(2), rev	169.9	163.2	161.2	171.9	--	--

(1.9 kJ/mol) is obtained for the ZPVE correction. Regarding the influence of the unit cell size on the reverse reactions, only the first barrier of the two-step mechanism is affected. The reverse barrier of this step is lower by 10.2 kJ/mol for the UC2 set of cell parameters which is a consequence of the lower stability of the ethoxide species in this unit cell. The frequency analysis revealed the presence of exactly one imaginary frequency for all transition structures, which are illustrated in figure 11.8.

Cluster model convergence

Figure 11.9 shows the cluster size dependence of the apparent energy barriers, $E_{\text{app}}^\ddagger(\mathbf{C})$, for forward and reverse reaction steps obtained from single-point MP2 and PBE cluster calculations. Note that for the first step of the 2-step mechanism, an apparent energy barrier for the reverse reaction is not required because the intrinsic barrier is calculated from the apparent energy barrier of the forward reaction and the reaction energy for ethoxide formation from the unloaded zeolite cluster and ethene in the gas phase. For the second step of the 2-step mechanism we calculated the apparent energy barrier of the forward reaction with respect to the unloaded cluster and ethene and benzene in the gas phase and not with respect to ethoxide and benzene in the gas phase because a better fit of the MP2-PBE difference was achieved for the former choice. In contrast to the adsorption energies, the apparent energy barriers decrease uniformly with increasing cluster size. However, even for the largest cluster they have not converged and in most cases differ substantially from the periodic limit (see figure 11.9(b)). If the difference between the MP2

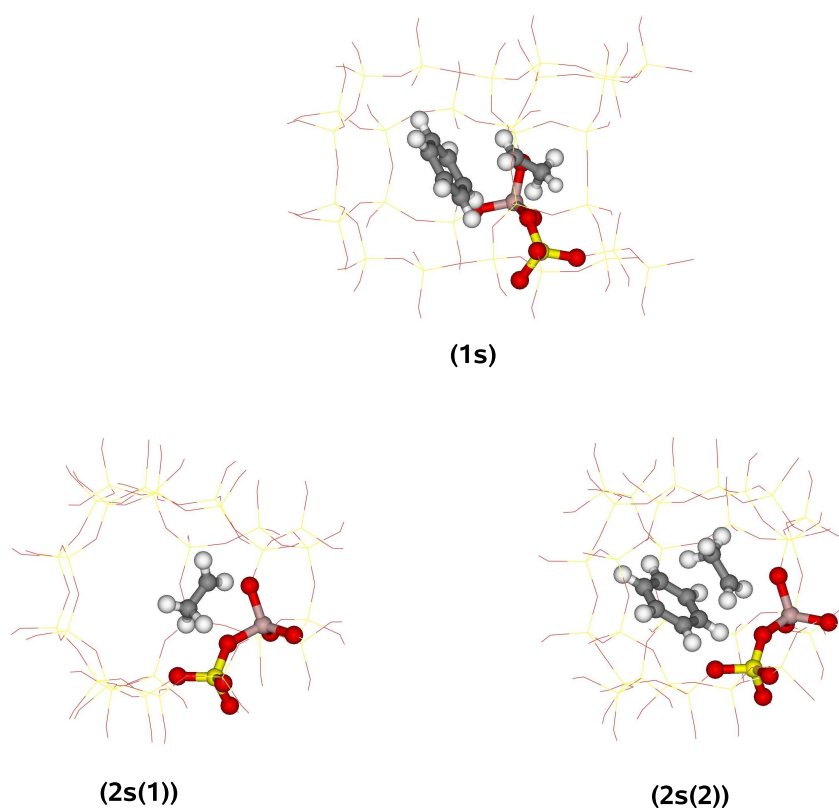


Figure 11.8: Transition state structures for one-step and two-step alkylation.

and PBE apparent energy barriers is plotted, decaying curves are obtained that converge asymptotically and can be fitted to the analytical expression given in equation 11.6 (see figure 11.10). The fit parameters and mean errors are presented in section D.4 of the supporting information accompanying this chapter. Contrary to the apparent energy barriers, the differences between MP2 and PBE intrinsic energy barriers do not show a convergent behavior with the cluster size and therefore cannot be fitted to the analytical dispersion energy expression. The corresponding graphs are presented in section D.3 of the supporting information. The high-level corrections for the intrinsic energy barriers have been obtained by taking the difference between the high-level corrections for the apparent energy barriers and the high-level corrections of the corresponding adsorbate complexes. These energies are listed in the second row of table 11.5. The PBE intrinsic barriers for the one-step scheme and for the first step of the two-step scheme are substantially

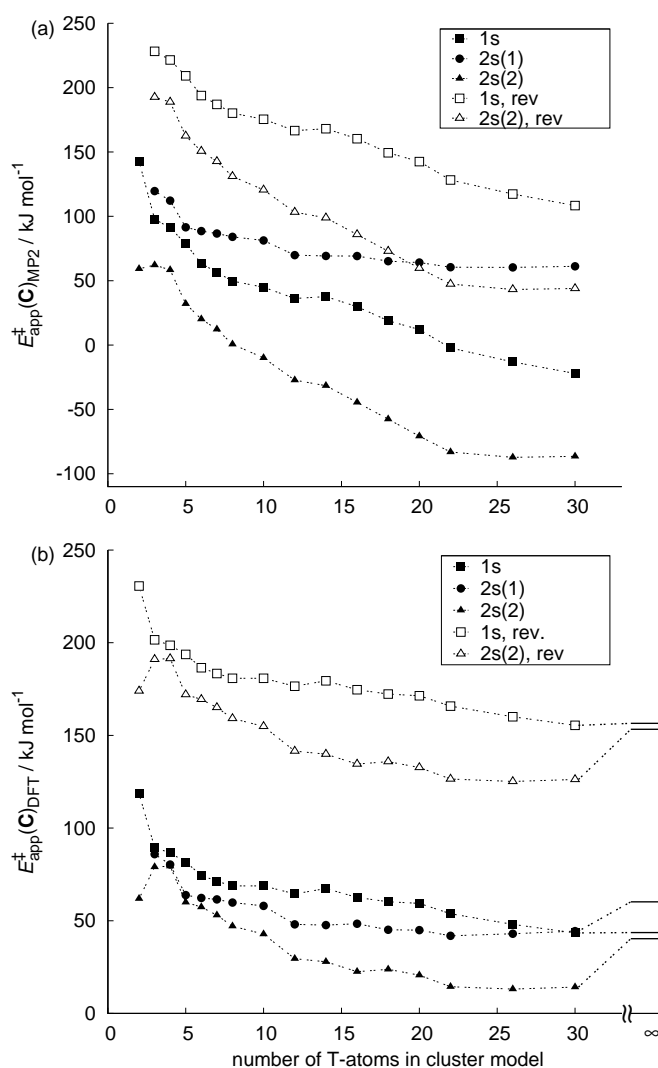


Figure 11.9: Apparent activation energies for the one- and two-step alkylation obtained from single-point energy calculations on cluster models of increasing size. (a) MP2/TZVP(P) results. (b) DFT (PBE/QZVP) results. The periodic model limit is included for comparison.

increased by the high-level corrections. For the second barrier of the two-step scheme the high-level correction is significantly smaller.

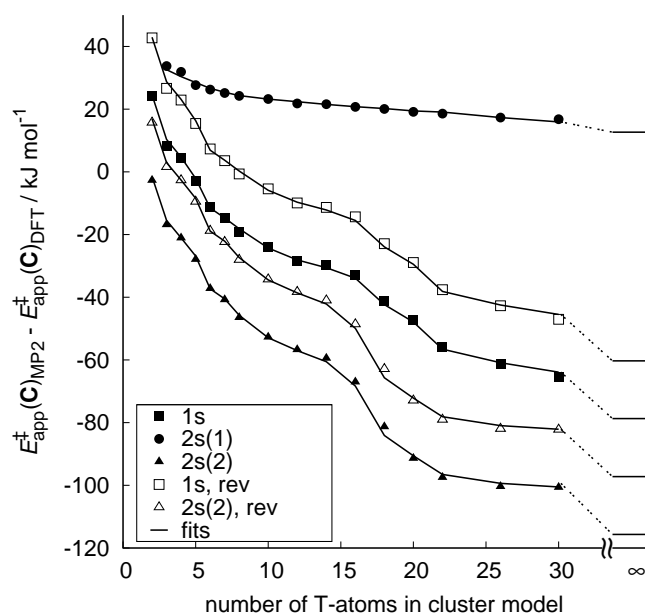


Figure 11.10: Differences between the two series of apparent activation energies shown in figure 11.9 and extrapolation to the periodic limit.

Extrapolation to complete basis set limit

The complete basis set limit correction for each intrinsic energy barrier has been determined as the difference between the CBS-limit correction for the apparent energy barrier and the CBS-limit correction for the formation of the corresponding adsorption complex. Depending on the reaction channel, different fragmentations of the system have been used in the counterpoise calculation (see section D.5 of the supporting information for details). The CBS-limit corrections for the intrinsic energy barriers are listed in the third row of table 11.5.

CCSD(T) corrections

CCSD(T) corrections are listed in the fourth row of table 11.5. For the forward reaction steps the difference between CCSD(T) and RI-MP2 is relatively small (+0.5, -1.9, and -1.0 kJ/mol) showing that RI-MP2 yields energy barriers of CCSD(T) quality. For the reverse reactions larger CCSD(T) corrections are obtained (-12.8, -4.7, and -11.0 kJ/mol) which indicate an overstabilization of the reaction product, adsorbed ethylbenzene, by MP2.

Table 11.5: Intrinsic energy barriers obtained using the hybrid MP2:DFT scheme and PBE+D intrinsic energy barriers at the PBE optimized structures as predicted by the parameters of Grimme.³⁹⁹ Zero-point vibrational energies and thermal contributions to enthalpy barriers are also included. Energies are reported in kJ/mol.

	1s	1s, rev	2s(1)	2s(1), rev	2s(2)	2s(2), rev
$E^\ddagger(\mathbf{S})_{\text{PBE}}$	84.3	173.1	91.6	113.7	95.9	169.9
$\Delta\tilde{E}^\ddagger(\mathbf{S})_{\text{high}}$	43.9	58.1	39.9	40.2	7.4	21.1
$\Delta E^\ddagger(\mathbf{C}_{16})_{\text{MP2}}^{\text{CBS}}$	1.0	2.5	0.6	-6.5	0.2	10.4
$\Delta E^\ddagger(\mathbf{C}_3)_{\text{CCSD(T)}^{\text{a}}}$	0.5	-12.8	-1.9	-4.7	-1.0	-11.0
$\tilde{E}^\ddagger(\mathbf{S})_{\text{final estimate}}$	129.7	220.9	129.7	142.7	102.5	190.3
difference to PBE	45.4	47.8	38.1	29.0	6.6	20.4
$\Delta E^\ddagger(\mathbf{S})_{\text{ZPV}}$	-4.8	-14.7	-2.4	-11.4	-5.0	-6.7
$H^\ddagger(\mathbf{S})_{653} - E_0^\ddagger(\mathbf{S})_{\text{PBE}}^{\text{b}}$	-7.7	-0.4	-8.6	-2.5	-3.8	-1.9
$\Delta E^\ddagger(\mathbf{S})_{\text{D//PBE}}$	-14.4	2.1	-7.5	-3.0	-22.7	-15.9
$E^\ddagger(\mathbf{S})_{\text{PBE+D//PBE}}$	69.9	175.3	84.1	110.7	73.2	154.0

^adifference between CCSD(T) and RI-MP2 energy barriers on a 3T cluster.

^bcontribution to enthalpy at 653 K ($E_0^\ddagger(\mathbf{S})_{\text{PBE}}$ is the ZPVE corrected energy barrier).

Final estimates for energy barriers

Table 11.5 shows the *final estimate* for intrinsic energy barriers, which are obtained from the PBE energy barrier, the high-level corrections extrapolated to the periodic limit, the basis set limit corrections, and the CCSD(T) corrections, see equation 11.3. For the one-step scheme, the energy barrier is 129.7 kJ/mol. For the two-step scheme we obtained 129.7 kJ/mol for the first step and 102.5 kJ/mol for the second step. While the energy barrier for the one-step scheme determined in the present study differs only slightly from that determined in our B3LYP cluster study ($E^\ddagger = 123.2$ kJ/mol) presented in chapter 8, there are significant deviations for the two-step scheme. For the first step the *final estimate* barrier is 24 kJ/mol higher, while it is 13 kJ/mol lower for the second step. The *final estimates* of the present study provide a significant improvement in the theoretical description of benzene alkylation over H-ZSM-5, if we keep in mind that the intrinsic barriers from the DFT cluster study strongly depend on the cluster size. This is the result of a partial compensation of two types of errors in DFT:²⁵⁸ Missing dispersion which results in too high barriers and self-interaction correction errors which result in systematically too low barriers. Because the former depends much

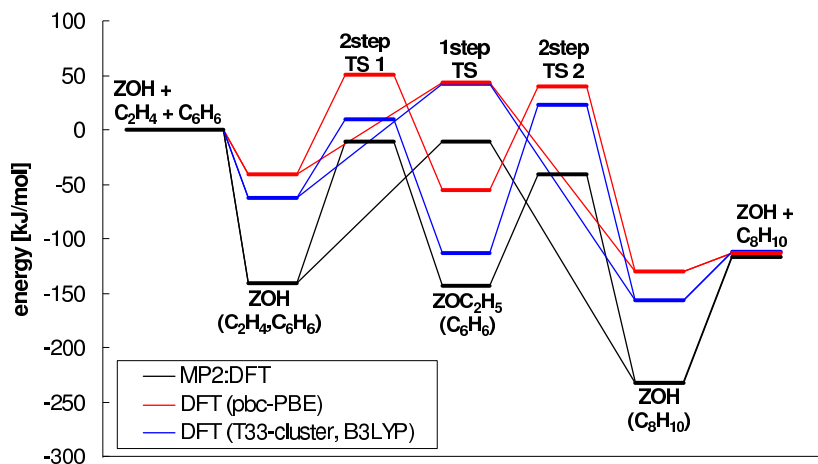


Figure 11.11: Potential energy profiles for the alkylation of benzene obtained with different methods.

more on the cluster size than the latter, the extend of the compensation and the resulting barriers strongly depend on the cluster size.

This is illustrated further by comparison of our *final estimates* with the PBE results, which show both types of errors, and the PBE+D results (table 11.5, last row), evaluated as difference between the reactants and the transition structures using the transferable C_6 -parameters of Grimme³⁹⁹ which show only the self-interaction correction error. The PBE+D barriers are too low by 59.8, 45.6, and 29.3 kJ/mol for **1s**, **2s(1)**, and **2s(2)** steps, which is in the range of 12 – 62 kJ/mol by which the PBE barriers for different type of reactions are known to be too low.¹⁹⁹ The PBE barriers are too low by 45.4, 38.1, and 6.6 kJ/mol, respectively, due to partial compensation with missing dispersion (–14.4, –7.5, and –22.7 kJ/mol, row 9 in table 11.5).

While the hybrid MP2:DFT approach is expected to provide highly accurate energy barriers for the alkylation there are the same sources of uncertainties as in the calculation of adsorption energies. Therefore, a range of ± 10 kJ/mol is expected to account for all uncertainties of our methodology.

Figure 11.11 compares the *final estimate* potential energy profile with the PBE profile and the B3LYP profile for the T33 cluster calculated in chapter 8. The *final estimate* profile is shifted down substantially relative to the DFT profiles. More importantly this shift is different for reactants and transition states due to different self-interaction errors.

Table 11.6: Intrinsic rate coefficients for the one-step and two-step mechanism.

reaction	constant	T,K		
		603	653	703
HOZ(C ₂ H ₄ +C ₆ H ₆)	k_1, s^{-1}	5.04×10^0	3.28×10^1	1.64×10^2
↔ HOZ(C ₈ H ₁₀)	k_{-1}, s^{-1}	3.85×10^{-6}	9.68×10^{-5}	1.54×10^{-3}
HOZ(C ₂ H ₄)	k_1, s^{-1}	8.87×10^0	5.91×10^1	3.00×10^2
↔ C ₂ H ₅ OZ	k_{-1}, s^{-1}	4.92×10^2	3.81×10^3	2.22×10^4
C ₂ H ₅ OZ(C ₆ H ₆)	k_1, s^{-1}	2.85×10^4	1.29×10^5	4.75×10^5
↔ HOZ(C ₈ H ₁₀)	k_{-1}, s^{-1}	4.40×10^{-5}	7.65×10^{-4}	8.89×10^{-3}

Rate coefficients for elementary steps and comparison with experimental data

Enthalpy barriers are obtained from our *final estimate* energy barriers by adding the zero-point vibrational energies and thermal corrections (rows 7 and 8 in table 11.5, respectively), both calculated from PBE frequencies. The intrinsic energy and enthalpy barriers have to be converted into apparent activation energies before they can be compared to experimental data.

Rate coefficients for all elementary reaction steps were calculated according to equation 11.13. As is justified in section D.2 of the supporting information, the partition functions of reactant and transition state were evaluated from vibrational contributions only. For the one-step mechanism the reaction path symmetry number was set to $\sigma = 12$ in order to account for the fact that each of the two C-atoms of ethene can react with each of the six C-atoms of benzene. The rate coefficient is therefore larger by a factor of 12 compared to the single-event rate coefficient obtained if all C-atoms were distinguishable. For the first step of the two-step mechanism we used $\sigma = 2$ while for the second step $\sigma = 6$ was employed. The rate coefficients obtained are listed in table 11.6 for relevant reaction temperatures. It should be noted that the pre-exponential factors determined in the present study are similar to those obtained in the cluster study reported in chapter 8 (see table 11.7). The largest deviation is observed for the ethoxide formation. For this process the pre-exponential factor obtained in the present study is higher by a factor of 4 compared to the value obtained in our cluster study. The changes in the rate coefficients compared to the cluster study are therefore mostly due to differences in the calculation of intrinsic activation energies as well as the consideration of reaction path symmetry numbers.

Experimentally determined rate data for the alkylation of benzene depend

Table 11.7: Preexponential factors of elementary steps in s^{-1} obtained from calculations on a T33-cluster using B3LYP/SV(P) and from DFT calculations with periodic boundary conditions.

reaction	approach	T, K		
		603	653	703
HOZ($\text{C}_2\text{H}_4 + \text{C}_6\text{H}_6$)	T33-cluster	2.60×10^{10}	2.46×10^{10}	2.35×10^{10}
\leftrightarrow HOZ(C_8H_{10})	pbc-DFT	2.78×10^{10}	2.68×10^{10}	2.60×10^{10}
HOZ(C_2H_4)	T33-cluster	1.11×10^{11}	1.07×10^{11}	1.03×10^{11}
\leftrightarrow $\text{C}_2\text{H}_5\text{OZ}$	pbc-DFT	4.77×10^{11}	4.53×10^{11}	4.34×10^{11}
$\text{C}_2\text{H}_5\text{OZ}(\text{C}_6\text{H}_6)$	T33-cluster	1.41×10^{12}	1.47×10^{12}	1.53×10^{12}
\leftrightarrow HOZ(C_8H_{10})	pbc-DFT	1.33×10^{12}	1.36×10^{12}	1.39×10^{12}

on a number of items in addition to the intrinsic rate coefficients. These are in particular the external conditions such as pressure, temperature, and gas phase composition but also the particle size and shape. All of these factors determine the average concentration of precursor states inside the zeolite channel system and consequently the effective rate of reaction via

$$r = k_1 \langle N_{\text{pre},1} \rangle - k_{-1} \langle N_{\text{pre},-1} \rangle. \quad (11.14)$$

In this equation r denotes the overall rate of reaction in $\text{mol kg}^{-1} \text{s}^{-1}$, k_i are the intrinsic rate coefficients for forward and reverse reaction, and $\langle N_{\text{pre},i} \rangle$ are the average concentrations of precursors for forward and reverse reaction, respectively, in mol kg^{-1} . In chapter 9 we have introduced a phenomenological model that relates the external conditions (temperature, pressure, and composition) to the concentration of precursor states based on the multicomponent adsorption behavior of the ethene-benzene-ethylbenzene mixture as well as on the distribution of these species inside the zeolite channel system. As a result, the rates calculated by means of equation 11.14 can be compared to experimental data. Alternatively we can use turnover frequencies obtained from

$$\text{TOF} = r/c_{\text{H}^+}, \quad (11.15)$$

where r is the rate of reaction according to equation 11.14 and c_{H^+} is the concentration of acid sites in mol kg^{-1} , respectively. From calculated turnover frequencies at different temperatures we can obtain the apparent activation energy by means of an Arrhenius plot. Figure 11.12 shows simulated Arrhenius plots at 2.5 bar overall gas pressure, and a fixed benzene to ethene ratio of 5:1. For the one-step scheme the average concentrations $\langle N_{\text{pre},1} \rangle$ in equation 11.14 at 603 and 653 K are 1.73×10^{-3} and 7.31×10^{-4} molecules per unit cell.³⁸⁵ Note that $\langle N_{\text{pre},-1} \rangle$ was essentially equal to zero in the calculations, as

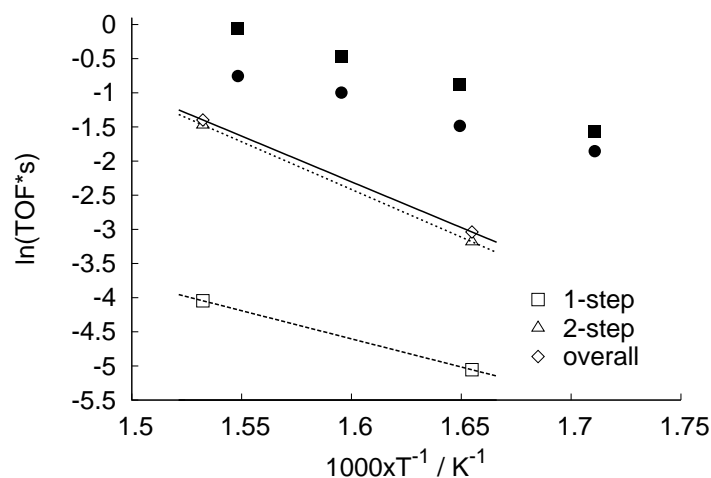


Figure 11.12: Experimental and simulated Arrhenius plots for the alkylation of benzene at 2.5 bar and a benzene to ethene ratio in the gas phase of 5:1. The experimental data were obtained for mesoporous (■) and conventional (●) H-ZSM-5.²⁷⁶ The simulated turnover frequencies are plotted for the one-step mechanism, the two-step mechanism and the sum of both.

virtually no ethylbenzene was present in the gas phase. Some experimental points²⁷⁶ are also included in figure 11.12. They were determined in a mesoporous and a conventional ZSM-5 sample, respectively. The difference in the activity among the two samples was attributed to diffusional limitation in the case of the conventional zeolite sample. It should be noted though, that differences in the multicomponent adsorption equilibrium between the two samples might contribute to the observed differences in activities, in addition to the effects of intraparticle diffusion. Therefore, the experimental points shown in figure 11.12 define a range of possible turnover frequencies for benzene alkylation over H-ZSM-5 samples. The simulated curves for the one- and two-step schemes both underestimate the experimental data. An overall turnover frequency obtained from the summation of the two contributions¹⁰⁴ is also included in figure 11.12. The positions of the simulated Arrhenius plots depend on three factors which are, first, our *final estimates* for the intrinsic barriers, second, our estimates of the intrinsic preexponential factors, and third, the estimation of precursor concentrations by means of our phenomenological model.³⁸⁵ Table 11.8 compares apparent Arrhenius parameters calculated from our *final estimates* with Arrhenius parameters determined from experimental data. The calculated apparent activation energies of the

Table 11.8: Comparison of apparent Arrhenius parameters obtained from *final estimates* with experiments (in kJ/mol and 1/s).

	Calcd		Obsd	
	E_{app}	A_{app}	E_{app}	A_{app}
1s	66.1	3.41×10^3		
2s	112.0	2.09×10^8	58 –	2.44×10^4 –
total	107.5	9.74×10^7	76	1.38×10^6

two reaction mechanisms, 66.1 and 112.0 kJ/mol differ substantially. Only the apparent activation energy of the one-step scheme agrees with the experimental data within the uncertainty limit of our calculations. While this could lead to the conclusion that our results for the two-step scheme are not correct, it has to be kept in mind that the energy barrier for the two-step scheme was calculated assuming that ethene enters an empty intersection. This assumption, though, is not correct since an excess of benzene was used in the experiments reported in ref. 276. As a result, the probability of ethene finding an unoccupied intersection is lowered considerably because benzene adsorbs much more strongly than ethene in the channel intersection. Therefore, it is likely that under such conditions the two-step mechanism is much less relevant than the one-step scheme because any protonated ethene would react with benzene directly instead of forming a surface ethoxide. Therefore, we limit the comparison with experiments to the one-step mechanism. Under the conditions of a significant excess of benzene in the gas phase the apparent activation energy can also be estimated directly (i. e. without using our continuum model³⁸⁵) from our calculated adsorption energies and energy barriers reported in tables 11.2 and 11.5. Then the reaction can be assumed to be intrinsic with respect to benzene but apparent with respect to ethene. As a result we can add the difference of the adsorption enthalpies for reaction **4** and **2** at 653 K (-120.5 and -72.2 kJ/mol) to the intrinsic activation enthalpy at 653 K (117.2 kJ/mol) to obtain the apparent activation enthalpy (69.0 kJ/mol). The apparent activation energy is then obtained after adding RT . The result, 74.4 kJ/mol, is in reasonable agreement with the value obtained from our continuum model. The difference of 8 kJ/mol indicates the importance of an accurate calculation of the precursor concentration.

One reason for underestimation of the experimental turnover numbers might be connected with uncertainties in the estimation of precursor concentrations. An error range is hard to quantify because reliable high temperature

adsorption data are not available to test whether force fields parameterized at ambient temperature are still valid at reaction temperature. Moreover it has been shown that adsorption can be very sensitive to small deviations in the crystal structure of the zeolite under study, especially at low pressure.⁴⁴⁹ However, taking into account the results of the latter study it is unlikely that the uncertainties included in the estimation of the precursor concentration are responsible for the one order of magnitude deviation. The second reason is most likely be connected to the calculation of intrinsic pre-exponential factors by means of the harmonic approximation which faces its limits at temperatures as high as needed for hydrocarbon reactions in zeolites. These limitations can be overcome by taking into account entropy effects beyond the harmonic approximation, for example by means of transition path sampling.⁴⁵⁰ Finally, it should be noted that the experimental data are also subject to uncertainties, the estimation of which is beyond the scope of the present study.

11.4 Conclusion

A hybrid MP2:DFT approach was used to study elementary adsorption and reaction steps involved in the alkylation of benzene with ethene over H-ZSM-5. The dispersion energy contributes substantially to the *final estimates* for the adsorption energies leading to a reversal of the stability sequence predicted by plane-wave PBE calculations for the adsorption of ethene, benzene, and ethylbenzene on the Brønsted acid site. By augmenting PBE with a semiempirical dispersion term (PBE+D), adsorption energies are predicted which deviate from the *final estimates* by a maximum of $\pm 8\%$ except for ethene physisorption and ethoxide formation where PBE+D overestimates the binding energies significantly. Calculated adsorption enthalpies are more negative than experimental data by 2–4 kJ/mol per CH_X unit which can be ascribed to the fact that our calculations refer to one particular site in the zeolite in contrast to experimental data which are averages over a distribution of sites.

The *final estimates* for intrinsic energy barriers deviate significantly from the plane wave PBE barriers which are systematically too low. Intrinsic energy barriers are converted to apparent activation energies by means of a phenomenological model based on the multicomponent adsorption equilibrium of the ethene-benzene-ethylbenzene mixture.³⁸⁵ The apparent activation energy for the one-step alkylation agrees with the experimental data within the uncertainty limit of our calculations. A comparison of the two-step mech-

anism with experiments is difficult because it is unlikely to occur under the conditions of the experiment. The main reason for the underestimation of the experimental turnover frequencies is most likely due to the harmonic approximation applied in the calculation of pre-exponentials. Future improvements are possible by means of dynamical sampling techniques.

Part V

Back matter

“This is not the end. It is not even the beginning of the end. But it is, perhaps, the end of the beginning.”

Winston Churchill

12

Summary

In this thesis two industrially important zeolite catalyzed reaction systems have been investigated by multiscale approaches involving quantum chemical calculations, molecular simulations, microkinetic modeling, and continuum simulations. The first system, nitrous oxide (N_2O) decomposition over dinuclear iron sites in Fe-ZSM-5, was studied by density functional theory in combination with microkinetic modeling. The second system, benzene alkylation with ethene and ethane, respectively, was studied using a hierarchy of quantum chemical methods combined with classical molecular simulations and continuum modeling based on partial differential equations.

For the N_2O decomposition, three catalytic cycles on dinuclear oxygen bridged extraframework iron sites in Fe-ZSM-5 have been investigated using density functional theory. The hydroxylated iron site, $\text{Z}^-[\text{HOFeOFeOH}]^{2+}\text{Z}^-$, is projected to dominate the catalytic surface at low temperatures. This site shows a low activity for N_2O decomposition. At higher temperatures water can desorb, and N_2O decomposition on $\text{Z}^-[\text{FeOFe}]^{2+}\text{Z}^-$ becomes the slow process in the overall kinetic. On this site N_2O decomposition deposits an oxygen atom on each iron atom, followed by subsequent oxygen atom recombination and desorption of O_2 . This sequence is favoured over decomposition of two N_2O molecules occurring on the same iron atom. In all of the catalytic cycles examined in this work, oxygen desorption was found to be fast and N_2O decomposition was found to be first order with respect to N_2O partial pressure. Therefore, there are many qualitative similarities between the mechanism of N_2O decomposition on single iron sites reported earlier by Heyden et al.¹¹⁵ and that on dinuclear oxygen bridged iron sites studied in the present work. Both type of sites are poisoned by small amounts of water. As a result, the nuclearity (mono- or dinuclear iron site) of the catalytically active site for N_2O decomposition appears to be less important than catalyst poisoning by traces of water in the gas streams. Antiferromagnetic coupling was shown to

have no effect on the reaction mechanism.

A microkinetic model based on the rate parameters for each elementary step was then used to study the influence of water vapor on the distribution of dinuclear iron sites between catalytically active and inactive forms and on the apparent first-order rate constant. The presence of low concentrations of water vapor in the feed stream (ppb to ppm levels) affects the calculated values for the apparent activation energy and preexponential factor and, hence, can explain the wide spread in the experimental values for these quantities, as well as the appearance of an apparent compensation effect. This pattern is very similar to that reported previously for mononuclear iron species in Fe-ZSM-5.^{115,116} Simulations of temperature-programmed reaction experiments reported in the literature were carried out based on the mechanism and kinetics developed for mononuclear and dinuclear iron sites. The results obtained for mononuclear sites are in very good agreement with the experimental findings for Fe-ZSM-5 with an iron loading of 0.08 wt% (Fe/Al = 0.017). The simulations suggest that all of the iron in the catalyst is active. Simulations based on mono- and dinuclear sites were carried out and compared with experiments conducted with Fe-ZSM-5 containing 4 wt% iron (Fe/Al = 1.1). In this case, good agreement was obtained with the simulations carried out assuming that 65% of the total iron in the catalyst is in the form of dinuclear sites or that 15% of the total iron in the catalyst is in the form of mononuclear sites, and that the content of water vapor in the feed is 100 ppb. The sensitivity of the simulations with respect to the water content was small for both, the low iron loaded and high iron loaded catalyst, since the experiments all involved temperatures >700 K.

For the alkylation of benzene with ethene we have elucidated two reaction channels using density functional theory. In the one-step mechanism ethylbenzene is formed from coadsorbed ethene and benzene in one single step. The two-step mechanism involves the formation of covalently bonded ethoxide via a carbenium ion-like transition state in the first step. The ethoxide then reacts with benzene to form ethylbenzene. Rate coefficients for all elementary reactions have been calculated using transition state theory.

In order to simulate the influence of adsorption thermodynamics and diffusional limitations on the overall rate of reaction for the alkylation, a continuum model of a zeolite crystal based on the diffusion-reaction equation has been implemented. The solution of this partial differential equation requires the description of the multicomponent adsorption and diffusion of all species. This was achieved by using analytical theories such as the ideal adsorbed solution theory for the multicomponent adsorption and the Maxwell-Stefan equations for the multicomponent diffusion. Both theor-

ies require pure component data (adsorption isotherms and diffusion coefficients, respectively) as input. Adsorption isotherm for all species have been determined by Monte Carlo simulations in the grand-canonical ensemble. Diffusion coefficients have been calculated by means of molecular dynamics simulations. Moreover, a model is proposed to couple the intrinsic rate coefficients to the continuum variables. The continuum model was then used to calculate concentration profiles of all reactants and products along the radial coordinate of the crystal. Furthermore, it has been demonstrated that the apparent rate coefficients and the reaction orders are not constant but, in fact, a complex function of the zeolite architecture, particle size, and reaction conditions. Moreover, the usual approaches to calculate effectiveness factors for reactions in porous media can only be used at low loadings of the reactants inside the zeolite. In fact, the effectiveness factor depends strongly on the reaction conditions. The adopted simulation model can be used to predict the effectiveness factor for any set of reaction conditions.

A further increase of the length scale was achieved by implementing the continuum model for a zeolite crystal into a reactor model for a fixed-bed plug-flow reactor. Kinetic data obtained from reactor simulations in the differential operation mode have been employed to parameterize Langmuir-Hinshelwood (LH) and power-law (PL) rate expressions. These rate expressions were then used to extrapolate to higher pressure and temperature and in a design equation of a fixed-bed plug-flow reactor. It was demonstrated that the LH rate expression shows extrapolation capabilities comparable to predictions of the continuum model as long as the gas-phase composition remains within the fitting range. By contrast, the predictions of the power-law rate expression deviate from those of the LH rate expression and the continuum model. In particular, a lower maximum conversion achievable in a fixed-bed reactor was predicted. When the gas-phase composition deviates significantly from that used for fitting, both the LH and the PL rate expressions deviate considerably from the predictions of the full continuum model and predict a higher maximum conversion in fixed-bed reactor simulations. These results suggest that for zeolite-catalyzed reactions producing strongly adsorbed products such as ethylbenzene, LH and PL rate expressions may lack the required flexibility to describe the limit of full conversion.

A further objective was to include the dehydrogenation of ethane into the continuum model. The rate coefficients for this reaction were estimated by means of density functional calculations and transition state theory. The full model was shown to predict correctly the behavior of a fixed-bed reactor for the dehydroalkylation. Moreover we have demonstrated the potential of a membrane reactor for this reaction. The removal of hydrogen from the

reactant mixture can increase the benzene conversion significantly.

Finally the reaction mechanism for benzene alkylation was reconsidered using a hybrid MP2:DFT approach which is designed to study problems that involve both bond rearrangements and van der Waals interactions with almost chemical accuracy. The calculated adsorption enthalpies for ethene, benzene, and ethylbenzene are in good agreement with experimental data. The calculated intrinsic rate coefficients have been converted to apparent kinetic parameters by means of the continuum model and compared to experimental data. The agreement is remarkably good, demonstrating that recent quantum chemical approaches can be used to study hydrocarbon reactions in zeolites almost quantitatively.

To conclude, the present thesis contributes to the development of multiscale approaches for the theoretical investigation of reactions in porous media. It was demonstrated how detailed atomistic simulations can be used to generate data which can be combined with continuum modeling to achieve a superior predictability compared to empirical kinetic rate expressions. It is therefore anticipated that theoretical investigations of the combined effects of adsorption thermodynamics, diffusion, and reaction kinetics on the rates of catalyzed reactions will continue to be a fertile area for future research.

Supporting information for chapter 7

A

This material contains all rate parameters computed from DFT calculations. Calculated enthalpies of reaction are averaged over the temperature range of 600–800 K. To evaluate whether low spin-inversion probabilities could result in a significant reduction of the rates of spin-surface crossing, thermally averaged Landau-Zener transition probabilities were calculated for spin-orbit coupling energies of 395 and 825 J/mol at several temperatures. All spin-inversion transmission coefficients were >0.03 at 700 K. As a result, failure to correct reaction rates for spin-inversion probabilities <1 creates errors smaller than the error in the activation barrier of 5 kcal/mol at 700 K.

Table A.1: Computed rate parameters for elementary steps in nitrous oxide dissociation on ferromagnetically coupled dinuclear oxygen bridged iron sites in Fe-ZSM-5. The numbers in braces denote the spin multiplicity.

Reaction	$E^\ddagger{}^a, \Delta H^b$ (kcal/mol)	Constant	T (K)		
			600	700	800
1. $Z^-[\text{HOFeOH}\cdot\text{HOFeOH}]^{2+}Z^-\{11\}$ $\leftrightarrow Z^-[\text{HOFeOHFe}(\text{OH})_2]^{2+}Z^-\{11\}$	$\Delta H_1 = 2.5$	$K_1, -$	2.29×10^{-2}	3.08×10^{-2}	3.85×10^{-2}
	$E_1^\ddagger = 2.5$	A_1, s^{-1}	1.25×10^{13}	1.46×10^{13}	1.67×10^{13}
		k_1, s^{-1}	1.58×10^{12}	2.48×10^{12}	3.53×10^{12}
	$E_{-1}^\ddagger = 0.0$	A_{-1}, s^{-1}	6.91×10^{13}	8.05×10^{13}	9.18×10^{13}
		k_{-1}, s^{-1}	6.91×10^{13}	8.05×10^{13}	9.18×10^{13}
2. $Z^-[\text{HOFeOHFe}(\text{OH})_2]^{2+}Z^-\{11\}$ $\leftrightarrow Z^-[\text{HOFeOFeOH}(\text{OH}_2)]^{2+}Z^-\{11\}$	$\Delta H_2 = 2.4$	$K_2, -$	1.05×10^{-1}	1.40×10^{-1}	1.73×10^{-1}
	$E_2^\ddagger = 8.1$	A_2, s^{-1}	1.34×10^{12}	1.34×10^{12}	1.33×10^{12}
		k_2, s^{-1}	1.45×10^9	3.82×10^9	7.93×10^9
	$E_{-2}^\ddagger = 5.8$	A_{-2}, s^{-1}	1.74×10^{12}	1.72×10^{12}	1.72×10^{12}
		k_{-2}, s^{-1}	1.39×10^{10}	2.73×10^{10}	4.57×10^{10}
3. $Z^-[\text{HOFeOFeOH}(\text{OH})_2]^{2+}Z^-\{11\}$ $\leftrightarrow Z^-[\text{HOFeOFeOH}]^{2+}Z^-\{11\}$ $+ \text{H}_2\text{O}(\text{g})$	$\Delta H_3 = 13.9$	K_3, bar	7.88×10^1	4.24×10^2	1.45×10^3
	$E_3^\ddagger = 14.3$	A_3, s^{-1}	1.25×10^{13}	1.46×10^{13}	1.67×10^{13}
		k_3, s^{-1}	7.40×10^7	4.82×10^8	2.00×10^9
	$E_{-3}^\ddagger = 0.0$	$A_{-3}, s^{-1}\text{bar}^{-1}$	9.40×10^5	1.14×10^6	1.38×10^6
		$k_{-3}, s^{-1}\text{bar}^{-1}$	9.40×10^5	1.14×10^6	1.38×10^6
4. $Z^-[\text{HOFeOFeOH}]^{2+}Z^-\{11\} + \text{N}_2\text{O}(\text{g})$ $\leftrightarrow Z^-[\text{HOFeOFeOH}(\text{ON}_2)]^{2+}Z^-\{11\}$	$\Delta H_4 = -0.8$	K_4, bar^{-1}	5.97×10^{-6}	5.33×10^{-6}	5.02×10^{-6}
	$E_4^\ddagger = 0.0$	$A_4, s^{-1}\text{bar}^{-1}$	9.51×10^6	1.33×10^7	1.78×10^7
		$k_4, s^{-1}\text{bar}^{-1}$	9.51×10^6	1.33×10^7	1.78×10^7
	$E_{-4}^\ddagger = 2.5$	A_{-4}, s^{-1}	1.25×10^{13}	1.46×10^{13}	1.67×10^{13}
		k_{-4}, s^{-1}	1.59×10^{12}	2.49×10^{12}	3.56×10^{12}
5. $Z^-[\text{HOFeOFeOH}(\text{ON}_2)]^{2+}Z^-\{11\}$ $\leftrightarrow Z^-[\text{HOFeOFeOH}]^{2+}Z^-\{11\}$ $+ \text{N}_2(\text{g})$	$\Delta H_5 = -1.4$	K_5, bar	3.95×10^6	3.37×10^6	2.93×10^6
	$E_5^\ddagger = 40.2$	A_5, s^{-1}	9.73×10^{11}	1.10×10^{12}	1.21×10^{12}
		k_5, s^{-1}	2.19×10^{-3}	3.06×10^{-1}	1.25×10^1
	$E_{-5}^\ddagger = 41.3$	$A_{-5}, s^{-1}\text{bar}^{-1}$	6.31×10^5	7.03×10^5	8.39×10^5
		$k_{-5}, s^{-1}\text{bar}^{-1}$	5.53×10^{-10}	9.07×10^{-8}	4.28×10^{-6}
6. $Z^-[\text{HOFeOFeOH}]^{2+}Z^-\{11\}$ $\leftrightarrow Z^-[\text{HOFe}\cdot\text{O}_2\text{FeOH}]^{2+}Z^-\{11\}$	$\Delta H_6 = 5.2$	$K_6, -$	4.10×10^0	7.61×10^0	1.21×10^1
	$E_6^\ddagger = 6.4$	A_6, s^{-1}	1.14×10^{13}	1.24×10^{13}	1.33×10^{13}
		k_6, s^{-1}	5.15×10^{10}	1.22×10^{11}	2.32×10^{11}
	$E_{-6}^\ddagger = 2.1$	A_{-6}, s^{-1}	7.36×10^{10}	7.27×10^{10}	7.22×10^{10}
		k_{-6}, s^{-1}	1.26×10^{10}	1.60×10^{10}	1.92×10^{10}
7. $Z^-[\text{HOFe}\cdot\text{O}_2\text{FeOH}]^{2+}Z^-\{11\}$ $\leftrightarrow Z^-[\text{HOFe}\cdot\text{FeOH}]^{2+}Z^-\{9\} + \text{O}_2(\text{g})$	$\Delta H_7 = 1.7$	K_7, bar	1.50×10^5	1.88×10^5	2.15×10^5
	$E_7^\ddagger = 9.2$	A_7, s^{-1}	1.04×10^{14}	1.18×10^{14}	1.29×10^{14}
		k_7, s^{-1}	4.81×10^{10}	1.62×10^{11}	4.04×10^{11}
	$E_{-7}^\ddagger = 5.8$	$A_{-7}, s^{-1}\text{bar}^{-1}$	4.06×10^7	5.48×10^7	7.09×10^7
		$k_{-7}, s^{-1}\text{bar}^{-1}$	3.20×10^5	8.64×10^5	1.88×10^6
8. $Z^-[\text{HOFe}\cdot\text{FeOH}]^{2+}Z^-\{9\} + \text{N}_2\text{O}(\text{g})$ $\leftrightarrow Z^-[\text{HOFe}(\text{ON}_2)\cdot\text{FeOH}]^{2+}Z^-\{9\}$	$\Delta H_8 = -0.2$	K_8, bar^{-1}	3.97×10^{-6}	3.79×10^{-6}	3.78×10^{-6}
	$E_8^\ddagger = 0.0$	$A_8, s^{-1}\text{bar}^{-1}$	6.56×10^6	9.76×10^6	1.38×10^7
		$k_8, s^{-1}\text{bar}^{-1}$	6.56×10^6	9.76×10^6	1.38×10^7
	$E_{-8}^\ddagger = 2.4$	A_{-8}, s^{-1}	1.25×10^{13}	1.46×10^{13}	1.67×10^{13}
		k_{-8}, s^{-1}	1.65×10^{12}	2.58×10^{12}	3.66×10^{12}
9. $Z^-[\text{HOFe}(\text{ON}_2)\cdot\text{FeOH}]^{2+}Z^-\{9\}$ $\leftrightarrow Z^-[\text{HOFeO}\cdot\text{FeOH}]^{2+}Z^-\{9\} + \text{N}_2(\text{g})$	$\Delta H_9 = -15.0$	K_9, bar	4.06×10^{10}	6.86×10^9	1.76×10^9
	$E_9^\ddagger = 25.9$	A_9, s^{-1}	1.52×10^{12}	1.66×10^{12}	1.80×10^{12}
		k_9, s^{-1}	5.66×10^2	1.38×10^4	1.53×10^5
	$E_{-9}^\ddagger = 39.4$	$A_{-9}, s^{-1}\text{bar}^{-1}$	3.31×10^6	4.22×10^6	5.25×10^6
		$k_{-9}, s^{-1}\text{bar}^{-1}$	1.39×10^{-8}	2.01×10^{-6}	8.66×10^{-5}
10. $Z^-[\text{HOFeO}\cdot\text{FeOH}]^{2+}Z^-\{9\}$ $\leftrightarrow Z^-[\text{HOFeOFeOH}]^{2+}Z^-\{11\}$	$\Delta H_{10} = -27.9$	$K_{10}, -$	2.85×10^9	9.95×10^7	8.09×10^6
	$E_{10}^\ddagger = 0.1$	A_{10}, s^{-1}	2.18×10^{12}	2.39×10^{12}	2.59×10^{12}
		k_{10}, s^{-1}	2.06×10^{12}	2.28×10^{12}	2.48×10^{12}
	$E_{-10}^\ddagger = 28.4$	A_{-10}, s^{-1}	1.61×10^{13}	1.70×10^{13}	1.77×10^{13}
		k_{-10}, s^{-1}	7.22×10^2	2.29×10^4	3.07×10^5

(continued on next page)

Table A.1 (continued)

Reaction	$E^\ddagger{}^a, \Delta H^b$ (kcal/mol)	Constant	T (K)		
			600	700	800
11. $Z^-[\text{HOFeO}_-\text{FeOH}]^{2+}Z^-\{9\} + \text{N}_2\text{O}(\text{g})$ $\leftrightarrow Z^-[\text{HOFeO}_-(\text{N}_2\text{O})\text{FeOH}]^{2+}Z^-\{9\}$	$\Delta H_{11} = 0.2$ $E_{11}^\ddagger = 0.0$ $E_{-11}^\ddagger = 1.7$	K_{11}, bar $A_{11}, \text{s}^{-1}\text{bar}^{-1}$ $k_{11}, \text{s}^{-1}\text{bar}^{-1}$ A_{-11}, s^{-1} k_{-11}, s^{-1}	5.31×10^{-6} 1.56×10^7 1.56×10^7 1.25×10^{13} 2.93×10^{12}	5.35×10^{-6} 2.25×10^7 2.25×10^7 1.46×10^{13} 4.21×10^{12}	5.54×10^{-6} 3.11×10^7 3.11×10^7 1.67×10^{13} 5.62×10^{12}
12. $Z^-[\text{HOFeO}_-(\text{N}_2\text{O})\text{FeOH}]^{2+}Z^-\{9\}$ $\leftrightarrow Z^-[\text{HOFeO}_-\text{OFeOH}]^{2+}Z^-\{9\}$ $+ \text{N}_2(\text{g})$	$\Delta H_{12} = -11.9$ $E_{12}^\ddagger = 25.0$ $E_{-12}^\ddagger = 35.5$	K_{12}, bar A_{12}, s^{-1} k_{12}, s^{-1} $A_{-12}, \text{s}^{-1}\text{bar}^{-1}$ $k_{-12}, \text{s}^{-1}\text{bar}^{-1}$	9.38×10^8 6.55×10^{12} 5.12×10^3 4.87×10^7 5.46×10^{-6}	2.28×10^8 7.45×10^{12} 1.17×10^5 6.45×10^7 5.11×10^{-4}	7.70×10^7 8.29×10^{12} 1.23×10^6 8.22×10^7 1.59×10^{-2}
13. $Z^-[\text{HOFeO}_-\text{OFeOH}]^{2+}Z^-\{9\}$ $\leftrightarrow Z^-[\text{HOFeOOFeOH}]^{2+}Z^-\{11\}$	$\Delta H_{13} = -18.5$ $E_{13}^\ddagger = 9.4$ $E_{-13}^\ddagger = 29.0$	$K_{13} -$ A_{13}, s^{-1} k_{13}, s^{-1} A_{-13}, s^{-1} k_{-13}, s^{-1}	1.35×10^7 7.72×10^{12} 3.01×10^9 8.13×10^{12} 2.23×10^2	1.46×10^6 9.15×10^{12} 1.09×10^{10} 8.46×10^{12} 7.48×10^3	2.79×10^5 1.05×10^{13} 2.91×10^{10} 8.72×10^{12} 1.04×10^5
14. $Z^-[\text{HOFe}_-\text{FeOH}]^{2+}Z^-\{9\}$ $\leftrightarrow Z^-[\text{FeOHFeOH}]^{2+}Z^-\{9\}$	$\Delta H_{14} = -10.9$ $E_{14}^\ddagger = 1.9$ $E_{-14}^\ddagger = 12.7$	$K_{14} -$ A_{14}, s^{-1} k_{14}, s^{-1} A_{-14}, s^{-1} k_{-14}, s^{-1}	4.20×10^2 2.46×10^{11} 4.85×10^{10} 5.09×10^{12} 1.15×10^8	1.13×10^2 2.06×10^{11} 5.13×10^{10} 4.33×10^{12} 4.53×10^8	4.25×10^1 1.78×10^{11} 5.27×10^{10} 3.77×10^{12} 1.24×10^9
15. $Z^-[\text{FeOHFeOH}]^{2+}Z^-\{9\} + \text{N}_2\text{O}(\text{g})$ $\leftrightarrow Z^-[(\text{N}_2\text{O})\text{FeOHFeOH}]^{2+}Z^-\{9\}$	$\Delta H_{15} = -2.2$ $E_{15}^\ddagger = 0.0$ $E_{-15}^\ddagger = 4.0$	K_{15}, bar^{-1} $A_{15}, \text{s}^{-1}\text{bar}^{-1}$ $k_{15}, \text{s}^{-1}\text{bar}^{-1}$ A_{-15}, s^{-1} k_{-15}, s^{-1}	7.07×10^{-5} 2.99×10^7 2.99×10^7 1.25×10^{13} 4.23×10^{11}	5.33×10^{-5} 4.26×10^7 4.26×10^7 1.46×10^{13} 8.01×10^{11}	4.43×10^{-5} 5.82×10^7 5.82×10^7 1.67×10^{13} 1.32×10^{12}
16. $Z^-[(\text{N}_2\text{O})\text{FeOHFeOH}]^{2+}Z^-\{9\}$ $\leftrightarrow Z^-[\text{OFeOHFeOH}]^{2+}Z^-\{9\} + \text{N}_2(\text{g})$	$\Delta H_{16} = -8.4$ $E_{16}^\ddagger = 32.3$ $E_{-16}^\ddagger = 39.7$	K_{16}, bar A_{16}, s^{-1} k_{16}, s^{-1} $A_{-16}, \text{s}^{-1}\text{bar}^{-1}$ $k_{-16}, \text{s}^{-1}\text{bar}^{-1}$	7.05×10^7 2.25×10^{12} 3.74×10^0 1.58×10^7 5.30×10^{-8}	2.61×10^7 2.29×10^{12} 1.83×10^2 1.79×10^7 7.01×10^{-6}	1.21×10^7 2.30×10^{12} 3.37×10^3 1.99×10^7 2.77×10^{-4}
17. $Z^-[\text{OFeOHFeOH}]^{2+}Z^-\{11\}$ $\leftrightarrow Z^-[\text{OFeOHFeOH}]^{2+}Z^-\{9\}$	$\Delta H_{17} = 3.6$ $E_{17}^\ddagger = 5.6$ $E_{-17}^\ddagger = 1.6$	$K_{17} -$ A_{17}, s^{-1} k_{17}, s^{-1} A_{-17}, s^{-1} k_{-17}, s^{-1}	5.60×10^{-3} 1.25×10^{13} 1.18×10^{11} 7.73×10^{13} 2.10×10^{13}	8.67×10^{-3} 1.46×10^{13} 2.68×10^{11} 9.42×10^{13} 3.09×10^{13}	1.20×10^{-2} 1.67×10^{13} 5.04×10^{11} 1.11×10^{14} 4.19×10^{13}
18. $Z^-[\text{HOFeOFeOH}]^{2+}Z^-\{11\}$ $\leftrightarrow Z^-[\text{OFeOHFeOH}]^{2+}Z^-\{11\}$	$\Delta H_{18} = 18.0$ $E_{18}^\ddagger = 24.3$ $E_{-18}^\ddagger = 6.2$	$K_{18} -$ A_{18}, s^{-1} k_{18}, s^{-1} A_{-18}, s^{-1} k_{-18}, s^{-1}	8.14×10^{-7} 3.76×10^{12} 5.39×10^3 1.20×10^{12} 6.62×10^9	7.03×10^{-6} 3.76×10^{12} 9.87×10^4 1.21×10^{12} 1.40×10^{10}	3.53×10^{-5} 3.76×10^{12} 8.76×10^5 1.23×10^{12} 2.48×10^{10}
19. $Z^-[\text{HOFeOHFeO}]^{2+}Z^-\{11\}$ $\leftrightarrow Z^-[\text{HOFeOHFeO}]^{2+}Z^-\{9\}^c$	$\Delta H_{19} = 2.8$ $E_{19}^\ddagger = 5.4$ $E_{-19}^\ddagger = 1.8$	$K_{19} -$ A_{19}, s^{-1} k_{19}, s^{-1} A_{-19}, s^{-1} k_{-19}, s^{-1}	4.70×10^{-3} 1.25×10^{13} 1.36×10^{11} 1.32×10^{14} 2.90×10^{13}	6.84×10^{-3} 1.46×10^{13} 3.04×10^{11} 1.62×10^{14} 4.44×10^{13}	9.03×10^{-3} 1.67×10^{13} 5.63×10^{11} 1.94×10^{14} 6.23×10^{13}
20. $Z^-[\text{HOFeOFeOH}]^{2+}Z^-\{11\}$ $\leftrightarrow Z^-[\text{HOFeOHFeO}]^{2+}Z^-\{11\}^c$	$\Delta H_{20} = 17.1$ $E_{20}^\ddagger = 23.9$ $E_{-20}^\ddagger = 6.3$	$K_{20} -$ A_{20}, s^{-1} k_{20}, s^{-1} A_{-20}, s^{-1} k_{-20}, s^{-1}	1.07×10^{-6} 6.56×10^{11} 1.32×10^3 2.38×10^{11} 1.23×10^9	8.61×10^{-6} 5.66×10^{11} 1.98×10^4 2.10×10^{11} 2.30×10^9	4.10×10^{-5} 4.98×10^{11} 1.49×10^5 1.89×10^{11} 3.64×10^{09}

(continued on next page)

Table A.1 (continued)

Reaction	$E^{\ddagger a}$, ΔH^b (kcal/mol)	Constant	T (K)		
			600	700	800
21. $Z^-[\text{OFeOHFeOH}]^{2+}Z^{-}\{11\} + \text{N}_2\text{O}(\text{g})$ $\leftrightarrow Z^-[(\text{N}_2\text{O})\text{OFeOHFeOH}]^{2+}Z^{-}\{11\}$	$\Delta H_{21} = 0.0$ $E_{21}^{\ddagger} = 0.0$ $E_{-21}^{\ddagger} = 1.6$	K_{21}, bar^{-1} $A_{21}, \text{s}^{-1}\text{bar}^{-1}$ $k_{21}, \text{s}^{-1}\text{bar}^{-1}$ A_{-21}, s^{-1} k_{-21}, s^{-1}	2.28×10^{-5} 7.41×10^7 7.41×10^7 1.25×10^{13} 3.25×10^{12}	2.25×10^{-5} 1.03×10^8 1.03×10^8 1.46×10^{13} 4.60×10^{12}	2.29×10^{-5} 1.39×10^8 1.39×10^8 1.67×10^{13} 6.07×10^{12}
22. $Z^-[(\text{N}_2\text{O})\text{OFeOHFeOH}]^{2+}Z^{-}\{11\}$ $\leftrightarrow Z^-[\text{OFeOHFeOH}]^{2+}Z^{-}\{11\}$ $+ \text{N}_2(\text{g})$	$\Delta H_{22} = -6.8$ $E_{22}^{\ddagger} = 34.7$ $E_{-22}^{\ddagger} = 40.9$	K_{22}, bar A_{22}, s^{-1} k_{22}, s^{-1} $A_{-22}, \text{s}^{-1}\text{bar}^{-1}$ $k_{-22}, \text{s}^{-1}\text{bar}^{-1}$	1.12×10^7 2.73×10^{11} 6.39×10^{-2} 4.53×10^6 5.72×10^{-9}	5.02×10^6 3.00×10^{11} 4.46×10^0 5.25×10^6 8.90×10^{-7}	2.70×10^6 3.24×10^{11} 1.09×10^2 6.03×10^6 4.03×10^{-5}
23. $Z^-[\text{OFeOHFeOH}]^{2+}Z^{-}\{11\}$ $\leftrightarrow Z^-[\text{O}_2\text{FeOHFeOH}]^{2+}Z^{-}\{11\}$	$\Delta H_{23} = -15.0$ $E_{23}^{\ddagger} = 11.1$ $E_{-23}^{\ddagger} = 26.5$	$K_{23} -$ A_{23}, s^{-1} k_{23}, s^{-1} A_{-23}, s^{-1} k_{-23}, s^{-1}	3.30×10^6 1.11×10^{13} 9.83×10^8 1.40×10^{12} 2.98×10^2	5.45×10^5 1.18×10^{13} 3.95×10^9 1.41×10^{12} 7.24×10^3	1.41×10^5 1.23×10^{13} 1.12×10^{10} 1.42×10^{12} 7.94×10^4
24. $Z^-[\text{O}_2\text{FeOHFeOH}]^{2+}Z^{-}\{11\}$ $\leftrightarrow Z^-[\text{FeOHFeOH}]^{2+}Z^{-}\{9\} + \text{O}_2(\text{g})$	$\Delta H_{24} = -2.5$ $E_{24}^{\ddagger} = 0.2$ $E_{-24}^{\ddagger} = 1.7$	K_{24}, bar A_{24}, s^{-1} k_{24}, s^{-1} $A_{-24}, \text{s}^{-1}\text{bar}^{-1}$ $k_{-24}, \text{s}^{-1}\text{bar}^{-1}$	8.93×10^6 1.52×10^9 1.31×10^9 6.00×10^2 1.46×10^2	6.72×10^6 6.25×10^9 5.48×10^9 2.74×10^3 8.16×10^2	5.28×10^6 1.80×10^{10} 1.61×10^{10} 8.78×10^3 3.05×10^3
25. $Z^-[\text{OFeOHFeOH}]^{2+}Z^{-}\{9\}$ $\leftrightarrow Z^-[\text{OFeOFeOH}_2]^{2+}Z^{-}\{9\}$	$\Delta H_{25} = 3.9$ $E_{25}^{\ddagger} = 7.9$ $E_{-25}^{\ddagger} = 4.0$	$K_{25} -$ A_{25}, s^{-1} k_{25}, s^{-1} A_{-25}, s^{-1} k_{-25}, s^{-1}	2.27×10^{-1} 1.74×10^{12} 2.38×10^9 3.07×10^{11} 1.05×10^{10}	3.64×10^{-1} 1.50×10^{12} 5.28×10^9 2.62×10^{11} 1.45×10^{10}	5.17×10^{-1} 1.32×10^{12} 9.41×10^9 2.29×10^{11} 1.82×10^{10}
26. $Z^-[\text{OFeOFeOH}_2]^{2+}Z^{-}\{9\}$ $\leftrightarrow Z^-[\text{OFeOFe}]^{2+}Z^{-}\{9\} + \text{H}_2\text{O}(\text{g})$	$\Delta H_{26} = 16.5$ $E_{26}^{\ddagger} = 17.7$ $E_{-26}^{\ddagger} = 0.0$	K_{24}, bar A_{24}, s^{-1} k_{24}, s^{-1} $A_{-24}, \text{s}^{-1}\text{bar}^{-1}$ $k_{-24}, \text{s}^{-1}\text{bar}^{-1}$	8.48×10^{-2} 1.25×10^{13} 4.48×10^6 5.29×10^7 5.29×10^7	6.28×10^{-1} 1.46×10^{13} 4.36×10^7 6.94×10^7 6.94×10^7	2.74×10^0 1.67×10^{13} 2.44×10^8 8.93×10^7 8.93×10^7
27. $Z^-[\text{HOFeOHFeO}]^{2+}Z^{-}\{9\}$ $\leftrightarrow Z^-[\text{H}_2\text{OFeOFeO}]^{2+}Z^{-}\{9\}^c$	$\Delta H_{27} = 7.7$ $E_{27}^{\ddagger} = 10.7$ $E_{-27}^{\ddagger} = 6.1$	$K_{27} -$ A_{27}, s^{-1} k_{27}, s^{-1} A_{-27}, s^{-1} k_{-27}, s^{-1}	1.79×10^{-1} 5.12×10^{12} 6.28×10^8 5.68×10^{11} 3.50×10^9	3.19×10^{-1} 5.07×10^{12} 2.25×10^9 5.54×10^{11} 7.07×10^9	4.88×10^{-1} 5.04×10^{12} 5.87×10^9 5.47×10^{11} 1.20×10^{10}
28. $Z^-[\text{H}_2\text{OFeOFeO}]^{2+}Z^{-}\{9\}$ $\leftrightarrow Z^-[\text{FeOFeO}]^{2+}Z^{-}\{9\} + \text{H}_2\text{O}(\text{g})^c$	$\Delta H_{28} = 16.9$ $E_{28}^{\ddagger} = 14.3$ $E_{-28}^{\ddagger} = 0.0$	K_{28}, bar A_{28}, s^{-1} k_{28}, s^{-1} $A_{-28}, \text{s}^{-1}\text{bar}^{-1}$ $k_{-28}, \text{s}^{-1}\text{bar}^{-1}$	1.36×10^0 1.25×10^{13} 7.58×10^7 5.57×10^7 5.57×10^7	6.81×10^0 1.46×10^{13} 4.92×10^8 7.22×10^7 7.22×10^7	2.21×10^1 1.67×10^{13} 2.04×10^9 9.22×10^7 9.22×10^7
29. $Z^-[\text{FeOHFeOH}]^{2+}Z^{-}\{9\}$ $\leftrightarrow Z^-[\text{FeOFeOH}_2]^{2+}Z^{-}\{9\}$	$\Delta H_{29} = 8.8$ $E_{29}^{\ddagger} = 13.7$ $E_{-29}^{\ddagger} = 4.7$	$K_{29} -$ A_{29}, s^{-1} k_{29}, s^{-1} A_{-29}, s^{-1} k_{-29}, s^{-1}	1.17×10^{-2} 2.79×10^{12} 2.89×10^7 1.29×10^{11} 2.48×10^9	3.37×10^{-2} 2.68×10^{12} 1.43×10^8 1.26×10^{11} 4.24×10^9	7.43×10^{-2} 2.60×10^{12} 4.74×10^8 1.24×10^{11} 6.38×10^9
30. $Z^-[\text{FeOFeOH}_2]^{2+}Z^{-}\{9\}$ $\leftrightarrow Z^-[\text{FeOFe}]^{2+}Z^{-}\{9\} + \text{H}_2\text{O}(\text{g})$	$\Delta H_{30} = 12.8$ $E_{30}^{\ddagger} = 13.9$ $E_{-30}^{\ddagger} = 0.0$	K_{30}, bar A_{30}, s^{-1} k_{30}, s^{-1} $A_{-30}, \text{s}^{-1}\text{bar}^{-1}$ $k_{-30}, \text{s}^{-1}\text{bar}^{-1}$	7.97×10^{-1} 1.25×10^{13} 1.11×10^8 1.40×10^8 1.40×10^8	3.76×10^0 1.46×10^{13} 6.84×10^8 1.82×10^8 1.82×10^8	1.17×10^1 1.67×10^{13} 2.72×10^9 2.33×10^8 2.33×10^8

(continued on next page)

Table A.1 (continued)

Reaction	$E_{\ddagger}^{\ddagger a}$, ΔH^b (kcal/mol)	Constant	T (K)		
			600	700	800
31. $Z^-[\text{FeOFe}]^{2+}Z^-{\{9\}} + \text{N}_2\text{O}(\text{g})$ $\leftrightarrow Z^-[(\text{N}_2\text{O})\text{FeOFe}]^{2+}Z^-{\{9\}}$	$\Delta H_{31} = -2.6$	K_{31}, bar^{-1}	5.46×10^{-5}	3.93×10^{-5}	3.16×10^{-5}
	$E_{31}^{\ddagger} = 0.0$	$A_{31}, \text{s}^{-1}\text{bar}^{-1}$	1.79×10^7	2.53×10^7	3.44×10^7
	$E_{-31}^{\ddagger} = 4.3$	$k_{31}, \text{s}^{-1}\text{bar}^{-1}$	1.79×10^7	2.53×10^7	3.44×10^7
32. $Z^-[(\text{N}_2\text{O})\text{FeOFe}]^{2+}Z^-{\{9\}}$ $\leftrightarrow Z^-[\text{OFeOFe}]^{2+}Z^-{\{9\}} + \text{N}_2(\text{g})$	$\Delta H_{32} = -9.0$	K_{32}, bar	1.89×10^8	6.38×10^7	2.77×10^7
	$E_{32}^{\ddagger} = 27.5$	A_{32}, s^{-1}	9.83×10^{12}	1.13×10^{13}	1.27×10^{13}
	$E_{-32}^{\ddagger} = 35.9$	k_{32}, s^{-1}	9.07×10^2	2.83×10^4	3.77×10^5
33. $Z^-[\text{OFeOFe}]^{2+}Z^-{\{9\}} + \text{N}_2\text{O}(\text{g})$ $\leftrightarrow Z^-[\text{OFeOFe}(\text{ON}_2)]^{2+}Z^-{\{9\}}$	$\Delta H_{33} = -3.0$	K_{33}, bar^{-1}	7.06×10^{-5}	4.82×10^{-5}	3.72×10^{-5}
	$E_{33}^{\ddagger} = 0.0$	$A_{33}, \text{s}^{-1}\text{bar}^{-1}$	1.64×10^7	2.31×10^7	3.12×10^7
	$E_{-33}^{\ddagger} = 4.7$	$k_{33}, \text{s}^{-1}\text{bar}^{-1}$	1.64×10^7	2.31×10^7	3.12×10^7
34. $Z^-[\text{OFeOFe}(\text{ON}_2)]^{2+}Z^-{\{9\}}$ $\leftrightarrow Z^-[\text{OFeOFeO}]^{2+}Z^-{\{9\}} + \text{N}_2(\text{g})$	$\Delta H_{34} = -9.6$	K_{34}, bar	1.04×10^8	3.35×10^7	1.40×10^7
	$E_{34}^{\ddagger} = 27.7$	A_{34}, s^{-1}	8.53×10^{13}	9.89×10^{13}	1.12×10^{14}
	$E_{-34}^{\ddagger} = 36.3$	k_{34}, s^{-1}	6.93×10^3	2.22×10^5	3.02×10^6
35. $Z^-[\text{FeOFe}]^{2+}Z^-{\{9\}} + \text{N}_2\text{O}(\text{g})$ $\leftrightarrow Z^-[\text{FeOFe}(\text{ON}_2)]^{2+}Z^-{\{9\}}$	$\Delta H_{35} = -2.7$	K_{35}, bar^{-1}	9.38×10^{-5}	6.63×10^{-5}	5.25×10^{-5}
	$E_{35}^{\ddagger} = 0.0$	$A_{35}, \text{s}^{-1}\text{bar}^{-1}$	2.63×10^7	3.73×10^7	5.07×10^7
	$E_{-35}^{\ddagger} = 4.5$	$k_{35}, \text{s}^{-1}\text{bar}^{-1}$	2.63×10^7	3.73×10^7	5.07×10^7
36. $Z^-[\text{FeOFe}(\text{ON}_2)]^{2+}Z^-{\{9\}}$ $\leftrightarrow Z^-[\text{FeOFeO}]^{2+}Z^-{\{9\}} + \text{N}_2(\text{g})$	$\Delta H_{36} = -12.6$	K_{36}, bar	1.55×10^9	3.47×10^8	1.11×10^8
	$E_{36}^{\ddagger} = 25.6$	A_{36}, s^{-1}	7.09×10^{11}	7.93×10^{11}	8.71×10^{11}
	$E_{-36}^{\ddagger} = 37.2$	k_{36}, s^{-1}	3.45×10^2	8.26×10^3	9.03×10^4
37. $Z^-[\text{FeOFeO}]^{2+}Z^-{\{9\}} + \text{N}_2\text{O}(\text{g})$ $\leftrightarrow Z^-[(\text{N}_2\text{O})\text{FeOFeO}]^{2+}Z^-{\{9\}}$	$\Delta H_{37} = -3.6$	K_{37}, bar^{-1}	1.01×10^{-4}	6.44×10^{-5}	4.72×10^{-5}
	$E_{37}^{\ddagger} = 0.0$	$A_{37}, \text{s}^{-1}\text{bar}^{-1}$	1.42×10^7	2.00×10^7	2.71×10^7
	$E_{-37}^{\ddagger} = 5.3$	$k_{37}, \text{s}^{-1}\text{bar}^{-1}$	1.42×10^7	2.00×10^7	2.71×10^7
38. $Z^-[\text{N}_2\text{O})\text{FeOFeO}]^{2+}Z^-{\{9\}}$ $\leftrightarrow Z^-[\text{FeOFeO}]^{2+}Z^-{\{9\}} + \text{N}_2(\text{g})$	$\Delta H_{38} = -5.4$	K_{38}, bar	5.17×10^6	2.73×10^6	1.66×10^6
	$E_{38}^{\ddagger} = 30.1$	A_{38}, s^{-1}	5.05×10^{13}	5.89×10^{13}	6.66×10^{13}
	$E_{-38}^{\ddagger} = 34.7$	k_{38}, s^{-1}	5.26×10^2	2.27×10^4	3.86×10^5
39. $Z^-[\text{OFeOFeO}]^{2+}Z^-{\{9\}}$ $\leftrightarrow Z^-[\text{FeOFeO}]^{2+}Z^-{\{9\}}$	$\Delta H_{39} = 8.3$	$K_{39} -$	1.91×10^{-1}	5.18×10^{-1}	1.10×10^0
	$E_{39}^{\ddagger} = 27.3$	A_{39}, s^{-1}	3.26×10^{14}	3.90×10^{14}	4.48×10^{14}
	$E_{-39}^{\ddagger} = 20.0$	k_{39}, s^{-1}	3.79×10^4	1.19×10^6	1.58×10^7
40. $Z^-[\text{FeOFeO}]^{2+}Z^-{\{9\}}$ $\leftrightarrow Z^-[\text{FeO}_2\text{FeO}]^{2+}Z^-{\{9\}}$	$\Delta H_{40} = -5.3$	$K_{40} -$	4.74×10^0	2.51×10^0	1.55×10^0
	$E_{40}^{\ddagger} = 6.2$	A_{40}, s^{-1}	9.36×10^{12}	9.88×10^{12}	1.03×10^{13}
	$E_{-40}^{\ddagger} = 11.0$	k_{40}, s^{-1}	5.05×10^{10}	1.12×10^{11}	2.05×10^{11}
			1.08×10^{14}	1.22×10^{14}	1.33×10^{14}
			1.07×10^{10}	4.49×10^{10}	1.32×10^{11}

(continued on next page)

Table A.1 (*continued*)

Reaction	$E^\ddagger^a, \Delta H^b$ (kcal/mol)	Constant	T (K)		
			600	700	800
41. $Z^-[\text{FeO}_2\text{FeO}]^{2+}Z^-\{9\}$ $\leftrightarrow Z^-[\text{FeOFeO}_2]^{2+}Z^-\{9\}$	$\Delta H_{41} = -19.4$	K_{41}	1.10×10^8	1.06×10^7	1.85×10^6
	$E_{41}^\ddagger = 25.3$	A_{41}, s^{-1}	1.07×10^{13}	1.20×10^{13}	1.32×10^{13}
		k_{41}, s^{-1}	6.48×10^3	1.51×10^5	1.61×10^6
42. $Z^-[\text{FeOFeO}_2]^{2+}Z^-\{9\}$ $\leftrightarrow Z^-[\text{FeOFeO}_2]^{2+}Z^-\{11\}$	$\Delta H_{42} = -4.8$	K_{42}	1.06×10^2	5.95×10^1	3.86×10^1
	$E_{42}^\ddagger = 7.6$	A_{42}, s^{-1}	1.25×10^{13}	1.46×10^{13}	1.67×10^{13}
		k_{42}, s^{-1}	2.21×10^{10}	6.36×10^{10}	1.43×10^{11}
43. $Z^-[\text{FeOFeO}_2]^{2+}Z^-\{11\}$ $\leftrightarrow Z^-[\text{FeOFe}]^{2+}Z^-\{9\} + \text{O}_2(\text{g})$	$\Delta H_{43} = 7.1$	K_{43}, bar	8.41×10^3	2.00×10^4	3.72×10^4
	$E_{43}^\ddagger = 8.1$	A_{43}, s^{-1}	7.78×10^{13}	8.46×10^{13}	9.00×10^{13}
		k_{43}, s^{-1}	9.00×10^{10}	2.57×10^{11}	5.64×10^{11}
	$E_{-43}^\ddagger = 0.02$	$A_{-43}, \text{s}^{-1} \text{bar}^{-1}$	1.08×10^7	1.30×10^7	1.53×10^7
		$k_{-43}, \text{s}^{-1} \text{bar}^{-1}$	1.07×10^7	1.28×10^7	1.52×10^7

^a Calculated activation energy including zero-point energy corrections

^b Calculated enthalpy averaged over 600-800 K.

^c Reaction has not been described in chapter 6.

Table A.2: Computed rate parameters for elementary steps in nitrous oxide dissociation on antiferromagnetically coupled dinuclear oxygen bridged iron sites in Fe-ZSM-5. The numbers in braces denote the spin multiplicity.

Reaction ^a	$E^\ddagger^b, \Delta H^c$ (kcal/mol)	Constant	T (K)		
			600	700	800
1. $Z^-[\text{HOFeOFeOH}]^{2+}Z^-\{1\}$ $\leftrightarrow Z^-[\text{OFeOFe}]^{2+}Z^-\{1\} + \text{H}_2\text{O}(\text{g})^d$	$\Delta H_1 = 46.7$	K_1, bar	3.74×10^{-12}	1.04×10^{-9}	6.84×10^{-8}
	$E_1^\ddagger = 48.1$	A_1, s^{-1}	1.25×10^{13}	1.46×10^{13}	1.67×10^{13}
		k_1, s^{-1}	3.74×10^{-5}	1.39×10^{-2}	1.20×10^0
2. $Z^-[\text{HOFeOFeOH}]^{2+}Z^-\{1\}$ $\leftrightarrow Z^-[\text{FeOFeO}]^{2+}Z^-\{1\} + \text{H}_2\text{O}(\text{g})^d$	$\Delta H_2 = 43.2$	K_2, bar	6.89×10^{-11}	1.27×10^{-8}	6.08×10^{-7}
	$E_2^\ddagger = 44.7$	A_2, s^{-1}	1.25×10^{13}	1.46×10^{13}	1.67×10^{13}
		k_2, s^{-1}	6.53×10^{-4}	1.61×10^{-1}	1.02×10^1
3. (31.) $Z^-[\text{FeOFe}]^{2+}Z^-\{1\} + \text{N}_2\text{O}(\text{g})$ $\leftrightarrow Z^-[(\text{N}_2\text{O})\text{FeOFe}]^{2+}Z^-\{1\}$	$\Delta H_3 = -2.3$	K_3, bar^{-1}	3.27×10^{-5}	2.43×10^{-5}	1.99×10^{-5}
	$E_3^\ddagger = 0.0$	$A_3, \text{s}^{-1} \text{bar}^{-1}$	1.37×10^7	1.93×10^7	2.60×10^7
		$k_3, \text{s}^{-1} \text{bar}^{-1}$	1.37×10^7	1.93×10^7	2.60×10^7
	$E_{-3}^\ddagger = 4.0$	A_{-3}, s^{-1}	1.25×10^{13}	1.46×10^{13}	1.67×10^{13}
		k_{-3}, s^{-1}	4.19×10^{11}	7.94×10^{11}	1.31×10^{12}

(*continued on next page*)

Table A.2 (continued)

Reaction ^a	$E^{\ddagger b}$, ΔH^c (kcal/mol)	Constant	T (K)		
			600	700	800
4. (32.) $Z^-[(N_2O)FeOFe]^{2+}Z^- \{1\}$ $\leftrightarrow Z^- [OFeOFe]^{2+}Z^- \{1\} + N_2(g)$	$\Delta H_4 = -8.2$	K_4, bar	7.99×10^7	3.05×10^7	1.45×10^7
	$E_4^{\ddagger} = 26.1$	A_4, s^{-1}	1.03×10^{13}	1.18×10^{13}	1.32×10^{13}
	$E_{-4}^{\ddagger} = 33.4$	k_4, s^{-1}	3.30×10^3	8.58×10^4	9.98×10^5
5. (33.) $Z^- [OFeOFe]^{2+}Z^- \{1\} + N_2O(g)$ $\leftrightarrow Z^- [OFeOFe(ON_2)]^{2+}Z^- \{1\}$	$\Delta H_5 = -3.0$	K_5, bar^{-1}	6.64×10^{-5}	4.54×10^{-5}	3.50×10^{-5}
	$E_5^{\ddagger} = 0.0$	$A_5, s^{-1} \text{bar}^{-1}$	1.56×10^7	2.20×10^7	2.97×10^7
	$E_{-5}^{\ddagger} = 4.7$	$k_5, s^{-1} \text{bar}^{-1}$	1.56×10^7	2.20×10^7	2.97×10^7
6. (34.) $Z^- [OFeOFe(ON_2)]^{2+}Z^- \{1\}$ $\leftrightarrow Z^- [OFeOFeO]^{2+}Z^- \{1\} + N_2(g)$	$\Delta H_6 = -8.6$	K_6, bar	3.91×10^7	1.41×10^7	6.44×10^6
	$E_6^{\ddagger} = 27.4$	A_6, s^{-1}	1.09×10^{14}	1.26×10^{14}	1.41×10^{14}
	$E_{-6}^{\ddagger} = 35.0$	k_6, s^{-1}	1.11×10^4	3.43×10^5	4.53×10^6
7. (35.) $Z^- [FeOFe]^{2+}Z^- \{1\} + N_2O(g)$ $\leftrightarrow Z^- [FeOFe(ON_2)]^{2+}Z^- \{1\}$	$\Delta H_7 = -2.6$	K_7, bar^{-1}	7.01×10^{-5}	5.02×10^{-5}	4.01×10^{-5}
	$E_7^{\ddagger} = 0.0$	$A_7, s^{-1} \text{bar}^{-1}$	2.23×10^7	3.14×10^7	4.26×10^7
	$E_{-7}^{\ddagger} = 4.4$	$k_7, s^{-1} \text{bar}^{-1}$	2.23×10^7	3.14×10^7	4.26×10^7
8. (36.) $Z^- [FeOFe(ON_2)]^{2+}Z^- \{1\}$ $\leftrightarrow Z^- [FeOFeO]^{2+}Z^- \{1\} + N_2(g)$	$\Delta H_8 = -11.3$	K_8, bar	6.88×10^8	1.79×10^8	6.40×10^7
	$E_8^{\ddagger} = 24.0$	A_8, s^{-1}	1.08×10^{13}	1.23×10^{13}	1.38×10^{13}
	$E_{-8}^{\ddagger} = 34.4$	k_8, s^{-1}	2.01×10^4	4.06×10^5	3.91×10^6
9. (37.) $Z^- [FeOFeO]^{2+}Z^- \{1\} + N_2O(g)$ $\leftrightarrow Z^- [(N_2O)FeOFeO]^{2+}Z^- \{1\}$	$\Delta H_9 = -3.3$	K_9, bar^{-1}	5.77×10^{-5}	3.81×10^{-5}	2.88×10^{-5}
	$E_9^{\ddagger} = 0.0$	$A_9, s^{-1} \text{bar}^{-1}$	1.11×10^7	1.56×10^7	2.10×10^7
	$E_{-9}^{\ddagger} = 5.0$	$k_9, s^{-1} \text{bar}^{-1}$	1.11×10^7	1.56×10^7	2.10×10^7
10. (38.) $Z^- [(N_2O)FeOFeO]^{2+}Z^- \{1\}$ $\leftrightarrow Z^- [OFeOFeO]^{2+}Z^- \{1\} + N_2(g)$	$\Delta H_{10} = -4.9$	K_{10}, bar	2.45×10^6	1.38×10^6	8.83×10^5
	$E_{10}^{\ddagger} = 30.1$	A_{10}, s^{-1}	2.67×10^{13}	3.01×10^{13}	3.33×10^{13}
	$E_{-10}^{\ddagger} = 34.7$	k_{10}, s^{-1}	2.77×10^2	1.16×10^4	1.93×10^5
11. (39.) $Z^- [OFeOFeO]^{2+}Z^- \{1\}$ $\leftrightarrow Z^- [FeOOFeO]^{2+}Z^- \{1\}$	$\Delta H_{11} = 9.9$	$K_{11} -$	3.40×10^{-2}	1.11×10^{-1}	2.71×10^{-1}
	$E_{11}^{\ddagger} = 31.0$	A_{11}, s^{-1}	4.01×10^{14}	4.96×10^{14}	5.84×10^{14}
	$E_{-11}^{\ddagger} = 22.1$	k_{11}, s^{-1}	2.02×10^3	1.02×10^5	1.96×10^6
12. (40.) $Z^- [FeOOFeO]^{2+}Z^- \{1\}$ $\leftrightarrow Z^- [FeO_2FeO]^{2+}Z^- \{1\}$	$\Delta H_{12} = -4.9$	$K_{12} -$	7.23×10^0	4.00×10^0	2.57×10^0
	$E_{12}^{\ddagger} = 6.4$	A_{12}, s^{-1}	1.95×10^{12}	1.84×10^{12}	1.74×10^{12}
	$E_{-12}^{\ddagger} = 10.6$	k_{12}, s^{-1}	9.40×10^9	1.90×10^{10}	3.18×10^{10}
13. (41.) $Z^- [FeO_2FeO]^{2+}Z^- \{1\}$ $\leftrightarrow Z^- [FeOFeO_2]^{2+}Z^- \{1\}$	$\Delta H_{13} = -25.1$	$K_{13} -$	1.03×10^{10}	5.04×10^8	5.25×10^7
	$E_{13}^{\ddagger} = 22.0$	A_{13}, s^{-1}	4.47×10^{12}	4.84×10^{12}	5.16×10^{12}
	$E_{-13}^{\ddagger} = 47.5$	k_{13}, s^{-1}	4.21×10^4	6.38×10^5	4.92×10^6
			8.76×10^{11}	9.07×10^{11}	9.34×10^{11}
			4.09×10^{-6}	1.27×10^{-3}	9.38×10^{-2}

(continued on next page)

Table A.2 (*continued*)

Reaction ^a	$E^{\ddagger b}$, ΔH^c (kcal/mol)	Constant	T (K)		
			600	700	800
14. (42.) $Z^-[\text{FeOFeO}_2]^{2+}Z^- \{1\}$ $\leftrightarrow Z^-[\text{FeOFeO}_2]^{2+}Z^- \{3\}$	$\Delta H_{14} = -4.7$	$K_{14} -$	1.57×10^2	8.94×10^1	5.85×10^1
	$E_{14}^{\ddagger} = 7.9$	A_{14}, s^{-1}	1.25×10^{13}	1.46×10^{13}	1.67×10^{13}
	$E_{-14}^{\ddagger} = 12.6$	k_{14}, s^{-1}	1.67×10^{10}	5.01×10^{10}	1.16×10^{11}
15. (43.) $Z^-[\text{FeOFeO}_2]^{2+}Z^- \{3\}$ $\leftrightarrow Z^-[\text{FeOFe}]^{2+}Z^- \{1\} + \text{O}_2(\text{g})$	$\Delta H_{15} = 7.1$	K_{15}, bar	2.47×10^3	6.97×10^3	1.48×10^4
	$E_{15}^{\ddagger} = 8.8$	A_{15}, s^{-1}	7.03×10^{13}	7.09×10^{13}	7.13×10^{13}
		k_{15}, s^{-1}	2.47×10^{10}	7.75×10^{10}	1.83×10^{11}
	$E_{-15}^{\ddagger} = 0.0$	$A_{-15}, \text{s}^{-1} \text{bar}^{-1}$	1.00×10^7	1.11×10^7	1.24×10^7
	$k_{-15}, \text{s}^{-1} \text{bar}^{-1}$	1.00×10^7	1.11×10^7	1.24×10^7	

^a Numbers in brackets refer to the corresponding reaction in table A.1.

^b Calculated activation energy including zero-point energy correction

^c Calculated enthalpy averaged over 600-800 K.

^d Reaction has not been described in chapter 6.

Table A.3: Norm of the gradient difference at the point of spin surface crossing and thermally averaged Landau-Zener transition probabilities at temperatures of 600, 700, and 800 K^a

Reaction ^b	$ \text{grad}(E_1) - \text{grad}(E_2) $ (kJ/mol/Å)	$P_{\text{LZ}}(H_{12} = 395 \text{ J/mol})$			$P_{\text{LZ}}(H_{12} = 825 \text{ J/mol})$			
		T (K)	600	700	800	T (K)	600	700
<i>Ferromagnetically coupled iron atoms</i>								
10. $Z^-[\text{HOFeO-FeOH}]^{2+}Z^- \{9\}$ $\leftrightarrow Z^-[\text{HOFeOFeOH}]^{2+}Z^- \{11\}$	240	0.045	0.042	0.040	0.139	0.131	0.125	
13. $Z^-[\text{HOFeO-OFeOH}]^{2+}Z^- \{9\}$ $\leftrightarrow Z^-[\text{HOFeOOFeOH}]^{2+}Z^- \{11\}$	158	0.066	0.062	0.059	0.196	0.185	0.177	
17. $Z^-[\text{OFeOHFeOH}]^{2+}Z^- \{11\}$ $\leftrightarrow Z^-[\text{OFeOHFeOH}]^{2+}Z^- \{9\}$	428	0.032	0.030	0.028	0.101	0.096	0.091	
19. $Z^-[\text{HOFeOFeOH}]^{2+}Z^- \{11\}$ $\leftrightarrow Z^-[\text{HOFeOHFeO}]^{2+}Z^- \{9\}$	414	0.029	0.027	0.025	0.094	0.088	0.084	
42. $Z^-[\text{FeOFeO}_2]^{2+}Z^- \{9\}$ $\leftrightarrow Z^-[\text{FeOFeO}_2]^{2+}Z^- \{11\}$	128	0.085	0.080	0.076	0.244	0.232	0.221	
<i>Antiferromagnetically coupled iron atoms</i>								
14. $Z^-[\text{FeOFeO}_2]^{2+}Z^- \{1\}$ $\leftrightarrow Z^-[\text{FeOFeO}_2]^{2+}Z^- \{3\}$	125	0.086	0.081	0.077	0.248	0.235	0.225	

^a Landau-Zener probabilities are calculated for spin-orbit coupling energy of $H_{12} = 395$ and 825 J/mol.

^b Reaction numbers are the same as those in tables A.1 and A.2, respectively.

Supporting information for chapter 9

B

This material includes a description of the simulation methodologies and force fields used as well as details on the fitting of adsorption isotherms and determination of Maxwell-Stefan (M-S) diffusivities from molecular dynamics (MD) data. Moreover, it contains information on the derivation of rate expressions, the solution of the diffusion-reaction equation, the comparison between experimental and simulated rates, and additional simulation data.

B.1 Simulation methodologies

B.1.1 GCMC simulation methodology

Configurational-bias Monte Carlo (CBMC) simulations have been carried out to determine the adsorption isotherms for ethene (E), benzene (B), and ethylbenzene (EB) in MFI (all silica silicalite-1) at a variety of temperatures; the crystallographic data are available elsewhere.^{451,452} We use the united atom model. The zeolite framework is considered to be rigid. We consider the CH_x groups as single, chargeless interaction centers with their own effective potentials. The beads in the chain are connected by harmonic bonding potentials. A harmonic cosine bending potential models the bond bending between three neighboring beads, a Ryckaert-Bellemans potential controls the torsion angle. Beads in a chain separated by more than three bonds interact with each other through a Lennard-Jones potential. The Lennard-Jones potentials are shifted and cut at 12 Å. The CBMC simulation details, along with the force fields are given in detail in elsewhere.^{98,453} The simulation box consists of $2 \times 2 \times 3$ unit cells for MFI. Periodic boundary conditions were employed. It was verified that the size of the simulation box was large enough to yield reliable data on adsorption.

Simulations for the adsorption isotherms of ethene and benzene was carried out with the force field of Ban et al.⁴⁵⁴ For ethylbenzene, the force field of benzene was used as a starting point and the force field parameters for the ethyl side chain were adapted using the alkane force field parameters of Dubbeldam et al.^{98,453} as basis. The ethylbenzene molecule was assumed rigid. The CH_2 pseudo-atom is in the plane of the benzene ring, with a fixed bond of 1.54 Å connecting the CH_2 pseudo-atom to the benzene ring. The CH_3 pseudo atom is located at a distance of 1.54 Å from the CH_2 pseudo-atom. The bond angle between the aromatic ring, the CH_2 pseudo-atom and the CH_3 pseudo atom is 114 degrees. This bond angle is in a plane perpendicular to the plane containing the aromatic ring. Lorentz-Berthelot mixing rules are used to describe the interaction between the pseudo atoms of the aromatic rings and the two pseudo atoms of the ethyl group and the zeolite atoms. The van der Waals interactions are cut and shifted at 12 Å. An Ewald summation method is used for evaluation of the charge interactions, that model the zeolite and the dipole moment of the aromatic ring.

Additionally CBMC simulations were carried out to determine the component loadings for various binary mixtures; in these simulations the partial gas phase fugacities were equal, i. e. $f_1 = f_2$.

The CBMC simulations were performed in the Van't Hoff Institute for

Molecular Sciences at the University of Amsterdam using the BIGMAC code developed by T.J.H. Vlugt⁴⁵⁵ as basis.

B.1.2 MD simulation methodology

Diffusion is simulated using Newton's equations of motion until the system properties, on average, no longer change in time. The Verlet algorithm is used for time integration. A time step of 1 fs was used in all simulations. For each simulation, *initializing* GCMC moves are used to place the molecules in the domain, minimizing the energy. Next, follows an *equilibration* stage. Equilibration cycles are essentially the same as the production cycles, only the statistics are not yet taken into account. This removes any initial large disturbances in the system to not affect statistics. After a fixed number of initialization and equilibrium steps, the MD simulation *production* cycles start. For every cycle, the statistics for determining the mean square displacements (MSDs) are updated. The MSDs are determined for time intervals ranging from 2 fs to 1 ns. In order to do this, an order- N algorithm, as detailed in Chapter 4 of Frenkel and Smit⁸⁷ is implemented. The Nosé-Hoover thermostat is applied to all the diffusing particles.

The DL_POLY code⁴⁵⁶ was used along with the force field implementation as described in the previous section. DL_POLY is a molecular dynamics simulation package written by W. Smith, T.R. Forester and I.T. Todorov and has been obtained from CCLRCs Daresbury Laboratory via the website.⁴⁵⁷

The MD simulations were carried out for a variety of molecular loadings. All simulations were performed in the Van't Hoff Institute of Molecular Sciences at the University of Amsterdam on clusters of PCs equipped with Intel Xeon processors running at 3.4 GHz on the Linux operating system. Each MD simulation, for a specified loading, was run for 120 h, determined to be long enough to obtain reliable statistics for determination of the diffusivities.

The self-diffusivities, $D_{i,\text{self}}$, were computed by analyzing the mean square displacement of each species i for each of the coordinate directions:

$$D_{i,\text{self}} = \frac{1}{2n_i} \lim_{\Delta t \rightarrow \infty} \frac{1}{\Delta t} \left\langle \left\langle \sum_{l=1}^{n_i} (\mathbf{r}_{l,i}(t + \Delta t) - \mathbf{r}_{l,i}(t))^2 \right\rangle \right\rangle. \quad (\text{B.1})$$

In this expression, n_i represents the number of molecules of species i respectively, and $\mathbf{r}_{l,i}(t)$ is the position of molecule l of species i at any time t . Equation B.1 also defines the self-diffusivity in a n -component mixture.

In the Maxwell-Stefan (M-S) formulation, the flux of any species in a

binary mixture is related to its chemical potential gradient by²⁹⁸

$$-\rho \frac{\theta_i}{RT} \frac{d\mu_i}{dx} = \sum_{\substack{j=1 \\ j \neq i}}^n \frac{q_j N_i - q_i N_j}{q_{i,\text{sat}} q_{j,\text{sat}} \mathcal{D}_{ij}} + \frac{N_i}{q_{i,\text{sat}} \mathcal{D}_i}; \quad i = 1, 2, \dots, n, \quad (\text{B.2})$$

where N_i is the molar flux, ρ is the zeolite framework density, q_i is the molar loading, $q_{i,\text{sat}}$ is the saturation capacity, $d\mu_i/dx$ is the chemical potential gradient, R is the gas constant, T is the absolute temperature, \mathcal{D}_i is the M-S diffusivity, and \mathcal{D}_{ij} are the binary exchange coefficients. Conformity with the Onsager Reciprocal Relations demands that

$$q_{j,\text{sat}} \mathcal{D}_{ij} = q_{i,\text{sat}} \mathcal{D}_{ji}. \quad (\text{B.3})$$

The gradient of the chemical potentials in equation B.2 can be related to the gradients in the loadings by defining a 2×2 dimensional matrix of thermodynamic factors $[\Gamma]$:

$$\frac{q_i}{RT} \frac{d\mu_i}{dx} = \sum_{j=1}^2 \Gamma_{ij} \frac{dq_j}{dx}; \quad \Gamma_{ij} \equiv \frac{q_i}{f_i} \frac{\partial f_i}{\partial q_j}; \quad i, j = 1, 2. \quad (\text{B.4})$$

The elements Γ_{ij} in equation B.4 can be estimated, for example, using the Ideal Adsorbed Solution Theory of Myers and Prausnitz³⁰⁶ and the fits of the pure component isotherm data. The fluxes N_i can be explicitly expressed as functions of the gradients in the loading,

$$(\mathbf{N}) = -\rho[\Delta][\Gamma] \frac{d(\mathbf{q})}{dx} \quad (\text{B.5})$$

where $[\Delta]$ is a square matrix of M-S diffusivities. Compliance with the Onsager Reciprocal Relations demand that

$$q_2 \Delta_{12} = q_1 \Delta_{21}. \quad (\text{B.6})$$

The diagonal elements Δ_{ii} in each of the coordinate directions for the linear alkanes were obtained from

$$\Delta_{ii} = \frac{1}{2} \lim_{\Delta t \rightarrow \infty} \frac{1}{n_i} \frac{1}{\Delta t} \left\langle \left(\sum_{l=1}^{n_i} (\mathbf{r}_{l,i}(t + \Delta t) - \mathbf{r}_{l,i}(t))^2 \right) \right\rangle. \quad (\text{B.7})$$

In this expression, n_i represents the number of molecules of species i , and $\mathbf{r}_{l,i}(t)$ is the position of molecule l of species i at any time t . The values of Δ_{ii} for benzene and ethylbenzene are about 2–3 orders of magnitude lower than that of ethene; these are too low to be accurately determined from MD simulations and are not reported here.

B.2 Fitting of adsorption isotherms for C₂H₄, C₆H₆, and C₈H₁₀ in MFI and validation of ideal adsorbed solution theory

B.2.1 Methodology

Adsorption isotherms at three different temperatures have been obtained from CBMC simulations in the grand canonical ensemble as outline in section B.1. The simulation data were fitted to a three-site Langmuir model,

$$q = \frac{q_{i,\text{sat},\text{A}} b_{i,\text{A}} f_i}{1 + b_{i,\text{A}} f_i} + \frac{q_{i,\text{sat},\text{B}} b_{i,\text{B}} f_i}{1 + b_{i,\text{B}} f_i} + \frac{q_{i,\text{sat},\text{C}} b_{i,\text{C}} f_i}{1 + b_{i,\text{C}} f_i}, \quad (\text{B.8})$$

where $q_{i,\text{sat},\text{X}}$ denotes the saturation capacity of species i on site X in molecules per unit cell, $b_{i,\text{X}}$ is the affinity constant in Pa⁻¹, and f_i is the gas phase fugacity of species i in Pa. As can be seen in figure B.1, the agreement between simulation and isotherm model is good over the whole range of fugacities. The values of the fit-parameters are given in table B.1. We used the ideal adsorbed solution theory (IAST)³⁰⁶ to calculate multicomponent mixture adsorption from the knowledge of the pure component adsorption isotherms. Due to segregation effects in mixture adsorption, predictions from IAST might deviate from GCMC predictions.⁴⁵⁸⁻⁴⁶⁰ Therefore we compared our results from a GCMC simulation of a binary ethene-benzene mixture with equal partial fugacities adsorbed in MFI to the predictions from the IAS theory. As can be seen in figure B.2 both data sets agree well up to a partial gas phase fugacity of 10⁶ Pa which covers the industrially relevant process conditions.

B.2.2 Tables

Table B.1: Three-site Langmuir parameters for C_2H_4 , C_6H_6 , and C_8H_{10} in MFI. The saturation capacity q_{sat} has the unit of molecules per unit cell. The Langmuir affinity constants are given in Pa^{-1} .

molecule	temp.	three-site Langmuir parameters					
		$q_{i,\text{sat},A}$	$b_{i,A}$	$q_{i,\text{sat},B}$	$b_{i,B}$	$q_{i,\text{sat},C}$	$b_{i,C}$
C_2H_4	603 K	12	1.31×10^{-7}	5	2.37×10^{-9}	2	5.58×10^{-12}
C_2H_4	653 K	12	8.40×10^{-8}	5	1.50×10^{-9}	2	4.46×10^{-12}
C_2H_4	703 K	12	5.62×10^{-8}	5	1.03×10^{-9}	2	4.26×10^{-12}
C_6H_6	603 K	4	4.15×10^{-6}	4	8.20×10^{-9}	4	1.42×10^{-10}
C_6H_6	653 K	4	1.97×10^{-6}	4	4.44×10^{-9}	4	7.58×10^{-11}
C_6H_6	703 K	4	9.76×10^{-7}	4	2.50×10^{-9}	4	4.94×10^{-11}
C_8H_{10}	603 K	4	9.24×10^{-6}	2	1.40×10^{-9}	2	9.94×10^{-12}
C_8H_{10}	653 K	4	3.13×10^{-6}	2	5.58×10^{-10}	0	0
C_8H_{10}	703 K	4	1.16×10^{-6}	2	2.11×10^{-10}	2	6.37×10^{-12}

B.2.3 Figures

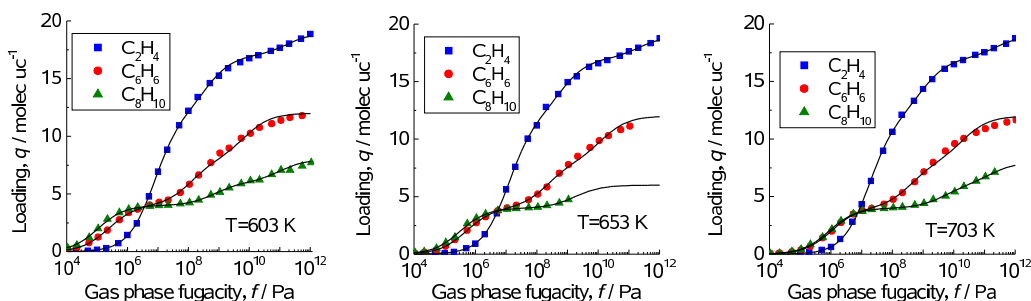


Figure B.1: Pure component adsorption isotherms of ethene, benzene, and ethylbenzene in MFI at three different temperatures. The symbols represent results from GCMC simulations. The lines are three-site Langmuir fits of the GCMC simulated isotherms.

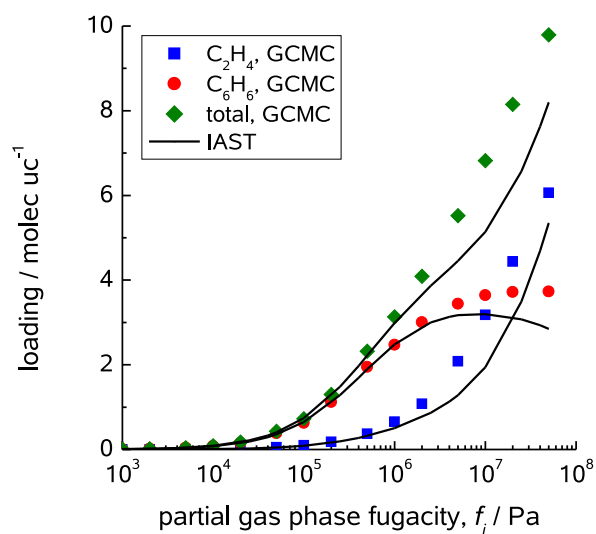


Figure B.2: Total and partial adsorption isotherms in MFI at 653 K for an ethene-benzene mixture at equal partial gas phase fugacities. The symbols represent GCMC simulations, the lines are predictions of the IAST theory.

B.3 Extraction of M-S diffusivities from MD simulation data

B.3.1 Methodology

Diffusivity data for ethene have been obtained from MD simulations at three different temperatures. Figure B.3 (left column) shows the simulated self- and M-S-diffusivity as a function of loading along with the Reed-Ehrlich fit of the M-S-diffusivity for three different temperatures. The simulated self-exchange diffusivity is shown in the right column. It has been fitted to the analytical expression given in equation 9.11. All fit parameters for ethene are summarized in table B.2. The diffusivities of benzene and ethylbenzene are too small to obtain reliable results from MD simulations. However, the required zero loading M-S diffusion coefficients can be obtained indirectly by comparing predictions from the M-S equation against data from mixture MD simulations. The M-S equations lead to the following expression for the self-diffusivity of ethene (species 1) in mixtures with either benzene or ethylbenzene (species 2):²⁹⁸

$$D_{1,\text{self}} = 1 / \left(\frac{1}{D_1} + \frac{\theta_1}{D_{11}} + \frac{\theta_2}{D_{12}} \right). \quad (\text{B.9})$$

Equation B.9 has been verified to be of good accuracy for a wide variety of alkane mixtures in different zeolites.²⁹⁸ Usage of equation B.9 requires an assumption for the M-S diffusivity of benzene (or ethylbenzene) at zero loading, $D_2(0)$, along with the constants in equation 9.11. For the latter it is reasonable to use information on kMC simulations for 2-methyl-hexane (2MH) in MFI as starting point³¹¹ because of a similar diffusion mechanism. Both the zero loading M-S diffusivity and the constants appearing in equation 9.11 can then be used as fit parameters to obtain coincidence between the predictions from the M-S equations and the mixture MD simulations. A crucial point is the proper choice of the $q_{i,\text{sat}}$ for the calculation of the fractional occupancies in the mixture. While for ethene the maximum saturation capacity can be taken directly from MC simulations ($q_{\text{E,sat}} = 22$ molecules per unit cell) this is not the case for benzene and ethylbenzene. Only for $q_{\text{sat}} = 4$ molecules per unit cell do the predictions from the M-S equation coincide with the MD results. The usage of the maximum saturation capacity from MC simulation (12 molecules per unit cell for benzene and 8 molecules per unit cell for ethylbenzene) does not lead to reasonable results. The reason is that at a loading of four molecules per unit cell all intersections are blocked and consequently the diffusive transport is virtually disrupted.

The influence of preferential location of branched alkanes and benzene on the diffusion of partner molecules has been investigated both experimentally^{461,462} and by using molecular dynamics.⁴⁶³ There is evidence to indicate that MD simulations are able to capture the influence of intersection blocking by branched alkanes and benzene on the diffusivity of partner molecules, not only qualitatively but also reasonably quantitatively.⁴⁶³ This bodes well the applicability of the MD simulations in the current study to obtain diffusivity data. The intersection blocking effect in MFI by benzene and ethylbenzene during diffusion of mixtures is best appreciated by viewing the animations of MD simulations.⁴⁶⁴ This behavior cannot be captured correctly when using the maximum saturation capacities for benzene and ethylbenzene, respectively. A further check will be provided by the data on the diagonal element Δ_{11} of the inverse matrix appearing in equation 9.5. For a binary mixture Δ_{11} is related to the M-S diffusivities by²⁹⁴

$$\Delta_{11} = \frac{\mathcal{D}_1}{\theta_2} \cdot \frac{1}{1 + \frac{\mathcal{D}_{12}/\mathcal{D}_1}{1 + \frac{\theta_1}{\mathcal{D}_{21}/\mathcal{D}_2}}}. \quad (\text{B.10})$$

In order to evaluate equations B.9 and B.10 the following MD mixture simulation campaigns were conducted. At 653 K, MD simulations of ethene-benzene mixtures with benzene loadings of 1, 2, and 3 molecules per unit cell were performed as well as simulations at total loadings of 4 molecules per unit cell. Moreover ethene-ethylbenzene mixtures with ethylbenzene loadings of 2 molecules per unit cell and total loadings of 4 molecules per unit cell were carried out. At 603 K and 703 K, MD simulations of ethene-benzene mixtures with benzene loadings of 2 molecules per unit cell and total loadings of 4 molecules per unit cell were conducted. Note that no simulations for ethene-ethylbenzene mixtures were performed at these temperatures. Instead the ratio between the zero loading diffusivities of benzene and ethylbenzene was assumed to be constant for all temperatures and taken from the results at 653 K.

Figure B.4 shows that good agreement between predictions from the M-S equations and the MD mixture data at 653 K can be achieved when setting $\mathcal{D}_2(0) = 5 \times 10^{-10} \text{ m}^2\text{s}^{-1}$ for benzene and $\mathcal{D}_2(0) = 4 \times 10^{-10} \text{ m}^2\text{s}^{-1}$ for ethylbenzene. The fit parameter a_1 appearing in equation 9.11 was set to 3 while a_2 to a_4 were all set to zero. Good agreement is also achieved at 603 K and 703 K (see figure B.5). The reason for the not so good agreement between the M-S equations and the MD data for Δ_{11} compared to $D_{1,\text{self}}$ is

that (i) Δ_{11} is less accurately determined by MD as is $D_{1,\text{self}}$ and (ii) Δ_{11} depends explicitly on D_2 which is not known exactly. By contrast, $D_{1,\text{self}}$ does not explicitly depend on D_2 .

B.3.2 Tables

Table B.2: Diffusion data for ethene in MFI

temp.	$q_{\text{sat}}^{\text{a}}$	$D_i(0)^{\text{b}}$	Reed-Ehrlich param. (eqns 9.16, 9.17)			Parameters for self-exchange (eq 9.11)			
			z	a	b	a_1	a_2	a_3	a_4
603 K	22	2.2	2.5	0.9074	0.1271	0.3135	26.79	0.4192	1.17
653 K	22	2.5	2.5	0.7687	0.3651	0.1088	1.4554	0.3063	0.90
703 K	22	2.5	2.5	0.9709	-0.0399	4.14	71.77	0.3908	0.8947

^ain molecules per unit cell

^bin $10^{-8} \text{ m}^2 \text{ s}^{-1}$

Table B.3: Diffusion data for benzene and ethylbenzene in MFI

molecule	temp.	$q_{\text{sat}}^{\text{a}}$	$D_i(0)^{\text{b}}$	Parameters for self exchange (eq 9.11)			
				a_1	a_2	a_3	a_4
C_6H_6	603 K	4	4.0	3	0	0	0
C_6H_6	653 K	4	5.0	3	0	0	0
C_6H_6	703 K	4	7.0	3	0	0	0
C_8H_{10}	603 K	4	3.2	3	0	0	0
C_8H_{10}	653 K	4	4.0	3	0	0	0
C_8H_{10}	703 K	4	5.6	3	0	0	0

^ain molecules per unit cell

^bin $10^{-8} \text{ m}^2 \text{ s}^{-1}$

B.3.3 Figures

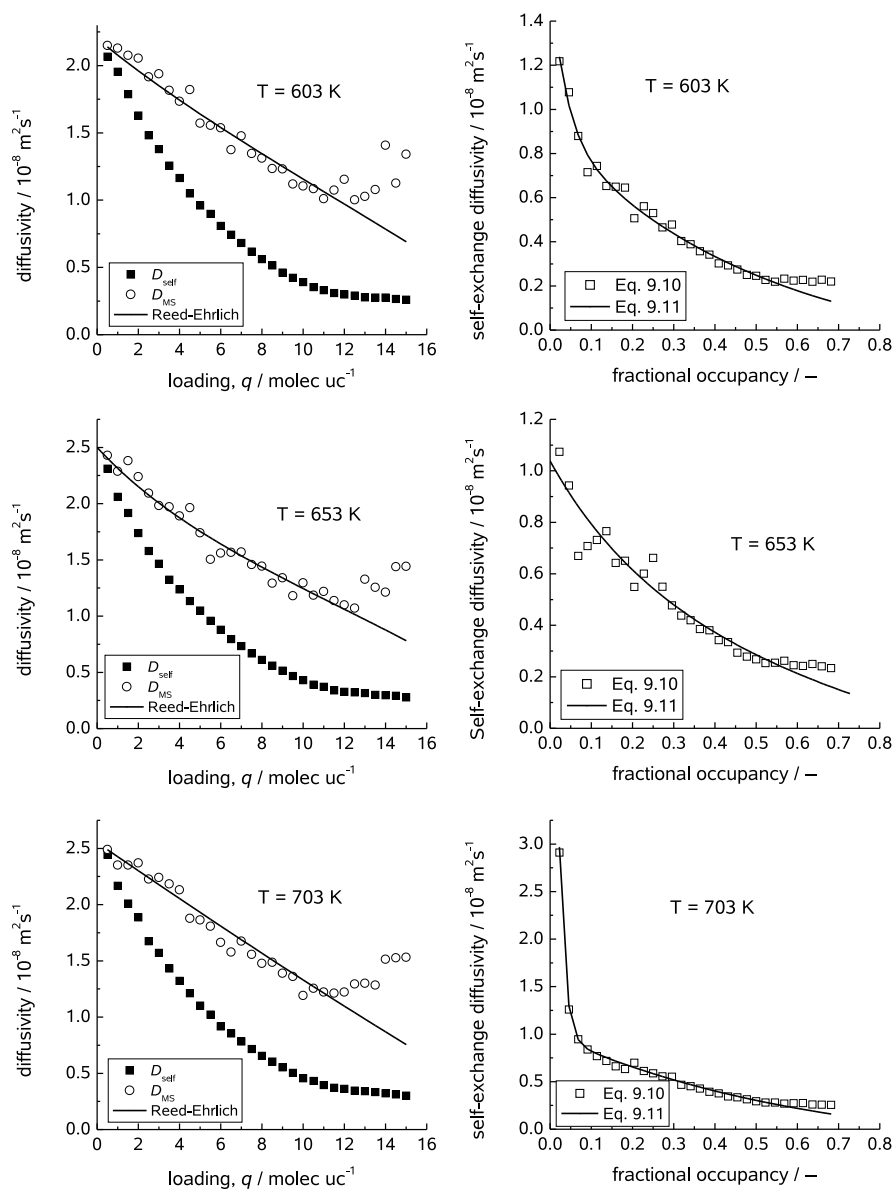


Figure B.3: Diffusion data for ethene in MFI at 603, 653, and 703 K. Left column: Self and M-S diffusivity; right column: Self-exchange diffusivity.

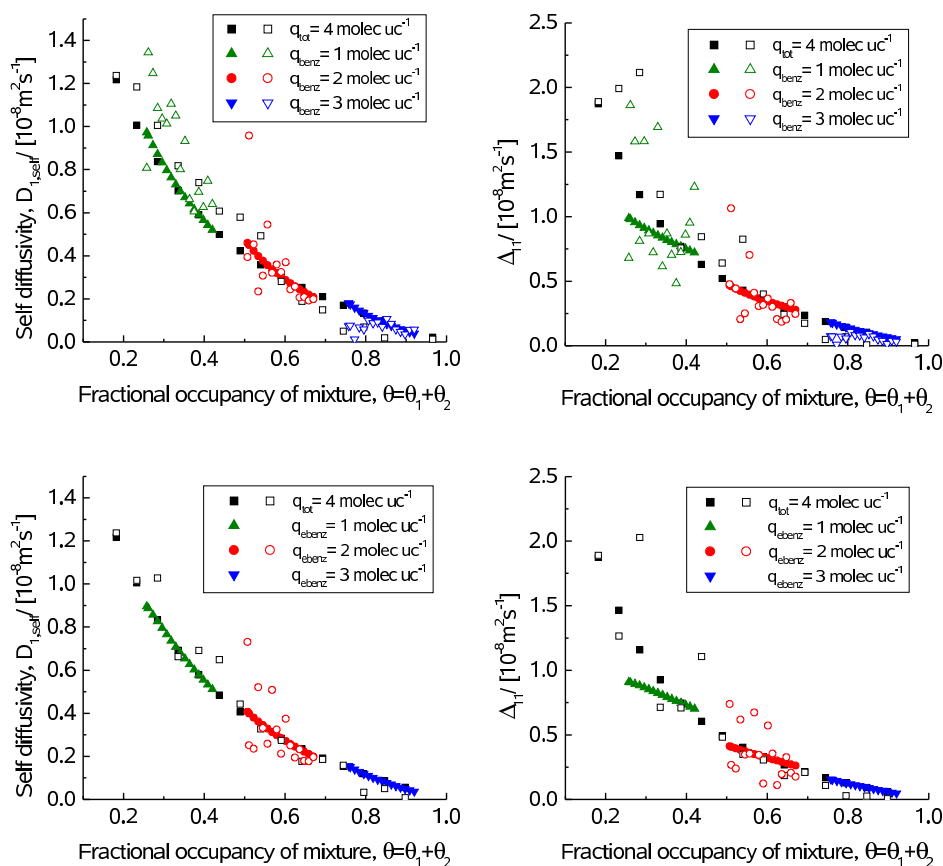


Figure B.4: Diffusion data for ethene-benzene (top row) and ethene-ethylbenzene (bottom row) binary mixtures in MFI at 653 K. The MD simulation results (open symbols) for the self diffusivity (left figures) and the Δ_{11} element (right figures) are compared to the predictions from the M-S equations (filled symbols) at different loadings.

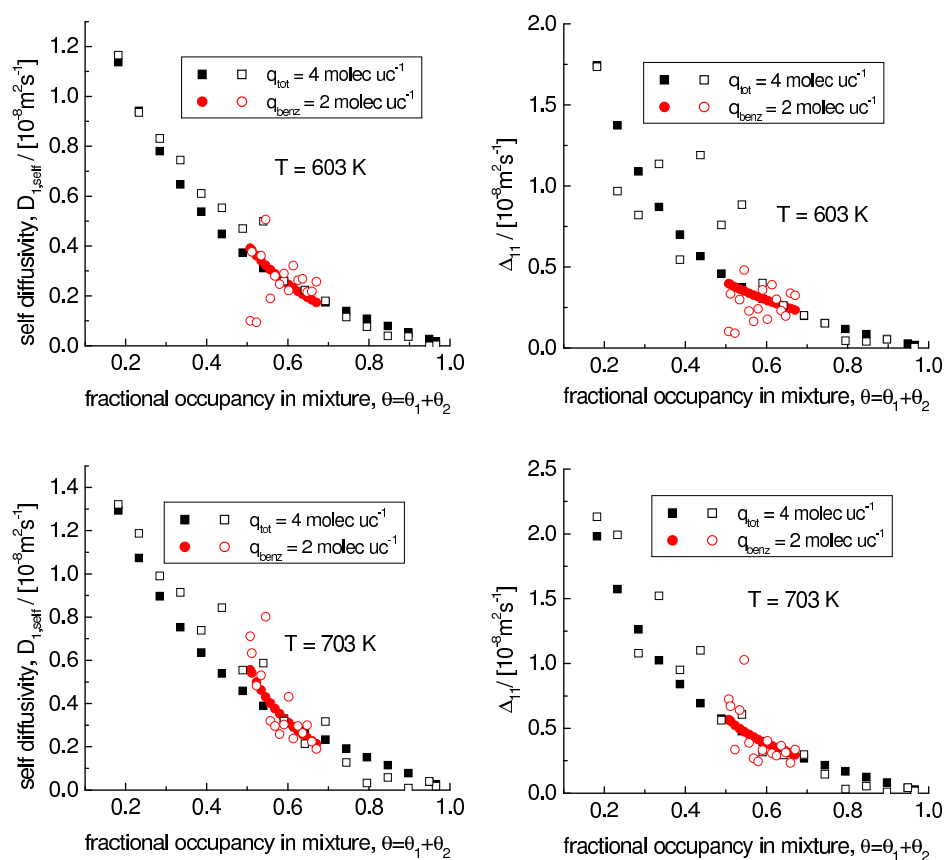


Figure B.5: Diffusion data for ethene-benzene binary mixtures in MFI at 603 K (top row) and at 703 K (bottom row). The MD simulation results (open symbols) for the self diffusivity (left figures) and the Δ_{11} element (right figures) are compared to predictions from the M-S equations (filled symbols) at different loadings.

B.4 Derivation of the rate expression for the two-step alkylation

The first step in the two-step scheme is the formation of an ethoxide species via the reaction of adsorbed ethene with the Brønsted acid proton of the zeolite. The second step is the reaction of benzene adsorbed next to the ethoxide species to form ethylbenzene. The fraction of Brønsted sites occupied by ethoxide species will depend on the rate of formation and consumption of these species. The rate expression for the first step reads

$$r_{\text{eth}} = k_1 q_{\text{E,H}^+} - k_{-1} q_{\text{eth}}, \quad (\text{B.11})$$

where $q_{\text{E,H}^+}$ is the concentration of ethene molecules adsorbed at a Brønsted acid site and q_{eth} is the concentration of ethoxide species. The rate expression for the second step is

$$r_{\text{EB}} = k_2 q_{\text{eth+B}} - k_{-2} q_{\text{EB,H}^+}, \quad (\text{B.12})$$

where $q_{\text{eth+B}}$ is the concentration of benzene adsorbed next to an ethoxide and $q_{\text{EB,H}^+}$ is the concentration of ethylbenzene located in acid site containing intersections.

Using a similar derivation of the rate expression as for the one-step scheme we can express the number of adsorption sites for ethene in a mixture of ethene, benzene, ethylbenzene, and ethoxide as

$$q_{\text{E,tot}} = 22 - 3.25q_{\text{B}} - 3.5q_{\text{EB}} - q_{\text{eth}}. \quad (\text{B.13})$$

The only difference to equation 9.19 is the additional term q_{eth} accounting for the fact that each ethoxide reduces the number of adsorption sites for ethene by 1 (assumed). Now we need to know how many of these $q_{\text{E,tot}}$ sites are located in intersections where the formation of ethoxide takes place. From MC simulations we know that the maximum ethene adsorption capacity of MFI with all intersections blocked by benzene is 9 molecules per unit cell. We can therefore estimate the ethene adsorption capacity of the intersections as $22 - 9 = 13$ molecules per unit cell or 3.25 molecules per intersection. Each benzene and each ethylbenzene block an entire intersection, i. e. reduce the number of sites available for ethene by 3.25 molecules per unit cell. Moreover an intersection containing already an ethoxide is not available for ethoxide formation, i. e. reduces the number of sites also by 3.25 molecules per unit cell. Therefore we can express the concentration of ethene molecules adsorbed at a Brønsted acid site, $q_{\text{E,H}^+}$, as

$$q_{\text{E,H}^+} = \frac{13 - 3.25(q_{\text{B}} + q_{\text{EB}} + q_{\text{eth}})}{22 - 3.25q_{\text{B}} - 3.5q_{\text{EB}} - q_{\text{eth}}} \cdot q_{\text{E}} \cdot \lambda. \quad (\text{B.14})$$

For the second step we need to estimate the concentration of benzene adsorbed next to an ethoxide species. If we assume that benzene occupies an empty intersection with the same probability than one which contains an ethoxide, we can write for the concentration of benzene adsorbed next to an ethoxide, $q_{\text{eth+B}}$,

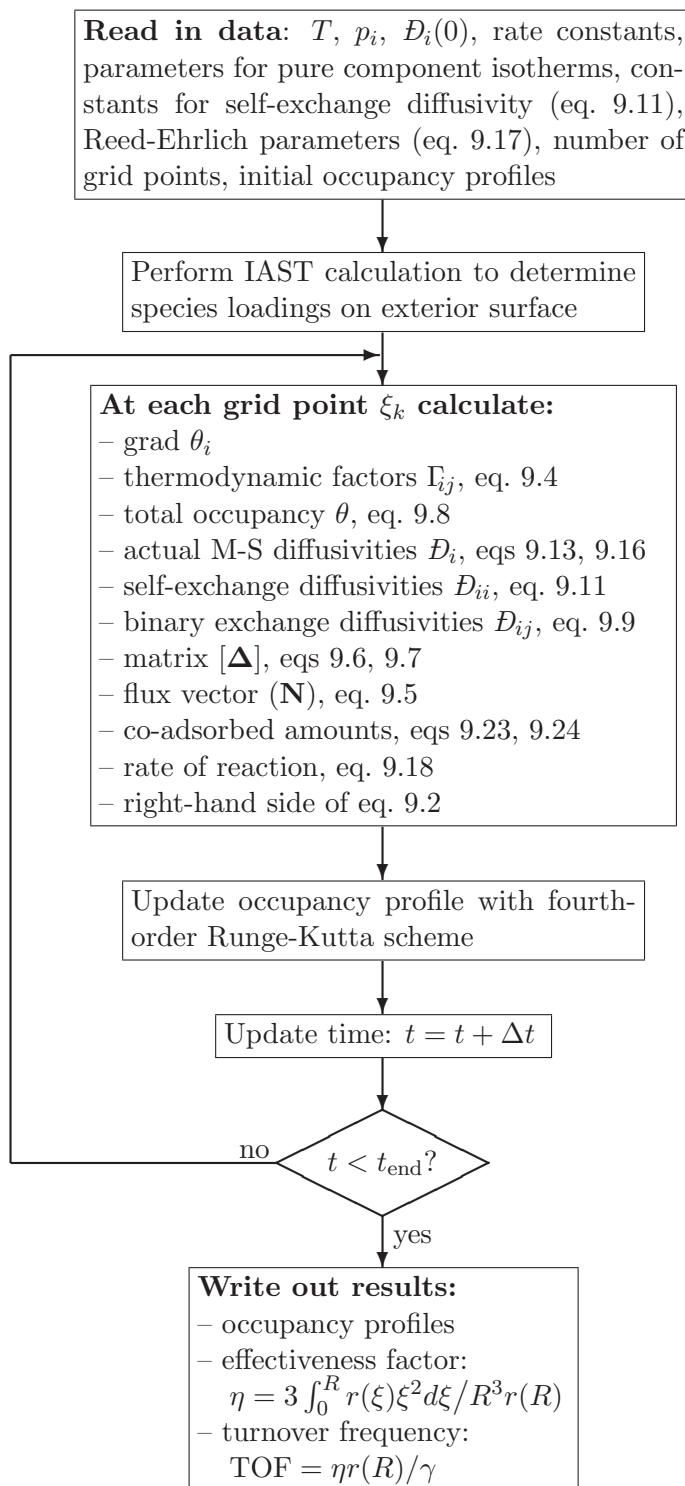
$$q_{\text{Eth+B}} = \frac{q_{\text{B}}}{4 - q_{\text{EB}}} \cdot q_{\text{eth}}, \quad (\text{B.15})$$

The concentration of ethoxide is treated as unknown variable such as the concentrations of benzene, ethylbenzene, and ethene. The difference is that the diffusivity of ethoxide is zero. The exterior surface concentration of ethoxide is determined numerically by solving $r_{\text{eth}} - r_{\text{EB}} = 0$ at the surface conditions.

B.5 conversion between simulated rates on MFI and experimental rates on AB-97TM

ABTM series catalysts are synthetic zeolite catalysts used for vapor phase alkylation of benzene to ethylbenzene. The AB-97TM catalyst is commercially employed in several Mobil/Badger-licensed process plants in China.⁴⁶⁵ For the bulk density of the catalyst used by Lu et al., a value of $\rho_{\text{bulk}} = 600 - 700 \text{ kg m}^{-3}$ is reported.³²¹ We assume that (i) the catalyst consists only of MFI ($\rho = 1785.1 \text{ kg m}^{-3}$) and alumina ($\rho = 801 \text{ kg m}^{-3}$)⁴⁶⁶ and (ii) the bed porosity has a value of 0.5. Then, a bulk density of $\rho_{\text{bulk}} = 646.5 \text{ kg m}^{-3}$ is obtained, in good agreement with the reported bulk density. The factor to convert simulated rates per unit mass of MFI to rates per unit mass of AB-97TM is thus $f = 0.69 \text{ kg}_{\text{MFI}} \text{ kg}_{\text{cat}}^{-1}$.

B.6 Program structure for the solution of the diffusion-reaction equation



B.7 Additional data illustrating the influence of temperature and partial pressures on observed macroscopic rate orders

B.7.1 Description of data

The data presented in this section are intended to illustrate how macroscopic rate orders depend on the adsorption equilibrium of the multicomponent mixture as well as diffusional limitations. They are supporting the conclusions drawn in section 9.4.

B.7.2 Figures

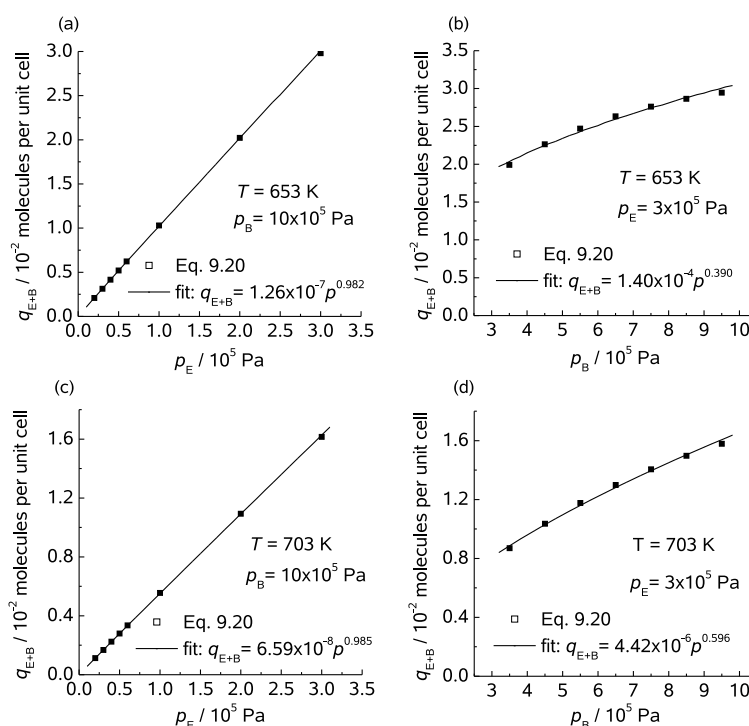


Figure B.6: Dependence of the amount of co-adsorbed $C_2H_4 + C_6H_6$ on the ethene partial pressure at (a) $T = 653\text{ K}$ and $p_B = 10 \times 10^5\text{ Pa}$, (c) $T = 703\text{ K}$ and $p_B = 10 \times 10^5\text{ Pa}$. Dependence of the amount of co-adsorbed $C_2H_4 + C_6H_6$ on the benzene partial pressure at (b) $T = 653\text{ K}$ and $p_E = 3 \times 10^5\text{ Pa}$, (d) $T = 703\text{ K}$ and $p_E = 3 \times 10^5\text{ Pa}$. The ethylbenzene pressure was fixed to 35 Pa in each case.

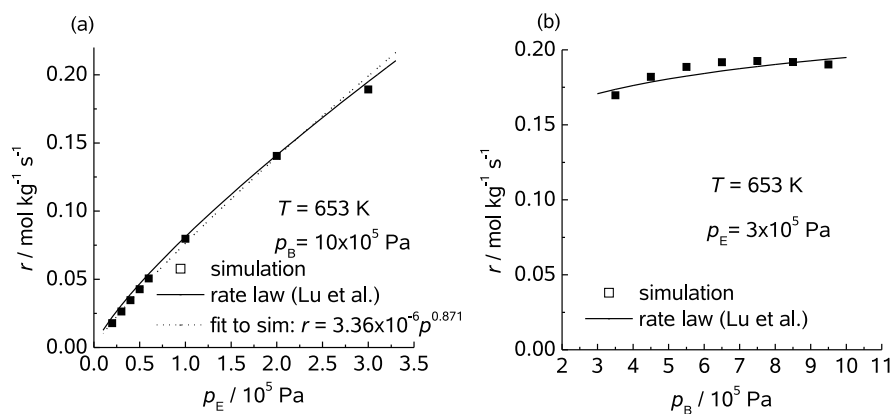


Figure B.7: Simulated and experimental rates per unit mass of catalyst for the alkylation of benzene with ethene. (a) Constant benzene partial pressure of 10×10^5 Pa at 653 K; (b) constant ethene partial pressure of 3×10^5 Pa at 653 K. The ethylbenzene partial pressure was fixed to 35 Pa in each case.

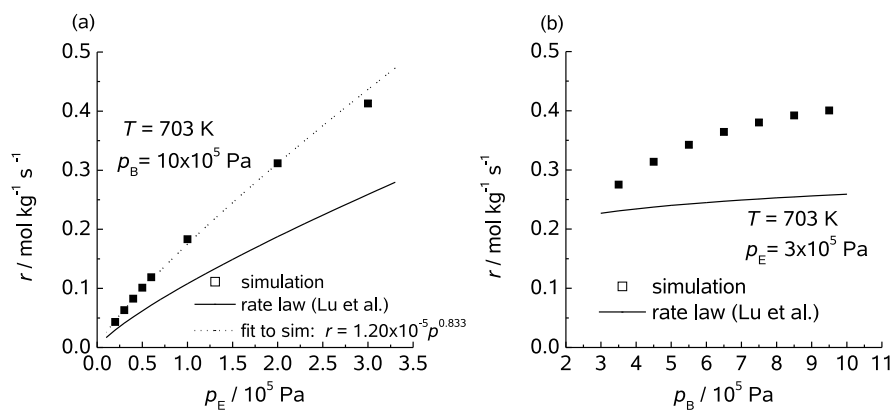


Figure B.8: Simulated and experimental rates per unit mass of catalyst for the alkylation of benzene with ethene. (a) Constant benzene partial pressure of 10×10^5 Pa at 703 K; (b) constant ethene partial pressure of 3×10^5 Pa at 703 K. The ethylbenzene partial pressure was fixed to 35 Pa in each case.

Supporting information for chapter 10

C

This material includes a description of the simulation methodologies and force fields used as well as details on the fitting of adsorption isotherms and determination of Maxwell-Stefan diffusivities from molecular dynamics data. Moreover, it contains the calculation of rate coefficients for the dehydrogenation of ethane as well as power-law and Langmuir-Hinshelwood fit parameters.

C.1 Simulation methodologies

C.1.1 GCMC simulation methodology

Configurational-bias Monte Carlo (CBMC) simulations have been carried out to determine the adsorption isotherms for ethane (C_2H_6), and hydrogen (H_2) in MFI (all silica silicalite-1) at a variety of temperatures; the crystallographic data are available elsewhere.⁴⁵¹ The zeolite framework is considered to be rigid.

For ethane, we use the united atom model and the alkane-zeolite force field developed in earlier publications.^{98,453} The CH_x groups are treated as single, chargeless interaction centers with their own effective potentials. The beads in the chain are connected by harmonic bonding potentials. A harmonic cosine bending potential models the bond bending between three neighboring beads, a Ryckaert-Bellemans potential controls the torsion angle. Beads in a chain separated by more than three bonds interact with each other through a Lennard-Jones potential.

The force field for H_2 corresponds to that given by Kumar et al.⁴⁶⁷ In implementing this force field, quantum effects for H_2 have been ignored because the work of Kumar et al.⁴⁶⁷ has shown that quantum effects are of negligible importance for temperatures above 200 K; all our simulations were performed at 653 K and 703 K, respectively. The force field of Kumar et al.⁴⁶⁷ is quite similar to that used by Gallo et al.⁴⁶⁸

The Lennard-Jones potentials are shifted and cut at 12 Å. The CBMC simulation details, along with the force fields have been given in detail in earlier publications.^{98,453} The simulation box consists of $2 \times 2 \times 3$ unit cells for MFI. Periodic boundary conditions were employed. It was verified that the size of the simulation box was large enough to yield reliable data on adsorption.

The CBMC simulations were performed in the Van't Hoff Institute for Molecular Sciences at the University of Amsterdam using the BIGMAC code developed by T.J.H. Vlugt⁴⁵⁵ as basis.

C.1.2 MD simulation methodology

Diffusion is simulated using Newton's equations of motion until the system properties, on average, no longer change in time. The Verlet algorithm is used for time integration. A time step of 1 fs was used in all simulations. For each simulation, *initializing* GCMC moves are used to place the molecules

in the domain, minimizing the energy. Next, follows an *equilibration* stage. These are essentially the same as the production cycles, only the statistics are not yet taken into account. This removes any initial large disturbances in the system to not affect statistics. After a fixed number of initialization and equilibrium steps, the MD simulation *production* cycles start. For every cycle, the statistics for determining the mean square displacements (MSDs) are updated. The MSDs are determined for time intervals ranging from 2 fs to 1 ns. In order to do this, an order- N algorithm, as detailed in Chapter 4 of Frenkel and Smit⁸⁷ is implemented. The Nosé-Hoover thermostat is applied to all the diffusing particles.

The DL_POLY code⁴⁵⁶ was used along with the force field implementation as described in the previous section. DL_POLY is a molecular dynamics simulation package written by W. Smith, T.R. Forester and I.T. Todorov and has been obtained from CCLRCs Daresbury Laboratory via the website.⁴⁵⁷

The MD simulations were carried out for a variety of molecular loadings. All simulations were performed in the Van't Hoff Institute of Molecular Sciences at the University of Amsterdam on clusters of PCs equipped with Intel Xeon processors running at 3.4 GHz on the Linux operating system. Each MD simulation, for a specified loading, was run for 120 h, determined to be long enough to obtain reliable statistics for determination of the diffusivities.

The self-diffusivities, $D_{i,\text{self}}$, were computed by analyzing the mean square displacement of each species i for each of the coordinate directions:

$$D_{i,\text{self}} = \frac{1}{2n_i} \lim_{\Delta t \rightarrow \infty} \frac{1}{\Delta t} \left\langle \left(\sum_{l=1}^{n_i} (\mathbf{r}_{l,i}(t + \Delta t) - \mathbf{r}_{l,i}(t))^2 \right) \right\rangle. \quad (\text{C.1})$$

In this expression, n_i represents the number of molecules of species i respectively, and $\mathbf{r}_{l,i}(t)$ is the position of molecule l of species i at any time t . Equation C.1 also defines the self-diffusivity in a n -component mixture.

For single component diffusion, the Maxwell-Stefan diffusivity was determined for each of the coordinate directions from

$$\mathcal{D}_i = \frac{1}{2} \lim_{\Delta t \rightarrow \infty} \frac{1}{n_i} \frac{1}{\Delta t} \left\langle \left(\sum_{l=1}^{n_i} (\mathbf{r}_{l,i}(t + \Delta t) - \mathbf{r}_{l,i}(t)) \right)^2 \right\rangle. \quad (\text{C.2})$$

For the three dimensional intersecting channel structure of MFI the average values calculated according to $\mathcal{D}_i = (\mathcal{D}_x + \mathcal{D}_y + \mathcal{D}_z) / 3$ are presented, and used.

C.2 Fitting of adsorption isotherms for C₂H₆ and H₂ in MFI

C.2.1 Methodology

Adsorption isotherms at 653 K and 703 K have been obtained from CBMC simulations in the grand canonical ensemble as outline in section C.1. The simulation data for ethane were fitted to a three-site Langmuir model,

$$q = \frac{q_{i,\text{sat},\text{A}} b_{i,\text{A}} f_i}{1 + b_{i,\text{A}} f_i} + \frac{q_{i,\text{sat},\text{B}} b_{i,\text{B}} f_i}{1 + b_{i,\text{B}} f_i} + \frac{q_{i,\text{sat},\text{C}} b_{i,\text{C}} f_i}{1 + b_{i,\text{C}} f_i}, \quad (\text{C.3})$$

where $q_{i,\text{sat},\text{X}}$ denotes the saturation capacity of species i on site X in molecules per unit cell, $b_{i,\text{X}}$ is the affinity constant in Pa⁻¹, and f_i is the gas phase fugacity of species i in Pa. As can be seen in figure C.1, the agreement between simulation and isotherm model is good over the whole range of fugacities. The values of the fit-parameters are given in table C.1. For hydrogen, a Langmuir-type description is only successful up to 10⁸ Pa. Therefore, the analytical description of the hydrogen isotherm is done piecewise:

$$\begin{aligned} q &= \frac{q_{\text{sat}} b f}{1 + b f}, \quad f \leq 10^8 \text{ Pa} \\ q &= A \log(f) + B, \quad 10^8 \text{ Pa} < f \leq 10^{12} \text{ Pa} \end{aligned} \quad (\text{C.4})$$

It should be emphasized that the fugacity range beyond 10⁸ Pa is of no practical relevance for the simulations carried out in the present work. The hydrogen isotherms are also included in figure C.1. The fit-parameters are presented in table C.2.

C.2.2 Tables

Table C.1: Three-site Langmuir parameters for C₂H₆ in MFI. The saturation capacity q_{sat} has the unit of molecules per unit cell. The Langmuir affinity constants are given in Pa⁻¹.

molecule	temp.	three-site Langmuir parameters					
		$q_{i,\text{sat},\text{A}}$	$b_{i,\text{A}}$	$q_{i,\text{sat},\text{B}}$	$b_{i,\text{B}}$	$q_{i,\text{sat},\text{C}}$	$b_{i,\text{C}}$
C ₂ H ₆	653 K	11	1.18×10^{-7}	5	1.91×10^{-9}	2	6.48×10^{-12}
C ₂ H ₆	703 K	11	7.08×10^{-8}	5	1.35×10^{-9}	2	5.37×10^{-12}

Table C.2: Isotherm parameters for H₂ in MFI. The saturation capacity q_{sat} has the unit of molecules per unit cell. The Langmuir affinity constants are given in Pa⁻¹. The fit-parameters A and B have the unit molecules per unit cell.

molecule	temp.	q_{sat}	b	A	B
H ₂	653 K	80	1.97×10^{-9}	27.6288	-209.857
H ₂	703 K	80	1.80×10^{-9}	28.2821	-216.771

C.2.3 Figures

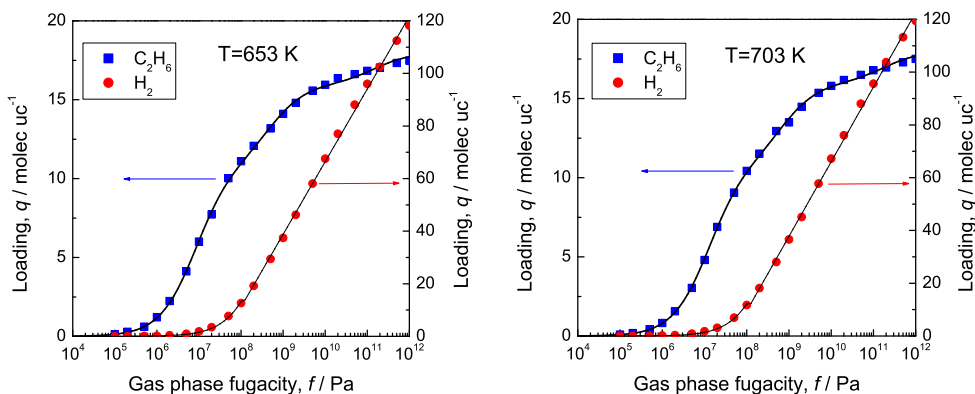


Figure C.1: Pure component adsorption isotherms of ethane and hydrogen in MFI at 653 K and 703 K. The symbols represent results from GCMC simulations. The lines are fits of the GCMC simulated isotherms.

C.3 Extraction of M-S diffusivities from MD simulation data

C.3.1 Methodology

Diffusivity data for ethane and hydrogen have been obtained from MD simulations at 653 K and 703 K. The left column of figures C.2 and C.3 show the simulated self- and M-S diffusivity as a function of the loading for ethane

and hydrogen, respectively. The M-S diffusivity has been fitted to the model of Reed and Ehrlich:³¹⁶

$$\mathcal{D} = \mathcal{D}(0) \frac{(1 + \varepsilon)^{z-1}}{(1 + \varepsilon/f)^z}, \quad (\text{C.5})$$

with

$$\varepsilon = \frac{(\beta - 1 + 2\theta)f}{2(1 - \theta)}; \quad \beta = \sqrt{1 - 4\theta(1 - \theta)(1 - 1/f)}; \quad f = a \exp(b\theta). \quad (\text{C.6})$$

The parameter z is the coordination number representing the maximum number of nearest neighbors. The factor f accounts for interaction between neighboring molecules. The parameters a and b are obtained by fitting them to MD data (see Krishna et al.³⁰⁹ for more detailed discussions and derivations). The simulated self-exchange diffusivities is shown in the right columns of figures C.2 and C.3. They were obtained from

$$\mathcal{D}_{ii} = \frac{\theta_i}{\frac{1}{D_{i,\text{self}}} - \frac{1}{\mathcal{D}_i}}. \quad (\text{C.7})$$

The self-exchange coefficients have been related to the M-S diffusivity by an empirical correlation:³⁰⁹

$$\frac{\mathcal{D}_{ii}}{\mathcal{D}_i} = a_1 \exp(-a_2\theta_i) + a_3 \exp(-a_4\theta_i). \quad (\text{C.8})$$

The fit-parameters a_i as well as the Reed-Ehrlich parameters are summarized in table C.3.

C.3.2 Tables

Table C.3: Diffusion data for ethane and hydrogen in MFI.

molec.	temp.	q_{sat}^a	$\mathcal{D}_i(0)^b$	Reed-Ehrlich param. (eqns C.5, C.6)			Parameters for self-exchange (eq C.8)			
				z	a	b	a_1	a_2	a_3	a_4
C ₂ H ₆	653 K	22	2.25	2.5	0.7806	-0.04349	0.3566	1.817	0.1265	0.8369
C ₂ H ₆	703 K	22	2.35	2.5	0.8072	-0.01888	0.06306	8.757	0.4505	1.284
H ₂	653 K	200	16.0	2.5	0.4334	2.0490	0.06275	-1.526	0.02923	0.877
H ₂	703 K	200	17.0	2.5	0.4069	3.215	0.04258	-1.244	0.05251	0.5359

^ain molecules per unit cell

^bin $10^{-8} \text{ m}^2 \text{ s}^{-1}$

C.3.3 Figures

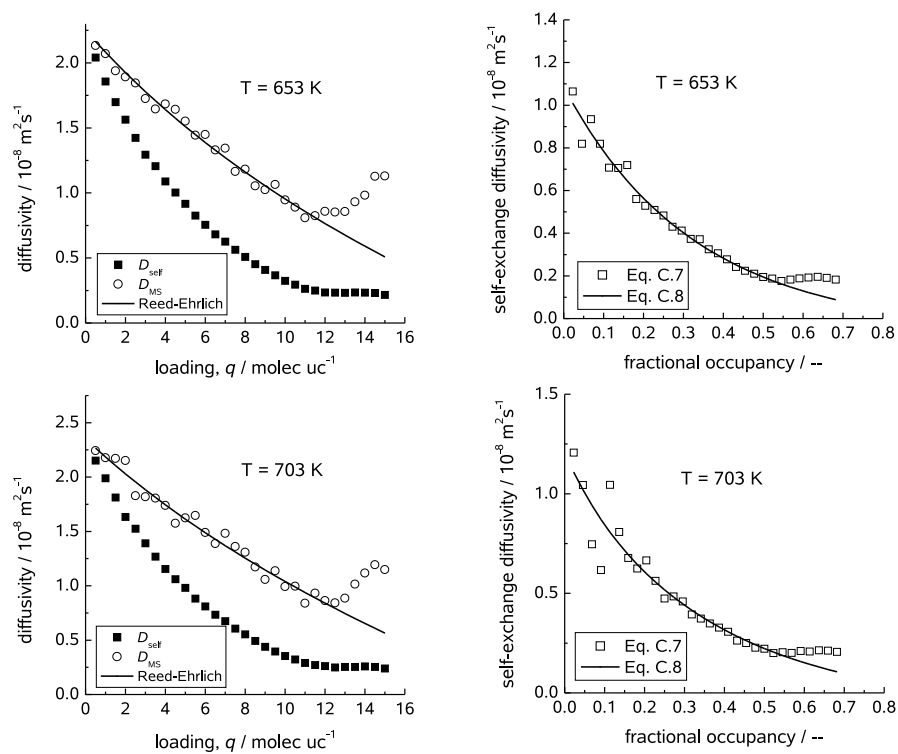


Figure C.2: Diffusion data for ethane in MFI at 653 K and 703 K. Left column: Self- and M-S diffusivity; right column: Self-exchange diffusivity.

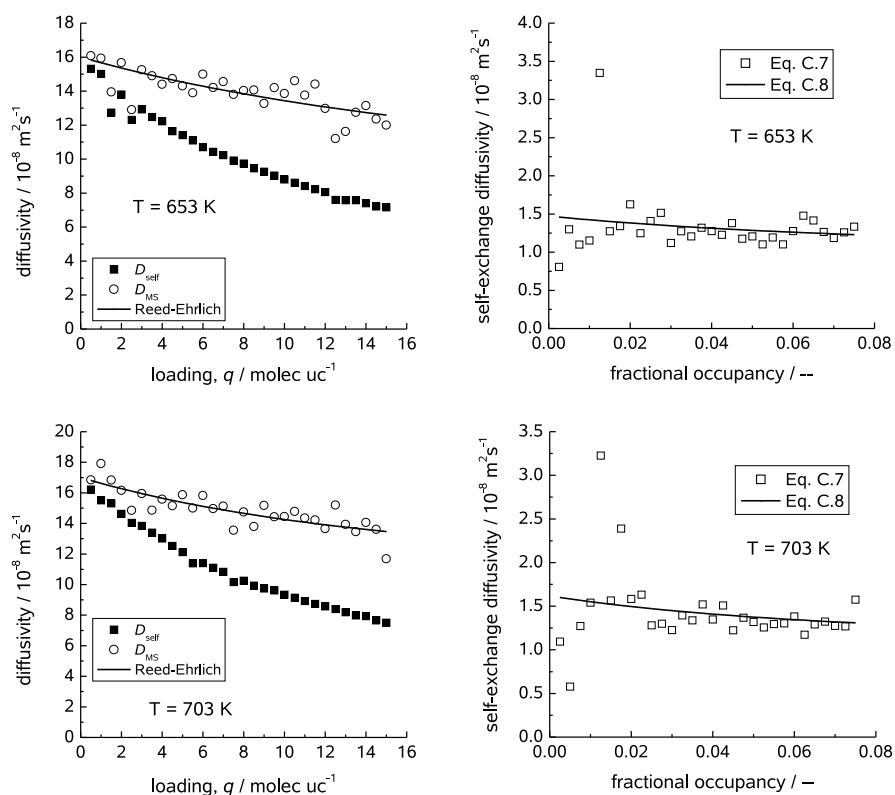


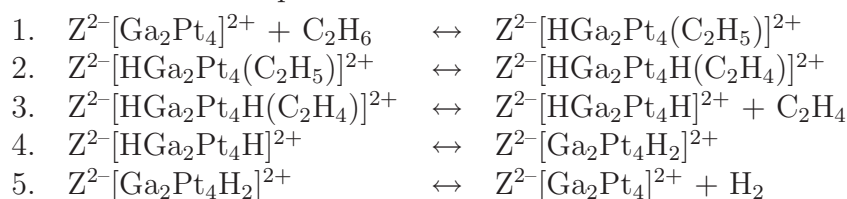
Figure C.3: Diffusion data for hydrogen in MFI at 653 K and 703 K. Left column: Self- and M-S diffusivity; right column: Self-exchange diffusivity.

C.4 Determination of rate coefficients for ethane dehydrogenation

C.4.1 Introduction

In the present work the dehydrogenation of ethane is assumed to take place on Ga_xPt_y species located inside the zeolite channels. The reason for choosing Ga_xPt_y instead of purely Pt is the better time on stream behaviour of the mixed species.^{376,381,469} The nature of the active site in GaPt/H-ZSM-5 is, however unclear. EXAFS experiments conducted by Chao et al.⁴⁷⁰ provide evidence for the formation of small GaPt clusters. In a recent DFT-study Mikhailov et al.⁴⁷¹ reported a reaction mechanism for ethane dehydrogenation

on an extraframework $[\text{Ga}_2\text{Pt}_4]^{2+}$ complex. The reaction mechanism was found to consist of 5 steps:



In these equations Z^{2-} represents the charge exchange site in the zeolite. The potential energy profile for this reaction mechanism shows quite low activation energies for all elementary steps⁴⁷¹ and therefore gives an explanation for the high dehydrogenation activity of GaPt/H-ZSM-5 systems. It is, however, unlikely that only one clear defined Ga_xPt_y species is located in the zeolitic pore space. Therefore we have investigated two different active sites ($[\text{GaPt}]^+$ and $[\text{GaPt}_2]^+$).

C.4.2 Methodology

The catalytically active center and a portion of the zeolite framework were represented by clusters containing 5 T-sites, respectively. Initially all Si atoms were placed at their crystallographic positions, as reported by Olson et al.¹⁴⁶ The location of Al in the zeolite framework is difficult to define. Both experimental^{145,229–232} and theoretical^{231–234} studies aimed at determining the preferential locations for Al substitution into ZSM-5 do not lead to a definitive conclusion because the differences in the energies associated with replacement of a Si by Al at different T sites are small. Thus, the location of Al atoms in the zeolite framework is controlled more by the kinetics of zeolite synthesis than by thermodynamics. Nevertheless, there is some evidence that Al siting is not random and that the T12 site is preferred.^{229,233} Based on these findings and other theoretical studies on H-ZSM-5,^{235–237} Al was located at the T12 position (see figure C.4). Terminal Si-O bonds were replaced by Si-H bonds oriented in the direction of the former Si-O bond. The Si-H bond length was set to 1.487 Å, which is the optimized bond length for SiH4 at the B3LYP/TZVP level of theory. For the T5 cluster, the resulting coordinates for the terminal H atoms along with the coordinates for the Si atoms were held fixed throughout all subsequent calculations. Quantum chemical calculations were performed with the TURBOMOLE suite of programs¹⁶² in C1 symmetry, using gradient-corrected density-functional theory (DFT). To represent the effects of exchange and correlation, Becke's 3-parameter exchange functional⁷⁵ and the correlation functional of Lee, Yang and Parr (B3LYP)⁷⁶ were used with a very fine numerical grid size (m5).¹⁵⁶ Basis sets the triple- ζ

level with polarization functions (TZVP)¹⁶¹ were used for all atoms. To represent the core electrons of Pt the effective core potential (ECP) from the TURBOMOLE library (def-ecp) was employed.

During the structure optimizations, energies were converged to 10^{-7} Ha and the maximum norm of the cartesian gradient was converged to 10^{-4} Ha/bohr. Transition states were localized using a combination of interpolation and local methods. The growing-string method¹⁶⁴ was used in mass-weighted coordinates with a maximum of 13 to 16 nodes. After the two ends of the growing string joined, the growing-string method was terminated and an approximate saddle point was identified. The improved dimer method¹⁶⁵ was employed to refine the position of the saddle point. A gradient-norm convergence criterion of 5×10^{-4} Ha/bohr was used for the transition-state searches. Intrinsic reaction rate constants were computed using standard statistical mechanics and absolute rate theory.¹⁹³ We used the harmonic approximation, and assumed that adsorbate and transition state are rigid in space and have only vibrational degrees of freedom.

For a fixed gas phase composition and temperature, the steady state material balance for surface species can be written as a set of linear equations that can be readily solved using standard methods.^{195,196} Here we are exclusively interested in the rate coefficient for the forward reaction. Therefore we have solved the set of rate equations for $p_H = p_E = 0$. An apparent first order rate constant for the forward reaction was then obtained from

$$k_{\text{app}} = \frac{r}{p_E} \quad (\text{C.9})$$

This rate coefficient was then converted into an intrinsic rate coefficient by means of the Henry isotherm:

$$k_f = \frac{k_{\text{app}}}{K_H} \quad (\text{C.10})$$

C.4.3 Results and discussion

Two models of the active site ($[\text{GaPt}]^+$ and $[\text{GaPt}_2]^+$) have been studied. The potential energy profiles are shown in figure C.5 along with the energy profile obtained by Mikhailov et al.⁴⁷¹ for the $[\text{Ga}_2\text{Pt}_4]^+$ -model. All profiles show relative low activation energies. The intermediates are more strongly adsorbed on the $[\text{GaPt}_2]^+$ species than on the $[\text{GaPt}]^+$ site. This is physically reasonable because Ga increases the electron density of Pt which leads to a weaker adsorption of the hydrocarbons if the Ga/Pt ratio becomes larger.

We have also calculated the chemisorption energy on $[\text{HPt}]^+$ species. Ethane is more strongly chemisorbed by 96.4 kJ/mol than on $[\text{GaPt}_2]^+$.

The intrinsic rate coefficients for the two active sites are listed in table C.4. They are of the order of 10^3 s^{-1} at 653 K.

C.4.4 Tables

Table C.4: Henry constants for ethane adsorption in MFI and intrinsic rate coefficients for ethane dehydrogenation

active site	temp. [K]	K_{H} [molec uc ⁻¹ Pa ⁻¹]	k_{app} [molec site ⁻¹ s ⁻¹ Pa ⁻¹]	k_f [s ⁻¹]
$[\text{GaPt}]^+$	653	0.137×10^{-5}	136×10^{-5}	992.7
$[\text{GaPt}_2]^+$	653	0.137×10^{-5}	719×10^{-5}	5248.2

C.4.5 Figures

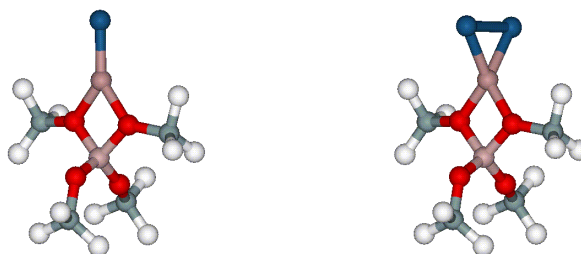


Figure C.4: T5 cluster models of the active site in H-ZSM-5. Left: $[\text{GaPt}]^+$; right: $[\text{GaPt}_2]^+$.

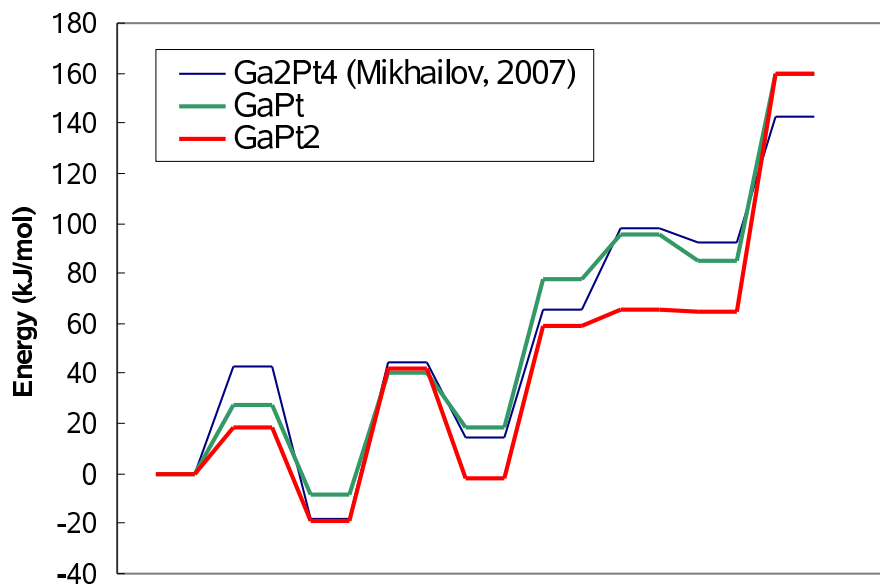


Figure C.5: Potential energy profile for dehydrogenation of ethane on different representations of the active site.

C.5 Langmuir-Hinshelwood and power law fit parameters

C.5.1 Description of data

The tables presented in this section are the raw data used to determine the parameters appearing in the Langmuir-Hinshelwood and power-law expressions.

C.5.2 Tables

Table C.5: Input data and results from reactor simulations at 603 K. The last three columns contain the mean pressures used in the PL and LH expressions. The rate of benzene consumption, r_B , has been calculated according to equation 10.6.

m_{cat} [kg]	n_{in} [mol s ⁻¹]	$p_{\text{B,in}}$ [kPa]	$p_{\text{E,in}}$ [kPa]	$p_{\text{EB,in}}$ [kPa]	τ [10 ⁻³ h]	X [%]	$p_{\text{B,out}}$ [kPa]	$p_{\text{E,out}}$ [kPa]	$p_{\text{EB,out}}$ [kPa]	n_{out} [mol s ⁻¹]	$-r_B$ [mol kg ⁻¹ s ⁻¹]	$p_{\text{B,m}}$ [kPa]	$p_{\text{E,m}}$ [kPa]	$p_{\text{EB,m}}$ [kPa]
3.0 × 10 ⁻⁵	1.0 × 10 ⁻⁴	90	5	5	1.0837	0.05847	89.99473	4.94998	5.05529	9.99 × 10 ⁻⁵	1.75 × 10 ⁻³	89.99737	4.974990	5.02764
3.0 × 10 ⁻⁵	1.0 × 10 ⁻⁴	70	15	15	1.1156	0.13176	69.97230	14.92153	15.10616	9.99 × 10 ⁻⁵	3.07 × 10 ⁻³	69.98615	14.96077	15.05308
3.0 × 10 ⁻⁵	1.0 × 10 ⁻⁴	50	25	25	1.1494	0.14925	49.96266	24.94399	25.09335	9.99 × 10 ⁻⁵	2.49 × 10 ⁻³	49.98133	24.97200	25.04667
3.0 × 10 ⁻⁵	1.0 × 10 ⁻⁴	90	9	1	1.1295	0.11853	89.98932	8.90282	1.10785	9.99 × 10 ⁻⁵	3.56 × 10 ⁻³	89.99466	8.95141	1.05393
3.0 × 10 ⁻⁵	1.0 × 10 ⁻⁴	70	29	1	1.3066	0.40236	69.91527	28.79946	1.28527	9.97 × 10 ⁻⁵	9.39 × 10 ⁻³	69.95763	28.89973	1.14264
3.0 × 10 ⁻⁵	1.0 × 10 ⁻⁴	50	49	1	1.5495	0.71448	49.82074	48.81715	1.36211	9.96 × 10 ⁻⁵	1.19 × 10 ⁻²	49.91037	48.90858	1.18105
3.0 × 10 ⁻⁵	1.0 × 10 ⁻⁴	90	1	9	1.0414	0.01017	89.99908	0.99094	9.00997	1.00 × 10 ⁻⁴	3.05 × 10 ⁻⁴	89.99954	0.99547	9.00499
3.0 × 10 ⁻⁵	1.0 × 10 ⁻⁴	70	11	19	1.0708	0.08576	69.98198	10.94654	19.07148	9.99 × 10 ⁻⁵	2.00 × 10 ⁻³	69.99099	10.97327	19.03574
3.0 × 10 ⁻⁵	1.0 × 10 ⁻⁴	50	11	39	0.9990	0.03943	49.99014	10.98245	39.02741	1.00 × 10 ⁻⁴	6.57 × 10 ⁻⁴	49.99507	10.99122	39.01371
2.0 × 10 ⁻⁵	1.0 × 10 ⁻⁴	180	10	10	0.7224	0.11544	179.97920	9.80239	10.21842	9.99 × 10 ⁻⁵	5.20 × 10 ⁻³	179.98960	9.90119	10.10921
2.0 × 10 ⁻⁵	1.0 × 10 ⁻⁴	140	30	30	0.7437	0.26066	139.89032	29.68925	30.42043	9.98 × 10 ⁻⁵	9.12 × 10 ⁻³	139.94516	29.84463	30.21021
2.0 × 10 ⁻⁵	1.0 × 10 ⁻⁴	100	50	50	0.7663	0.29806	99.85075	49.77612	50.37313	9.99 × 10 ⁻⁵	7.45 × 10 ⁻³	99.92537	49.88806	50.18656
2.0 × 10 ⁻⁵	1.0 × 10 ⁻⁴	180	18	2	0.7530	0.23693	179.95726	17.61109	2.43165	9.98 × 10 ⁻⁵	1.07 × 10 ⁻²	179.97863	17.80554	2.21583
2.0 × 10 ⁻⁵	1.0 × 10 ⁻⁴	140	58	2	0.8710	0.83233	139.64837	57.16781	3.18382	9.94 × 10 ⁻⁵	2.91 × 10 ⁻²	139.82419	57.58391	2.59191
2.0 × 10 ⁻⁵	1.0 × 10 ⁻⁴	100	98	2	1.0330	1.53719	99.22545	97.20996	3.56459	9.92 × 10 ⁻⁵	3.84 × 10 ⁻²	99.61273	97.60498	2.78229
2.0 × 10 ⁻⁵	1.0 × 10 ⁻⁴	180	2	18	0.6943	0.02012	179.99638	1.96414	18.03949	1.00 × 10 ⁻⁴	9.05 × 10 ⁻⁴	179.99819	1.98207	18.01974
2.0 × 10 ⁻⁵	1.0 × 10 ⁻⁴	140	22	38	0.7139	0.16846	139.92916	21.78984	38.28099	9.99 × 10 ⁻⁵	5.90 × 10 ⁻³	139.96458	21.89492	38.14050
2.0 × 10 ⁻⁵	1.0 × 10 ⁻⁴	100	22	78	0.6660	0.08215	99.95891	21.92685	78.11424	1.00 × 10 ⁻⁴	2.05 × 10 ⁻³	99.97945	21.96343	78.05712
1.0 × 10 ⁻⁵	1.0 × 10 ⁻⁴	270	15	15	0.3612	0.10222	269.97237	14.73756	15.29007	9.99 × 10 ⁻⁵	9.20 × 10 ⁻³	269.98619	14.86878	15.14503
1.0 × 10 ⁻⁵	1.0 × 10 ⁻⁴	210	45	45	0.3719	0.23060	209.85449	44.58771	45.55780	9.98 × 10 ⁻⁵	1.61 × 10 ⁻²	209.92724	44.79386	45.27890
1.0 × 10 ⁻⁵	1.0 × 10 ⁻⁴	150	75	75	0.3831	0.26410	149.80167	74.70250	75.49584	9.99 × 10 ⁻⁵	1.32 × 10 ⁻²	149.90083	74.85125	75.24792
1.0 × 10 ⁻⁵	1.0 × 10 ⁻⁴	270	27	3	0.3765	0.21175	269.94272	26.47874	3.57855	9.98 × 10 ⁻⁵	1.91 × 10 ⁻²	269.97136	26.73937	3.28927
1.0 × 10 ⁻⁵	1.0 × 10 ⁻⁴	210	87	3	0.4355	0.76285	209.51683	85.85649	4.62669	9.95 × 10 ⁻⁵	5.34 × 10 ⁻²	209.75841	86.42824	3.81334
1.0 × 10 ⁻⁵	1.0 × 10 ⁻⁴	150	147	3	0.5165	1.45334	148.90202	145.88006	5.21792	9.93 × 10 ⁻⁵	7.27 × 10 ⁻²	149.45101	146.44003	4.10896
1.0 × 10 ⁻⁵	1.0 × 10 ⁻⁴	270	3	27	0.3471	0.01775	269.99521	2.95255	27.05224	1.00 × 10 ⁻⁴	1.60 × 10 ⁻³	269.99760	2.97627	27.02612
1.0 × 10 ⁻⁵	1.0 × 10 ⁻⁴	210	33	57	0.3569	0.14803	209.90665	32.72305	57.37030	9.99 × 10 ⁻⁵	1.04 × 10 ⁻²	209.95332	32.86153	57.18515
1.0 × 10 ⁻⁵	1.0 × 10 ⁻⁴	150	33	117	0.3330	0.07271	149.94545	32.90290	117.15165	1.00 × 10 ⁻⁴	3.64 × 10 ⁻³	149.97272	32.95145	117.07583
1.0 × 10 ⁻⁵	1.0 × 10 ⁻⁴	360	20	20	0.3612	0.14763	359.94678	19.49443	20.55879	9.99 × 10 ⁻⁵	1.33 × 10 ⁻²	359.97339	19.74721	20.27939
1.0 × 10 ⁻⁵	1.0 × 10 ⁻⁴	280	60	60	0.3719	0.33323	279.71943	59.20506	61.07550	9.98 × 10 ⁻⁵	2.33 × 10 ⁻²	279.85972	59.60253	60.53775
1.0 × 10 ⁻⁵	1.0 × 10 ⁻⁴	200	100	100	0.3831	0.38230	199.61697	99.42545	100.95758	9.98 × 10 ⁻⁵	1.91 × 10 ⁻²	199.80848	99.71273	100.47879
1.0 × 10 ⁻⁵	1.0 × 10 ⁻⁴	360	36	4	0.3765	0.30731	359.88906	34.99047	5.12046	9.97 × 10 ⁻⁵	2.77 × 10 ⁻²	359.94453	35.49524	4.56023
1.0 × 10 ⁻⁵	1.0 × 10 ⁻⁴	280	116	4	0.4355	1.12339	279.04888	113.74901	7.20211	9.92 × 10 ⁻⁵	7.86 × 10 ⁻²	279.52444	114.87450	5.60106
1.0 × 10 ⁻⁵	1.0 × 10 ⁻⁴	200	196	4	0.5165	2.18040	197.79557	193.75148	8.45295	9.89 × 10 ⁻⁵	1.09 × 10 ⁻¹	198.89779	194.87574	6.22647

(continued on next page)

Table C.5 (continued)

m_{cat} [kg]	n_{in} [mol s ⁻¹]	$p_{\text{B,in}}$ [kPa]	$p_{\text{E,in}}$ [kPa]	$p_{\text{EB,in}}$ [kPa]	τ [10 ⁻³ h]	X [%]	$p_{\text{B,out}}$ [kPa]	$p_{\text{E,out}}$ [kPa]	$p_{\text{EB,out}}$ [kPa]	n_{out} [mol s ⁻¹]	$-r_{\text{B}}$ [mol kg ⁻¹ s ⁻¹]	$p_{\text{B,m}}$ [kPa]	$p_{\text{E,m}}$ [kPa]	$p_{\text{EB,m}}$ [kPa]
1.0×10^{-5}	1.0×10^{-4}	360	4	36	0.3471	0.02558	359.99079	3.90882	36.10039	1.00×10^{-4}	2.30×10^{-3}	359.99540	3.95441	36.05019
1.0×10^{-5}	1.0×10^{-4}	280	44	76	0.3569	0.21305	279.82077	43.46829	76.71093	9.99×10^{-5}	1.49×10^{-2}	279.91039	43.73415	76.35547
1.0×10^{-5}	1.0×10^{-4}	200	44	156	0.3330	0.10489	199.89506	43.81320	156.29174	9.99×10^{-5}	5.24×10^{-3}	199.94753	43.90660	156.14587
1.0×10^{-5}	1.0×10^{-4}	450	25	25	0.3612	0.19260	449.91318	24.17520	25.91162	9.98×10^{-5}	1.73×10^{-2}	449.95659	24.58760	25.45581
1.0×10^{-5}	1.0×10^{-4}	350	75	75	0.3719	0.43506	349.54179	73.70175	76.75646	9.97×10^{-5}	3.05×10^{-2}	349.77090	74.35087	75.87823
1.0×10^{-5}	1.0×10^{-4}	250	125	125	0.3831	0.49986	249.37361	124.06041	126.56598	9.98×10^{-5}	2.50×10^{-2}	249.68680	124.53021	125.78299
1.0×10^{-5}	1.0×10^{-4}	450	45	5	0.3765	0.40210	449.81840	43.34744	6.83416	9.96×10^{-5}	3.62×10^{-2}	449.90920	44.17372	5.91708
1.0×10^{-5}	1.0×10^{-4}	350	145	5	0.4355	1.48405	348.42539	141.27343	10.30117	9.90×10^{-5}	1.04×10^{-1}	349.21270	143.13672	7.65059
1.0×10^{-5}	1.5×10^{-4}	250	245	5	0.3443	1.98089	247.49912	242.44910	10.05178	1.49×10^{-4}	1.49×10^{-1}	248.74956	243.72455	7.52589
1.0×10^{-5}	1.0×10^{-4}	450	5	45	0.3471	0.03332	449.98500	4.85151	45.16349	1.00×10^{-4}	3.00×10^{-3}	449.99250	4.92576	45.08174
1.0×10^{-5}	1.0×10^{-4}	350	55	95	0.3569	0.27744	349.70812	54.13408	96.15780	9.98×10^{-5}	1.94×10^{-2}	349.85406	54.56704	95.57890
1.0×10^{-5}	1.0×10^{-4}	250	55	195	0.3330	0.13676	249.82893	54.69549	195.47558	9.99×10^{-5}	6.84×10^{-3}	249.91446	54.84775	195.23779

Table C.6: Input data and results from reactor simulations at 653 K. The last three columns contain the mean pressures used in the PL and LH expressions. The rate of benzene consumption, r_B , has been calculated according to equation 10.6.

m_{cat} [kg]	n_{in} [mol s ⁻¹]	$p_{B,\text{in}}$ [kPa]	$p_{E,\text{in}}$ [kPa]	$p_{EB,\text{in}}$ [kPa]	τ [10 ⁻³ h]	X [%]	$p_{B,\text{out}}$ [kPa]	$p_{E,\text{out}}$ [kPa]	$p_{EB,\text{out}}$ [kPa]	n_{out} [mol s ⁻¹]	$-r_B$ [mol kg ⁻¹ s ⁻¹]	$p_{B,\text{m}}$ [kPa]	$p_{E,\text{m}}$ [kPa]	$p_{EB,\text{m}}$ [kPa]
3.0 × 10 ⁻⁵	2.0 × 10 ⁻⁴	90	5	5	0.5418	0.0679	89.99389	4.94191	5.06420	2.00 × 10 ⁻⁴	4.07 × 10 ⁻³	89.99694	4.97096	5.0321
3.0 × 10 ⁻⁵	2.0 × 10 ⁻⁴	70	15	15	0.5578	0.1624	69.96587	14.90328	15.13085	2.00 × 10 ⁻⁴	7.58 × 10 ⁻³	69.98293	14.95164	15.06543
3.0 × 10 ⁻⁵	2.0 × 10 ⁻⁴	50	25	25	0.5747	0.1881	49.95293	24.92940	25.11767	2.00 × 10 ⁻⁴	6.27 × 10 ⁻³	49.97647	24.96470	25.05884
3.0 × 10 ⁻⁵	2.0 × 10 ⁻⁴	90	9	1	0.5647	0.1327	89.98804	8.89119	1.12077	2.00 × 10 ⁻⁴	7.96 × 10 ⁻³	89.99402	8.94559	1.06039
3.0 × 10 ⁻⁵	2.0 × 10 ⁻⁴	70	29	1	0.6533	0.4388	69.90757	28.78124	1.31120	1.99 × 10 ⁻⁴	2.05 × 10 ⁻²	69.95378	28.89062	1.1556
3.0 × 10 ⁻⁵	2.0 × 10 ⁻⁴	50	49	1	0.7748	0.7581	49.80976	48.80595	1.38429	1.99 × 10 ⁻⁴	2.53 × 10 ⁻²	49.90488	48.90298	1.19215
3.0 × 10 ⁻⁵	2.0 × 10 ⁻⁴	90	1	9	0.5207	0.0114	89.99898	0.98988	9.01114	2.00 × 10 ⁻⁴	6.81 × 10 ⁻⁴	89.99949	0.99494	9.00557
3.0 × 10 ⁻⁵	2.0 × 10 ⁻⁴	70	11	19	0.5354	0.1061	69.97771	10.93388	19.08841	2.00 × 10 ⁻⁴	4.95 × 10 ⁻³	69.98886	10.96694	19.0442
3.0 × 10 ⁻⁵	2.0 × 10 ⁻⁴	50	11	39	0.4995	0.0292	49.99270	10.98701	39.02029	2.00 × 10 ⁻⁴	9.73 × 10 ⁻⁴	49.99635	10.99350	39.01015
2.0 × 10 ⁻⁵	2.0 × 10 ⁻⁴	180	10	10	0.3612	0.1525	179.97252	9.73891	10.28858	2.00 × 10 ⁻⁴	1.37 × 10 ⁻²	179.98626	9.86945	10.14429
2.0 × 10 ⁻⁵	2.0 × 10 ⁻⁴	140	30	30	0.3719	0.3722	139.84329	29.55598	30.60074	1.99 × 10 ⁻⁴	2.61 × 10 ⁻²	139.92164	29.77799	30.30037
2.0 × 10 ⁻⁵	2.0 × 10 ⁻⁴	100	50	50	0.3831	0.4525	99.77324	49.65986	50.56689	2.00 × 10 ⁻⁴	2.26 × 10 ⁻²	99.88662	49.82993	50.28345
2.0 × 10 ⁻⁵	2.0 × 10 ⁻⁴	180	18	2	0.3765	0.2988	179.94608	17.50929	2.54463	1.99 × 10 ⁻⁴	2.69 × 10 ⁻²	179.97304	17.75465	2.27232
2.0 × 10 ⁻⁵	2.0 × 10 ⁻⁴	140	58	2	0.4355	1.0102	139.57268	56.98867	3.43865	1.99 × 10 ⁻⁴	7.07 × 10 ⁻²	139.78634	57.49433	2.71933
2.0 × 10 ⁻⁵	2.0 × 10 ⁻⁴	100	98	2	0.5165	1.7867	99.09861	97.08058	3.82082	1.98 × 10 ⁻⁴	8.93 × 10 ⁻²	99.54930	97.54029	2.91041
2.0 × 10 ⁻⁵	2.0 × 10 ⁻⁴	180	2	18	0.3471	0.0268	179.99518	1.95226	18.05256	2.00 × 10 ⁻⁴	2.41 × 10 ⁻³	179.99759	1.97613	18.02628
2.0 × 10 ⁻⁵	2.0 × 10 ⁻⁴	140	22	38	0.3569	0.2468	139.89618	21.69199	38.41183	2.00 × 10 ⁻⁴	1.73 × 10 ⁻²	139.94809	21.84600	38.20592
2.0 × 10 ⁻⁵	2.0 × 10 ⁻⁴	100	22	78	0.3330	0.1121	99.94392	21.90017	78.15591	2.00 × 10 ⁻⁴	5.61 × 10 ⁻³	99.97196	21.95009	78.07795
1.0 × 10 ⁻⁵	2.0 × 10 ⁻⁴	270	15	15	0.1806	0.1482	269.95993	14.61929	15.42078	2.00 × 10 ⁻⁴	2.67 × 10 ⁻²	269.97996	14.80965	15.21039
1.0 × 10 ⁻⁵	2.0 × 10 ⁻⁴	210	45	45	0.1859	0.3649	209.76954	44.34704	45.88341	1.99 × 10 ⁻⁴	5.11 × 10 ⁻²	209.88477	44.67352	45.44171
1.0 × 10 ⁻⁵	2.0 × 10 ⁻⁴	150	75	75	0.1916	0.4514	149.66066	74.49100	75.84834	2.00 × 10 ⁻⁴	4.51 × 10 ⁻²	149.83033	74.74550	75.42417
1.0 × 10 ⁻⁵	2.0 × 10 ⁻⁴	270	27	3	0.1882	0.2916	269.92106	26.28163	3.79731	1.99 × 10 ⁻⁴	5.25 × 10 ⁻²	269.96053	26.64081	3.39866
1.0 × 10 ⁻⁵	2.0 × 10 ⁻⁴	210	87	3	0.2178	1.0043	209.36279	85.49193	5.14528	1.99 × 10 ⁻⁴	1.41 × 10 ⁻¹	209.68139	86.24596	4.07264
1.0 × 10 ⁻⁵	2.0 × 10 ⁻⁴	150	147	3	0.2583	1.8143	148.62680	145.59933	5.77387	1.98 × 10 ⁻⁴	1.81 × 10 ⁻¹	149.31340	146.29967	4.38693
1.0 × 10 ⁻⁵	2.0 × 10 ⁻⁴	270	3	27	0.1736	0.0264	269.99288	2.92950	27.07762	2.00 × 10 ⁻⁴	4.75 × 10 ⁻³	269.99644	2.96475	27.03881
1.0 × 10 ⁻⁵	2.0 × 10 ⁻⁴	210	33	57	0.1785	0.2424	209.84706	32.54628	57.60666	2.00 × 10 ⁻⁴	3.39 × 10 ⁻²	209.92353	32.77314	57.30333
1.0 × 10 ⁻⁵	2.0 × 10 ⁻⁴	150	33	117	0.1665	0.1230	149.90770	32.83570	117.25661	2.00 × 10 ⁻⁴	1.23 × 10 ⁻²	149.95385	32.91785	117.1283
1.0 × 10 ⁻⁵	2.0 × 10 ⁻⁴	360	20	20	0.1806	0.2293	359.91730	19.21430	20.86840	2.00 × 10 ⁻⁴	4.13 × 10 ⁻²	359.95865	19.60715	20.4342
1.0 × 10 ⁻⁵	2.0 × 10 ⁻⁴	280	60	60	0.1859	0.5684	279.52062	58.64175	61.83763	1.99 × 10 ⁻⁴	7.96 × 10 ⁻²	279.76031	59.32088	60.91881
1.0 × 10 ⁻⁵	2.0 × 10 ⁻⁴	200	100	100	0.1916	0.7114	199.28607	98.92911	101.78482	1.99 × 10 ⁻⁴	7.11 × 10 ⁻²	199.64304	99.46455	100.89241
1.0 × 10 ⁻⁵	2.0 × 10 ⁻⁴	360	36	4	0.1882	0.4520	359.83661	34.51313	5.65026	1.99 × 10 ⁻⁴	8.14 × 10 ⁻²	359.91830	35.25657	4.82513
1.0 × 10 ⁻⁵	2.0 × 10 ⁻⁴	280	116	4	0.2178	1.5768	278.66073	112.83038	8.50889	1.98 × 10 ⁻⁴	2.21 × 10 ⁻¹	279.33036	114.41519	6.25445
7.0 × 10 ⁻⁶	2.0 × 10 ⁻⁴	200	196	4	0.1808	2.0465	197.93239	193.89104	8.17656	1.98 × 10 ⁻⁴	2.92 × 10 ⁻¹	198.96620	194.94552	6.08828

(continued on next page)

Table C.6 (continued)

m_{cat} [kg]	n_{in} [mol s ⁻¹]	$p_{\text{B,in}}$ [kPa]	$p_{\text{E,in}}$ [kPa]	$p_{\text{EB,in}}$ [kPa]	τ [10 ⁻³ h]	X [%]	$p_{\text{B,out}}$ [kPa]	$p_{\text{E,out}}$ [kPa]	$p_{\text{EB,out}}$ [kPa]	n_{out} [mol s ⁻¹]	$-r_{\text{B}}$ [mol kg ⁻¹ s ⁻¹]	$p_{\text{B,m}}$ [kPa]	$p_{\text{E,m}}$ [kPa]	$p_{\text{EB,m}}$ [kPa]
1.0×10^{-5}	2.0×10^{-4}	360	4	36	0.1736	0.0410	359.98522	3.85373	36.16105	2.00×10^{-4}	7.38×10^{-3}	359.99261	3.92686	36.08052
1.0×10^{-5}	2.0×10^{-4}	280	44	76	0.1785	0.3777	279.68191	43.05633	77.26176	1.99×10^{-4}	5.29×10^{-2}	279.84096	43.52817	76.63088
1.0×10^{-5}	2.0×10^{-4}	200	44	156	0.1665	0.2016	199.79822	43.64084	156.56093	2.00×10^{-4}	2.02×10^{-2}	199.89911	43.82042	156.28047
1.0×10^{-5}	2.0×10^{-4}	450	25	25	0.1806	0.3153	449.85770	23.64818	26.49412	1.99×10^{-4}	5.68×10^{-2}	449.92885	24.32409	25.74706
1.0×10^{-5}	2.0×10^{-4}	350	75	75	0.1859	0.7864	349.16976	72.64764	78.18260	1.99×10^{-4}	1.10×10^{-1}	349.58488	73.82382	76.5913
1.0×10^{-5}	2.0×10^{-4}	250	125	125	0.1916	0.9925	248.75324	123.12986	128.11690	1.99×10^{-4}	9.92×10^{-2}	249.37662	124.06493	126.55845
1.0×10^{-5}	2.0×10^{-4}	450	45	5	0.1882	0.6225	449.71828	42.43638	7.84534	1.99×10^{-4}	1.12×10^{-1}	449.85914	43.71819	6.42267
1.0×10^{-5}	2.0×10^{-4}	350	145	5	0.2178	2.1923	347.66225	139.46733	12.87042	1.97×10^{-4}	3.07×10^{-1}	348.83113	142.23366	8.93521
5.0×10^{-6}	2.0×10^{-4}	250	245	5	0.1291	2.0881	247.36230	242.30955	10.32816	1.98×10^{-4}	4.18×10^{-1}	248.68115	243.65477	7.66408
1.0×10^{-5}	2.0×10^{-4}	450	5	45	0.1736	0.0566	449.97451	4.74763	45.27786	2.00×10^{-4}	1.02×10^{-2}	449.98725	4.87382	45.13893
1.0×10^{-5}	2.0×10^{-4}	350	55	95	0.1785	0.5225	349.44939	53.36654	97.18407	1.99×10^{-4}	7.31×10^{-2}	349.72470	54.18327	96.09203
1.0×10^{-5}	2.0×10^{-4}	250	55	195	0.1665	0.2871	249.64061	54.36028	195.99911	2.00×10^{-4}	2.87×10^{-2}	249.82030	54.68014	195.49956

Table C.7: Fitted and extrapolated Langmuir-Hinshelwood parameters. The activation energies E_i and pre-exponential factors $k_{0,i}$ and $K_{0,i}$, respectively, are obtained from the fitted LH parameters by assuming Arrhenius-type behavior.

constant	fitted		extrapolated
	603 K	653 K	703 K
k_1 [mol kg ⁻¹ s ⁻¹ kPa ⁻²]	5.678×10^{-6}	1.120×10^{-5}	2.004×10^{-5}
k_{-1} [mol kg ⁻¹ s ⁻¹ kPa ⁻²]	7.112×10^{-5}	1.575×10^{-4}	3.115×10^{-4}
K_B [kPa ⁻¹]	1.539×10^{-3}	7.781×10^{-4}	4.335×10^{-4}
K_E [kPa ⁻¹]	2.915×10^{-4}	1.876×10^{-4}	1.285×10^{-4}
K_{EB} [kPa ⁻¹]	9.050×10^{-3}	4.558×10^{-3}	2.530×10^{-3}
E_1 [kJ mol ⁻¹]	44.45		
E_{-1} [kJ mol ⁻¹]	52.06		
E_B [kJ mol ⁻¹]	44.64		
E_E [kJ mol ⁻¹]	28.86		
E_{EB} [kJ mol ⁻¹]	44.91		
$k_{0,1}$ [mol kg ⁻¹ s ⁻¹ kPa ⁻²]	4.029×10^{-2}		
$k_{0,-1}$ [mol kg ⁻¹ s ⁻¹ kPa ⁻¹]	2.301×10^0		
$k_{0,B}$ [kPa ⁻¹]	2.088×10^{-7}		
$k_{0,E}$ [kPa ⁻¹]	9.209×10^{-7}		
$k_{0,EB}$ [kPa ⁻¹]	1.164×10^{-6}		

Table C.8: Fitted power-law parameters. The activation energies E_i and pre-exponential factors $k_{0,i}$ are obtained from the jointly fitted PL-parameters by assuming Arrhenius-type behavior.

constant	individually fitted		jointly fitted	
	603 K	653 K	603 K	653 K
k_1 [mol kg ⁻¹ s ⁻¹ kPa ^{-(n_B+n_E)}]	5.674×10^{-5}	5.124×10^{-5}	2.078×10^{-5}	5.866×10^{-5}
k_{-1} [mol kg ⁻¹ s ⁻¹ kPa ^{-n_{EB}}]	1.937×10^{-4}	2.954×10^{-4}	1.369×10^{-4}	3.142×10^{-4}
n_B [-]	0.4602	0.6566	0.6336	
n_E [-]	0.9648	0.9752	0.9736	
n_{EB} [-]	0.9992	1.0765	1.0649	
E_1 [kJ mol ⁻¹]			67.96	
E_{-1} [kJ mol ⁻¹]			54.39	
$k_{0,1}$ [mol kg ⁻¹ s ⁻¹ kPa ^{-(n_B+n_E)}]			1.602×10^1	
$k_{0,-1}$ [mol kg ⁻¹ s ⁻¹ kPa ^{-n_{EB}}]			7.044×10^0	

Supporting information for chapter 11

D

This material includes a discussion of the possible location of the acidic site in H-ZSM-5, a discussion of different approaches to evaluate the reactant partition function, additional data illustrating the cluster size dependence of adsorption and activation energies, fit parameters, and details about the calculation of the basis set superposition error in the determination of apparent activation energies.

D.1 Location of the acidic site in the MFI framework

The orthorhombic structure of ZSM-5 has 12 unique T-atom positions into which Al can be substituted. Several experimental and computational studies indicate that there is little energetic preference for Al in different sites.^{145,229–232} Thus the location of Al atoms in the zeolite framework is controlled more by the kinetics of zeolite synthesis than by thermodynamics. In the present study we consider the T12 site for Al substitution in accordance with previous theoretical works.^{258,317,408} In contrast to the siting of the Al atom, the position of the acidic proton is likely determined by thermodynamics because proton jumps between oxygen atoms bonded to the same aluminium are facile, in particular when adsorbates are present.^{257,472,473} In the present work we computed the total energies of the Al12-O24(H)-Si12, Al12-O20(H)-Si3, and Al12-O11(H)-Si11 sites for both sets of unit cell parameters (crystallographic position numbers according to Olson et al.¹⁴⁶). The results are summarized in table D.1. The order of stability depends on the unit cell parameters used, although the differences between Al12-O11(H)-Si11 and Al12-O20(H)-Si3 are rather small. Because the latter site is more easily accessible for reactants due to its location at the intersection between straight and sinusoidal channels we use Al12-O20(H)-Si3 as reference site in this work. In the recent work of Svelle et al.²⁵⁸ the Al12-O20(H)-Si3 site was reported to be more stable than the Al12-O24(H)-Si12 by 12.4 kJ/mol compared to 7.7 kJ/mol calculated in the present work. These deviations are a consequence of some differences in the set-up of the VASP calculations (PREC-tag, EDIFFG-tag, LREAL-tag) as confirmed by reproducing the electronic energy of the H-ZSM-5 unit cell using the input set-up of Svelle et al.²⁵⁸

Table D.1: Relative stabilities (in kJ/mol) of different bridging hydroxyl groups for Al-substitution at T12 position and two different sets of unit cell parameters.

Bridging hydroxyl group	UC1	UC2	UC2 (ref. 258)
Al12-O20(H)-Si3	0.0	0.0	0.0
Al12-O24(H)-Si12	6.3	7.7	12.4
Al12-O11(H)-Si11	-0.6	0.2	5.5

D.2 Partition functions for reactant and transition states

The partition functions are most easily computed for the case of immobile adsorption because only vibrational contributions are taken into account, which are directly obtained from the dynamical matrix of the stationary point. If the energy of the ground vibrational state is chosen to be $\sum h\nu/2$, the partition function of the reactant as appearing in equation 11.13 of the main text is given by

$$Q_{\text{R}}(T) = \prod_{i=1}^{3n-6} \frac{\exp(-\Theta_{\text{vib},i}/(2T))}{1 - \exp(-\Theta_{\text{vib},i}/T)}, \quad (\text{D.1})$$

with $\Theta_{\text{vib},i}$ being the vibrational temperature defined as

$$\Theta_{\text{vib},i} = \frac{\tilde{\nu}_i c h}{k_{\text{B}}}, \quad (\text{D.2})$$

where $\tilde{\nu}_i$ is the i th wave number, c is the speed of light, h is Planck's constant and k_{B} is Boltzmann's constant. The partition function of the transition state is also evaluated with equation D.1 but with the product running from $i=1$ to $3n-7$ as the vibrational degree of freedom corresponding to the reaction coordinate is missing. The frequency spectrum of physisorbed complexes often displays low wave number modes in the range 0 to 100 cm^{-1} which correspond to frustrated rotations and translations of the physisorbed molecules. As these low modes make the largest contribution to the partition function it has to be carefully analyzed whether a treatment as vibrations may lead to spurious results and whether the contribution from these modes should be replaced by translational and (hindered) rotational contributions, respectively. In a recent study reported by De Moor et al.⁴³⁹ on the adsorption of alkanes and alkenes in H-FAU it was demonstrated how the treatment of low wave number modes influences the enthalpy and entropy of adsorption. Here we are mainly interested in the contributions of physisorbed benzene and ethene to the partition function of the reactant state. Visualization of the vibrations corresponding to harmonic frequencies in the range 0 to 100 cm^{-1} for coadsorbed ethene and benzene in H-ZSM-5 indicate that some frequencies correspond to a rotation of the hydrocarbon relative to the zeolite. For benzene a frequency of 47 cm^{-1} could be associated with a rotation around the C_6 -symmetry axis (see figure D.1(a)). For ethene, a frequency of 53 cm^{-1} could be associated with a rotation around the $C_2(x)$ -symmetry axis (see figure D.1(b)). However, both movements were accompanied by significant vibrations of the zeolite lattice itself. Therefore we have estimated

the barriers for a rigid rotation of benzene around its C_6 -axis and for ethene around two of its C_2 -axes by performing single point energy calculations for discrete points along the rotational pathway. As can be seen from figure D.2 a rotation of benzene of 60° is associated with a barrier of 6 kJ/mol. For ethene, a rigid rotation of 180° around the $C_2(x)$ -axis which is perpendicular to the molecular plane is associated with a barrier of around 13 kJ/mol. A frustrated rotation around the $C_2(y)$ -axis which goes through the C=C bond is associated with a barrier of 46 kJ/mol and can therefore safely be treated as vibration. If the two remaining rotations were treated as harmonic vibrations the corresponding frequencies can be obtained from⁴⁷⁴

$$\nu = \frac{n_r}{2\pi} \left(\frac{V_0}{2I_A} \right)^{1/2}, \quad (\text{D.3})$$

where I_A denotes the moment of inertia and n_r acquires the sense of degeneration degree during rotation of 2π ($n_r = 2$ for ethene; $n_r = 6$ for benzene). The contributions to the partition functions are then given by equation D.1. For the case of free rotation, the contribution to the partition function is given by

$$q_{\text{free}} = \frac{1}{n_r} \frac{(2\pi k_B T I_A)^{1/2}}{h} 2\pi. \quad (\text{D.4})$$

In the case of hindered rotation it can be estimated by using the tables of Pitzer and Gwinn⁴⁷⁵ which tabulate contributions from hindered rotation to the free energy function F_{hind}/T as function of q_{free} and V_0/RT , where V_0 is the rotational barrier. The contributions to the partition function resulting from the hindered rotation can then be obtained from

$$F_{\text{hind}} = -RT \ln q_{\text{hind}}. \quad (\text{D.5})$$

To proceed we compare the contributions of each rotational movement to the reactant partition function for (i) immobile adsorption (equations D.1 and D.3), (ii) free rotation (equation D.4), and (iii) hindered rotation (equation D.5) in order to decide whether the partition function directly calculated from the vibrational spectrum is a reasonable approximation. The results are summarized in table D.2. It can be seen that at relevant reaction temperatures the treatment as free rotation leads to a almost twofold increase of the partition function for benzene and an almost threefold increase for ethene, when compared to the assumption of immobile adsorption. However, the treatment as hindered rotations lead to numbers close to the treatment as immobile adsorption leading us to conclude that the calculation of the partition function for the reactant state directly from the frequency spectrum

treating all frustrated modes as vibrations is a reasonable approximation in the present study. Similar investigations were also carried out for ethene adsorbed on the acid site (without benzene coadsorbed) and for benzene adsorbed next to the ethoxide. For ethene adsorbed on the acid site the barrier for rotation around the $C_2(y)$ -axis was calculated to 46 kJ/mol while for rotation around the $C_2(x)$ -axis a barrier of only 3.5 kJ/mol was determined. While the first barrier is large enough to treat the corresponding movement as normal vibration, the rotation around the $C_2(x)$ -axis could also be regarded as a free rotation. However, a comparison of the contributions to the reactant partition function for free rotation around the $C_2(x)$ -axis and a vibrational contribution from a frequency of 31 cm^{-1} (corresponding to a barrier height of 3.5 kJ/mol according to equation D.3) revealed that the final rate coefficients at reaction temperature are not affected significantly. When assuming free rotation the rate coefficient is smaller by a factor of 1.3 to 1.4 in the temperature range 600 to 700 K. For reasons of simplicity we therefore decided to treat the adsorbate as immobile.

For benzene adsorption next to an ethoxide species we have calculated a barrier of only 2 kJ/mol for rotation around the C_6 -axis. This barrier corresponds to a frequency of 24 cm^{-1} according to equation D.3. However, in the relevant temperature range from 600 to 700 K the rate coefficient is smaller by a factor of 1.03 to 1.11 when assuming free rotation instead of treating the degree of freedom as vibrational contribution. For reasons of simplicity we have therefore used again the immobile adsorbate assumption. Another argument in favor of the immobile adsorbate assumption is the fact that we also assume immobile transition states although these structures also display low modes in the range 0 to 100 cm^{-1} . Therefore the contributions from low modes will cancel out to a significant portion in the calculation of the rate coefficients.

Table D.2: Contributions to the reactant partition functions of benzene and ethene for different treatments of the rotational motion around the C_6 -symmetry axis (C_6H_6) and the $C_2(x)$ -symmetry axis (C_2H_4), respectively.

T [K]	Benzene			Ethene		
	immobile ^a	free rot. ^b	hind. rot	immobile ^a	free rot. ^b	hind. rot
298	5.044	13.810	6.368	3.440	14.042	4.252
600	10.167	19.596	12.360	6.944	19.924	8.565
650	11.015	20.369	13.241	7.524	20.738	9.296
700	11.863	21.166	14.086	8.104	21.521	10.034

^awavenumbers: 41 cm^{-1} (C_6H_6); 60 cm^{-1} (C_2H_4)

^bmoments of inertia: $2.954 \times 10^{-45}\text{ kg m}^2$ (C_6H_6); $3.393 \times 10^{-46}\text{ kg m}^2$ (C_2H_4)

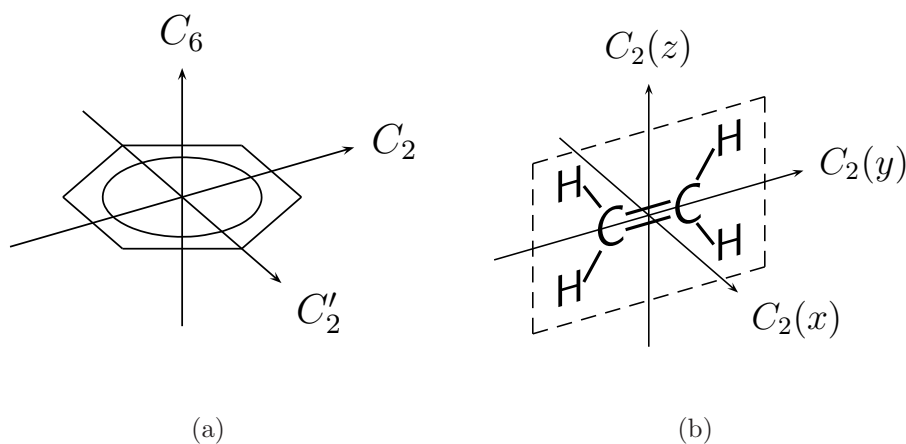


Figure D.1: Definition of symmetry axes for (a) benzene and (b) ethene.

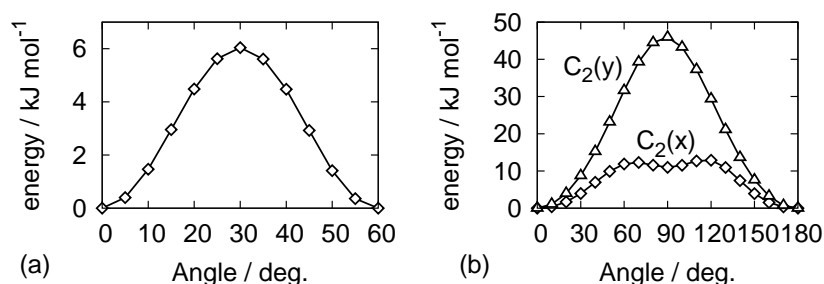


Figure D.2: PBE-barriers for rigid rotations of (a) benzene around the C_6 -symmetry axis and (b) ethene around the $C_2(x)$ -axis and $C_2(y)$ -axis, respectively, for the case of coadsorbed ethene and benzene.

D.3 Cluster size dependence of adsorption energies and intrinsic energy barriers

In addition to the calculations discussed in section 11.3.1, two further sets of computations were carried out to study (i) the influence of the cluster termination and (ii) the influence of the size of the unit cell from which the clusters were cut out. For ethene adsorption on the acid site we have studied the influence of an Al-O-Si(OH)₃ termination on the high-level correction to see whether it gives results that are different from those of an Al-O-H termination. All clusters used for calculating the data presented in

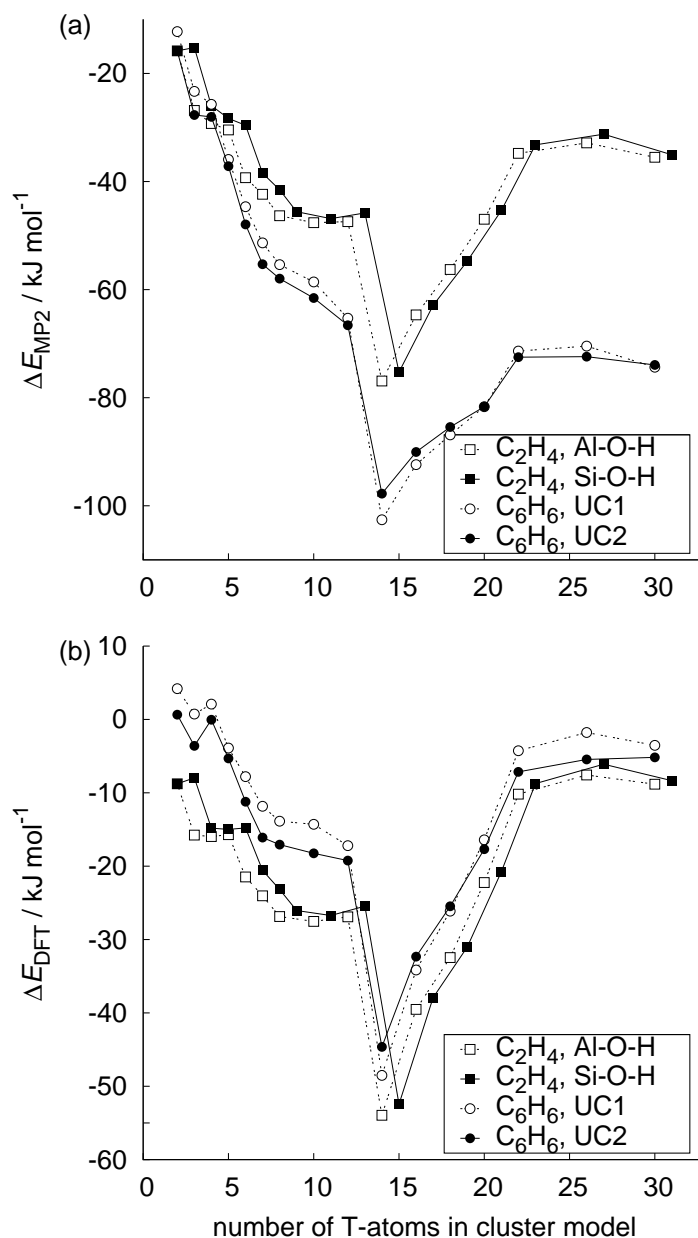


Figure D.3: Adsorption energies of ethene for two different cluster terminations and adsorption energies of benzene for two different sets of unit cell parameters obtained from single-point energy calculations on cluster models of increasing size. (a) MP2/TZVP(P) results. (b) DFT (PBE/QZVP) results.

chapter 11 which contain more than 10 T-atoms contain one Al-O-H termination. This termination was replaced by Al-O-Si(OH)₃. As can be seen from figure D.3 the MP2 and PBE adsorption energies are essentially shifted but do not deviate significantly between the two cluster terminations (open and filled squares). Even more important, the difference between MP2 and PBE adsorption energies, extrapolated to the periodic limit is the same in both cases (see figure D.4). In addition we have also studied the influence of the unit cell parameters on the high level correction for the case of benzene adsorption on the acid site. In chapter 11 the influence of the unit cell size on the PBE adsorption energies was evaluated for all elementary steps. It was found that energy differences are within ± 5 kJ/mol with the exception of ethoxide formation (9.7 kJ/mol). As can be seen from figure D.3, the size of the unit cell used for constructing the cluster series affects the MP2 and PBE adsorption energies, as expected. However, the number of interest is the difference between MP2 and PBE energies, extrapolated to the periodic limit (see figure D.4). These numbers differ by only 0.3 kJ/mol which means for the case of benzene adsorption that the UC2 set cell parameters results in

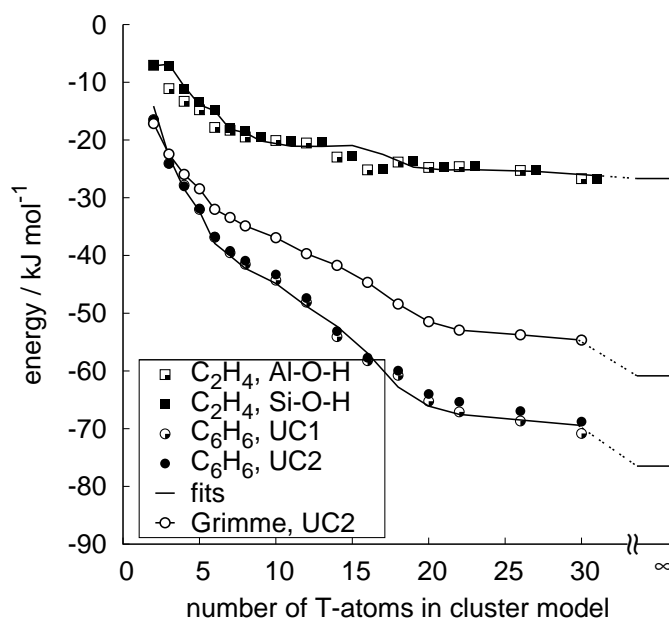


Figure D.4: Differences in adsorption energies between MP2 and PBE (filled and partly filled symbols) and dispersion contribution to the adsorption energies as predicted by the parameter set published by Grimme³⁹⁹ (open symbols). Extrapolations to the full periodic limit are also included.

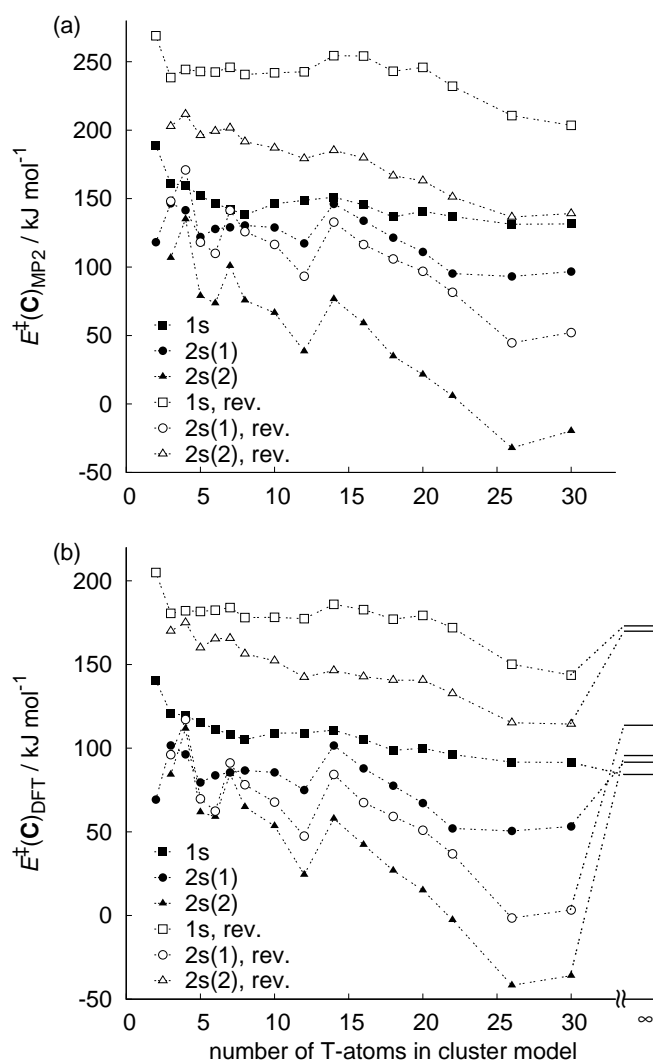


Figure D.5: Intrinsic activation energies of forward and reverse reaction steps in the one- and two-step alkylation obtained from single-point energy calculations on cluster models of increasing size. (a) MP2/TZVP(P) results. (b) DFT (PBE/QZVP) results. The periodic model limit is given for comparison.

an adsorption enthalpy which is less negative by 4.9 kJ/mol if the CBS-limit correction is assumed to be independent of the unit cell size.

Figure D.5 shows the intrinsic energy barriers obtained from single point MP2 (D.5(a)) and PBE (D.5(b)) calculations for all forward and reverse reac-

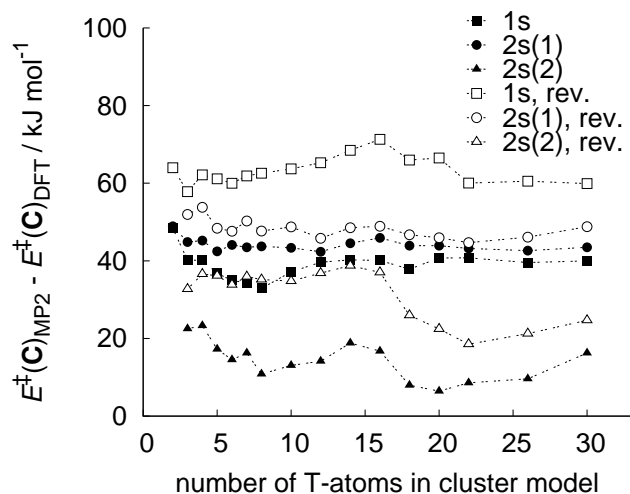


Figure D.6: Differences between MP2 and PBE intrinsic activation energies for forward and reverse reaction steps.

tions steps as function of the cluster size. Similar to the adsorption energies and apparent energy barriers, the intrinsic energy barriers do not show a systematic behavior with cluster size. The second barrier of the two-step scheme becomes even negative for larger clusters. The PBE barriers calculated for the T30 clusters are significantly different from the periodic limit. The difference between MP2 and PBE intrinsic energy barriers is plotted in figure D.6. Contrary to the corresponding plots for adsorption energies and apparent energy barriers (figures 11.4, 11.5 and 11.9 in the main text) the curves do not decay monotonically with cluster size. Therefore, an unambiguous extrapolation to the periodic limit is not possible. Consequently we have determined the high-level corrections for the intrinsic energy barriers indirectly from the high-level corrections for the apparent energy barriers and the corresponding adsorbate structures.

D.4 Fit parameters

Table D.3: Sets of C_6 parameters (in $\text{J nm}^6 \text{mol}^{-1}$) for H, C, Al, Si, and O atoms as well as additive constants, E_{add} (in kJ mol^{-1}) obtained by fitting differences between MP2/TZVP(P) and PBE/QZVP cluster model adsorption energies. Root mean squared errors and the maximum deviation between reference data points and the corresponding fitted values are also given (in kJ mol^{-1}).

struc.	C_6 -parameters					E_{add}	RMS	max. dev.
	H	C	Al	Si	O			
1	0.8452	7.1538	1.1972	0.9679	0.7975	-31.367	0.9637	2.5429
2	0.6961	4.2544	1.1108	3.7348	0.7126	-24.868	1.3311	2.7806
3	0.5322	1.5908	10.7892	9.2059	0.6713	-25.748	1.2070	-2.2698
4	0.4963	0.8444	11.0260	18.9362	0.7117	-9.322	1.4480	3.7220
5	0.9640	2.3837	1.1514	0.8894	0.7922	-26.621	1.2595	2.3010
6	0.4857	1.0667	10.6240	18.4515	0.6698	-7.879	1.5979	3.6477
7	0.7909	5.0719	--	1.1226	0.8271	-5.885	0.9631	2.2704

Table D.4: Sets of C_6 parameters (in $\text{J nm}^6 \text{mol}^{-1}$) for H, C, Al, Si, and O atoms as well as additive constants, E_{add} (in kJ mol^{-1}) obtained by fitting differences between MP2/TZVP(P) and PBE/QZVP cluster model apparent energy barriers. Root mean squared errors and the maximum deviation between reference data points and the corresponding fitted values are also given (in kJ mol^{-1}).

struc.	C_6 -parameters					E_{add}	RMS	max. dev.
	H	C	Al	Si	O			
1s	0.6299	0.7685	23.7305	13.0105	0.9660	-57.613	0.8992	2.1083
1s,r	0.6299	0.7685	23.7305	13.0105	0.9660	-113.797	0.8992	2.1083
2s(1)	0.9328	23.6100	7.6409	1.4142	0.9722	-153.161	0.6268	-1.5038
2s(2)	0.5151	1.4267	23.7126	10.4534	0.7634	-48.387	1.0766	-2.7929
2s(2),r	0.5151	1.4267	23.7126	10.4534	0.7634	-91.543	1.0766	-2.7929

D.5 BSSE calculations on transition structures

Basis set superposition errors (BSSE) were calculated with the counterpoise procedure⁴²⁶ (CP). As noted in the main text, CP-corrected CBS-limit corrections for intrinsic energy barriers have been obtained from the CP-corrected CBS-limits for the apparent energy barriers and those of the corresponding adsorbate complexes. Depending on the reaction channel, two-body or three-body CP calculations were performed. The closed-shell subsystems used in these calculations are listed in table D.5.

Table D.5: Subsystems used for calculating BSSE-corrected CBS-limit corrections for apparent activation energies (f: forward reaction; r: reverse reaction).

Subsystem	1s		2s(1)		2s(2)	
	f	r	f	r	f	r
zeolite cluster (charge: -1)	+	+	+	+	-	+
protonated ethene (charge: +1)	+	-	+	+	-	-
benzene (charge: 0)	+	-	-	-	+	-
benzene + protonated ethene (charge: +1)	-	+	-	-	-	+
zeolite cluster + protonated ethene (charge: 0)	-	-	-	-	+	-

Bibliography

- [1] H. J. C. Berendsen, *Simulating the Physical World*, Cambridge University Press, New York **2007**.
- [2] A. Groß, The virtual chemistry lab for reactions at surfaces: Is it possible? Will it be useful?, *Surf. Sci.* **2002**, 500, 347–367.
- [3] M. E. Davis, Ordered porous materials for emerging applications, *Nature* **2002**, 417, 813–821.
- [4] E. A. Carter, Challenges in modeling materials properties without experimental input, *Science* **2008**, 321, 800–803.
- [5] F. Starrost, E. A. Carter, Modeling the full monty: Baring the nature of surfaces across time and space, *Surf. Sci.* **2002**, 500, 323–346.
- [6] E. E. Santiso, K. E. Gubbins, Multi-scale molecular modeling of chemical reactivity, *Mol. Sim.* **2004**, 30, 699–748.
- [7] D. G. Vlachos, A review of multiscale analysis: Examples from systems biology, materials engineering, and other fluid-surface interacting systems, *Adv. Chem. Eng.* **2005**, 30, 1–61.
- [8] P. Sherwood, B. R. Brooks, M. S. P. Sansom, Multiscale methods for macromolecular simulations, *Curr. Opin. Struct. Biol.* **2008**, 18, 630–640.
- [9] A. Lyubartsev, Y. Q. Tu, A. Laaksonen, Hierarchical multiscale modelling scheme from first principles to mesoscale, *J. Comput. Theor. Nanosci.* **2009**, 6, 951–959.
- [10] P. Kočí, V. Novák, F. Štěpánek, M. Marek, M. Kubíček, Multi-scale modelling of reaction and transport in porous catalysts, *Chem. Eng. Sci.* **2010**, 65, 412–419.
- [11] J. Grotendorst, N. Attig, S. Blügel, D. Marx (eds.), *Multiscale Simulation Methods in Molecular Sciences*, Jülich Supercomputing Centre, Jülich **2009**.
- [12] C. H. Christensen, J. K. Nørskov, A molecular view of heterogeneous catalysis, *J. Chem. Phys.* **2008**, 128, 182503–1/8.
- [13] A. A. Gokhale, J. A. Dumesic, M. Mavrikakis, On the mechanism of low-temperature water gas shift reaction on copper, *J. Am. Chem. Soc.*

- 2008**, 130, 1402–1414.
- [14] J. K. Nørskov, T. Bligaard, J. Rossmeisl, C. H. Christensen, Towards the computational design of solid catalysts, *Nature Chemistry* **2009**, 1, 37–46.
- [15] V. J. Frilette, P. B. Weisz, R. L. Golden, Catalysis by crystalline aluminosilicates. 1. Cracking of hydrocarbon types over sodium and calcium-X zeolites, *J. Catal.* **1962**, 1, 301–306.
- [16] P. B. Weisz, V. J. Frilette, R. W. Maatman, E. B. Mower, Catalysis by crystalline aluminosilicates. 2. Molecular-shape selective reactions, *J. Catal.* **1962**, 1, 307–312.
- [17] D. J. Earl, M. W. Deen, Toward a database of hypothetical zeolite structures, *Ind. Eng. Chem. Res.* **2006**, 45, 5449–5454.
- [18] C. Baerlocher, L. B. McCusker, D. H. Olson, *Atlas of Zeolite Framework Types*, Elsevier Science B. V., Amsterdam, 6th ed. **2007**.
- [19] W. Vermeiren, J.-P. Gilson, Impact of zeolites on the petroleum and petrochemical industry, *Top. Catal.* **2009**, 52, 1131–1161.
- [20] J. Weitkamp, L. Puppe (eds.), *Catalysis and Zeolites - Fundamentals and Applications*, Springer, Berlin **1999**.
- [21] B. Smit, T. L. M. Maesen, Towards a molecular understanding of shape selectivity, *Nature* **2008**, 451, 671–678.
- [22] B. Smit, T. L. M. Maesen, Molecular simulations of zeolites: Adsorption, diffusion, and shape selectivity, *Chem. Rev.* **2008**, 108, 4125–4184.
- [23] R. Krishna, Describing the diffusion of guest molecules inside porous structures, *J. Phys. Chem. C* **2009**, 113, 19756–19781.
- [24] R. Millini, C. Perego, The role of molecular mechanics and dynamics methods in the development of zeolite catalytic processes, *Top. Catal.* **2009**, 52, 42–66.
- [25] M. Hunger, W. Wang, Characterization of solid catalysts in the functioning state by nuclear magnetic resonance spectroscopy, *Adv. Catal.* **2006**, 50, 149–225.
- [26] A. T. Bell, Watching catalysts at work, *Nature* **2008**, 456, 185–186.
- [27] E. de Smit, I. Swart, J. F. Creemer, G. H. Hoveling, M. K. Gilles, T. Tyliszczak, P. J. Kooyman, H. W. Zandbergen, C. Morin, B. M. Weckhuysen, F. M. F. de Groot, Nanoscale chemical imaging of a working catalyst by scanning transmission X-ray microscopy, *Nature* **2008**, 456, 222–225.
- [28] B. M. Weckhuysen, Spatial heterogeneities in catalysis, *Angew. Chem. Int. Ed.* **2009**, 48, 4910–4943.
- [29] D. Tzoulaki, L. Heinke, H. Lim, J. Li, D. Olson, J. Caro, R. Krishna, C. Chmelik, J. Kärger, Assessing surface permeabilities from transient

- guest profiles in nanoporous materials, *Angew. Chem. Int. Ed.* **2009**, 48, 3525–3528.
- [30] L. Heinke, D. Tzoulaki, C. Chmelik, F. Hibbe, J. M. van Baten, H. Lim, J. Li, R. Krishna, J. Kärger, Assessing guest diffusivities in porous hosts from transient concentration profiles, *Phys. Rev. Lett.* **2009**, 102, 065901–1/4.
- [31] J. Kärger, J. Caro, P. Cool, M.-O. Coppens, D. Jones, F. Kapteijn, F. Rodríguez-Reinoso, M. Stöcker, D. Theodorou, E. F. Vansant, J. Weitkamp, Benefit of microscopic diffusion measurement for the characterization of nanoporous materials, *Chem. Eng. Technol.* **2009**, 32, 1494–1511.
- [32] A. Goodrow, A. T. Bell, A theoretical investigation of the selective oxidation of methanol to formaldehyde on isolated vanadate species supported on titania, *J. Phys. Chem. C* **2008**, 112, 13204–13214.
- [33] D. M. McCann, D. Lesthaeghe, P. W. Kletnieks, D. R. Guenther, M. J. Hayman, V. Van Speybroeck, M. Waroquier, J. F. Haw, A complete catalytic cycle for supramolecular methanol-to-olefins conversion by linking theory with experiment, *Angew. Chem. Int. Ed.* **2008**, 47, 5179–5182.
- [34] M. Boronat, P. Concepción, A. Corma, M. T. Navarro, M. Renz, S. Valenzia, Reactivity in the confined spaces of zeolites: The interplay between spectroscopy and theory to develop structure-activity relationships for catalysis, *Phys. Chem. Chem. Phys.* **2009**, 11, 2876–2884.
- [35] J. Dědeček, S. Sklenak, C. Li, B. Wichterlová, V. Gábová, J. Brus, M. Sierka, J. Sauer, Effect of Al-Si-Al and Al-Si-Si-Al pairs in the ZSM-5 zeolite framework on the ^{27}Al NMR spectra. A combined high resolution ^{27}Al NMR and DFT/MM study, *J. Phys. Chem. C* **2009**, 113, 1447–1458.
- [36] D. A. McQuarrie, J. D. Simon, *Physical Chemistry – A Molecular approach*, University Science Books, Sausalito **1997**.
- [37] I. N. Levine, *Quantum Chemistry*, Prentice-Hall, Upper Saddle River, 5th ed. **2000**.
- [38] A. R. Leach, *Molecular Modelling: Principles and Applications*, Prentice Hall, Harlow, 2nd ed. **2001**.
- [39] M. Born, R. Oppenheimer, Zur Quantentheorie der Molekeln, *Ann. Phys.* **1927**, 84, 457–484.
- [40] W. Kolos, L. Wolniewicz, Accurate adiabatic treatment of the ground state of the hydrogen molecule, *J. Chem. Phys.* **1964**, 41, 3663–3673.
- [41] M. Born, V. Fock, Beweis des Adiabatenatzes, *Z. Phys. A* **1928**, 51, 165–180.
- [42] W. J. Hehre, L. Radom, P. v. R. Schleyer, J. A. Pople, *Ab Initio Mo-*

- lecular Orbital Theory*, John Wiley & Sons, New York **1986**.
- [43] J. Grotendorst, S. Blügel, D. Marx (eds.), *Computational Nanoscience: Do it Yourself*, NIC-Directors, Jülich **2006**.
- [44] M. Springborg, *Methods of Electronic-Structure Calculations*, John Wiley & Sons, Chichester **2000**.
- [45] A. E. Stearn, H. Eyring, Nonadiabatic reactions. The decomposition of N_2O , *J. Chem. Phys.* **1935**, 3, 778–785.
- [46] A. Heyden, *Theoretical investigation of the nitrous oxide decomposition over iron zeolite catalysts*, Ph.D. thesis, Technische Universität Hamburg-Harburg **2005**.
- [47] J. C. Slater, The theory of complex spectra, *Phys. Rev.* **1929**, 34, 1293–1322.
- [48] A. Szabo, N. S. Ostlund, *Modern Quantum Chemistry*, Dover Publications, Mineola **1996**.
- [49] C. C. J. Roothaan, New developments in molecular orbital theory, *Rev. Modern Phys.* **1951**, 23, 69–89.
- [50] T. Helgaker, P. Jørgensen, J. Olsen, *Molecular Electronic-Structure Theory*, John Wiley & Sons, New York **2002**.
- [51] R. L. Snow, J. L. Bills, A simple illustration of the SCF-LCAO-MO method, *J. Chem. Edu.* **1975**, 52, 506–509.
- [52] J. A. Pople, R. K. Nesbet, Self-consistent orbitals for radicals, *J. Chem. Phys.* **1954**, 22, 571–572.
- [53] M. Feyereisen, G. Fitzgerald, A. Komornicki, Use of approximate integrals in ab initio theory. An application in MP2 energy calculations, *Chem. Phys. Lett.* **1993**, 208, 359–363.
- [54] D. E. Bernholdt, R. J. Harrison, Large-scale correlated electronic structure calculations: The RI-MP2 method on parallel computers, *Chem. Phys. Lett.* **1996**, 250, 477–484.
- [55] F. Weigend, M. Häser, RI-MP2: First derivatives and global consistency, *Theor. Chem. Acc.* **1997**, 97, 331–340.
- [56] S. Grimme, M. Waletzke, Multi-reference Møller-Plesset theory: Computational strategies for large molecules, *Phys. Chem. Chem. Phys.* **2000**, 2, 2075–2081.
- [57] H.-J. Werner, F. R. Manby, P. J. Knowles, Fast linear scaling second-order Møller-Plesset perturbation theory (MP2) using local and density fitting, *J. Chem. Phys.* **2003**, 118, 8149–8160.
- [58] M. Schütz, H.-J. Werner, R. Lindh, F. R. Manby, Analytical energy gradients for local second-order Møller-Plesset perturbation theory using density fitting approximations, *J. Chem. Phys.* **2004**, 121, 737–750.
- [59] C. Tuma, *A QM/QM hybrid method for MP2/plane-wave-DFT studies of extended systems*, Ph.D. thesis, Humboldt-Universität zu Berlin

- 2006.**
- [60] F. Jensen, *Introduction to Computational Chemistry*, John Wiley & Sons, Chichester **1999**.
- [61] C. J. Cramer, *Essentials of Computational Chemistry - Theory and Models*, John Wiley & Sons, Chichester **2002**.
- [62] K. Raghavachari, G. W. Trucks, J. A. Pople, M. Head-Gordon, A fifth-order perturbation comparison of electron correlation theories, *Chem. Phys. Lett.* **1989**, 157, 479–483.
- [63] P. Hohenberg, W. Kohn, Inhomogeneous electron gas, *Phys. Rev.* **1964**, 136, B864–B871.
- [64] W. Kohn, L. J. Sham, Self-consistent equations including exchange and correlation effects, *Phys. Rev.* **1965**, 140, A1133–A1138.
- [65] D. Rappoport, N. R. M. Crawford, F. Furche, K. Burke, Approximate Density Functionals: Which Should I Choose, in *Computational Inorganic and Bioinorganic Chemistry*, E. I. Solomon, R. B. King, R. A. Scott, eds., Wiley, Chichester **2009**, pp. 159–172.
- [66] C. J. Cramer, D. G. Truhlar, Density functional theory for transition metals and transition metal chemistry, *Phys. Chem. Chem. Phys.* **2009**, 11, 10757–10816.
- [67] F. Neese, Prediction of molecular properties and molecular spectroscopy with density functional theory: From fundamental theory to exchange coupling, *Coord. Chem. Rev.* **2009**, 253, 526–563.
- [68] S. F. Sousa, P. A. Fernandes, M. J. Ramos, General performance of density functionals, *J. Phys. Chem. A* **2007**, 111, 10439–10452.
- [69] L. Goerigk, S. Grimme, A general database for main group thermochemistry, kinetics, and noncovalent interactions - assessment of common and reparameterized (meta-)GGA density functionals, *J. Chem. Theory Comput.* **2010**, 6, 107–126.
- [70] D. M. Ceperley, B. J. Alder, Ground state of the electron-gas by a stochastic method, *Phys. Rev. Lett.* **1980**, 45, 566–569.
- [71] S. H. Vosko, L. Wilk, M. Nusair, Accurate spin-dependent electron liquid correlation energies for local spin density calculations: A critical analysis, *Can. J. Phys.* **1980**, 58, 1200–1211.
- [72] J. P. Perdew, K. Burke, M. Ernzerhof, Generalized gradient approximation made simple, *Phys. Rev. Lett.* **1996**, 77, 3865–3868.
- [73] J. P. Perdew, K. Burke, M. Ernzerhof, Generalized gradient approximation made simple [Phys. Rev. Lett. 77, 3865 (1996)], *Phys. Rev. Lett.* **1997**, 78, 1396.
- [74] P. J. Stephens, F. J. Devlin, C. F. Chabalowski, M. J. Frisch, Ab initio calculation of vibrational absorption and circular-dichroism spectra using density functional force fields, *J. Phys. Chem.* **1996**, 98, 11623–

- 11627.
- [75] A. D. Becke, Density-functional exchange-energy approximation with correct asymptotic behavior, *Phys. Rev. A* **1988**, 38, 3098–3100.
- [76] C. Lee, W. Yang, R. G. Parr, Development of the Colle-Salvetti correlation-energy formula into a functional of the electron density, *Phys. Rev. B* **1988**, 37, 785–789.
- [77] N. W. Ashcroft, N. D. Mermin, *Solid State Physics*, Saunders College Publishing, Philadelphia **1976**.
- [78] V. Heine, The Pseudopotential Concept, in *Solid State Physics*, H. Ehrenreich, F. Seitz, D. Turnbull, eds., vol. 24, Academic Press, New York **1970**, pp. 1–36.
- [79] M. C. Payne, M. P. Teter, D. C. Allan, T. A. Arias, J. D. Joannopoulos, Iterative minimization techniques for *ab initio* total-energy calculations: Molecular dynamics and conjugate gradients, *Rev. Mod. Phys.* **1992**, 64, 1045–1097.
- [80] J. Kohanoff, *Electronic Structure Calculations for Solids and Molecules*, Cambridge University Press, New York **2006**.
- [81] E. J. Maginn, From discovery to data: What must happen for molecular simulation to become a mainstream chemical engineering tool, *AIChE J.* **2009**, 55, 1304–1310.
- [82] A. Loisruangsin, S. Fritzsche, S. Hannongbua, Newly developed *ab initio* fitted potentials for molecular dynamics simulations of *n*-pentane in the zeolite silicalite-1, *Chem. Phys. Lett.* **2004**, 390, 485–490.
- [83] L. Liu, L. Zhao, H. Sun, Simulation of NH₃ temperature programmed desorption curves using an *ab initio* force field, *J. Phys. Chem. C* **2009**, 113, 16051–16057.
- [84] M. Tafipolsky, R. Schmid, Systematic first principles parameterization of force fields for metal-organic frameworks using a genetic algorithm approach, *J. Phys. Chem. B* **2009**, 113, 1341–1352.
- [85] S. Jakobtorweihen, *Molecular simulation of technically relevant molecules in nanoporous materials – carbon nanotubes and zeolites*, Ph.D. thesis, Technische Universität Hamburg-Harburg **2007**.
- [86] M. P. Allen, D. J. Tildesley, *Computer Simulation of Liquids*, Clarendon Press, Oxford **1987**.
- [87] D. Frenkel, B. Smit, *Understanding molecular simulations: From algorithms to applications*, Academic Press, San Diego, 2nd ed. **2002**.
- [88] D. Dubbeldam, R. Q. Snurr, Recent developments in the molecular modeling of diffusion in nanoporous materials, *Mol. Sim.* **2007**, 33, 305–325.
- [89] C. H. Turner, J. K. Brennan, M. Lísal, W. R. Smith, J. K. Johnson, K. E. Gubbins, Simulation of chemical reaction equilibria by the re-

- action ensemble Monte Carlo method: A review, *Mol. Sim.* **2008**, 34, 119–146.
- [90] E. Tylianakis, G. E. Froudakis, Grand canonical Monte Carlo method for gas adsorption and separation, *J. Comput. Theor. Nanosci.* **2009**, 6, 335–348.
- [91] D. Chandler, *Introduction to Modern Statistical Mechanics*, Oxford University Press, New York **1987**.
- [92] W. Göpel, H.-D. Wiemhöfer, *Statistische Thermodynamik*, Spektrum Akademischer Verlag, Heidelberg **2000**.
- [93] L. Verlet, Computer “experiments” on classical fluids. I. Thermodynamic properties of Lennard-Jones molecules, *Phys. Rev.* **1967**, 159, 98–103.
- [94] N. Metropolis, A. W. Rosenbluth, M. N. Rosenbluth, A. H. Teller, E. Teller, Equation of state calculations by fast computing machines, *J. Chem. Phys.* **1953**, 21, 1087–1092.
- [95] M. E. J. Newman, G. T. Barkema, *Monte Carlo Methods in Statistical Physics*, Clarendon Press, Oxford **1999**.
- [96] B. Smit, Grand canonical Monte Carlo simulations of chain molecules: Adsorption isotherms of alkanes in zeolites, *Mol. Phys.* **1995**, 85, 153–172.
- [97] M. D. Macedonia, E. J. Maginn, A biased grand canonical Monte Carlo method for simulating adsorption using all-atom and branched united atom models, *Mol. Phys.* **1999**, 96, 1375–1390.
- [98] D. Dubbeldam, S. Calero, T. J. H. Vlucht, R. Krishna, T. L. M. Maesen, B. Smit, United atom force field for alkanes in nanoporous materials, *J. Phys. Chem. B* **2004**, 108, 12301–12313.
- [99] J. I. Siepmann, D. Frenkel, Configurational bias Monte Carlo: A new sampling scheme for flexible chains, *Mol. Phys.* **1992**, 75, 59–70.
- [100] D. Frenkel, G. Mooij, B. Smit, Novel scheme to study structural and thermal properties of continuously deformable molecules, *J. Phys.: Condens. Mat.* **1992**, 4, 3053–3076.
- [101] M. G. Evans, M. Polanyi, Some applications of the transition state method to the calculation of reaction velocities, especially in solution, *Trans. Faraday Soc.* **1935**, 31, 875–894.
- [102] H. Eyring, The activated complex in chemical reactions, *J. Chem. Phys.* **1935**, 3, 107–115.
- [103] P. Hänggi, P. Talkner, M. Borkovec, Reaction-rate theory: Fifty years after Kramers, *Rev. Mod. Phys.* **1990**, 62, 251–341.
- [104] K. J. Laidler, *Chemical Kinetics*, Harper & Row, New York, 3rd ed. **1987**.
- [105] W. M. H. Sachtler, Metal clusters in zeolites: An intriguing class of

- catalysts, *Acc. Chem. Res.* **1993**, 26, 383–387.
- [106] F. Kapteijn, J. Rodriguez-Mirasol, J. A. Moulijn, Heterogeneous catalytic decomposition of nitrous oxide, *Appl. Catal. B* **1996**, 9, 25–64.
- [107] G. I. Panov, V. I. Sobolev, A. S. Kharitonov, The role of iron in N₂O decomposition on ZSM-5 zeolite and the reactivity of the surface oxygen formed, *J. Mol. Catal.* **1990**, 61, 85–97.
- [108] J. Pérez-Ramírez, F. Kapteijn, G. Mul, X. Xu, J. A. Moulijn, Extraframework FeZSM-5 for control of N₂O in tail-gases, *Catal. Today*. **2002**, 76, 55–74.
- [109] B. R. Wood, J. A. Reimer, A. T. Bell, M. T. Janicke, K. C. Ott, Nitrous oxide decomposition and surface oxygen formation on Fe-ZSM-5, *J. Catal.* **2004**, 224, 148–155.
- [110] G. Berlier, G. Ricchiardi, S. Bordiga, A. Zecchina, Catalytic activity of Fe ions in iron-based crystalline and amorphous systems: Role of dispersion, coordinative unsaturation and Al content, *J. Catal.* **2005**, 229, 127–135.
- [111] J. Pérez-Ramírez, Active iron sites associated with the reaction mechanism of N₂O conversion over steam-activated FeMFI zeolites, *J. Catal.* **2004**, 227, 512–522.
- [112] T. Nobukawa, M. Yoshida, K. Okumura, K. Tomishige, K. Kunimori, Effect of reductants in N₂O reduction over Fe-MFI catalysts, *J. Catal.* **2005**, 229, 374–388.
- [113] F. Kapteijn, G. Marbán, J. Rodriguez-Mirasol, J. A. Moulijn, Kinetic analysis of the decomposition of nitrous oxide over ZSM-5 catalysts, *J. Catal.* **1997**, 167, 256–265.
- [114] C. Sang, B. H. Kim, C. R. F. Lund, Effect of NO upon N₂O decomposition over Fe/ZSM-5 with low iron loading, *J. Phys. Chem. B* **2005**, 109, 2295–2301.
- [115] A. Heyden, B. Peters, A. T. Bell, F. J. Keil, Comprehensive DFT study of nitrous oxide decomposition over Fe-ZSM-5, *J. Phys. Chem. B* **2005**, 109, 1857–1873.
- [116] A. Heyden, A. T. Bell, F. J. Keil, Kinetic modeling of nitrous oxide decomposition on Fe-ZSM-5 based on parameters obtained from first principles calculations, *J. Catal.* **2005**, 233, 26–35.
- [117] D. A. Bulushev, L. Kiwi-Minsker, A. Renken, Dynamics of N₂O decomposition over HZSM-5 with low Fe content, *J. Catal.* **2004**, 222, 389–396.
- [118] K. Sun, H. Xia, E. Hensen, R. A. van Santen, C. Li, Chemistry of N₂O decomposition on active sites with different nature: Effect of high-temperature treatment of Fe/ZSM-5, *J. Catal.* **2006**, 238, 186–195.
- [119] W. M. Heijboer, *New frontiers in X-ray spectroscopy of Fe-ZSM-5*,

- Ph.D. thesis, Utrecht University **2005**.
- [120] A. Heyden, N. Hansen, A. T. Bell, F. J. Keil, Nitrous oxide decomposition over Fe-ZSM-5 in the presence of nitric oxide: A comprehensive DFT study, *J. Phys. Chem. B* **2006**, 110, 17096–17114.
- [121] P. Marturano, L. Drozdová, A. Kogelbauer, R. Prins, Fe/ZSM-5 prepared by sublimation of FeCl₃: The structure of the Fe species as determined by IR, ²⁷Al MAS NMR, and EXAFS spectroscopy, *J. Catal.* **2000**, 192, 236–247.
- [122] A. A. Battiston, J. H. Bitter, F. M. F. de Groot, A. R. Overweg, O. Stephan, J. A. van Bokhoven, P. J. Kooyman, C. van der Spek, G. Vankó, D. C. Koningsberger, Evolution of Fe species during the synthesis of over-exchanged Fe/ZSM5 obtained by chemical vapor deposition of FeCl₃, *J. Catal.* **2003**, 213, 251–271.
- [123] L. Kiwi-Minsker, D. A. Bulushev, A. Renken, Active sites in HZSM-5 with low Fe content for the formation of surface oxygen by decomposing N₂O: Is every deposited oxygen active?, *J. Catal.* **2003**, 219, 273–285.
- [124] G. D. Pirngruber, M. Luechinger, P. K. Roy, A. Cecchetto, P. Smirniotis, N₂O decomposition over iron-containing zeolites prepared by different methods: A comparison of the reaction mechanism, *J. Catal.* **2004**, 224, 429–440.
- [125] K. A. Dubkov, N. S. Ovanesyan, A. A. Shteinman, E. V. Starokon, G. I. Panov, Evolution of iron states and formation of α -sites upon activation of FeZSM-5 zeolites, *J. Catal.* **2002**, 207, 341–352.
- [126] A. A. Battiston, J. H. Bitter, W. M. Heijboer, F. M. F. de Groot, D. C. Koningsberger, Reactivity of Fe-binuclear complexes in over-exchanged Fe/ZSM-5, studied by in situ XAFS spectroscopy. Part 1: Heat treatment in He and O₂, *J. Catal.* **2003**, 215, 279–293.
- [127] H. Y. Chen, W. M. H. Sachtler, Activity and durability of Fe/ZSM-5 catalysts for lean burn NO_x reduction in the presence of water vapor, *Catal. Today* **1998**, 42, 73–83.
- [128] E. El-Malki, R. A. van Santen, W. M. H. Sachtler, Introduction of Zn, Ga, and Fe into HZSM-5 cavities by sublimation: Identification of acid sites, *J. Phys. Chem. B* **1999**, 103, 4611–4622.
- [129] P. Marturano, L. Drozdová, G. D. Pirngruber, A. Kogelbauer, R. Prins, The mechanism of formation of Fe species in Fe/ZSM-5 prepared by CVD, *Phys. Chem. Chem. Phys.* **2001**, 3, 5585–5595.
- [130] G. Čík, M. Hubinová, F. Šeršen, V. Brezová, Study of the influence of water on oxidative properties of Fe³⁺ in ZSM-5 zeolite channels, *Collect. Czech. Chem. Commun.* **2002**, 67, 1743–1759.
- [131] E. V. Starokon, K. A. Dubkov, L. V. Pirutko, G. I. Panov, Mechanisms of iron activation on Fe-containing zeolites and the charge of α -oxygen,

- Top. Catal.* **2003**, *23*, 137–143.
- [132] M. J. Filatov, A. G. Pelmenschikov, G. M. Zhidomirov, On the nature of superactive centers in H-ZSM-5 zeolites: Quantum chemical calculations, *J. Mol. Catal.* **1993**, *80*, 243–251.
- [133] A. V. Arbuznikov, G. M. Zhidomirov, Selective oxidation of methane by dinitrogen monoxide on FeZSM-5 zeolites. Ab initio quantum chemical analysis, *Catal. Lett.* **1996**, *40*, 17–23.
- [134] G. M. Zhidomirov, A. L. Yakovlev, M. A. Milov, N. A. Kachurovskaya, I. V. Yudanov, Molecular models of catalytically active sites in zeolites. Quantum chemical approach, *Catal. Today* **1999**, *51*, 397–410.
- [135] A. L. Yakovlev, G. M. Zhidomirov, R. A. van Santen, DFT calculations on N₂O decomposition by binuclear Fe complexes in Fe/ZSM-5, *J. Phys. Chem. B* **2001**, *105*, 12297–12302.
- [136] D. W. Lewis, C. R. A. Catlow, G. Sankar, S. W. Carr, Structure of iron-substituted ZSM-5, *J. Phys. Chem.* **1995**, *99*, 2377–2383.
- [137] X. Feng, W. K. Hall, Limitations on the formation of oxygen-bridged divalent cations in FeZSM-5, *Catal. Lett.* **1997**, *46*, 11–16.
- [138] M. J. Rice, A. K. Chakraborty, A. T. Bell, Al next nearest neighbor, ring occupation, and proximity statistics in ZSM-5, *J. Catal.* **1999**, *186*, 222–227.
- [139] M. J. Rice, A. K. Chakraborty, A. T. Bell, Site availability and competitive siting of divalent metal cations in ZSM-5, *J. Catal.* **2000**, *194*, 278–285.
- [140] B. R. Goodman, K. C. Hass, W. F. Schneider, J. B. Adams, Statistical analysis of Al distributions and metal ion pairing probabilities in zeolites, *Catal. Lett.* **2000**, *68*, 85–93.
- [141] P. J. O'Malley, J. Dwyer, Ab-initio molecular orbital calculations on the siting of aluminium in the Theta-1 framework: Some general guidelines governing the site preferences of aluminium in zeolites, *Zeolites* **1988**, *8*, 317–321.
- [142] A. E. Alvarado-Swaisgood, M. K. Barr, P. J. Hay, A. Redondo, Ab initio quantum chemical calculations of aluminum substitution in zeolite ZSM-5, *J. Phys. Chem.* **1991**, *95*, 10031–10036.
- [143] A. Redondo, P. J. Hay, Quantum chemical studies of acid sites in zeolite ZSM-5, *J. Phys. Chem.* **1993**, *97*, 11754–11761.
- [144] M. S. Stave, J. B. Nicholas, Density functional studies of zeolites. 2. Structure and acidity of [T]-ZSM-5 models (T=B, Al, Ga, and Fe), *J. Phys. Chem.* **1995**, *99*, 15046–15061.
- [145] O. H. Han, C.-S. Kim, S. B. Hong, Direct evidence for the nonrandom nature of Al substitution in zeolite ZSM-5: An investigation by ²⁷Al MAS and MQ MAS NMR, *Angew. Chem. Int. Ed.* **2002**, *41*, 469–472.

- [146] D. H. Olson, G. T. Koktailo, S. L. Lawton, W. M. Meier, Crystal structure and structure-related properties of ZSM-5, *J. Phys. Chem.* **1981**, 85, 2238–2243.
- [147] J. G. Norman, P. B. Ryan, L. Noodleman, Electronic structure of 2-Fe ferredoxin models by $X\alpha$ valence bond theory, *J. Am. Chem. Soc.* **1980**, 80, 4279–4282.
- [148] L. Noodleman, E. J. Baerends, Electronic structure, magnetic properties, ESR, and optical spectra for 2-Fe ferredoxin models by LCAO- $X\alpha$ valence bond theory, *J. Am. Chem. Soc.* **1984**, 106, 2316–2327.
- [149] L. Noodleman, D. A. Case, Density-functional theory of spin polarization and spin coupling in iron-sulfur clusters, *Adv. Inorg. Chem.* **1992**, 38, 423–470.
- [150] L. Noodleman, C. Y. Peng, D. A. Case, J.-M. Mouesca, Orbital interactions, electron delocalization and spin coupling in iron-sulfur clusters, *Coord. Chem. Rev.* **1995**, 144, 199–244.
- [151] L. Noodleman, Valence bond description of antiferromagnetic coupling in transition metal dimers, *J. Chem. Phys.* **1981**, 74, 5737–5743.
- [152] E. Ruiz, S. Alvarez, J. Cano, V. Polo, About the calculation of exchange coupling constants using density-functional theory: The role of the self-interaction error, *J. Chem. Phys.* **2005**, 123, 164110–1/7.
- [153] E. Ruiz, J. Cano, S. Alvarez, P. Alemany, Broken symmetry approach to calculation of exchange coupling constants for homobinuclear and heterobinuclear transition metal complexes, *J. Comput. Chem.* **1999**, 20, 1391–1400.
- [154] K. Yoshizawa, A. Suzuki, Y. Shiota, T. Yamabe, Conversion of methane to methanol on diiron and dicopper enzyme models of methane monooxygenase: A theoretical study on a concerted reaction pathway, *Bull. Chem. Soc. Jpn.* **2000**, 73, 815–827.
- [155] M. Torrent, D. Musaev, H. Basch, K. Morokuma, Computational studies of reaction mechanisms of methane monooxygenase and ribonucleotide reductase, *J. Comput. Chem.* **2002**, 23, 59–76.
- [156] O. Treutler, R. Ahlrichs, Efficient molecular numerical integration schemes, *J. Chem. Phys.* **1995**, 102, 346–354.
- [157] S. A. Zygmunt, R. M. Mueller, L. A. Curtiss, L. E. Eton, An assessment of density functional methods for studying molecular adsorption in cluster models of zeolites, *J. Mol. Struct. (Theochem)* **1998**, 430, 9–16.
- [158] K. Yoshizawa, Y. Shiota, T. Yamabe, Intrinsic reaction coordinate analysis of the conversion of methane to methanol by an iron oxo species: A study of crossing seams of potential energy surfaces, *J. Chem. Phys.* **1999**, 111, 538–545.

- [159] I. Zilberberg, R. W. Gora, G. M. Zhidomirov, J. Leszczynski, Bonding in the oxo ferrous iron species: A complete active-space self-consistent-field theory verification of the molecular-oxygen-like pattern, *J. Chem. Phys.* **2002**, 117, 7153–7161.
- [160] F. Furche, J. P. Perdew, The performance of semilocal and hybrid density functionals in 3d transition-metal chemistry, *J. Chem. Phys.* **2006**, 124, 044103–1/27.
- [161] A. Schäfer, C. Huber, R. Ahlrichs, Fully optimized contracted Gaussian basis sets of triple zeta valence quality for atoms Li to Kr, *J. Chem. Phys.* **1994**, 100, 5829–5835.
- [162] R. Ahlrichs, M. Bär, M. Häser, H. Horn, C. Kölmel, Electronic structure calculations on workstation computers: The program system turbomole, *Chem. Phys. Lett.* **1989**, 162, 165–169.
- [163] B. F. Ghermann, M.-H. Baik, S. J. Lippard, R. A. Friesner, Dioxygen activation in methane monooxygenase: A theoretical study, *J. Am. Chem. Soc.* **2004**, 126, 2978–2990.
- [164] B. Peters, A. Heyden, A. T. Bell, A. Chakraborty, A growing string method for determining transition states: Comparison to the nudged elastic band and string methods, *J. Chem. Phys.* **2004**, 120, 7877–7886.
- [165] A. Heyden, A. T. Bell, F. J. Keil, Efficient methods for finding transition states in chemical reactions: Comparison of improved dimer method and partitioned rational function optimization method, *J. Chem. Phys.* **2005**, 123, 224101–1/14.
- [166] S. H. Choi, B. R. Wood, J. A. Ryder, A. T. Bell, X-ray absorption fine structure characterization of the local structure of Fe in Fe-ZSM-5, *J. Phys. Chem. B* **2003**, 107, 11843–11851.
- [167] S. H. Choi, B. R. Wood, A. T. Bell, M. T. Janicke, K. C. Ott, X-ray absorption fine structure analysis of the local environment of Fe in Fe/Al-MFI, *J. Phys. Chem. B* **2004**, 108, 8970–8975.
- [168] K. Krishna, M. Makkee, Preparation and pretreatment influence on iron species distribution and N₂O decomposition in Fe-ZSM-5, *Catal. Lett.* **2006**, 106, 183–193.
- [169] J. C. Slater, The self-consistent field for molecules and solids, in *Quantum theory of molecules and solids, International series in pure and applied physics*, vol. 4, McGraw-Hill, New York **1974**.
- [170] J. P. Perdew, Y. Wang, Accurate and simple analytic representation of the electron gas correlation energy, *Phys. Rev. B* **1992**, 45, 13244–13249.
- [171] L. Kiwi-Minsker, D. A. Bulushev, A. Renken, Low temperature decomposition of nitrous oxide over Fe/ZSM-5: Modelling of the dynamic

- behaviour, *Catal. Today* **2005**, 110, 191–198.
- [172] D. M. Kurtz, Oxo- and hydroxo-bridged diiron complexes: A chemical perspective on a biological unit, *Chem. Rev.* **1990**, 90, 585–606.
- [173] R. M. Cornell, U. Schwertmann, *The iron oxides: Structure, Properties, Reactions, Occurrence and Uses*, VCH, Weinheim, Germany **1996**.
- [174] D. J. Wuebbles, A. Jain, J. Edmonds, D. Harvey, K. Hayhoe, Global change: State of the science, *Environ. Pollution* **1999**, 100, 57–86.
- [175] G. C. Rhoderick, W. D. Dorko, Standards development of global warming gas species: Methane, nitrous oxide, trichlorofluoromethane, and dichlorodifluoromethane, *Environ. Sci. Technol.* **2004**, 38, 2685–2692.
- [176] Y. Li, J. N. Armor, Catalytic decomposition of nitrous oxide on metal exchanged zeolites, *Appl. Catal. B* **1992**, 1, L21–L29.
- [177] J. Pérez-Ramírez, F. Kapteijn, K. Schöffel, J. A. Moulijn, Formation and control of N₂O in nitric acid production. Where do we stand today?, *Appl. Catal. B* **2003**, 44, 117–151.
- [178] T. V. Voskoboinikov, H.-Y. Chen, W. M. H. Sachtler, On the nature of active sites in Fe/ZSM-5 catalysts for NO_x abatement, *Appl. Catal. B* **1998**, 19, 279–287.
- [179] Q. Zhu, B. L. Mojet, R. A. J. Janssen, E. J. M. Hensen, J. van Grondelle, P. C. M. M. Magusin, R. A. van Santen, N₂O decomposition over Fe/ZSM-5: Effect of high-temperature calcination and steaming, *Catal. Lett.* **2002**, 81, 205–212.
- [180] J. Pérez-Ramírez, F. Kapteijn, J. C. Groen, A. Doménech, G. Mul, J. A. Moulijn, Steam-activated FeMFI zeolites. Evolution of iron species and activity in direct N₂O decomposition, *J. Catal.* **2003**, 214, 33–45.
- [181] P. K. Roy, G. D. Pirngruber, The surface chemistry of N₂O decomposition on iron-containing zeolites(II)—the effect of high-temperature pretreatments, *J. Catal.* **2004**, 227, 164–174.
- [182] T. Nobukawa, M. Yoshida, S. Kameoka, S. Ito, K. Tomishige, K. Kunimori, Selective catalytic reduction of N₂O with CH₄ and N₂O decomposition over Fe-zeolite catalysts, *Stud. Surf. Sci. Catal.* **2004**, 154, 2514–2521.
- [183] L. Kiwi-Minsker, D. A. Bulushev, A. Renken, Transient response method for characterization of active sites in HZSM-5 with low content of iron during N₂O decomposition, *Catal. Today* **2004**, 91–92, 165–170.
- [184] J. B. Taboada, A. R. Overweg, P. J. Kooyman, I. W. C. E. Arends, G. Mul, Following the evolution of iron from framework to extra-framework positions in isomorphously substituted [Fe,Al]MFI with ⁵⁷Fe Mössbauer spectroscopy, *J. Catal.* **2005**, 231, 56–66.
- [185] T. Turek, Kinetic oscillations during the catalytic decomposition of

- nitrous oxide, *Catal. Today* **2005**, 105, 275–282.
- [186] G. D. Pirngruber, J.-D. Grunwaldt, P. K. Roy, J. A. van Bokhoven, O. Safonova, P. Glatzel, The nature of the active site in the Fe-ZSM-5/N₂O system studied by (resonant) inelastic X-ray scattering, *Catal. Today* **2007**, 126, 127–134.
- [187] G. D. Pirngruber, P. K. Roy, R. Prins, On determining the nuclearity of iron sites in Fe-ZSM-5—a critical evaluation, *Phys. Chem. Chem. Phys.* **2006**, 3939–3950.
- [188] W. M. Heijboer, D. C. Koningsberger, B. M. Weckhuysen, F. M. F. de Groot, New frontiers in X-ray spectroscopy in heterogeneous catalysis: Using Fe/ZSM-5 as test-system, *Catal. Today* **2005**, 110, 228–238.
- [189] L. Čapek, V. Kreibich, J. Dědeček, T. Grygar, B. Wichterlová, Z. Sobalik, J. A. Martens, R. Brosius, V. Tokarová, Analysis of Fe species in zeolites by UV-VIS-NIR, IR spectra and voltammetry. Effect of preparation, Fe loading and zeolite type, *Microporous Mesoporous Mater.* **2005**, 80, 279–289.
- [190] S. Brandenberger, O. Kröcher, A. Tissler, R. Althoff, Estimation of the fractions of different nuclear iron species in uniformly metal-exchanged Fe-ZSM-5 samples based on a Poisson distribution, *Appl. Catal. A* **2010**, 373, 168–175.
- [191] L. J. Broadbelt, R. Q. Snurr, Applications of molecular modeling in heterogeneous catalysis research, *Appl. Catal. A* **2000**, 200, 23–46.
- [192] N. Hansen, A. Heyden, A. T. Bell, F. J. Keil, A reaction mechanism for the nitrous oxide decomposition on binuclear oxygen bridged iron sites in Fe-ZSM-5, *J. Phys. Chem. C* **2007**, 111, 2092–2101.
- [193] D. A. McQuarrie, *Statistical Mechanics*, Harper Collins, New York **1973**.
- [194] D. Danovich, S. Shaik, Spin–orbit coupling in the oxidative activation of H–H by FeO⁺. Selection rules and reactivity effects, *J. Am. Chem. Soc.* **1997**, 119, 1773–1786.
- [195] S. M. Rump, *Kleine Fehlerschranken bei Matrixproblemen*, Ph.D. thesis, Universität Karlsruhe **1980**.
- [196] S. M. Rump, Solving algebraic problems with high accuracy, in *A new approach to scientific computation*, Academic Press, New York **1983**, p. 51.
- [197] Numerical Algorithms Group Fortran Library, Mark 19, NAG GmbH, Garching, Routine: F07AEF.
- [198] R. Dittmeyer, G. Emig, Simultaneous Heat and Mass Transfer and Chemical Reaction, in *Handbook of heterogeneous Catalysis*, G. Ertl, H. Knözinger, F. Schüth, J. Weitkamp, eds., vol. 3, Wiley-VCH, 2nd

- ed. **2008**, p. 1727.
- [199] Y. Zhao, N. González-García, D. G. Truhlar, Benchmark database of barrier heights for heavy atom transfer, nucleophilic substitution, association, and unimolecular reactions and its use to test theoretical methods, *J. Phys. Chem. A* **2005**, 109, 2012–2018.
- [200] E. V. Kondratenko, J. Pérez-Ramírez, Mechanism and kinetics of direct N₂O decomposition over Fe-MFI zeolites with different iron speciation from temporal analysis of products, *J. Phys. Chem. B* **2006**, 110, 22586–22595.
- [201] J. A. Moulijn, M. Makkee, A. van Diepen, *Chemical Process Technology*, Wiley, Chichester **2001**.
- [202] T. F. Degnan, C. Morris Smith, C. R. Venkat, Alkylation of aromatics with ethylene and propylene: Recent developments in commercial processes, *Appl. Catal. A* **2001**, 221, 283–294.
- [203] M. Hartmann, Hierarchical zeolites: A proven strategy to combine shape selectivity with efficient mass transport, *Angew. Chem. Int. Ed.* **2004**, 43, 5880–5882.
- [204] C. Perego, P. Ingallina, Recent advances in the industrial alkylation of aromatics: New catalysts and new processes, *Catal. Today* **2002**, 73, 3–22.
- [205] N. Y. Chen, W. E. Garwood, Industrial application of shape-selectivity catalysis, *Catal. Rev.-Sci. Eng.* **1986**, 28, 185–264.
- [206] A. Corma, Inorganic solid acids and their use in acid-catalyzed hydrocarbon reactions, *Chem. Rev.* **1995**, 95, 559–614.
- [207] J. Čejka, B. Wichterlová, Acid-catalyzed synthesis of mono- and dialkyl benzenes over zeolites: Active sites, zeolite topology, and reaction mechanisms, *Catal. Rev.* **2002**, 44, 375–421.
- [208] A. Corma, State of the art and future challenges of zeolites as catalysts, *J. Catal.* **2003**, 216, 298–312.
- [209] M. Bejblová, N. Žilková, J. Čejka, Transformations of aromatic hydrocarbons over zeolites, *Res. Chem. Intermed.* **2008**, 34, 439–454.
- [210] F. G. Dwyer, P. J. Lewis, F. H. Schneider, Efficient, nonpolluting ethylbenzene process, *Chem. Eng.* **1976**, 83, 90–91.
- [211] W. O. Haag, D. H. Olson, P. B. Weisz, Shape-selective catalysis in aromatics processing, in *Chemistry for the Future*, H. Grünwald, ed., Proceedings of the 29th IUPAC Congress, Pergamon Press, Oxford **1984**, p. 327.
- [212] G. Caeiro, R. H. Carvalho, X. Wang, M. A. N. D. A. Lemos, F. Lemos, M. Guisnet, F. Ramôa Ribeiro, Activation of C₂–C₄ alkanes over acid and bifunctional zeolite catalysts, *J. Mol. Catal. A* **2006**, 255, 131–158.

- [213] A. P. Bolton, Hydrocracking, isomerization, and other industrial processes, in *Zeolite Chemistry and Catalysis*, J. A. Rabo, ed., *ACS Monograph*, vol. 171, American Chemical Society, Washington DC **1976**, pp. 714–779.
- [214] P. G. Smirniotis, E. Ruckenstein, Alkylation of benzene or toluene with MeOH or C₂H₄ over ZSM-5 or β zeolite: Effect of the zeolite pore openings and of the hydrocarbons involved on the mechanism of alkylation, *Ind. Eng. Chem. Res.* **1995**, *34*, 1517–1528.
- [215] H. You, W. Long, Y. Pan, The mechanism and kinetics for the alkylation of benzene with ethylene, *Petroleum Sci. Technol.* **2006**, *24*, 1079–1088.
- [216] Y. Huang, E. A. Havenga, Probing the locations of benzene molecules inside completely siliceous ZSM-5 by FT-Raman spectroscopy, *J. Phys. Chem. B* **2000**, *104*, 5084–5089.
- [217] R. Goyal, A. N. Fitch, H. Jovic, Powder neutron and X-ray diffraction studies of benzene adsorbed in zeolite ZSM-5, *J. Phys. Chem. B* **2000**, *104*, 2878–2884.
- [218] Y. Huang, E. A. Havenga, A fourier transform-Raman investigation of the host-guest interactions of p-chlorotoluene, toluene, and chlorobenzene sorbed on completely siliceous ZSM-5, *Chem. Mater.* **2001**, *13*, 738–746.
- [219] N. Floquet, J. P. Coulomb, G. Weber, O. Bertrand, J. P. Bellat, Structural signatures of type IV isotherm steps: Sorption of trichloroethene, tetrachloroethene, and benzene in silicalite-I, *J. Phys. Chem. B* **2003**, *107*, 685–693.
- [220] L. Song, Z. L. Sun, H. Y. Ban, M. Dai, L. V. C. Rees, Benzene adsorption in microporous materials, *Adsorption* **2005**, *11*, 325–339.
- [221] A. Corma, V. Martínez-Soria, E. Schnoefeld, Alkylation of benzene with short-chain olefins over MCM-22 zeolite: Catalytic behaviour and kinetic mechanism, *J. Catal.* **2000**, *192*, 163–173.
- [222] A. M. Vos, R. A. Schoonheydt, F. De Proft, P. Geerlings, Reactivity descriptors and rate constants for acid zeolite catalyzed ethylation and isopropylation of benzene, *J. Phys. Chem. B* **2003**, *107*, 2001–2008.
- [223] B. Arstad, S. Kolboe, O. Swang, Theoretical investigation of arene alkylation by ethene and propene over acidic zeolites, *J. Phys. Chem. B* **2004**, *108*, 2300–2308.
- [224] S. Namuangruk, P. Pantu, J. Limtrakul, Alkylation of benzene with ethylene over faujasite zeolite investigated by the ONIOM method, *J. Catal.* **2004**, *225*, 523–530.
- [225] S. Humbel, S. Sieber, K. Morokuma, The IMOMO method: Integration of different levels of molecular orbital approximations for geometry

- optimization of large systems: Test for *n*-butane conformation and S_N2 reaction: $RCl+Cl^-$, *J. Chem. Phys.* **1996**, 105, 1959–1967.
- [226] W. Panjan, J. Limtrakul, The influence of the framework on adsorption properties of ethylene/H-ZSM-5 system: An ONIOM study, *J. Molec. Struc.* **2003**, 654, 35–45.
- [227] C. Raksakoon, J. Limtrakul, Adsorption of aromatic hydrocarbon onto H-ZSM-5 zeolite investigated by ONIOM study, *J. Molec. Struc. (Theochem)* **2003**, 631, 147–156.
- [228] S. Kasuriya, S. Namuangruk, P. Treesukol, M. Tirtowidjojo, J. Limtrakul, Adsorption of ethylene, benzene, and ethylbenzene over faujasite zeolites investigated by the ONIOM method, *J. Catal.* **2003**, 219, 320–328.
- [229] D. H. Olson, N. Khosrovani, A. W. Peters, B. H. Toby, Crystal structure of dehydrated CsZSM-5 (5.8Al): Evidence for nonrandom aluminum distribution, *J. Phys. Chem. B* **2000**, 104, 4844–4848.
- [230] J. Dědeček, D. Kaucký, B. Wichterlová, Al distribution in ZSM-5 zeolites: An experimental study, *Chem. Commun.* **2001**, 970–971.
- [231] S. Sklenak, J. Dědeček, C. Li, B. Wichterlová, V. Gábová, M. Sierka, J. Sauer, Aluminum siting in silicon-rich zeolite frameworks: A combined high-resolution ^{27}Al NMR spectroscopy and quantum mechanics/molecular mechanics study of ZSM-5, *Angew. Chem. Int. Ed.* **2007**, 46, 7286–7289.
- [232] S. Sklenak, J. Dědeček, C. Li, B. Wichterlová, V. Gábová, M. Sierka, J. Sauer, Aluminium siting in the ZSM-5 framework by combination of high resolution ^{27}Al NMR and DFT/MM calculations, *Phys. Chem. Chem. Phys.* **2009**, 11, 1237–1247.
- [233] B. F. Mentzen, M. Sacerdote-Peronnet, Prediction of preferred proton locations in HMFI/benzene complexes by molecular mechanics calculations. Comparison with NMR, structural and calorimetric results, *Mat. Res. Bull.* **1994**, 29, 1341–1348.
- [234] G. Barone, G. Casella, S. Giuffrida, D. Duca, H-ZSM-5 modified zeolite: Quantum chemical models of acidic sites, *J. Phys. Chem. C* **2007**, 111, 13033–13043.
- [235] M. Brändle, J. Sauer, Acidity differences between inorganic solids induced by their framework structure. A combined quantum mechanics/molecular mechanics ab initio study on zeolites, *J. Am. Chem. Soc.* **1998**, 120, 1556–1570.
- [236] S. A. Zygmunt, L. A. Curtiss, P. Zapol, L. E. Iton, Ab initio and density functional study of the activation barrier for ethane cracking in cluster models of zeolite H-ZSM-5, *J. Phys. Chem. B* **2000**, 104, 1944–1949.
- [237] J. A. Ryder, A. K. Chakraborty, A. T. Bell, Density functional theory

- study of proton mobility in zeolites: Proton migration and hydrogen exchange in ZSM-5, *J. Phys. Chem. B* **2000**, 104, 6998–7011.
- [238] C. Tuma, J. Sauer, Treating dispersion effects in extended systems by hybrid MP2:DFT calculations —protonation of isobutene in zeolite ferrierite, *Phys. Chem. Chem. Phys.* **2006**, 8, 3955–3965.
- [239] J. B. Nicholas, Density functional theory studies of zeolite structure, acidity, and reactivity, *Top. Catal.* **1997**, 4, 157–171.
- [240] M. V. Frash, V. B. Kazansky, A. M. Rigby, R. A. van Santen, Cracking of hydrocarbons on zeolite catalysts: Density functional and Hartree–Fock calculations on the mechanism of the β -scission reaction, *J. Phys. Chem. B* **1998**, 102, 2232–2238.
- [241] E. A. Furtado, I. Milas, J. O. M. A. Lins, M. A. C. Nascimento, The dehydrogenation reaction of light alkanes catalyzed by zeolites, *phys. stat. sol. (a)* **2001**, 187, 275–288.
- [242] E. A. Pidko, V. B. Kazansky, E. J. M. Hensen, R. A. van Santen, A comprehensive density functional theory study of ethane dehydrogenation over reduced extra-framework gallium species in ZSM-5 zeolite, *J. Catal.* **2006**, 240, 73–84.
- [243] M. S. Pereira, M. A. C. Nascimento, Theoretical study on the dehydrogenation reaction of alkanes catalyzed by zeolites containing non-framework gallium species, *J. Phys. Chem. B* **2006**, 110, 3231–3238.
- [244] A. Schäfer, H. Horn, R. Ahlrichs, Fully optimized contracted Gaussian basis sets for atoms Li to Kr, *J. Chem. Phys.* **1992**, 97, 2571–2577.
- [245] J. Baker, An algorithm for the location of transition states, *J. Comp. Chem.* **1986**, 7, 385–395.
- [246] B. J. Lynch, D. G. Truhlar, How well can hybrid density functional methods predict transition state geometries and barrier heights?, *J. Phys. Chem. A* **2001**, 105, 2936–2941.
- [247] T. H. Dunning, Gaussian basis sets for use in correlated molecular calculations. I. The atoms boron through neon and hydrogen, *J. Chem. Phys.* **1989**, 90, 1007–1023.
- [248] C. Hättig, Geometry optimizations with the coupled-cluster model CC2 using the resolution-of-the-identity approximation, *J. Chem. Phys.* **2003**, 118, 7751–7761.
- [249] C. Hättig, A. Hellweg, A. Köhn, Distributed memory parallel implementation of energies and gradients for second-order Møller-Plesset perturbation theory with the resolution-of-the-identity approximation, *Phys. Chem. Chem. Phys.* **2006**, 8, 1159–1169.
- [250] O. Vahtras, J. Almlöf, M. W. Feyereisen, Integral approximations for LCAO-SCF calculations, *Chem. Phys. Lett.* **1993**, 213, 514–518.
- [251] J. L. Whitten, Coulombic potential energy integrals and approxima-

- tions, *J. Chem. Phys.* **1973**, 58, 4496–4500.
- [252] E. J. Baerends, D. E. Ellis, P. Ros, Self-consistent molecular Hartree-Fock-Slater calculations I. The computational procedure, *Chem. Phys.* **1973**, 2, 41–51.
- [253] B. I. Dunlap, J. W. D. Connolly, J. R. Sabin, On first-row diatomic molecules and local density models, *J. Chem. Phys.* **1979**, 71, 4993–4999.
- [254] C. van Alsenoy, Ab initio calculations on large molecules: The multiplicative integral approximation, *J. Comput. Chem.* **1988**, 9, 620–626.
- [255] F. Weigend, M. Häser, H. Patzelt, R. Ahlrichs, RI-MP2: Optimized auxiliary basis sets and demonstration of efficiency, *Chem. Phys. Lett.* **1998**, 294, 143–152.
- [256] F. Weigend, A. Köhn, C. Hättig, Efficient use of the correlation consistent basis sets in resolution of the identity MP2 calculations, *J. Chem. Phys.* **2002**, 116, 3175–3183.
- [257] C. Tuma, J. Sauer, A hybrid MP2/planewave-DFT scheme for large chemical systems: Proton jumps in zeolites, *Chem. Phys. Lett.* **2004**, 387, 388–394.
- [258] S. Svelle, C. Tuma, X. Rozanska, T. Kerber, J. Sauer, Quantum chemical modeling of zeolite-catalyzed methylation reactions: Toward chemical accuracy for barriers, *J. Am. Chem. Soc.* **2009**, 131, 816–825.
- [259] I. Milas, M. A. C. Nascimento, A density functional study on the effect of the zeolite cavity on its catalytic activity: The dehydrogenation and cracking reactions of isobutane over HZSM-5 and HY zeolites, *Chem. Phys. Lett.* **2006**, 418, 368–372.
- [260] M. Boronat, C. M. Zicovich-Wilson, P. Viruela, A. Corma, Cluster and periodic calculations of the ethene protonation reaction catalyzed by theta-1 zeolite: Influence of method, model size, and structural constraints, *Chem. Eur. J.* **2001**, 7, 1295–1303.
- [261] J. Sauer, M. Sierka, F. Haase, Acidic Catalysis by Zeolites: Ab Initio Modeling of Transition Structures, in *Transition State Modeling for Catalysis*, D. G. Truhlar, K. Morokuma, eds., ACS Symp. Ser. No. 721, American Chemical Society, Washington DC **1999**, pp. 358–367.
- [262] N. W. Cant, W. K. Hall, Studies of the hydrogen held by solids, *J. Catal.* **1972**, 25, 161–172.
- [263] A. Jentys, R. R. Mukti, H. Tanaka, J. A. Lercher, Energetic and entropic contributions controlling the sorption of benzene in zeolites, *Microporous Mesoporous Mater.* **2006**, 90, 284–292.
- [264] H. Thamm, Calorimetric study on the state of aromatic molecules sorbed on silicalite, *J. Phys. Chem.* **1987**, 91, 8–11.
- [265] W. Nießen, H. G. Karge, L. Jozefowicz, Thermodynamic and kinetics

- data of sorption in zeolites determined by FTIR, *Stud. Surf. Sci. Catal.* **1993**, 80, 475–481.
- [266] H. Thamm, H.-G. Jerschke, H. Stach, Calorimetric study on the state of benzene and cyclopentane sorbed on H-ZSM-5 with different Si/Al ratios, *Zeolites* **1988**, 8, 151–153.
- [267] M. Boronat, C. M. Zicovich-Wilson, P. Viruela, A. Corma, Influence of the local geometry of zeolite active sites and olefin size on the stability of alkoxide intermediates, *J. Phys. Chem. B* **2001**, 105, 11169–11177.
- [268] V. Nieminen, M. Sierka, D. Y. Murzin, J. Sauer, Stabilities of C₃–C₅ alkoxide species inside H-FER zeolite: A hybrid QM/MM study, *J. Catal.* **2005**, 231, 393–404.
- [269] R. J. Gorte, D. White, Interactions of chemical species with acid sites in zeolites, *Top. Catal.* **1997**, 4, 57–69.
- [270] T. J. G. Kofke, R. J. Gorte, A temperature-programmed desorption study of olefin oligomerization in H-ZSM-5, *J. Catal.* **1989**, 115, 233–243.
- [271] P. Sarv, T. Tuherm, E. Lippmaa, K. Keskinen, A. Root, Mobility of the acidic proton in Brønsted sites of H-Y, H-mordenite, and H-ZSM-5 zeolites, studied by high-temperature H MAS NMR, *J. Phys. Chem.* **1995**, 99, 13763–13768.
- [272] J. F. Haw, Zeolite acid strength and reaction mechanisms in catalysis, *Phys. Chem. Chem. Phys.* **2002**, 4, 5431–5441.
- [273] A. Simperler, R. G. Bell, M. D. Foster, A. E. Gray, D. W. Lewis, M. W. Anderson, Probing the acid strength of Brønsted acidic zeolites with acetonitrile: An atomistic and quantum chemical study, *J. Phys. Chem. B* **2004**, 108, 7152–7160.
- [274] B. Xu, C. Sievers, S. B. Hong, R. Prins, J. A. van Bokhoven, Catalytic activity of Brønsted acid sites in zeolites: Intrinsic activity, rate-limiting step, and influence of the local structure of the acid sites, *J. Catal.* **2006**, 244, 163–168.
- [275] K. Suzuki, T. Noda, N. Katada, M. Niwa, IRMS-TPD of ammonia: Direct and individual measurement of Brønsted acidity in zeolites and its relationship with the catalytic cracking activity, *J. Catal.* **2007**, 250, 151–160.
- [276] C. H. Christensen, K. Johannsen, I. Schmidt, C. H. Christensen, Catalytic benzene alkylation over mesoporous zeolite single crystals: Improving activity and selectivity with a new family of porous materials, *J. Am. Chem. Soc.* **2003**, 125, 13370–13371.
- [277] K. A. Becker, H. G. Karge, W. D. Streubel, Benzene alkylation with ethylene and propylene over H-mordenite as catalyst, *J. Catal.* **1973**, 28, 403–413.

- [278] M. Boronat, A. Corma, Are carbenium and carbonium ions reaction intermediates in zeolite-catalyzed reactions?, *Appl. Catal. A* **2008**, 336, 2–10.
- [279] V. B. Kazansky, M. V. Frash, R. A. van Santen, Quantum chemical study of the isobutane cracking on zeolites, *Appl. Catal. A* **1996**, 146, 225–247.
- [280] A. M. Rigby, G. J. Kramer, R. A. van Santen, Mechanisms of hydrocarbon conversion in zeolites: A quantum mechanical study, *J. Catal.* **1997**, 170, 1–10.
- [281] T. Demuth, P. Raybaud, S. Lacombe, H. Toulhoat, Effects of zeolite pore sizes on the mechanism and selectivity of xylene disproportionation—a DFT study, *J. Catal.* **2004**, 222, 323–337.
- [282] L. A. Clark, M. Sierka, J. Sauer, Stable mechanistically-relevant aromatic-based carbenium ions in zeolite catalysts, *J. Am. Chem. Soc.* **2003**, 125, 2136–2141.
- [283] M. Bjørgen, F. Bonino, S. Kolboe, K.-P. Lillerud, A. Zecchina, S. Bordiga, Spectroscopic evidence for a persistent benzenium cation in zeolite H-beta, *J. Am. Chem. Soc.* **2003**, 125, 15863–15868.
- [284] J. Weitkamp, Alkylation of hydrocarbons with zeolite catalysts - commercial applications and mechanistic aspects, *Acta Phys. et Chem.* **1985**, 31, 271–290.
- [285] C. H. Christensen, K. Johannsen, E. Törnquist, I. Schmidt, H. Topsøe, C. H. Christensen, Mesoporous zeolite single crystal catalysts: Diffusion and catalysis in hierarchical zeolites, *Catal. Today* **2007**, 128, 117–122.
- [286] D. B. Lukyanov, T. Vazhnova, Highly selective and stable alkylation of benzene with ethane into ethylbenzene over bifunctional PtH-MFI catalysts, *J. Mol. Catal. A* **2008**, 279, 128–132.
- [287] D. B. Lukyanov, T. Vazhnova, A kinetic study of benzene alkylation with ethane into ethylbenzene over bifunctional PtH-MFI catalyst, *J. Catal.* **2008**, 257, 382–389.
- [288] D. Theodorou, J. Wei, Diffusion and reaction in blocked and high occupancy zeolite catalysts, *J. Catal.* **1983**, 83, 205–224.
- [289] B. Frank, K. Dahlke, G. Emig, E. Aust, R. Broucek, M. Nywlt, A Monte-Carlo simulation of diffusion and reaction in zeolites, *Microporous Mater.* **1993**, 1, 43–56.
- [290] J. Hinderer, F. J. Keil, Three-dimensional Monte Carlo calculations of diffusion and reaction phenomena in zeolites, *Chem. Eng. Sci.* **1996**, 51, 2667–2672.
- [291] B. L. Trout, A. K. Chakraborty, A. T. Bell, Diffusion and reaction in ZSM-5 studied by dynamic Monte Carlo, *Chem. Eng. Sci.* **1997**, 52,

- 2265–2276.
- [292] P. Stoltze, Microkinetic simulation of catalytic reactions, *Prog. Surf. Sci.* **2000**, 65, 65–150.
- [293] F. J. Keil, M.-O. Coppens, Dynamic Monte Carlo simulations of diffusion and reaction in zeolites, in *Computer modelling of microporous materials*, C. R. A. Catlow, R. A. van Santen, B. Smit, eds., Elsevier, London **2004**, pp. 109–127.
- [294] R. Krishna, J. M. van Baten, Insights into diffusion of gases in zeolites gained from molecular dynamics simulations, *Microporous Mesoporous Mater.* **2008**, 109, 91–108.
- [295] R. Krishna, J. M. van Baten, Onsager coefficients for binary mixture diffusion in nanopores, *Chem. Eng. Sci.* **2008**, 63, 3120–3140.
- [296] R. Krishna, D. Paschek, Verification of the Maxwell-Stefan theory for diffusion of three-component mixtures in zeolites, *Chem. Eng. J.* **2002**, 87, 1–9.
- [297] R. Krishna, R. Baur, Modelling issues in zeolite based separation processes, *Sep. Purif. Technol.* **2003**, 33, 213–254.
- [298] R. Krishna, J. M. van Baten, Diffusion of alkane mixtures in zeolites: Validating the Maxwell-Stefan formulation using MD simulations, *J. Phys. Chem. B* **2005**, 109, 6386–6396.
- [299] V. Iyengar, M.-O. Coppens, Dynamic Monte-Carlo simulations of binary self-diffusion in zeolites: Effect of strong adsorption sites, *Chem. Eng. Sci.* **2004**, 59, 4747–4753.
- [300] M.-O. Coppens, V. Iyengar, Testing the consistency of the Maxwell-Stefan formulation when predicting self-diffusion in zeolites with strong adsorption sites, *Nanotechnology* **2005**, 16, S442–S448.
- [301] E. W. Thiele, Relation between catalytic activity and size of particle, *Ind. Eng. Chem.* **1939**, 31, 916–920.
- [302] F. Jüttner, Reaktionskinetik und Diffusion, *Z. phys. Chem.* **1909**, 65, 595–623.
- [303] R. Baur, R. Krishna, Effectiveness factor for zeolite catalysed isomerization reactions, *Chem. Eng. J.* **2004**, 99, 105–116.
- [304] R. Baur, R. Krishna, The effectiveness factor for zeolite catalysed reactions, *Catal. Today* **2005**, 105, 173–179.
- [305] R. Krishna, R. Baur, On the Langmuir–Hinshelwood formulation for zeolite catalysed reactions, *Chem. Eng. Sci.* **2005**, 60, 1155–1166.
- [306] A. L. Myers, J. M. Prausnitz, Thermodynamics of mixed gas adsorption, *AIChE J.* **1965**, 11, 121–127.
- [307] M. Köstner, E. Klemm, G. Emig, Multicomponent diffusion and sorption analysis of the direct hydroxylation of methyl-aromatics on zeolites, *Stud. Surf. Sci. Catal.* **2004**, 154, 2096–2103.

- [308] R. Aris, *The Mathematical Theory of Diffusion and Reaction in Permeable Catalysts*, Clarendon Press, Oxford **1975**.
- [309] R. Krishna, D. Paschek, R. Baur, Modeling the occupancy dependence of diffusivities in zeolites, *Microporous Mesoporous Mater.* **2004**, 76, 233–246.
- [310] R. Krishna, J. M. van Baten, E. Garcia-Perez, S. Calero, Incorporating the loading dependence of the Maxwell–Stefan diffusivity in the modeling of CH₄ and CO₂ permeation across zeolites membranes, *Ind. Eng. Chem. Res.* **2007**, 46, 2974–2986.
- [311] A. I. Skoulidas, D. S. Sholl, R. Krishna, Correlation effects in diffusion of CH₄/CF₄ mixtures in MFI zeolite. A study linking MD simulations with the Maxwell–Stefan formulation, *Langmuir* **2003**, 19, 7977–7988.
- [312] R. Krishna, J. M. van Baten, D. Dubbeldam, On the inflection in the concentration dependence of the Maxwell–Stefan diffusivity of CF₄ in MFI zeolite, *J. Phys. Chem. B* **2004**, 108, 14820–14822.
- [313] T. J. H. Vlugt, R. Krishna, B. Smit, Molecular simulations of adsorption isotherms for linear and branched alkanes and their mixtures in silicalite, *J. Phys. Chem. B* **1999**, 103, 1102–1118.
- [314] D. Paschek, R. Krishna, Monte Carlo simulations of self- and transport-diffusivities of 2-methylhexane in silicalite, *Phys. Chem. Chem. Phys.* **2000**, 2, 2389–2394.
- [315] C. Chmelik, L. Heinke, J. Kärger, W. Schmidt, D. B. Shah, J. M. van Baten, R. Krishna, Inflection in the loading dependence of the Maxwell–Stefan diffusivity of iso-butane in MFI zeolite, *Chem. Phys. Lett.* **2008**, 459, 141–145.
- [316] D. A. Reed, G. Ehrlich, Surface diffusion, atomic jump rates and thermodynamics, *Surf. Sci.* **1981**, 102, 588–609.
- [317] N. Hansen, T. Brüggemann, A. T. Bell, F. J. Keil, Theoretical investigation of benzene alkylation with ethene over H-ZSM-5, *J. Phys. Chem. C* **2008**, 112, 15402–15411.
- [318] R. Krishna, R. Baur, *Diffusion, Adsorption and Reaction in Zeolites: Modelling and Numerical issues*, University of Amsterdam, Amsterdam, <http://www.science.uva.nl/research/cr/zeolite/>, 1 December 2002.
- [319] D. D. Do, *Adsorption Analysis: Equilibria and Kinetics*, Imperial College Press, London **1998**.
- [320] C. J. H. Jacobsen, C. Madsen, J. Houzvicka, I. Schmidt, A. Carlsson, Mesoporous zeolite single crystals, *J. Am. Chem. Soc.* **2000**, 122, 7116–7117.
- [321] M. Lu, Y. Wu, Z. Zhu, H. Sun, Q. Chen, Ethylbenzene synthesis over AB-97 zeolite. I: The intrinsic kinetics and macrokinetics, *Petrochem-*

- ical Technol. (China)* **2001**, 30, 182–187.
- [322] J. Caro, M. Bülow, W. Schirmer, J. Kärger, W. Heink, H. Pfeifer, S. P. Zdanov, Microdynamics of methane, ethane and propane in ZSM-5 type zeolites, *J. Chem. Soc., Faraday Trans. I* **1985**, 81, 2541–2550.
- [323] N. Van-Den-Begin, L. V. C. Rees, J. Caro, M. Bülow, Fast adsorption-desorption kinetics of hydrocarbons in silicalite-1 by the single step frequency response method, *Zeolites* **1989**, 9, 287–292.
- [324] R. Q. Snurr, A. Hagen, H. B. Schwarz, S. Ernst, J. Weitkamp, J. Kärger, In *situ* PFG NMR study of intracrystalline diffusion during ethene conversion in ZSM-5, *J. Catal.* **1996**, 163, 130–137.
- [325] S. Chong, H. Jobic, M. Plazanet, D. S. Sholl, Concentration dependence of transport diffusion of ethane in silicalite. A comparison between neutron scattering experiments and atomically detailed simulations, *Chem. Phys. Lett.* **2005**, 408, 157–161.
- [326] M. Bülow, H. Schlodder, L. V. C. Rees, R. E. Richards, Molecular mobility of hydrocarbon ZSM5/silicalite systems studied by sorption uptake and frequency response methods, *Stud. Surf. Sci. Catal.* **1986**, 28, 579–586.
- [327] D. T. Hayhurst, A. Paravar, Diffusion of C₁ to C₅ normal paraffins in silicalite, *Zeolites* **1988**, 8, 27–29.
- [328] P. Wu, A. Debebe, Y. H. Ma, Adsorption and diffusion of C₆ and C₈ hydrocarbons in silicalite, *Zeolites* **1983**, 3, 118–122.
- [329] V. S. Nayak, L. Riekert, Factors influencing sorption and diffusion in pentasil zeolites, *Acta Phys. et Chem.* **1985**, 31, 157–166.
- [330] D. Prinz, L. Riekert, Observation of rates of sorption and diffusion in zeolite crystals at constant temperature and pressure, *Ber. Bunsenges. Phys. Chem.* **1986**, 90, 413–417.
- [331] A. Zikanova, M. Bülow, H. Schlodder, Intracrystalline diffusion of benzene in ZSM-5 and silicalite, *Zeolites* **1987**, 7, 115–118.
- [332] D. B. Shah, D. T. Hayhurst, G. Evanina, C. J. Guo, Sorption and diffusion of benzene in HZSM-5 and silicalite crystals, *AIChE J.* **1988**, 34, 1713–1717.
- [333] D. M. Shen, L. V. C. Rees, Diffusivities of benzene in HZSM-5, silicalite-I, and NaX determined by frequency-response techniques, *Zeolites* **1991**, 11, 666–671.
- [334] D. M. Ruthven, M. Eic, E. Richards, Diffusion of C₈ aromatic hydrocarbons in silicalite, *Zeolites* **1991**, 11, 647–653.
- [335] K. Hashimoto, T. Masuda, N. Murakami, Intracrystalline diffusivities of HZSM-5 zeolites, *Stud. Surf. Sci. Catal.* **1991**, 69, 477–484.
- [336] J. Xiao, J. Wei, Diffusion mechanism of hydrocarbons in zeolites-I. Theory, *Chem. Eng. Sci.* **1992**, 47, 1123–1141.

- [337] J. Xiao, J. Wei, Diffusion mechanism of hydrocarbons in zeolites—II. Analysis of experimental observations, *Chem. Eng. Sci.* **1992**, 47, 1143–1159.
- [338] T. Masuda, K. Hashimoto, Measurements of adsorption on outer surface of zeolite and their influence on evaluation of intracrystalline diffusivity, *Stud. Surf. Sci. Catal.* **1994**, 83, 225–232.
- [339] J. R. Hufton, D. M. Ruthven, R. P. Danner, Adsorption and diffusion of hydrocarbons in silicalite at very low concentration – effect of defect sites, *Microporous Mater.* **1995**, 5, 39–52.
- [340] R. Roque-Malherbe, R. Wendelbo, A. Mifsud, A. Corma, Diffusion of aromatic hydrocarbons in H-ZSM-5, H-Beta, and H-MCM-22 zeolites, *J. Phys. Chem.* **1995**, 99, 14064–14071.
- [341] T. Masuda, Y. Fujikata, T. Nishida, K. Hashimoto, The influence of acid sites on intracrystalline diffusivities within MFI-type zeolites, *Microporous Mesoporous Mater.* **1998**, 23, 157–167.
- [342] Y. Fujikata, T. Masuda, H. Ikeda, K. Hashimoto, Measurement of the diffusivities within MFI- and Y-type zeolite catalysts in adsorption and desorption processes, *Microporous Mesoporous Mater.* **1998**, 21, 679–686.
- [343] H. Jobic, M. Bee, S. Pouget, Diffusion of benzene in ZSM-5 measured by the Neutron Spin-Echo technique, *J. Phys. Chem. B* **2000**, 104, 7130–7133.
- [344] S. Brandani, M. Jama, D. Ruthven, Diffusion, self-diffusion and counter-diffusion of benzene and *p*-xylene in silicalite, *Microporous Mesoporous Mater.* **2000**, 35-36, 283–300.
- [345] J. W. P. Loos, P. J. T. Verheijen, J. A. Moulijn, Improved estimation of zeolite diffusion coefficients from zero-length column experiments, *Chem. Eng. Sci.* **2000**, 55, 51–65.
- [346] L. Song, L. V. C. Rees, Adsorption and diffusion of cyclic hydrocarbon in MFI-type zeolites studied by gravimetric and frequency-response techniques, *Microporous Mesoporous Mater.* **2000**, 35-36, 301–314.
- [347] L. Song, Z.-L. Sun, L. V. C. Rees, Experimental and molecular simulation studies of adsorption and diffusion of cyclic hydrocarbons in silicalite-1, *Microporous Mesoporous Mater.* **2002**, 55, 31–49.
- [348] L. Song, Z.-L. Sun, H.-Y. Ban, M. Dai, L. V. C. Rees, Studies of unusual adsorption and diffusion behaviour of benzene in silicalite-1, *Phys. Chem. Chem. Phys.* **2004**, 6, 4722–4731.
- [349] H. G. Karge, Infrared spectroscopic investigation of diffusion, co-diffusion and counter-diffusion of hydrocarbon molecules in zeolites, *C. R. Chimie* **2005**, 8, 303–319.
- [350] L. Song, Z.-L. Sun, L. Duan, J. Gui, G. S. McDougall, Adsorption and

- diffusion properties of hydrocarbons in zeolites, *Microporous Mesoporous Mater.* **2007**, 104, 115–128.
- [351] Y. Nakasaka, T. Tago, K. Odate, T. Masuda, Measurement of intracrystalline diffusivity of benzene within MFI-type zeolite from bulk benzene/cyclohexane liquid phase, *Microporous Mesoporous Mater.* **2008**, 112, 162–169.
- [352] O. C. Gobin, S. J. Reitmeier, A. Jentys, J. A. Lercher, Diffusion pathways of benzene, toluene and p-xylene in MFI, *Microporous Mesoporous Mater.* **2009**, 125, 3–10.
- [353] O. C. Gobin, S. J. Reitmeier, A. Jentys, J. A. Lercher, Comparison of the transport of aromatic compounds in small and large MFI particles, *J. Phys. Chem. C* **2009**, 113, 20435–20444.
- [354] R. Schumacher, H. G. Karge, Sorption and sorption kinetics of ethylbenzene in MFI-type zeolites studied by a barometric technique, *Collect. Czech. Chem. Commun.* **1999**, 64, 483–493.
- [355] R. Rungsisakun, T. Nanok, M. Probst, J. Limtrakul, Adsorption and diffusion of benzene in the nanoporous catalysts FAU, ZSM-5 and MCM-22. A molecular dynamics study, *J. Mol. Graphics Modell.* **2006**, 24, 373–382.
- [356] J. R. Fried, S. Weaver, Atomistic simulation of hydrocarbon diffusion in silicalite, *Comp. Mater. Sci.* **1998**, 11, 277–293.
- [357] X. Yue, X. Yang, Molecular simulation study of adsorption and diffusion on silicalite for a benzene/CO₂ mixture, *Langmuir* **2006**, 22, 3138–3147.
- [358] T. R. Forester, W. Smith, Bluemoon simulation of benzene in silicalite-1, *J. Chem. Soc., Faraday Trans.* **1997**, 93, 3249–3257.
- [359] F. J. Keil, J. Hinderer, A. R. Garayhi, Diffusion and reaction in ZSM-5 and composite catalysts for the methanol-to-olefins process, *Catal. Today* **1999**, 50, 637–650.
- [360] H. Takaba, T. Suzuki, S. Nakao, Estimation of diffusion coefficient and permeance of aromatic molecules in silicalite and MgZSM-5 using quantum calculation and dynamic Monte Carlo simulation, *Fluid Phase Equil.* **2004**, 219, 11–18.
- [361] R. Q. Snurr, A. T. Bell, D. N. Theodorou, Investigation of the dynamics of benzene in silicalite using transition-state theory, *J. Phys. Chem.* **1994**, 98, 11948–11961.
- [362] D. M. Ruthven, Effectiveness factors for molecular sieve catalysts, *J. Catal.* **1972**, 25, 259–264.
- [363] R. Krishna, D. Paschek, Separation of hydrocarbon mixtures using zeolite membranes: A modelling approach combining molecular simulations with the Maxwell-Stefan theory, *Separation Purification Technol.*

- 2000**, 21, 111–136.
- [364] R. Mezaki, H. Inoue (eds.), *Rate Equations of Solid-Catalyzed Reactions*, University of Tokyo Press, Tokyo **1991**.
- [365] A. N. R. Bos, L. Lefferts, G. B. Marin, M. H. G. M. Steijns, Kinetic research on heterogeneously catalysed processes: A questionnaire on the state-of-the-art in industry, *Appl. Catal. A* **1997**, 160, 185–190.
- [366] R. J. Berger, E. H. Stitt, G. B. Marin, F. Kapteijn, J. A. Moulijn, Chemical reaction kinetics in practice, *CATTECH* **2001**, 5, 30–60.
- [367] M. Boudart, Two-step catalytic reactions, *AIChE J.* **1972**, 18, 465–478.
- [368] B. Temel, H. Meskine, K. Reuter, M. Scheffler, H. Metiu, Does phenomenological kinetics provide an adequate description of heterogeneous catalytic reactions?, *J. Chem. Phys.* **2007**, 126, 204711–1/12.
- [369] P. O. Graf, L. Lefferts, Reactive separation of ethylene from the effluent gas of methane oxidative coupling via alkylation of benzene to ethylbenzene on ZSM-5, *Chem. Eng. Sci.* **2009**, 64, 2773–2780.
- [370] I. I. Ivanova, N. Blom, E. G. Derouane, ¹³C MAS NMR mechanistic study of benzene alkylation with propane over Ga-modified H-ZSM-5 catalyst, *J. Mol. Catal. A* **1996**, 109, 157–168.
- [371] E. G. Derouane, H. He, S. B. Derouane-Abd Hamid, D. Lambert, I. I. Ivanova, In situ MAS NMR spectroscopy study of catalytic reaction mechanisms, *J. Mol. Catal. A* **2000**, 158, 5–17.
- [372] A. V. Smirnov, E. V. Mazin, V. V. Yuschenko, E. E. Knyazeva, S. N. Nesterenko, I. I. Ivanova, L. Galperin, R. Jensen, S. Bradley, Benzene alkylation with propane over Pt-modified MFI zeolites, *J. Catal.* **2000**, 194, 266–277.
- [373] A. V. Smirnov, E. V. Mazin, O. A. Ponomoreva, E. E. Knyazeva, S. N. Nesterenko, I. I. Ivanova, Benzene alkylation with alkanes over modified MFI catalysts, *Stud. Surf. Sci. Catal.* **2001**, 135, 153–160.
- [374] S. Kato, K. Nakagawa, N. Ikenaga, T. Suzuki, Alkylation of benzene with ethane over platinum loaded zeolite catalyst, *Catal. Lett.* **2001**, 73, 175–180.
- [375] C. Bigey, B.-L. Su, Propane as alkylating agent for alkylation of benzene on HZSM-5 and Ga-modified HZSM-5 zeolites, *J. Mol. Catal. A* **2004**, 209, 179–187.
- [376] S. Todorova, B.-L. Su, Effects of acidity and combination of Ga and Pt on catalytic behavior of Ga-Pt modified ZSM-5 catalysts in benzene alkylation with pure propane, *Catal. Today* **2004**, 93-95, 417–424.
- [377] V. L. Zholobenko, G.-D. Lei, B. T. Carvill, B. A. Lerner, W. M. H. Sachtler, Identification of isolated Pt atoms in H-mordenite, *J. Chem. Soc. Faraday Trans.* **1994**, 90, 233–238.

- [378] A. Y. Stakheev, E. S. Shpiro, O. P. Tkachenko, N. I. Jaeger, G. Schulz-Ekloff, Evidence for monoatomic platinum species in H-ZSM-5 from FTIR spectroscopy of chemisorbed CO, *J. Catal.* **1997**, 169, 382–388.
- [379] E. S. Shpiro, D. P. Shevchenko, O. P. Tkachenko, R. V. Dmitriev, Platinum promoting effects in Pt/Ga zeolite catalysts of lower alkane aromatization. I. Ga and Pt electronic states, dispersion and distribution in zeolite crystals in dependence of preparation techniques. Dynamic effects caused by reaction mixture, *Appl. Catal. A* **1994**, 107, 147–164.
- [380] E. S. Shpiro, D. P. Shevchenko, R. V. Dmitriev, O. P. Tkachenko, K. M. Minachev, Platinum promoting effects in Pt/Ga zeolite catalysts of lower alkane aromatization. II. The catalytic properties in n-butane aromatization, formation of the catalytically active sites and reaction mechanism, *Appl. Catal. A* **1994**, 107, 165–180.
- [381] P. Meriaudeau, G. Sapaly, C. Naccache, T. E. M. and catalytic property study of Pt-Ga on HZSM-5, in *Proceedings from the ninth international zeolite conference*, Butterworth-Heinemann, Boston **1993**, pp. 583–589.
- [382] M. Santhosh Kumar, A. Holmen, D. Chen, The influence of pore geometry of Pt containing ZSM-5, Beta and SBA-15 catalysts on dehydrogenation of propane, *Microporous Mesoporous Mater.* **2009**, 126, 152–158.
- [383] Y. Shi, Y. Gao, Y. Dai, W. Yuan, Kinetics for benzene plus ethylene reaction in near critical regions, *Chem. Eng. Sci.* **2001**, 56, 1403–1410.
- [384] P. E. Gill, W. Murray, Algorithms for the solution of the nonlinear least-squares problem, *SIAM J. Numer. Anal.* **1978**, 15, 977–992, NAG-routine E04FYF.
- [385] N. Hansen, R. Krishna, J. M. van Baten, A. T. Bell, F. J. Keil, Analysis of diffusion limitation in the alkylation of benzene over H-ZSM-5 by combining quantum chemical calculations, molecular simulations, and a continuum approach, *J. Phys. Chem. C* **2009**, 113, 235–246.
- [386] J. P. Nolley, J. R. Katzer, Desorption influence on benzene alkylation with olefins over Y zeolites, *Adv. Chem.* **1973**, 121, 563–574.
- [387] J. A. Labinger, J. E. Bercaw, Understanding and exploiting C-H bond activation, *Nature* **2002**, 417, 507–514.
- [388] N. Hansen, S. Jakobtorweihen, F. J. Keil, Reactive Monte Carlo and grand-canonical Monte Carlo simulations of the propene metathesis reaction system, *J. Chem. Phys.* **2005**, 122, 164705–1/11.
- [389] S. Jakobtorweihen, N. Hansen, F. J. Keil, Combining reactive and configurational-bias Monte Carlo: Confinement influence on the propene metathesis reaction system in various zeolites, *J. Chem. Phys.* **2006**, 125, 224709–1/9.

- [390] S. A. S. Rezai, Y. Traa, Equilibrium shift in membrane reactors: A thermodynamic analysis of the dehydrogenative conversion of alkanes, *J. Membrane Sci.* **2008**, 319, 279–285.
- [391] M. P. Duducovic, Reaction engineering: Status and future challenges, *Chem. Eng. Sci.* **2010**, 65, 3–11.
- [392] B. Yilmaz, U. Müller, Catalytic applications of zeolites in chemical industry, *Top. Catal.* **2009**, 52, 888–895.
- [393] T. A. Wesolowski, O. Parisel, Y. Ellinger, J. Weber, Comparative study of benzene \cdots X (X = O₂, N₂, CO) complexes using density functional theory: the importance of an accurate exchange-correlation energy density at high reduced density gradients, *J. Phys. Chem. A* **1997**, 101, 7818–7825.
- [394] Y. Zhang, W. Pan, W. Yang, Describing van der Waals interaction in diatomic molecules with generalized gradient approximations: The role of the exchange functional, *J. Chem. Phys.* **1997**, 107, 7921–7925.
- [395] O. V. Gritsenko, B. Ensing, P. R. T. Schipper, E. J. Baerends, Comparison of the accurate Kohn-Sham solution with the generalized gradient approximations GGAs for the S_N2 reactions F⁻ + CH₃F → FCH₃ + F⁻: A qualitative rule to predict success or failure of GGAs, *J. Phys. Chem. A* **2000**, 104, 8558–8565.
- [396] D. Porezag, M. R. Pederson, Density functional based studies of transition states and barriers for hydrogen exchange and abstraction reactions, *J. Chem. Phys.* **1995**, 102, 9345–9349.
- [397] T. Kerber, M. Sierka, J. Sauer, Application of semiempirical long-range dispersion corrections to periodic systems in density functional theory, *J. Comput. Chem.* **2008**, 29, 2088–2097.
- [398] Y. Zhao, D. G. Truhlar, Density functionals with broad applicability in chemistry, *Acc. Chem. Res.* **2008**, 41, 157–167.
- [399] S. Grimme, Semiempirical GGA-type density functional constructed with a long-range dispersion correction, *J. Comput. Chem.* **2006**, 27, 1787–1799.
- [400] T. Schwabe, S. Grimme, Theoretical thermodynamics for large molecules: walking the thin line between accuracy and computational cost, *Acc. Chem. Res.* **2008**, 41, 569–579.
- [401] C. D. Sherrill, T. Takatani, E. G. Hohenstein, An assessment of theoretical methods for nonbonded interactions: Comparison to complete basis set limit coupled-cluster potential energy curves for the benzene dimer, the methane dimer, benzene-methane, and benzene-H₂S, *J. Phys. Chem. A* **2009**, 113, 10146–10159.
- [402] F. Ortman, F. Bechstedt, W. G. Schmidt, Semiempirical van der Waals correction to the density functional description of solids and

- molecular structures, *Phys. Rev. B* **2006**, 73, 205101–1/10.
- [403] B. Civalleri, C. M. Zicovich-Wilson, L. Valenzano, P. Ugliengo, B3LYP augmented with an empirical dispersion term (B3LYP-D*) as applied to molecular crystals, *Cryst. Eng. Commun.* **2008**, 10, 405–410.
- [404] L. Maschio, D. Usvyat, F. R. Manby, S. Casassa, C. Pisani, M. Schütz, Fast local-MP2 method with density fitting for crystals. I. Theory and algorithms, *Phys. Rev. B* **2007**, 76, 075101–1/9.
- [405] S. Casassa, M. Halo, L. Maschio, C. Roetti, C. Pisanti, Beyond a Hartree-Fock description of crystalline solids: the case of lithium hydride, *Theor. Chem. Acc.* **2007**, 117, 781–791.
- [406] C. Pisani, L. Maschio, S. Casassa, M. Halo, M. Schütz, D. Usvyat, Periodic local MP2 method for the study of electronic correlation in crystals: Theory and preliminary applications, *J. Comput. Chem.* **2008**, 29, 2113–2124.
- [407] C. Tuma, T. Kerber, J. Sauer, The tert-butyl cation in H-zeolites - deprotonation to isobutene and conversion to surface alkoxides, *Angew. Chem. Int. Ed.* **2010**, in press.
- [408] L. A. Clark, M. Sierka, J. Sauer, Computational elucidation of transition state shape selectivity phenomenon, *J. Am. Chem. Soc.* **2004**, 126, 936–947.
- [409] B. A. De Moor, M.-F. Reyniers, M. Sierka, J. Sauer, G. B. Marin, Physisorption and chemisorption of hydrocarbons in H-FAU using QM-Pot(MP2//B3LYP) calculations, *J. Phys. Chem. C* **2008**, 112, 11796–11812.
- [410] G. Kresse, J. Hafner, Ab initio molecular dynamics for open-shell transition metals, *Phys. Rev. B* **1993**, 48, 13115–13126.
- [411] G. Kresse, J. Hafner, Ab initio molecular-dynamics simulation of the liquid-metal-amorphous-semiconductor transition in germanium, *Phys. Rev. B* **1994**, 49, 14251–14296.
- [412] G. Kresse, J. Furthmüller, Efficiency of ab-initio total energy calculations for metals and semiconductors using a plane-wave basis set, *J. Comput. Mater. Sci.* **1996**, 6, 15–50.
- [413] G. Kresse, J. Furthmüller, Efficient iterative schemes for ab initio total energy calculations using a plane-wave basis set, *Phys. Rev. B* **1996**, 54, 11169–11186.
- [414] P. E. Blöchl, Projector augmented-wave method, *Phys. Rev. B* **1994**, 50, 17953–17979.
- [415] G. Kresse, D. Joubert, From ultrasoft pseudopotentials to the projector augmented wave method, *Phys. Rev. B* **1999**, 59, 1758–1775.
- [416] D. G. Hay, H. Jaeger, G. W. West, Examination of the monoclinic/orthorhombic transition in silicalite using XRD and silicon NMR,

- J. Phys. Chem.* **1985**, 89, 1070–1072.
- [417] H. van Koningsveld, J. C. Jansen, H. van Bekkum, The orthorhombic/monoclinic transition in single crystals of ZSM-5, *Zeolites* **1987**, 7, 564–568.
- [418] H. van Koningsveld, High-temperature (350 K) orthorhombic framework structure of zeolite H-ZSM-5, *Acta Crystallogr.* **1990**, B46, 731–735.
- [419] H. van Koningsveld, On the location and disorder of the tetrapropylammonium (TPA) ion in zeolite ZSM-5 with improved framework accuracy, *Acta Crystallogr.* **1987**, B43, 127–132.
- [420] M. Sierka, J. Sauer, Structure and reactivity of silica and zeolite catalysts by a combined quantum mechanics - shell model potential approach based on DFT, *Faraday Discuss.* **1997**, 106, 41–62.
- [421] K. Eichkorn, O. Treutler, H. Öhm, M. Häser, R. Ahlrichs, Auxiliary basis sets to approximate Coulomb potentials, *Chem. Phys. Lett.* **1995**, 240, 283–290.
- [422] K. Eichkorn, O. Treutler, H. Öhm, M. Häser, R. Ahlrichs, Auxiliary basis sets to approximate Coulomb potentials, *Chem. Phys. Lett.* **1995**, 242, 652–660.
- [423] K. Eichkorn, F. Weigend, O. Treutler, R. Ahlrichs, Auxiliary basis sets for main row atoms and transition metals and their use to approximate Coulomb potentials, *Theor. Chem. Acc.* **1997**, 97, 119–124.
- [424] F. Weigend, F. Furche, R. Ahlrichs, Gaussian basis sets of quadruple zeta valence quality for atoms H–Kr, *J. Chem. Phys.* **2003**, 119, 12753–12762.
- [425] S. Tosoni, C. Tuma, J. Sauer, B. Civalleri, P. Ugliengo, A comparison between plane wave and Gaussian-type orbital basis sets for hydrogen bonded systems: Formic acid as a test case, *J. Chem. Phys.* **2007**, 127, 154102–1/11.
- [426] S. F. Boys, F. Bernardi, The calculation of small molecular interactions by the differences of separate total energies. Some procedures with reduced errors, *Mol. Phys.* **1970**, 19, 553–566.
- [427] G. Lendvay, I. Mayer, Some difficulties in computing BSSE-corrected potential surfaces of chemical reactions, *Chem. Phys. Lett.* **1998**, 297, 365–373.
- [428] N. R. Kestner, J. E. Combariza, Basis set superposition errors: Theory and practice, in *Reviews in Computational Chemistry*, K. B. Lipkowitz, D. B. Boyd, eds., vol. 13, Wiley-VCH **1999**, pp. 99–132.
- [429] D. E. Woon, T. H. Dunning, Gaussian basis sets for use in correlated molecular calculations. 3. The atoms aluminum through argon, *J. Chem. Phys.* **1993**, 98, 1358–1371.

- [430] A. Halkier, T. Helgaker, P. Jørgensen, W. Klopper, J. Olsen, Basis set convergence of the energy in molecular Hartree-Fock calculations, *Chem. Phys. Lett.* **1999**, 302, 437–446.
- [431] F. Jensen, Estimating the Hartree-Fock limit from finite basis set calculations, *Theor. Chem. Acc.* **2005**, 113, 267–273.
- [432] T. Helgaker, W. Klopper, H. Koch, J. Noga, Basis set convergence of correlated calculations on water, *J. Chem. Phys.* **1997**, 106, 9639–9646.
- [433] J. A. Sordo, On the use of the Boys-Bernardi function counterpoise procedure to correct barrier heights for basis set superposition error, *J. Mol. Struct. (Theochem)* **2001**, 537, 245–251.
- [434] H.-J. Werner, P. J. Knowles, R. Lindh, F. R. Manby, M. Schütz, P. Celani, T. Korona, G. Rauhut, R. D. Amos, A. Bernhardsson, A. Berning, D. L. Cooper, M. J. O. Deegan, A. J. Dobbyn, F. Eckert, C. Hampel, G. Hetzer, A. W. Lloyd, S. J. McNicholas, W. Meyer, M. E. Mura, A. Nicklass, P. Palmieri, R. Pitzer, U. Schumann, H. Stoll, A. J. Stone, R. Tarroni, T. Thorsteinsson, MOLPRO – a package of ab initio programs (version 2006.1), Cardiff, UK **2006**.
- [435] F. Weigend, R. Ahlrichs, Balanced basis sets of split valence, triple zeta valence and quadruple zeta valence quality for H to Rn: Design and assessment of accuracy, *Phys. Chem. Chem. Phys.* **2005**, 7, 3297–3305.
- [436] D. Feller, The role of databases in support of computational chemistry calculations, *J. Comput. Chem.* **1996**, 17, 1571–1586.
- [437] K. L. Schuchardt, B. T. Didier, T. Elsethagen, L. Sun, V. Gurumoorthi, J. Chase, J. Li, T. L. Windhus, Basis set exchange: A community database for computational sciences, *J. Chem. Inf. Model.* **2007**, 47, 1045–1052.
- [438] A. Fernández-Ramos, B. A. Ellington, R. Meana-Pañeda, J. M. C. Marques, D. G. Truhlar, Symmetry numbers and chemical reaction rates, *Theor. Chem. Account.* **2007**, 118, 813–826.
- [439] B. A. De Moor, M.-F. Reyniers, G. B. Marin, Physisorption and chemisorption of alkanes and alkenes in H-FAU: a combined ab initio-statistical thermodynamics study, *Phys. Chem. Chem. Phys.* **2009**, 11, 2939–2958.
- [440] T. Bučko, L. Benco, T. Demuth, J. Hafner, Ab initio density functional investigation of the (001) surface of mordenite, *J. Chem. Phys.* **2002**, 117, 7295–7305.
- [441] M. Trombetta, T. Armaroli, A. Gutierrez Alejandro, J. Ramirez Solis, G. Busca, An FT-IR study of the internal and external surfaces of HZSM5 zeolite, *Appl. Catal. A* **2000**, 192, 125–136.
- [442] A. Zecchina, G. Spoto, S. Bordiga, Probing the acid sites in confined

- spaces of microporous materials by vibrational spectroscopy, *Phys. Chem. Chem. Phys.* **2005**, *7*, 1627–1642.
- [443] G. Spoto, S. Bordiga, G. Ricciardi, D. Scarano, A. Zecchina, E. Borello, IR study of ethene and propene oligomerization on H-ZSM-5: Hydrogen-bonded precursor formation, initiation and propagation mechanisms and structure of the entrapped oligomers, *J. Chem. Soc. Faraday Trans.* **1994**, *90*, 2827–2835.
- [444] R. R. Mukti, A. Jentys, J. A. Lercher, Orientation of alkyl-substituted aromatic molecules during sorption in the pores of H/ZSM-5 zeolites, *J. Phys. Chem. C* **2007**, *111*, 3973–3980.
- [445] C. Tuma, A. D. Boese, N. C. Handy, Predicting the binding energies of H-bonded complexes: A comparative DFT study, *Phys. Chem. Chem. Phys.* **1999**, *1*, 3939–3947.
- [446] S. Grimme, Improved second-order Møller-Plesset perturbation theory by separate scaling of parallel and antiparallel-spin pair correlation energies, *J. Chem. Phys.* **2003**, *118*, 9095–9102.
- [447] S. Jakobtorweihen, N. Hansen, F. J. Keil, Molecular simulation of alkene adsorption in zeolites, *Mol. Phys.* **2005**, *103*, 471–489.
- [448] H. Thamm, H. Stach, W. Fiebig, Calorimetric study of the absorption of n-butane and but-1-ene on a highly dealuminated Y-type zeolite and on silicalite, *Zeolites* **1983**, *3*, 95–97.
- [449] N. E. R. Zimmermann, M. Haranczyk, M. Sharma, B. Liu, B. Smit, F. J. Keil, Adsorption and diffusion in zeolites: The pitfall of isotopic crystal structures, *submitted*.
- [450] T. Bučko, L. Benco, O. Dubay, C. Dellago, J. Hafner, Mechanism of alkane dehydrogenation catalyzed by acidic zeolites: Ab initio transition path sampling, *J. Chem. Phys.* **2009**, *131*, 214508–1/11.
- [451] C. Baerlocher, L. B. McCusker, *Database of zeolite structures*, International Zeolite Organisation, <http://www.iza-structure.org/databases/>, 26 June 2001.
- [452] J. M. van Baten, R. Krishna, *MD simulations of diffusion in zeolites*, University of Amsterdam, Amsterdam, <http://www.science.uva.nl/research/cr/md/>.
- [453] D. Dubbeldam, S. Calero, T. J. H. Vlugt, R. Krishna, T. L. M. Maesen, E. Beerdsen, B. Smit, Force field parametrization through fitting on inflection points in isotherms, *Phys. Rev. Lett.* **2004**, *93*, 088302.
- [454] S. Ban, A. van Laak, P. E. de Jongh, J. P. J. M. van der Eerden, T. J. H. Vlugt, Adsorption selectivity of benzene and propene mixtures for various zeolites, *J. Phys. Chem. C* **2007**, *111*, 17241–17248.
- [455] T. J. H. Vlugt, *BIGMAC*, University of Amsterdam, Amsterdam, <http://molsim.chem.uva.nl/bigmac/>, 1 November 2000.

- [456] W. Smith, C. W. Yong, P. M. Rodger, DL_POLY: Application to molecular simulation, *Mol. Sim.* **2002**, 28, 385–471.
- [457] W. Smith, T. R. Forester, I. T. Todorov, *The DL_POLY molecular simulation package*, Warrington, England, http://www.cse.clrc.ac.uk/msi/software/DL_POLY/index.shtml, March 2006.
- [458] R. Krishna, D. Paschek, Molecular simulations of adsorption and siting of light alkanes in silicalite-1, *Phys. Chem. Chem. Phys.* **2001**, 3, 453–462.
- [459] R. Krishna, J. M. van Baten, Influence of segregated adsorption on mixture diffusion in DDR zeolite, *Chem. Phys. Lett.* **2007**, 446, 344–349.
- [460] M. Murthi, R. Q. Snurr, Effects of molecular siting and adsorbent heterogeneity on the ideality of adsorption equilibria, *Langmuir* **2004**, 20, 2489–2497.
- [461] C. Förste, A. Germanus, J. Kärger, H. Pfeifer, J. Caro, W. Pilz, A. Zikánová, Molecular mobility of methane adsorbed on ZSM-5 containing coadsorbed benzene, and the location of the benzene molecules, *J. Chem. Soc., Faraday Trans.* **1987**, 83, 2301–2309.
- [462] M. Fernandez, J. Kärger, D. Freude, A. Pampel, J. M. van Baten, R. Krishna, Mixture diffusion in zeolites studied by MAS PFG NMR and molecular simulation, *Microporous Mesoporous Mater.* **2007**, 105, 124–131.
- [463] R. Krishna, J. M. van Baten, Diffusion of hydrocarbon mixtures in MFI zeolite: Influence of intersection blocking, *Chem. Eng. J.* **2008**, 140, 614–620.
- [464] J. M. van Baten, R. Krishna, *MD animations of diffusion in nanoporous materials*, University of Amsterdam, Amsterdam, <http://www.science.uva.nl/research/cr/animateMD/>, 3 February 2008.
- [465] <http://www.sript.com.cn/er&d/er&d6-asp-m.pdf>, 14 May 2008.
- [466] R. H. Perry, C. H. Chilton (eds.), *Chemical Engineers' Handbook*, McGraw-Hill, New York, 5th ed. **1973**.
- [467] A. V. A. Kumar, H. Jobic, S. K. Bhatia, Quantum effects on adsorption and diffusion of hydrogen and deuterium in microporous materials, *J. Phys. Chem. B* **2006**, 110, 16666–16671.
- [468] M. Gallo, T. M. Nenoff, M. C. Mitchell, Selectivities for binary mixtures of hydrogen/methane and hydrogen/carbon dioxide in silicalite and ETS-10 by Grand Canonical Monte Carlo techniques, *Fluid Phase Equilib.* **2006**, 247, 135–142.
- [469] B. S. Kwak, W. M. H. Sachtler, W. O. Haag, Catalytic conversion of propane to aromatics: Effects of adding Ga and/or Pt to HZSM-5, *J. Catal.* **1994**, 149, 465–473.

- [470] K. J. Chao, A. C. Wei, H. C. Wu, J. F. Lee, X-ray absorption spectroscopic study on the states of gallium and platinum in Pt/Ga/H-beta zeolites, *Microporous Mesoporous Mater.* **2000**, 35.
- [471] M. N. Mikhailov, I. V. Mishin, L. M. Kustov, A. L. Lapidus, Structure and reactivity of Pt/GaZSM-5 aromatization catalyst, *Microporous Mesoporous Mater.* **2007**, 104, 145–150.
- [472] M. Sierka, J. Sauer, Proton mobility in chabazite, faujasite, and ZSM-5 zeolite catalysts, comparison based on ab initio calculations, *J. Phys. Chem. B* **2001**, 105, 1603–1613.
- [473] M. E. Franke, M. Sierka, U. Simon, J. Sauer, Translational proton mobility in zeolite H-ZSM-5. Energy barriers and jump rates from DFT calculations, *Phys. Chem. Chem. Phys.* **2002**, 4, 5207–5216.
- [474] M. Frenkel (ed.), *Thermochemistry and Equilibria of Organic Compounds*, VCH, New York **1993**.
- [475] K. S. Pitzer, W. D. Gwinn, Energy Levels and thermodynamic functions for molecules with internal rotation I. rigid frame with attached tops, *J. Chem. Phys.* **1942**, 10, 428–440.

Published work

- S. Jakobtorweihen, **N. Hansen**, and F. J. Keil,
Molecular simulation of alkene adsorption in zeolites,
Molec. Phys. **2005**, 103, 471-489.
- **N. Hansen**, S. Jakobtorweihen, and F. J. Keil,
Reactive Monte Carlo and grand canonical Monte Carlo simulations of
the propene metathesis reaction system,
J. Chem. Phys. **2005**, 122, 164705-1/11.
- A. Heyden, **N. Hansen**, A. T. Bell, and F. J. Keil,
Nitrous oxide decomposition over Fe-ZSM-5 in the presence of nitric
oxide: A comprehensive DFT study,
J. Phys. Chem. B **2006**, 110, 17096-17114.
- S. Jakobtorweihen, **N. Hansen**, and F. J. Keil,
Combining reactive and configurational-bias Monte Carlo: Confinement
influence on the propene metathesis reaction system in various
zeolites,
J. Chem. Phys. **2006**, 125, 224709-1/9.
- **N. Hansen**, A. Heyden, A. T. Bell, and F. J. Keil,
A reaction mechanism for the nitrous oxide decomposition on binuclear
oxygen bridged iron sites in Fe-ZSM-5,
J. Phys. Chem. C **2007**, 111, 2092-2101.
- **N. Hansen**, A. Heyden, A. T. Bell, and F. J. Keil,
Mikrokinetic modeling of nitrous oxide decomposition on dinuclear oxygen
bridged iron sites in Fe-ZSM-5,
J. Catal. **2007**, 248, 213-225.

- **N. Hansen**, F. A. B. Agbor, and F. J. Keil,
New force fields for nitrous oxide and oxygen and their application to phase equilibria simulations,
Fluid Phase Equil. **2007**, 259, 180-188.
- **N. Hansen**, T. Brüggemann, A. T. Bell, and F. J. Keil,
Theoretical investigation of benzene alkylation with ethene over H-ZSM-5,
J. Phys. Chem. C **2008**, 112, 15402-15411.
- **N. Hansen**, R. Krishna, J. M. van Baten, A. T. Bell, and F. J. Keil,
Analysis of diffusion limitation in the alkylation of benzene over H-ZSM-5 by combining quantum chemical calculations, molecular simulations, and a continuum approach,
J. Phys. Chem. C **2009**, 113, 235-246.
- **N. Hansen**, R. Krishna, J. M. van Baten, A. T. Bell, and F. J. Keil,
Reactor simulation of benzene ethylation and ethane dehydrogenation catalyzed by ZSM-5: A multiscale approach,
Chem. Eng. Sci. **2010**, 65, 2472-2480.
- **N. Hansen**, F. J. Keil,
Multiscale modelling of reaction and diffusion in zeolites: From the molecular level to the reactor,
submitted
- J. A. Swisher, **N. Hansen**, T. L. M. Maesen, F. J. Keil, B. Smit, and A. T. Bell,
Theoretical simulation of *n*-alkane cracking on zeolites,
submitted
- **N. Hansen**, T. Kerber, J. Sauer, A. T. Bell, and F. J. Keil,
Quantum chemical modeling of benzene ethylation over H-ZSM-5 approaching chemical accuracy: A hybrid MP2:DFT study,
submitted

Conferences

- A. Heyden, N. Hansen, A. T. Bell, and F. J. Keil, “A comprehensive DFT study of the NO-assisted N₂O decomposition over Fe-ZSM-5”, NIC Winter School, John-von-Neumann-Institut, FZ Jülich, Germany, 14th–22th Febr. 2006.
- N. Hansen, A. Heyden, A. T. Bell, and F. J. Keil, “A reaction mechanism for the N₂O decomposition on binuclear oxygen bridged iron sites in Fe-ZSM-5”, ICTAC-11, Berlin, Germany, 11th–14th June 2006.
- N. Hansen, A. Heyden, A. T. Bell, and F. J. Keil, “A reaction mechanism for the nitrous oxide decomposition on binuclear oxygen bridged iron sites in Fe-ZSM-5”, AIChE Annual Meeting, San Francisco, USA, 12th–17th Nov. 2006.
- N. Hansen, T. Brüggemann, A. T. Bell, and F. J. Keil, “Alkylierung von Benzol mit Ethen am Zeolithen H-ZSM-5 – Eine Multiskalenuntersuchung”, Jahrestreffen Reaktionstechnik, Würzburg, Germany, 18th–20th May 2008.
- N. Hansen, T. Brüggemann, R. Krishna, J. M. van Baten, A. T. Bell, and F. J. Keil, “Alkylation of benzene with ethene over H-ZSM-5 – A multiscale investigation”, AIChE Annual Meeting, Philadelphia, USA, 16th–21st Nov. 2008.
- N. Hansen, T. Brüggemann, R. Krishna, J. M. van Baten, A. T. Bell, and F. J. Keil, “Analysis of diffusion limitation in the alkylation of benzene over H-ZSM-5 by combining quantum chemical calculations, molecular simulations, and a continuum approach”, MaCKiE-2009, Ghent, Belgium, 9th–11th Feb. 2009.

-
- N. Hansen, T. Brüggemann, R. Krishna, J. M. van Baten, A. T. Bell, and F. J. Keil, “Analysis of diffusion limitation in the alkylation of benzene over H-ZSM-5 by combining quantum chemical calculations, molecular simulations, and a continuum approach” (invited talk), Eurokin 2009, Louvain-la-Neuve, Belgium, 12th Feb. 2009.
 - N. Hansen, F. J. Keil, “Molecular modeling of diffusion and reaction in porous media”, Meeting SPP1155 on Molecular Modeling and Simulation in Process Engineering, Hamburg, Germany, 5th–6th March, 2009.
 - N. Hansen, R. Krishna, J. M. van Baten, A. T. Bell, and F. J. Keil “Diffusion limitation in the alkylation of benzene: A multiscale investigation”, 21st North American Catalysis Society Meeting, San Francisco, USA, 7th–12th June 2009.
 - N. Hansen, F. J. Keil, “Diffusion and reaction in zeolites - A multiscale approach”, Meeting SPP1155 on Molecular Modeling and Simulation in Process Engineering, Köln, Germany, 28th–29th September, 2009.

Lebenslauf

Persönliche Daten

Name Niels Hansen
Geburtsdatum 22.07.1977
Geburtsort Hamburg

Schulbildung

1984 – 1988 Gorch-Fock Grundschule Blankenese
1988 – 1997 Gymnasium Blankenese
06/1997 Abitur

Zivildienst

08/1997 – 08/1998 Altenheim der Auguste-Victoria-Stiftung
in Hamburg

Studium

10/1998 – 09/2000 Allgemeine Ingenieurwissenschaften an der
TU Hamburg-Harburg
10/2000 – 04/2004 Verfahrenstechnik an der TU Hamburg-Harburg
01/2002 – 06/2002 Chemical Engineering am Royal Institute
of Technology, Stockholm
04/2004 Abschluss: Diplom-Ingenieur

Wissenschaftliche Tätigkeit

06/2004 – 01/2010 Wissenschaftlicher Mitarbeiter an der
TU Hamburg-Harburg,
Institut für Chemische Reaktionstechnik
08/2006 – 12/2006, 08/2007 – 12/2007, 09/2008 – 12/2008
Forschungsaufenthalte an der University of
California, Berkeley